University of Strathclyde

Wavelength Modulation Spectroscopy with Tunable Diode Lasers: a Calibration-Free Approach to the Recovery of Absolute Gas Absorption Line-Shapes

Kevin Duffin

Department of Electronic and Electrical Engineering

Centre for Microsystems and Photonics

A thesis submitted to the Department of Electronic and Electrical Engineering of the University of Strathclyde for the degree of Doctor of Philosophy

April 2007

Signed: 

Date: 24/04/07

Acknowledgements

Firstly, I would like to thank both Walter and George for guiding me through this challenge. Walter, your (apparent) unwavering confidence that "it would all work out in the end" was a much needed comfort in the darker days. Your clarity of vision and ability to communicate the essence of the problem and its solution is remarkable and was invaluable in getting this project down on paper. George, your patience and understated genius were very much appreciated. You are a true gentleman! I have been extremely fortunate to work for and with both of you. I am well aware you are extremely busy people and I thank you for giving up your time so often, for so long and with such grace. Although you do not need to hear it from me, you are a genuine credit to the university!

Andrew, thank you for coming in at the right time and adding a fresh energy and viewpoint to the project. It was a good laugh working with you, even down in the lab at 9 o'clock at night on a Friday! Hopefully, when this is all over, you'll let me buy you that beer. You are a top bloke and I wish you good luck in getting over the finishing line.

David, Iain and Doug at OptoSci, thank you for your technical help and guidance. Also, cheers for the lessons in football management and tactics!

Borja, thanks for all your help and encouragement. I really enjoyed your company in and out of the office and I think we kept everyone entertained with our week-long debates (arguments) and attempts at winding each other up. Unfortunately for you, I always had the last word!

To Amy, Colin, Anartz, Gillian, Joanna and Atique: thanks for the laughs and the best of luck to all of you in your new careers. Thanks to Alistair and Ian; top RAs and top blokes! Thanks to everyone else at CMP for your support.

Thank you to my parents, Robert and Karen. I am as proud of you as you are of me.

Jacqueline: you are my strength, my hope and my happiness. Where would I be without you? Thank you for giving me everything you have.

I would like to acknowledge the Engineering and Physical Sciences Research Council (EPSRC) and OptoSci Ltd. for supporting this work.

Abstract

Tunable diode laser spectroscopy (TDLS) has become the preferred option for industrial gas monitoring. TDLS with direct detection provides absolute measurement of a rotational / vibrational gas absorption line transmission function, facilitating the extraction of gas concentration (from line strength measurement). TDLS with wavelength modulation spectroscopy (WMS) enables AC detection of absorption line *derivatives* at frequencies where laser and 1/f noise is reduced. Coupled with lock-in detection, this provides a sensitivity improvement of up to 2 orders of magnitude. At fixed temperature and pressure, calibration to signals measured on a known gas composition has been used successfully to determine system scaling factors. However, demand has grown for gas monitoring in environments where the gas pressure is constantly varying and unknown. This introduces significant errors in the analysis as the primary system scaling factor is a function of linewidth, which is varying with the unknown pressure. Errors also arise from the inaccuracies in determining a number of instrument scaling factors, including the AM and FM characterisation of the laser. Pressure measurements may be made and the errors in concentration corrected, if the gas absorption linewidth can be accurately measured from the recovered signals and the instrument scaling factors can be accurately determined. However, the lack of accurate *in-situ* wavelength referencing schemes for use in the field, make linewidth measurement extremely difficult. Add to this the fact that conventional TDLS / WMS measurements are prone to systematic interference and the errors accumulated from inaccurate instrument scaling (noted above) and linewidth measurement, could determine a large final error on the derived concentration and / or pressure.

This work reports the proposal, development and validation of both an in-fibre wavelength referencing scheme and a new technique for measuring the absolute absorption line transmission function using TDLS with WMS. Measuring the absolute absorption line transmission profile, as a function of the laser's wavelength scan across the absorption line, facilitates the extraction of the gas concentration and

pressure via comparisons to theory (based on HITRAN data). Through novel signal processing techniques, the approach is free from systematic distortion and is absolute without the need for calibration. This new approach provides many of the benefits of TDLS / WMS, whilst offering the simplicity and accuracy of TDLS with direct detection. The promising results show that we have significantly advanced TDLS technology towards realising a stand-alone instrument for determining accurate gas composition measurements in harsh industrial environments.

Contents

Chapter 1 Introduction **1**

1.1 Gas Sensing in Industrial Environments 1

1.2 Thesis Aims and Objectives 9

1.3 Thesis Overview 10

1.4 References 12

Chapter 2 Review of Gas Monitoring Methods using Near IR Tunable Diode Laser Spectroscopy **16**

2.1 Introduction 16

2.2 Principles of Tunable Diode Laser Spectroscopy with Direct Detection 17

2.3 Principles of Tunable Diode Laser Spectroscopy with Wavelength Modulation Spectroscopy 20

2.4 Literature Review 23

2.5 Conclusions 27

2.6 References 30

Chapter 3 Analytical Methodologies: Fundamentals of Molecular Spectroscopy **35**

3.1 Introduction 35

3.2 Formation of Gas Absorption Line Spectra 36

3.3 Vibrational Spectroscopy and Infra-red Spectra 39

3.4 Width of Line Spectra 48

3.4.1 *Natural Broadening* 48

3.4.2 *Doppler Broadening* 50

3.4.3 *Collision Broadening* 51

3.4.4 *The Voigt Profile* 52

3.5 Intensity of Line Spectra 52

3.5.1 *Transition Probability* 52

3.5.2 *Population of States* 53

3.5.3 *The Beer – Lambert Law* 53
3.6 Extracting Concentration and Pressure from Line Spectra 54
3.6.1 *Concentration and Absolute and Derivative Signals* 54
3.6.2 *Pressure and Absolute and Derivative Signals* 57
3.7 Modelling Line Spectra 60
3.8 Conclusions 63
3.9 References 64

Chapter 4 Experimental Methodologies: Systems and Procedures 66
4.1 Introduction 66
4.2 Tunable Diode Laser Spectroscopy with Direct Detection 68
4.2.1 *Signal Source and Drive Electronics* 69
4.2.2 *Gas Measurement* 73
4.2.3 *Power Referencing* 75
4.2.4 *Wavelength Referencing* 76
4.2.5 *Data Collection* 86
4.2.6 *Measurement Procedure and Signal Processing* 87
4.3 Tunable Diode Laser Spectroscopy with Wavelength Modulation Spectroscopy 89
4.3.1 *Signal Source and Drive Electronics* 90
4.3.2 *Gas Measurement* 93
4.3.3 *Power Referencing* 98
4.3.4 *Wavelength Referencing* 98
4.3.5 *Data Collection* 102
4.3.6 *Measurement Procedure and Signal Processing* 103
4.4 Conclusions 105
4.5 References 106

Chapter 5 Results and Analysis 108
5.1 Introduction 108
5.2 TDLS with Direct Detection 109
5.2.1 *Introduction* 109

5.2.2 *The Need for Accurate Wavelength Referencing* 110
5.2.3 *Determining the N_2 Broadening Coefficient* 114
5.2.4 *Accurate and Simultaneous Measurement of Gas Concentration and Pressure using Curve Fitting* 119
5.2.5 *Conclusions* 124
5.3 Conventional TDLS with WMS Detection 125
5.3.1 *Introduction* 125
5.3.2 *Signal Analysis: Identification of Problems* 126
5.3.3 *Revised Analytical Treatment of Conventional TDLS with WMS Detection* 135
5.3.4 *Conclusions* 139
5.4 Novel Approach to Removing Systematic RAM Interference 141
5.4.1 *Theoretical Principle* 141
5.4.2 *Revised Experimental System and Procedure* 142
5.4.3 *Results and Discussion* 144
5.4.4 *Conclusions* 151
5.5 Novel Approach to Recovering the Absolute Absorption Line Transmission Function using TDLS with WMS Detection 152
5.5.1 *Theoretical Principle* 152
5.5.2 *Revised Experimental System and Procedure* 158
5.5.3 *Results and Discussion* 159
5.5.4 *Conclusions* 166
5.6 Conclusion 167
5.7 References 169

Chapter 6 Results and Analysis 2 **171**
6.1 Introduction 171
6.2 Increasing the Modulation Frequency 172
6.2.1 *Introduction* 172
6.2.2 *Revised Experimental System and Procedure* 173
6.2.3 *Results and Discussion* 173
6.2.4 *Conclusions* 185

6.3 Finding the 90 ° Separation Point 187
6.3.1 *Introduction* 187
6.3.2 *Revised Experimental System and Procedure* 187
6.3.3 *Results and Discussion* 189
6.4 Simultaneous Measurement of Gas Concentration and Pressure 192
6.5 Conclusions 203
6.6 References 205

Chapter 7 Conclusions and Further Work 206
7.1 Conclusions 206
7.2 Further Work 210
7.3 References 213

Appendix A Research Publications 214
Appendix B Fibre Ring-Resonator MATLAB Program 216
Appendix C:1 Direct Wavelength Referencing MATLAB Program 218
Appendix C:2 FINDPEAK MATLAB Program 221
Appendix C:3 Derivative Wavelength Referencing MATLAB Program 224
Appendix C:4 RAM Wavelength Referencing MATLAB Program 229
Appendix D 2^{nd} Order Taylor Series Expansion of Lorentzian Broadened Absorption Line 233

Chapter 1

Introduction

1.1 Gas Sensing in Industrial Environments

Initially gas detection in industrial environments consisted of relatively simple devices that were developed to satisfy elementary safety and environmental concerns. A typical implementation of this is known as a pellistor [1.1 and 1.2], which uses a process of catalytic combustion to detect methane / hydrocarbons in air. Pellistors are commonly used in such environments as oil and gas exploration sites, water treatment plants and landfill sites. Pellistor detector elements consist of a heated platinum wire coil encased in a bead of catalytic material. At temperatures above 300 °C oxidation of the hydrocarbon (burning) readily occurs at the detector element. This reaction increases the temperature of the platinum wire and hence its resistance, unbalancing the Wheatstone bridge arrangement in which it is placed. The temperature / resistance change is then proportional to the gas concentration.

This technique is very accurate when detecting hydrocarbon gas concentrations in the region between their upper and lower explosive limits, UEL and LEL[1] respectively. Pellistors can provide detection down to ppm levels; however, detecting above the UEL becomes difficult as there is insufficient oxygen for the *burning* to take place. With this device, discriminating between hydrocarbon gases and / or detecting gases other than hydrocarbons is impossible. In order to have sufficient heat for the reaction to take place, a constant DC current is required; this is not only expensive but not intrinsically safe. Pellistors are also susceptible to catalytic poisoning, leading to deterioration and calibration drift. Thus, they require regular calibration checks and eventually, replacement; again this is expensive. Finally, due to their poisoning issues and slow response time, pellistors are not suited to operating in the continuous presence of gas.

Non dispersive infra-red (NDIR) detection, using mid infra-red light emitting diodes (LEDs), [1.3] is an attractive alternative. These use wavelengths coinciding with the strong fundamental absorption bands of most atmospheric gases (2.5 to 3.5 μm). An illustration of two popular NDIR system configurations is shown in figure 1.1 [1.4]. As can be seen from the figure, the general approach of a mid infra-red gas analyser relies on two signal channels; a gas measurement channel and a reference channel. The channels are scaled and balanced to provide a fixed DC output when no target gas is present in the cell. When gas is present, absorption on the gas measurement signal leads to an imbalance, yielding an output proportional to the gas concentration. The two signals are generated in one of two ways. The first uses two broad band LEDs, shown in figure 1.1 (a). The "Gas LED" operates with emission wavelengths coinciding with the fundamental absorption band of the target gas. The "Reference LED" operates with emission wavelengths outside the gas absorption band. A second approach, shown in figure 1.1 (b), uses one broad band source LED emitting at a range of wavelengths covering the absorption band and a region away from any absorption. Two detectors employ filters at their input. The "Gas Detector" filter is chosen to have a spectral distribution over the absorption band of

[1] Lower explosive limit (LEL) of a gas is the lowest concentration of that gas by volume in air which, when ignited, will cause an explosion

the target gas, and the filter attached to the "Reference Detector" has a spectral distribution away from any target gas absorption.

NDIR gas sensors have many advantages over pellistor-based systems; for example, they do not rely on a catalytic combustion process, permitting the detection of gases other than hydrocarbons and gas concentrations from ppm level up to 100 %. The sensors also work effectively in the continuous presence of gas as they do not suffer from poisoning.

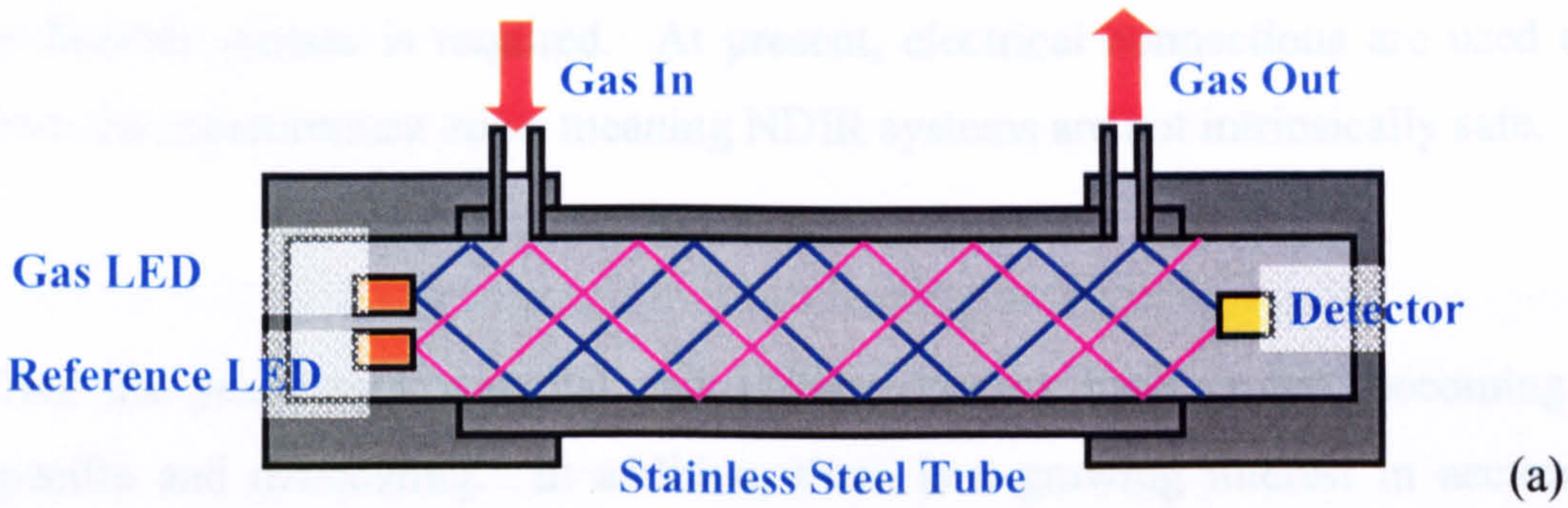

Figure 1.1: NDIR sensor configurations (a) Dual source, single detector (b) Single source, dual detector

There are still, however, a number of considerable limitations with NDIR approaches, which have been noted by fellow researchers within the group at Strathclyde in the past [1.4 and 1.5] and a summary is given here. The first, most

obvious limitation, is the calibration issues concerned with using two independent sources or receivers. For example, in [1.4] it was noted that two different LEDs responded to temperature change in different ways, yielding false signals through calibration drift. Secondly, the sensitivities of mid infra-red systems can be in the several ppm.m range; however, for reasonable signal-to-noise ratio the detectors must be cooled, adding further expense and complexity. Another major issue is that the broad band sources / detectors used in NDIR systems are susceptible to interference from other atmospheric gases that have absorption lines close to that of the target gas. It is not possible to use these systems with conventional silica optical fibres. The problem being that at wavelengths beyond 2 μm, silica is practically opaque. In order to achieve remote detection, further investigation into chalcogenide or fluoride glasses is required. At present, electrical connections are used to and from the measurement zone, meaning NDIR systems are not intrinsically safe.

Over the years environmental and safety concerns have grown, becoming more specific and demanding. In addition, there is a growing interest in accurate gas measurements for industrial process control applications, providing even greater challenges in terms of measurement reliability, calibration and robustness. Therefore, although the pellistor and NDIR approaches provide satisfactory levels of detection, the sensor-detector range, the power consumption, the high maintenance / calibration concerns and the intrinsic safety issues have encouraged the development of alternative optical measurement technologies. In particular, interest in tunable diode laser spectroscopy (TDLS) has grown enormously.

TDLS techniques involve sweeping the frequency of relatively high power, narrow band sources across individual vibration-rotation gas absorption lines. This technique of repeatedly frequency scanning the line, combined with "off-line zero-point referencing", has many advantages over NDIR spectroscopy by providing calibration-stable, gas-specific, concentration measurements of most environmental gases. Initially mid infra-red (IR) lasers were used to address the strong fundamental

absorption bands of the gases [1.6 - 1.11], but the potential of this technique in industrial applications was hindered by the poor quality detectors that required expensive cooling mechanisms. TDLS at near infra-red wavelengths [1.12 – 1.19] (addressing the weaker overtone absorption bands) offered greater potential due to the widespread availability of inexpensive, high quality laser sources and detectors. Near infra-red TDLS systems employing distributed feedback (DFB) lasers and InGaAs photodetectors provided similar detection sensitivities to mid infra-red schemes, even though the overtone bands addressed are up to two orders of magnitude weaker. Further development saw the exploitation of single mode optical fibre networks (compatible with near infra-red wavelengths and optical communications components), facilitating remote, multi-point detection in the most demanding of environments [1.5 & 1.20 – 1.22].

In TDLS with direct detection, the absolute rotational-vibrational gas absorption line transmission function is recovered. Direct measurements of the linewidth and line strength of the recovered transmission function can be used to measure the concentration and the pressure or to compensate for pressure variations in the analysis. Alternatively, a common approach is to employ curve fitting procedures, matching theoretical predictions of the transmission profile (based on spectroscopic data) to the recovered traces. The best fit to the linewidth and line strength then yields the pressure and concentration.

In the more sensitive adaptation, TDLS with wavelength modulation spectroscopy (WMS), the recovered 1^{st} or 2^{nd} harmonic signal relates to either the 1^{st} or 2^{nd} derivative of the gas absorption line transmission function respectively. When recovering 1^{st} derivative signals, the concentration is proportional to the signal amplitude and the slope through the mid-point zero. When recovering 2^{nd} derivative signals, the concentration is determined purely from the amplitude (this represents the slope through the mid-point zero on the 1^{st} derivative). Tunable diode laser spectroscopy with WMS, using calibration to a known gas composition, has proven

to be very successful in terms of gas concentration measurements at fixed temperature and pressure, and reflects the current state-of-the-art for commercial environmental TDLS gas monitoring systems [1.5 & 1.20].

In industrial applications gas pressures and consequently absorption linewidths are often varying and unknown, and it is in these situations that the extra sensitivity offered by TDLS / WMS techniques is balanced against the increased complexity in signal analysis and scope for error therein. In TDLS with WMS, the recovered derivative signal amplitudes have a strong dependency on the gas absorption linewidth, as described more accurately by equations (3.17) and (3.18) in chapter 3. These equations show that the amplitude of the 1st derivative signal has a dependency of $1/\gamma^2$ (where γ is the half-width-half-maximum linewidth) and the amplitude of the 2nd derivative has a dependency of $1/\gamma^3$. This dependency is illustrated in figure 1.2 below, where the measured 1st and 2nd derivatives of the overtone absorption line of methane (around 1650 nm) at 10 % concentration are shown for two different pressures (linewidths). As can be seen from the figure, extracting concentration from the signal amplitude and slope through the mid-point zero on the 1st derivative signal (figure 1.2 (b)) or from the signal amplitude at line centre on the 2nd derivative signal (figure 1.2 (c)), would lead to significant errors. Note also that the depth (signal amplitude) of the direct transmission function (figure 1.2 (a)) only shows a very weak dependence on the linewidth.

From the above analysis, pressure measurements may be made and the errors corrected (in both direct and derivative signals), if the gas absorption linewidth can be accurately determined from the recovered signals. However, the lack of reliable, *in-situ* wavelength referencing schemes (discussed later in chapters 2, 4 and 5) for use in the field, make accurate linewidth measurement extremely difficult. In addition, systematic interference [1.23 - 1.25] on derivative traces, recovered using current TDLS / WMS techniques, add further complexity and scope for error to linewidth recovery.

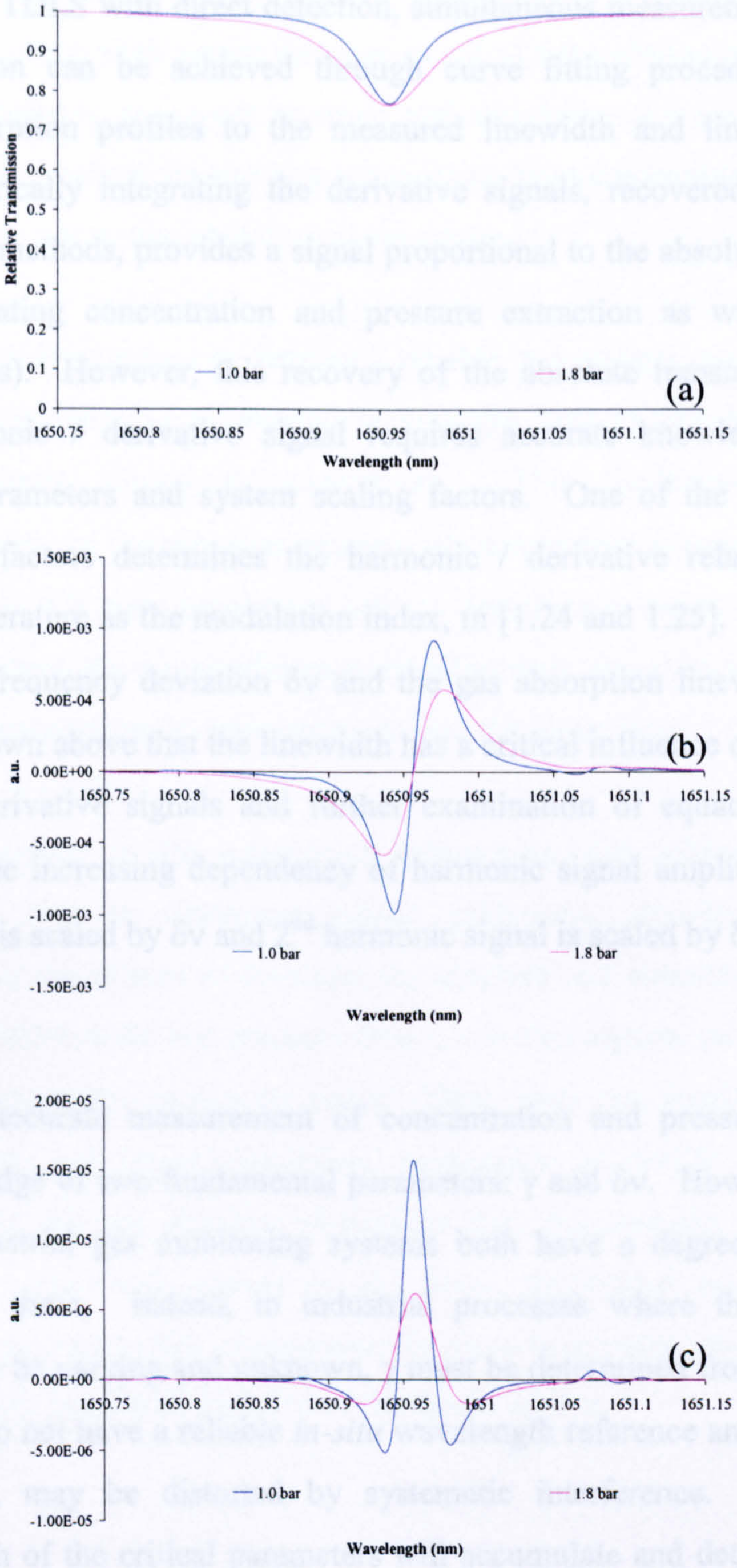

Figure 1.2: 10.13 % CH_4 in air at room temperature for 1.0 bar and 1.8 bar pressure (a) Absolute transmission function, (b) 1st derivative, (c) 2nd derivative

With accurate wavelength scales applied to the absolute transmission signals, recovered using TDLS with direct detection, simultaneous measurement of pressure and concentration can be achieved through curve fitting procedures, matching theoretical absorption profiles to the measured linewidth and line strength. In principle, numerically integrating the derivative signals, recovered from TDLS / WMS detection methods, provides a signal proportional to the absolute transmission function (facilitating concentration and pressure extraction as with the directly measured signals). However, this recovery of the absolute transmission function from the harmonic / derivative signal requires accurate knowledge of all the experimental parameters and system scaling factors. One of the most important system scaling factors determines the harmonic / derivative relationship and is quoted in the literature as the modulation index, m [1.24 and 1.25]. m is dependent on the applied frequency deviation $\delta\nu$ and the gas absorption linewidth, γ. It has already been shown above that the linewidth has a critical influence on the amplitude of recovered derivative signals and further examination of equations (3.17) and (3.18) reveals the increasing dependency of harmonic signal amplitudes on $\delta\nu$ (1^{st} harmonic signal is scaled by $\delta\nu$ and 2^{nd} harmonic signal is scaled by $\delta\nu^2$).

In conclusion, accurate measurement of concentration and pressure depends on accurate knowledge of two fundamental parameters: γ and $\delta\nu$. However, in current stand-alone industrial gas monitoring systems both have a degree of uncertainty associated with them. Indeed, in industrial processes where the pressure and temperature may be varying and unknown, γ must be determined from the recovered signals, which do not have a reliable *in-situ* wavelength reference and, in the case of TDLS / WMS, may be distorted by systematic interference. The errors in determining each of the critical parameters will accumulate and determine the final error on the extracted concentration and pressure.

1.2 Thesis Aims and Objectives

The overall aim of this work was to develop robust TDLS techniques (for both direct and WMS adaptations), to permit accurate and simultaneous measurement of gas concentration and pressure, for use in a stand-alone, field-deployable instrument. In order to achieve this aim, two objectives were devised.

1. The first objective was to develop a reliable wavelength referencing scheme to enable mapping of an absolute wavelength scale to time-based absorption measurements (direct or derivative). This facilitates the accurate measurement of the vibration-rotation gas absorption linewidth, γ. Previous attempts at this were researched and are described in chapter 2; however, in order to eliminate the interference and alignment issues associated with bulk optic approaches, an in-fibre approach was the target here.

2. Once accurate, *in-situ* wavelength referencing was achieved, the second objective was to determine robust calibration algorithms and signal processing procedures to facilitate the accurate and simultaneous extraction of gas concentration and pressure from recovered signals, paying attention to the system scaling factors $\delta\nu$ and γ. There were two possible curve fitting procedures: (a) fitting theoretical predictions of (either fundamental or derivatives of) the absolute absorption line transmission function to the respective measured signals or (b) fitting theoretical predictions of the absolute absorption line transmission function to directly recovered signals or numerically integrated derivative / harmonic signals.

1.3 Thesis Overview

Chapter 2 reviews two of the most common TDLS techniques used in current state-of-the-art industrial gas monitoring systems, namely: TDLS with direct detection and TDLS with wavelength modulation spectroscopy. The review includes a description of the principles of operation of the two techniques, highlighting the signal processing and calibration issues associated with them. The chapter also provides a more detailed account of the aims and objectives of this work.

Chapter 3 provides a theoretical appreciation of molecular gas absorption spectroscopy, describing in detail all the factors affecting the shape, depth and width of gas absorption spectra. Chapter 3 also describes the process of achieving highly accurate theoretical predictions of gas absorption spectra for the purposes of curve fitting to experimental data.

Chapter 4 explains in detail the realisation of robust direct TDLS and TDLS / WMS systems (reflecting the current state-of-the-art) in the laboratory, including vital calibrations against changes in signal power and system losses. This chapter also discusses the conventional method for removing systematic interference and the design, build and test of an in-fibre wavelength referencing scheme.

Chapter 5 gives an in-depth analysis of the results from the two TDLS approaches described in chapter 4. The issues that limited these conventional approaches are investigated and solved to provide the basis of two robust techniques for measuring gas concentration and pressure in stand-alone, field-deployable instruments. In so doing, chapter 5 validates the accuracy and reliability of our wavelength referencing approach and curve fitting procedure for extracting concentration and pressure, and proposes a novel technique for measuring the absolute absorption line transmission function using 1^{st} harmonic WMS detection.

Chapter 6 describes the development and improvement of the novel TDLS / WMS approach discussed in chapter 5, providing greater signal-to-noise ratio and increased accuracy in the measurement of pressure and concentration.

Finally, chapter 7 concludes the thesis and provides a discussion on some future work.

1.4 References

[1.1] http://www.citytech.com/technology/pellistors.asp

[1.2] http://www.crowcon.com/talking_gas_pellistor_systems.htm

[1.3] C. H. Wang, J. O. Crowder, V. Mannheim, T. Ashley, D. T. Dutton, A. D. Johnson, G. J. Pryce and S. D. Smith, "Detection of Nitrogen Dioxide Using a Room Temperature Operation Mid – Infrared LnSb Light Emitting Diode," Electronics Letters, Vol. 34, No. 3, February 1998.

[1.4] C. Massie, G. Stewart, G. McGregor and J. R. Gilchrist, "Design of a Portable Optical Sensor for Methane Gas Detection," Sensors and Actuators B: Chemical, Vol. 113, pp 830-836, February 2006.

[1.5] B. Culshaw, G. Stewart, F. Dong, C. Tandy and D. Moodie, "Fibre Optic Techniques for Remote Spectroscopic Methane Detection – from Concept to System Realisation," Sensors and Actuators B: Chemical, Vol. 51, pp 25-37, August 1998.

[1.6] E. D. Hinkley, "High-Resolution Infrared Spectroscopy with a Tunable Diode Laser," Applied Physics Letters, Vol. 16, No. 9, pp 351-354, May 1970.

[1.7] J. Reid, J. Shewchun, B. K. Garside and E. A. Ballik, "High Sensitivity Pollution Detection employing Tunable Diode Lasers," Applied Optics, Vol. 17, No. 2, pp 300-307, January 1978.

[1.8] J. Reid, B. K. Garside, J. Shewchun, M. El-Sherbiny and E. A. Ballik, "High Sensitivity Point Monitoring of Atmospheric Gases employing Tunable Diode Lasers," Applied Optics, Vol. 17, No. 11, pp 1806-1810, June 1978.

[1.9] D. T. Cassidy and J. Reid, "Atmospheric Pressure Monitoring of Trace Gases using Tunable Diode Lasers," Applied Optics, Vol. 21, No. 7, pp 1185-1190, April 1982.

[1.10] M. Lowenstein, "Diode Laser Harmonic Spectroscopy applied to in situ Measurements of Atmospheric Trace Molecules," Journal of Quantitative Spectroscopy and Radiative Transfer, Vol. 40, pp 249-256, September 1988.

[1.11] D. S. Bomse, A. C. Stanton and J. A. Silver, "Frequency Modulation and Wavelength Modulation Spectroscopies: Comparison of Experimental Methods using a Lead – Salt Diode Laser," Applied Optics, Vol. 31, No. 6, pp 718-731, February 1992.

[1.12] W. Lenth, "Optical Heterodyne Spectroscopy with Frequency- and Amplitude- Modulated Semiconductor Lasers," Optics Letters, Vol. 8, No. 11, pp 575-577, November 1983.

[1.13] D. T. Cassidy and L. J. Bonnell, "Trace Gas Detection with Short – External – Cavity InGaAsP Diode Laser Transmitter Modules Operating at 1.58 μm," Applied Optics, Vol. 27, No. 13, pp 2688-2693, July 1988.

[1.14] F. S. Pavone and M. Inguscio, "Frequency- and Wavelength- Modulation Spectroscopies: Comparison of Experimental Methods using an AlGaAs Diode Laser," Applied Physics B: Lasers and Optics, Vol. 56, No. 2, pp 118-122, February 1993.

[1.15] A. Lucchesini, I. Longo, C. Gabbanini, S. Gozzini and L. Moi, "Diode Laser Spectroscopy of Methane Overtone Transitions," Applied Optics, Vol. 32, No. 27, pp 5211-5216, September1993.

[1.16] A. Lucchesini, M. De Rosa, D. Pellicia, A. Ciucci, C. Gabbanini and S. Gozzini, "Diode Laser Spectroscopy of Overtone Bands of Acetylene,"

Applied Physics B: Lasers and Optics, Vol. 63, No. 3, pp 227-282, September 1996.

[1.17] M. Gabrysh, C. Corsi, F. S. Pavone and M. Inguscio, "Simultaneous Detection of CO and CO_2 using a Semiconductor DFB Diode Laser at 1.578 μm," Applied Physics B: Lasers and Optics, Vol. 65, No. 1, pp 75-79, July 1997.

[1.18] X. Zhu and D. T. Cassidy, "Modulation Spectroscopy with a Semiconductor Diode Laser by Injection - Current Modulation," Journal of the Optical Society of America B: Optical Physics, Vol. 14, No. 8, pp 1945-1950, August 1997.

[1.19] G. Hancock, V. L. Kasyutich and G. A. D. Ritchie, "Wavelength – Modulation Spectroscopy using a Frequency – Doubled Current – Modulated Diode Laser," Applied Physics B: Lasers and Optics, Vol. 74, No. 6, pp 569-575, April 2002.

[1.20] G. Stewart, C. Tandy, D. Moodie, M. A. Morante and F. Dong, "Design of a Fibre Optic Multi-Point Sensor for Gas Detection," Sensors and Actuators B: Chemical, Vol. 51, pp 227-232, August 1998.

[1.21] H. L. Ho, W. Jin, and M. S. Demokan, "Sensitive, Multipoint Gas Detection using TDM and Wavelength Modulation Spectroscopy," Electronics Letters, Vol. 36, No. 14, pp 1191-1193, July 2000.

[1.22] H. L. Ho, W. Jin, H. B. Yu, K. C. Chan, C. C. Chan and M. S. Demokan, "Experimental Demonstration of a Fiber-Optic Gas Sensor Network Addressed by FMCW," IEEE Photonics Technology Letters, Vol. 12, No. 11, pp 1546-1548, November 2000.

[1.23] L. C. Philippe and R. K. Hanson, "Laser Diode Wavelength-Modulation Spectroscopy for Simultaneous Measurement of Temperature, Pressure, and Velocity in Shock-Heated Oxygen Flows," Applied Optics, Vol. 32, No. 30, pp 6090-6103, October 1993.

[1.24] I. Linnerud, P. Kaspersen and T. Jaeger, "Gas Monitoring in the Process Industry using Diode Laser Spectroscopy," Applied Physics B: Lasers and Optics, Vol. 67, No. 3, pp 297-305, September1998.

[1.25] S. Schilt, L. Thevenaz and P. Robert, "Wavelength Modulation Spectroscopy: Combined Frequency and Intensity Laser Modulation," Applied Optics, Vol. 42, No. 33, pp 6728-6738, November 2003.

Chapter 2

Review of Gas Monitoring Methods using Near IR Tunable Diode Laser Spectroscopy

2.1 Introduction

Tunable diode laser spectroscopy (TDLS) offers major advantages over many other optical gas sensing approaches, particularly when considering application to industrial gas monitoring. The use of diode laser sources with high spectral power density allows for increased signal-to-noise ratio over broad band optical schemes. The high signal power, coupled with the use of optical fibres means that the laser source and control electronics can be housed remotely (even kilometres away) from the measurement zone, making TDLS gas analysers intrinsically safe. Narrow linewidths and precise tuning also permit the interrogation of individual rotation-vibration gas absorption lines, providing immunity to interference from other atmospheric gases. Thermal and current feedback control of the laser frequency and the use of a technique known as "off-line zero-point referencing" mean TDLS gas

analysers are extremely calibration stable. These are the main reasons why tunable diode laser spectroscopy offers the greatest potential in terms of delivering quantitative gas measurements in modern industrial applications.

In this chapter a review is presented of the two TDLS techniques most commonly used in current industrial gas monitoring applications: TDLS with direct detection and TDLS with wavelength modulation spectroscopy. This review provides a description of the principles of operation of the two techniques (based on references [2.1 – 2.16]) and discusses their limitations with regard to achieving accurate and simultaneous gas concentration and pressure measurements in a stand-alone, field-deployable instrument.

2.2 Principles of Tunable Diode Laser Spectroscopy with Direct Detection

A system diagram illustrating the basic approach to tunable diode laser spectroscopy with direct detection is shown below in figure 2.1.

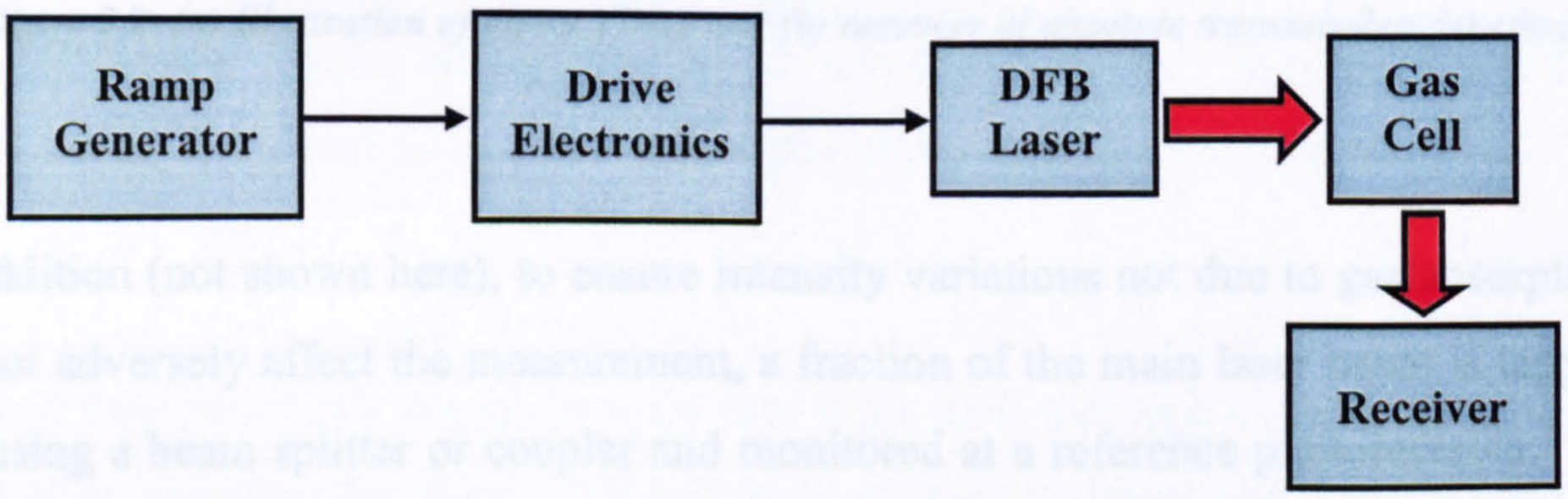

Figure 2.1: System diagram of direct TDLS

The principle of operation is illustrated in figure 2.2 and a description is provided here. The DFB laser is temperature tuned such that its centre frequency, f, is in close proximity to a known single vibrational-rotational absorption line of the target gas. The centre frequency is then swept across the full width of the line by the application of a time (t) varying, low frequency (several Hz) ramp to the laser's injection current, i. As the laser output is swept across the line the laser intensity is monitored at a photoreceiver situated beyond the interrogation region.

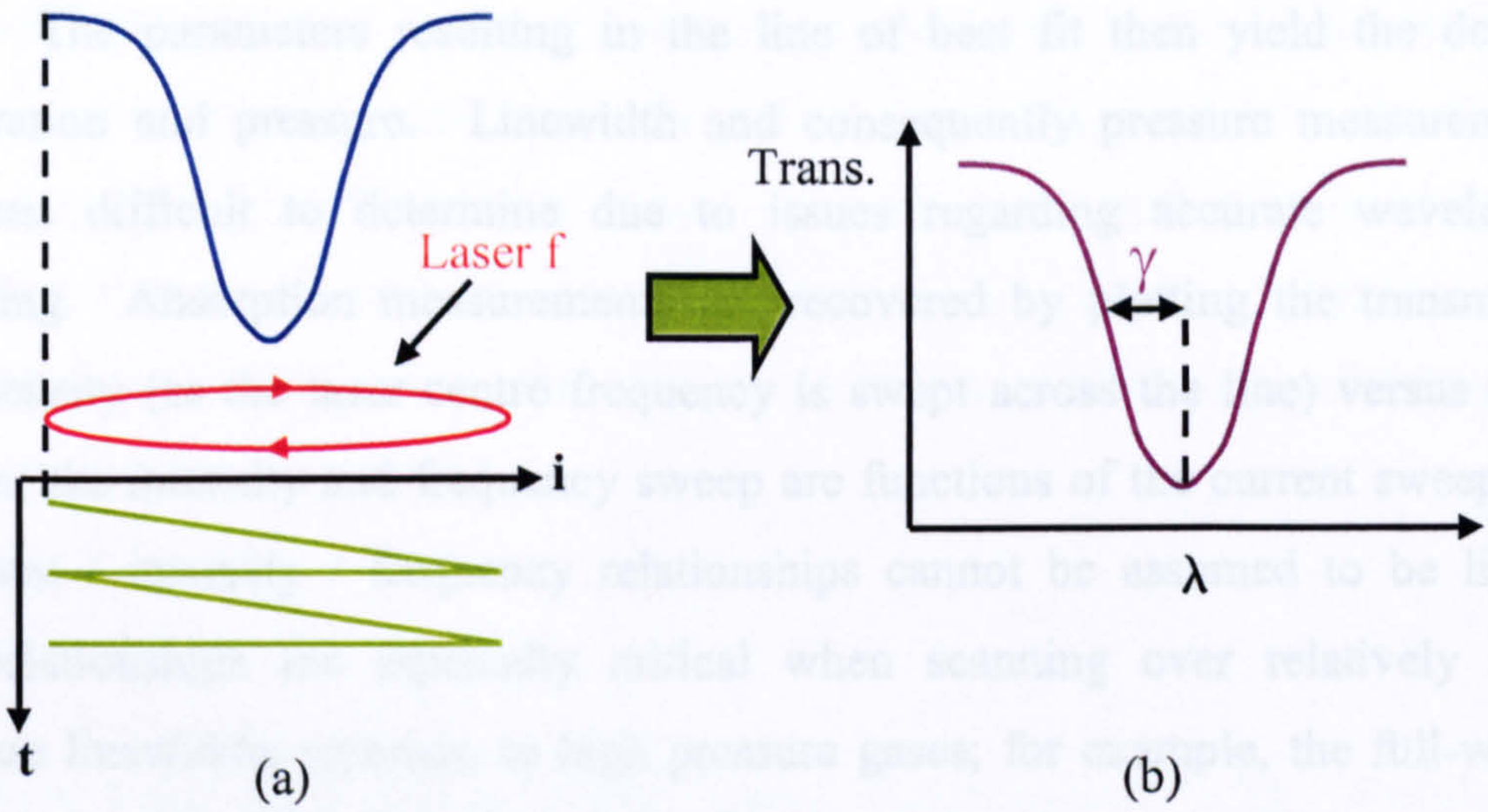

Figure 2.2: (a) Illustration of direct TDLS and (b) recovery of absolute transmission function

In addition (not shown here), to ensure intensity variations not due to gas absorption do not adversely affect the measurement, a fraction of the main laser beam is tapped off using a beam splitter or coupler and monitored at a reference photoreceiver. To compensate for the differences between the main beam and the reference beam, a ratio is taken of the two signals at a point away from any gas absorption, known as an "off-line" measurement; the ratio is known as a "zero-point reference". Normalisation to the intensity variation as the laser is scanned across the absorption feature and to the zero-point reference provides accurate recovery of the absolute absorption line transmission function, from which it is possible to determine

quantitative measurements of the gas composition. This particular method of normalisation provides immunity to calibration drift and system loss variations.

Chapter 3 describes in detail the influence of pressure and concentration on gas absorption lines; suffice to mention here that the gas concentration can be extracted from the depth of the transmission function, and the gas pressure can be extracted from the half-width-half-maximum (HWHM) linewidth, γ. Alternatively, models of the absorption line transmission function (based on spectroscopic data) can be used in curve fitting algorithms to match these profiles to the experimentally measured signals. The parameters resulting in the line of best fit then yield the desired concentration and pressure. Linewidth and consequently pressure measurements have been difficult to determine due to issues regarding accurate wavelength referencing. Absorption measurements are recovered by plotting the transmitted laser intensity (as the laser centre frequency is swept across the line) versus time. However, the intensity and frequency sweep are functions of the current sweep and the current / intensity / frequency relationships cannot be assumed to be linear. These relationships are especially critical when scanning over relatively large absorption linewidths common to high pressure gases; for example, the full-width-half-maximum (FWHM) linewidth of a CH_4 absorption line at 1650.956 nm and 2 atmospheres pressure is ~ 7.2 GHz. With inherent laser drift through a period of time, the sweep cannot be assumed to be repeatable either. Hence, for accurate linewidth measurement an *in-situ* wavelength referencing scheme is required.

In applications where signal powers are high and the target gases have high absorption linestrengths, direct TDLS is an inexpensive, simple and reliable solution to gas concentration measurement in industrial environments. However, when received signal powers are low and / or when the target gases have only weak absorption linestrengths or low concentrations, the sensitivity offered by direct TDLS is insufficient. A common solution to increase system sensitivity is to employ measurement cells with path lengths metres long, or with short multiple passes.

However, for stand-alone, field-deployable instruments, long measurement cells are impractical and when considering multi-point sensing, multiple pass cells, requiring highly reflective mirrors, would simply be too expensive. Besides, limitations in sensitivity essentially stem from the principle of detecting at DC. Firstly, there are resolution issues in attempting to resolve a small absorption on a large DC background [2.16]. The problem is exacerbated with increasing temperature, where significant and increasing levels of infra-red radiation (emitting from any object in the measurement zone) exist at the measurement wavelengths. This results in an increased DC background level (with noise fluctuations) that remains even after normalisation procedures, making even the strongest absorption difficult to resolve. In addition, DC detection is also susceptible to laser noise (1/f in nature and thus decreasing with increasing modulation frequency) and background drift. By shifting the detection to higher frequencies, where laser noise and drift is reduced [2.16], TDLS with wavelength modulation spectroscopy provides improved signal-to-noise ratio (SNR) and sensitivity and eliminates the problems with background DC signals in high temperature applications.

2.3 Principles of Tunable Diode Laser Spectroscopy with Wavelength Modulation Spectroscopy

Tunable diode laser spectroscopy with wavelength modulation spectroscopy (WMS) requires only minor adjustments to the direct TDLS system architecture; these are shown in the system diagram in figure 2.3.

In this technique there is a double modulation on the laser injection current: firstly, as with the direct version, there is a low frequency ramp (tens of Hz) to sweep the laser centre frequency over the entire width of the absorption feature; secondly, there is a smaller amplitude, higher frequency (tens of kHz) sinusoidal dither to interrogate the lineshape. The amplitude of the frequency deviation is usually defined in terms of

the modulation index, m ($m = \delta\nu/\gamma$, $\delta\nu$ is the frequency deviation about the laser centre frequency and γ is the HWHM linewidth as before). An illustration of the general principle of operation is shown in figure 2.4.

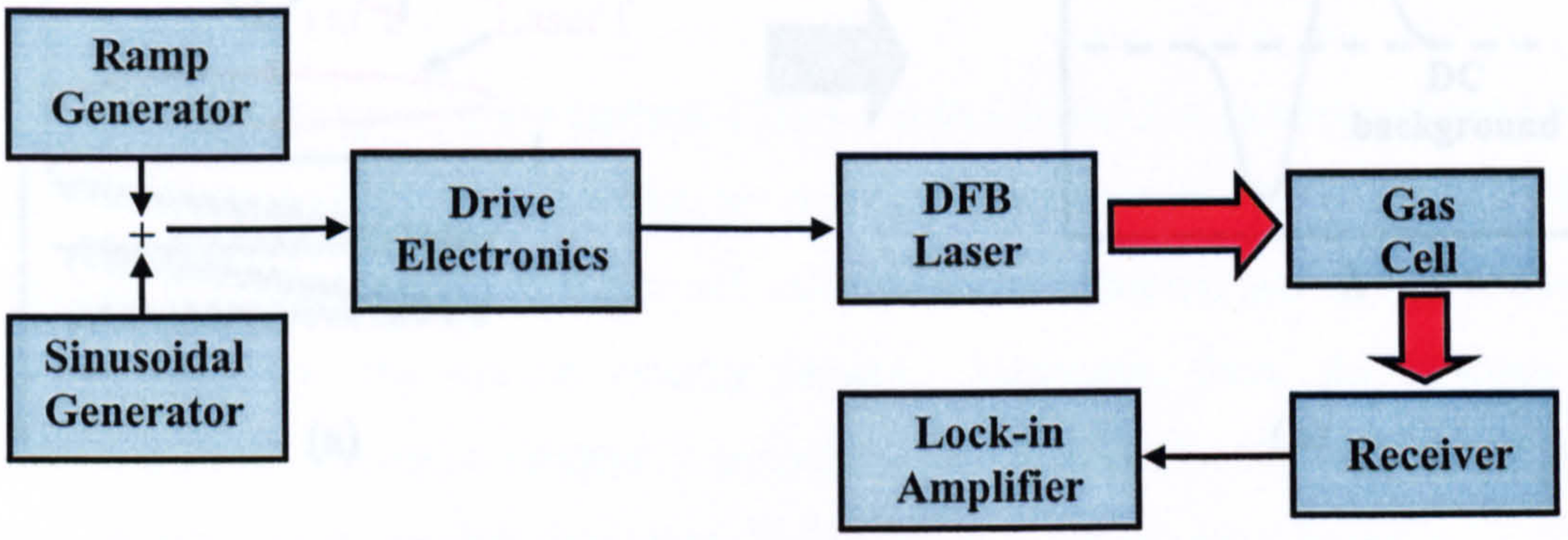

Figure 2.3: System diagram of TDLS / WMS

An amplitude modulation (AM) signal is produced when the frequency modulated (FM) light interacts with the gas absorption line (see figure 2.4). When the lock-in amplifier is set to measure the 1st harmonic, the output records the variation in the AM signal at the fundamental modulation frequency. The amplitude of the recovered signal is then proportional to the 1st derivative of the gas absorption line transmission function. Relationships between derivative signals and concentration and pressure are described in detail in chapter 3; both the amplitude and the gradient through the mid-point zero of the recovered 1st derivative are proportional to the gas concentration, and the positions of the maximum and minimum are related to the linewidth and consequently the pressure. Modulation of a DFB laser's injection current also (unavoidably) results in a modulation of the laser output power at the same frequency. Therefore the desired AM signal (induced by the interaction of the FM light with the gas absorption line) is accompanied at the detector by a relatively large, fixed, stable amplitude-modulated signal at the same frequency, commonly referred to in the literature as residual amplitude modulation (RAM) [2.6, 2.13, 2.15 & 2.16].

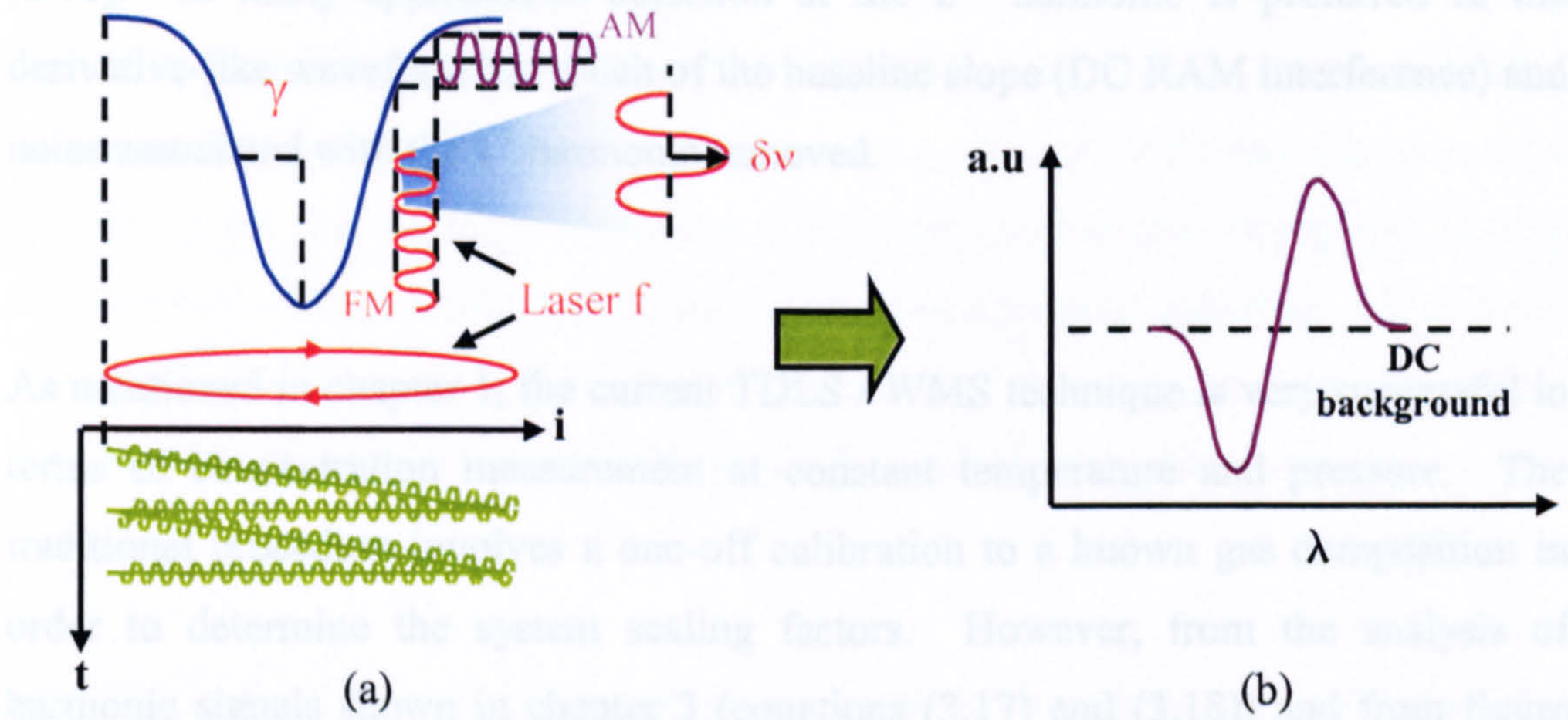

Figure 2.4: (a) Illustration of TDLS with WMS and (b) Recovered 1st derivative (1st harmonic) output from a lock-in amplifier

In 1st harmonic detection, a common limitation to achievable sensitivity is the large DC background produced by the lock-in amplifier's measurement of the RAM signal. Although removed from the FM derivative signal (usually by a DC offset or DC filter) to achieve a zero baseline, the DC RAM signal provides a useful reference for changes in system losses and detector sensitivities (common in industrial environments) and thus is monitored. As with the direct technique, the change in laser intensity as the centre frequency is scanned across the absorption feature is monitored at a reference photoreceiver. The off-line DC signal, in this case, provides a zero-point reference. Normalisation to these features then provides a useful derivative signal (immune to system loss variations and calibration drift) from which to determine gas measurements.

The interaction of the FM with the gas absorption line function also produces AM signals at higher harmonics of the fundamental modulation frequency. Indeed, it is the case that when the lock-in amplifier is set to record the variation in the AM signal at the n^{th} harmonic of the modulation frequency, the amplitude of the recovered

signal is proportional to the n^{th} derivative of the absorption line transmission function [2.16]. In many applications detection at the 2^{nd} harmonic is preferred as the derivative-like waveform has much of the baseline slope (DC RAM interference) and noise associated with the 1^{st} harmonic removed.

As mentioned in chapter 1, the current TDLS / WMS technique is very successful in terms of concentration measurement at constant temperature and pressure. The traditional procedure involves a one-off calibration to a known gas composition in order to determine the system scaling factors. However, from the analysis of harmonic signals shown in chapter 3 (equations (3.17) and (3.18)) and from figure 1.2 in chapter 1, it can be seen that the recovered signal amplitudes rely on a systematic scaling factor, dependent on the applied frequency deviation ($\delta\nu$) and the absorption HWHM linewidth (γ). Therefore, in order to extract accurate information relating to the gas composition, all of the system parameters, including $\delta\nu$, must be known precisely. In addition, in environments where the pressure is changing and unknown, the linewidths must be determined accurately from the recovered signals. As reported when discussing TDLS with direct detection, accurate linewidth measurement from signals recovered in stand alone, field-deployable instruments has been difficult to achieve, due to the lack of reliable, *in-situ* wavelength referencing schemes. Further complication arises in systems using TDLS / WMS techniques from the distortion of recovered derivatives by RAM interference (discussed further in section 2.4).

2.4 Literature Review

Tunable diode laser spectroscopy was originally reported in the 1970s [2.1 - 2.3]. Up until that time conventional spectrometers and gas lasers had been used to obtain gas absorption data, and the technique of using the unique capabilities of diode lasers, such as continuous tuning and narrow linewidths, was a novel approach to providing

high resolution measurements of absorption spectra. Through the next few years the use of the lead-salt diode lasers (IV – VI group of semiconductor materials) expanded, providing detection of most atmospheric gases via their strong mid infra-red absorption bands [2.4 – 2.6]. Unfortunately, the mid infra-red detectors (and sometimes the laser sources themselves) required cumbersome cryogenic cooling mechanisms. They were used in bulk optic measurement schemes, which were susceptible to vibrations and alignment issues. For these reasons, the use of mid infra-red TDLS detection never really took off in industrial applications.

After the optical fibre telecommunications boom in the 1990s, the technology for diode lasers constructed from the III – V group of semiconductor materials, extended to provide emission wavelengths in the near infra-red. There are much weaker (in some cases by a factor of 200) vibration-rotation absorption bands in the near infra-red; these are known as the overtones of the fundamental absorption bands, in the mid infra-red. The healthy comms market meant optical sources, such as distributed feed back (DFB) lasers and high quality receivers, such as InGaAs photodetectors, were widely available at low cost. DFBs, as tunable diode laser sources for near infra-red gas detection, offer many advantages; for example, although only weaker overtone absorption lines exist in the near infra-red, the high spectral density afforded by DFBs more than compensates. DFBs are also, inherently, single wavelength, allowing for species selectivity. With optical sources offering greater lifetime, gas specificity and lower operation cost, coupled with the high quality receivers offering similar detection to mid infra-red techniques, near infra-red TDLS gas measurements attracted great interest [2.7 – 2.14]. For a more in-depth review of the recent advances in laser based gas monitors see [2.15 & 2.16].

Another benefit of operating in the near infra-red was the ability to exploit optical fibre networks to provide remote, multi-point detection, [2.17 – 2.20] whilst overcoming the vibration and alignment issues that limited bulk-optic mid infra-red TDLS detection schemes. This finally meant tunable diode laser spectroscopy was

unrivalled in terms of potential to meet modern industrial gas monitoring challenges; providing solutions to the main calibration, reliability, sensitivity and cost issues. A general fibre system diagram is shown in figure 2.5. Fellow researchers within the group at Strathclyde University have had great success with this technique; developing a system that is, arguably, the current state-of-the-art, in terms of commercial environmental remote gas monitoring products [2.17 and 2.18]. Measurements, however, are only valid in the limit of constant pressure and temperature.

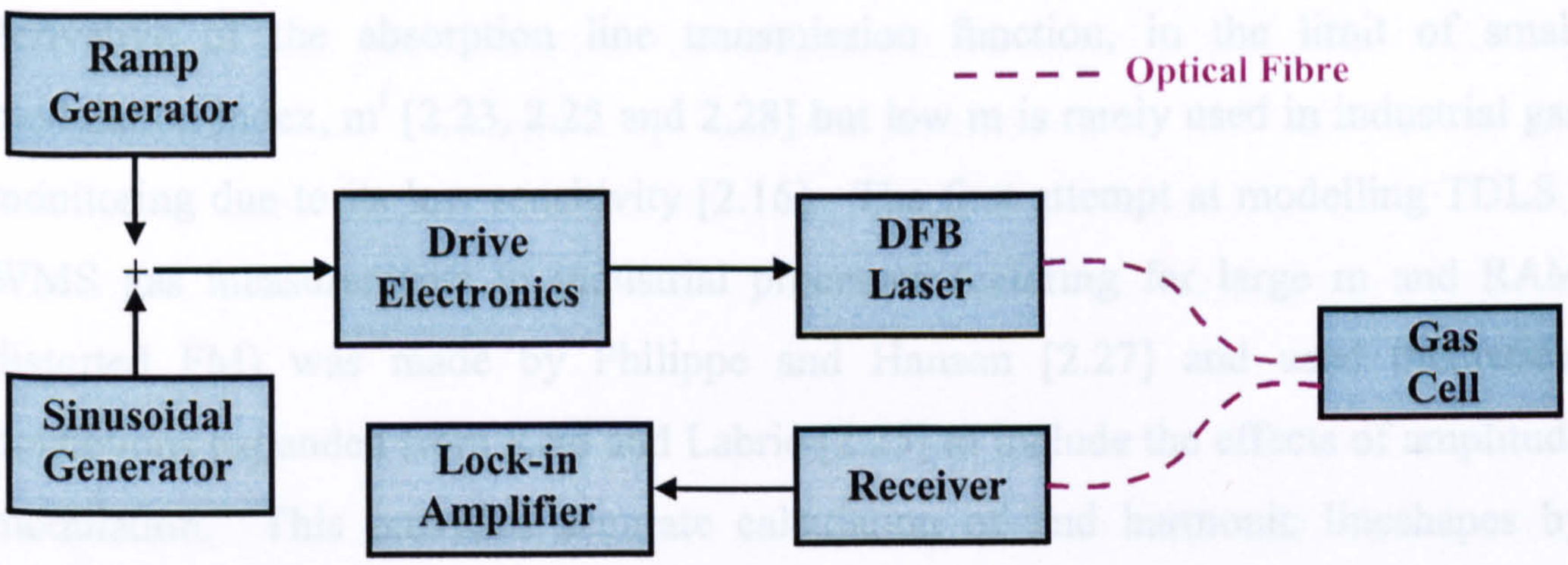

Figure 2.5: System diagram of TDLS / WMS over optical fibre

As has been highlighted from the beginning of this report, the greatest challenge for industrial gas monitoring is simultaneous gas concentration and pressure measurement / correction. The main limitations to achieving this are: (a) the dependence (increasing with increasing order of derivative / harmonic) of recovered signal amplitude on gas absorption linewidth and the need for its accurate determination from recovered signals; (b) the lack of reliable, *in-situ* wavelength referencing schemes to measure the absorption linewidth of the recovered signals accurately; both of which are applicable to signals recovered by both TDLS adaptations; (c) the RAM induced systematic distortion on the TDLS / WMS derivative signals and (d) the need for accurate knowledge of the system scaling factors, in particular, the amplitude of the sinusoidal frequency modulation, $\delta\nu$.

Although RAM has always been regarded as an unwanted side effect to frequency modulation that limits the achievable sensitivity [2.21 – 2.23], it had originally been treated as an independent and entirely separable noise source. Indeed, early attempts to extract lineshape / linewidth information, by comparing experimental measurements to theoretical predictions of TDLS / WMS signals that only considered the "ideal" pure FM case, [2.24 – 2.26] were flawed. This is because the pure FM scenario is not achievable in industrial process applications, as highlighted by Philippe et al [2.27]. The reason being, that RAM, as well as inducing a large DC background, also produces a marked distortion on the TDLS / WMS derivative signals. In addition, the n^{th} harmonic is only directly proportional to the n^{th} derivative of the absorption line transmission function, in the limit of small modulation index, m[1] [2.23, 2.25 and 2.28] but low m is rarely used in industrial gas monitoring due to its low sensitivity [2.16]. The first attempt at modelling TDLS / WMS gas measurements in industrial processes (catering for large m and RAM distorted FM) was made by Philippe and Hanson [2.27] and used theoretical predictions expanded from Reid and Labrie [2.25] to include the effects of amplitude modulation. This provided accurate calculation of 2nd harmonic lineshapes by Fourier analysis. Kluczynski et al [2.29 – 2.32] went a step further, also using Fourier analysis, but providing a more general formalism capable of dealing with any harmonic and background interference, such as interferometric noise. In light of these numerous approaches, a more recent attempt was made by Schilt et al [2.33]. The theoretical predictions developed in [2.33] used the original models by Arndt [2.24] and again added the effects of amplitude modulation to develop a combined, generalised AM – FM model. From this, analytical expressions for the 1^{st}, 2^{nd} and 3^{rd} harmonics were developed based on a Lorentzian absorption profile.

The theoretical calculations in each case take into account various modulation parameters and highlight the importance of parameter choice in achieving close comparisons to theory. The important point to note here is that, although each of the

---

[1] Reminder that the modulation index is the sinusoidal frequency deviation normalised relative to the HWHM linewidth. i.e. $m = \delta\nu/\gamma$.

latter, complex formalisms [2.27 and 2.29 – 2.33] boast the ability to cope with arbitrary modulation index values; often quoting the optimum of m = 2.00, 2.20 and 3.59 to maximise the harmonics 1, 2 and 3 respectively, it is essential that the experimental value of m be known precisely in order for the signals to match. That is to say, that for the theoretical predictions to remain consistently accurate over a range of gas pressures, the deviation of the laser frequency, $\delta\nu$, in relation to the gas absorption linewidth, γ, must be known precisely at each experimental measurement. As stated previously, as will be shown in equations (3.17) and (3.18) in chapter 3, and as described in [2.28], this relationship of the derivative signal amplitude (and consequently accurate concentration measurement) with the deviation of the laser frequency and the gas absorption linewidth becomes more critical with increasing order of derivative. Determining linewidth measurements and maintaining the modulation index ratio would be extremely difficult to achieve in a stand-alone instrument, deployed in environments where the pressures are varying and unknown.

As far as reliable, *in-situ*, wavelength referencing is concerned, again Philippe and Hanson [2.27] recognised the importance of accurate calibration of the laser frequency as it scans through the gas absorption feature and described a method of passing the modulated light through a low finesse, bulk-optic etalon. Known spectral characteristics of the etalon allow for accurate mapping of a relative frequency scale onto the time-based measurements. Philippe and Hanson then achieved an absolute scale through comparison to theory.

2.5 Conclusions

In today's industrialised world there is an ever-increasing need for gas monitoring systems in a number of varying applications and environments and there is at least as much emphasis on determining as much accurate and quantitative information on a particular gas composition as possible, as there is on determining minimum

detectable sensitivities [2.16]. In addition, modern industrial gas monitoring systems should require little maintenance with simple and infrequent calibration [2.34]. They should also have high reliability and be relatively inexpensive. From this review of current technologies, it is evident that (a) TDLS with wavelength modulation spectroscopy, operating at near infra-red wavelengths, over optical fibres provides the greatest potential for industrial gas monitoring and (b) that the main target to be reached remains the simultaneous and accurate measurement of gas concentration and pressure in stand-alone, field-deployable instruments. With this in mind, the objectives laid out in chapter 1 become much clearer.

Philippe and Hanson [2.27] provide the basis of a useful approach to measuring the laser emission frequency as it sweeps the gas absorption line by using a low finesse etalon. However, the use of bulk optics in the target applications would be expensive and alignment issues would require constant monitoring and calibration. The first objective of this research was then to develop a fibre-based solution, following a similar methodology as [2.27], capable of delivering a constant, reliable and accurate wavelength reference to the time-based TDLS measurements. For the direct TDLS system this provides a gas transmission function from which simultaneous concentration and linewidth / pressure measurements can be made.

Interference from residual amplitude modulation is still the major limiting factor in all WMS approaches, as discussed above. RAM limits both the sensitivity, due to problems associated with detecting a small signal on a large background, and the accuracy, due to the distortion of derivative traces. It is then imperative, in order to achieve accurate comparisons to theory, that the RAM is completely removed. The objective here was to develop novel signal processing techniques to completely remove the effects of amplitude modulation from measured frequency modulated signals.

Once both of these issues had been addressed, it remained an option to numerically integrate the un-distorted 1st derivative traces to reconstruct the absolute absorption line transmission function. For this, accurate knowledge of the system scaling factors, in particular $\delta\nu$, is required. Achieving accurate FM signal recovery, whilst maintaining reasonable signal-to-noise ratios, remains a significant challenge.

As touched on in chapter 1, the concentration can be measured from the amplitude and the pressure from the linewidth of recovered TDLS signals; however, a more sophisticated approach was to use a curve fitting procedure, matching theoretical predictions (based on the HITRAN database) to the measured traces. Two options were available here: either direct curve fits of the modelled profiles to the measured absolute transmission functions (measured either directly or through reconstruction of the derivatives) or, in regard to the TDLS / WMS signals, differentiate the theoretical predictions and fit to the measured derivatives. Novel software had been developed with industrial collaborators OptoSci Ltd., which permitted the modelling of the HITRAN data, whilst allowing control over gas pressure, temperature, concentration and line broadening parameters; thus allowing simulation of all possible gas conditions.

Current British Standards stipulate that the error associated with industrial methane detection is +/- 10 % of indication at atmospheric pressure. The success and merit of our investigations will be judged on this benchmark.

2.6 References

[2.1] E. D. Hinkley, "High-Resolution Infrared Spectroscopy with a Tunable Diode Laser," Applied Physics Letters, Vol. 16, No. 9, pp 351-354, May 1970.

[2.2] J. Reid, J. Shewchun, B. K. Garside and E. A. Ballik, "High Sensitivity Pollution Detection employing Tunable Diode Lasers," Applied Optics, Vol. 17, No. 2, pp 300-307, January 1978.

[2.3] J. Reid, B. K. Garside, J. Shewchun, M. El-Sherbiny and E. A. Ballik, "High Sensitivity Point Monitoring of Atmospheric Gases employing Tunable Diode Lasers," Applied Optics, Vol. 17, No. 11, pp 1806-1810, June 1978.

[2.4] D. T. Cassidy and J. Reid, "Atmospheric Pressure Monitoring of Trace Gases using Tunable Diode Lasers," Applied Optics, Vol. 21, No. 7, pp 1185-1190, April 1982.

[2.5] M. Lowenstein, "Diode Laser Harmonic Spectroscopy applied to in situ Measurements of Atmospheric Trace Molecules," Journal of Quantitative Spectroscopy and Radiative Transfer, Vol. 40, pp 249-256, September 1988.

[2.6] D. S. Bomse, A. C. Stanton and J. A. Silver, "Frequency Modulation and Wavelength Modulation Spectroscopies: Comparison of Experimental Methods using a Lead – Salt Diode Laser," Applied Optics, Vol. 31, No. 6, pp 718-731, February 1992.

[2.7] W. Lenth, "Optical Heterodyne Spectroscopy with Frequency- and Amplitude- Modulated Semiconductor Lasers," Optics Letters, Vol. 8, No. 11, pp 575-577, November 1983.

[2.8] D. T. Cassidy and L. J. Bonnell, "Trace Gas Detection with Short – External – Cavity InGaAsP Diode Laser Transmitter Modules Operating at 1.58 μm," Applied Optics, Vol. 27, No. 13, pp 2688-2693, July 1988.

[2.9] F. S. Pavone and M. Inguscio, "Frequency- and Wavelength- Modulation Spectroscopies: Comparison of Experimental Methods using an AlGaAs Diode Laser," Applied Physics B: Lasers and Optics, Vol. 56, No. 2, pp 118-122, February 1993.

[2.10] A. Lucchesini, I. Longo, C. Gabbanini, S. Gozzini and L. Moi, "Diode Laser Spectroscopy of Methane Overtone Transitions," Applied Optics, Vol. 32, No. 27, pp 5211-5216, September1993.

[2.11] A. Lucchesini, M. De Rosa, D. Pellicia, A. Ciucci, C. Gabbanini and S. Gozzini, "Diode Laser Spectroscopy of Overtone Bands of Acetylene," Applied Physics B: Lasers and Optics, Vol. 63, No. 3, pp 227-282, September 1996.

[2.12] M. Gabrysh, C. Corsi, F. S. Pavone and M. Inguscio, "Simultaneous Detection of CO and CO_2 using a Semiconductor DFB Diode Laser at 1.578 μm," Applied Physics B: Lasers and Optics, Vol. 65, No. 1, pp 75-79, July 1997.

[2.13] X. Zhu and D. T. Cassidy, "Modulation Spectroscopy with a Semiconductor Diode Laser by Injection - Current Modulation," Journal of the Optical Society of America B: Optical Physics, Vol. 14, No. 8, pp 1945-1950, August 1997.

[2.14] G. Hancock, V. L. Kasyutich and G. A. D. Ritchie, "Wavelength – Modulation Spectroscopy using a Frequency – Doubled Current – Modulated Diode Laser," Applied Physics B: Lasers and Optics, Vol. 74, No. 6, pp 569-575, April 2002.

[2.15] H. C. Sun, E. A. Whittaker, Y. W. Bae, C. K. Ng, V. Patel, W. H. Tam, S. McGuire, B. Singh and B. Gallois, "Combined Wavelength and Frequency Modulation Spectroscopy: a Novel Diagnostic Tool for Materials Processing," Applied Optics, Vol. 32, No. 6, pp 885-893, February 1993.

[2.16] P. Werle, "A Review of Recent Advances in Semiconductor Laser based Gas Monitors," Spectrochimica Acta Part A: Molecular and Biomolecular Spectroscopy, Vol. 54, No. 2, pp 197-236, February 1998.

[2.17] B. Culshaw, G. Stewart, F. Dong, C. Tandy and D. Moodie, "Fibre Optic Techniques for Remote Spectroscopic Methane Detection – from Concept to System Realisation," Sensors and Actuators B: Chemical, Vol. 51, pp 25-37, May 1998.

[2.18] G. Stewart, C. Tandy, D. Moodie, M. A. Morante and F. Dong, "Design of a Fibre Optic Multi-Point Sensor for Gas Detection," Sensors and Actuators B: Chemical, Vol. 51, pp 227-232, August 1998.

[2.19] H. L. Ho, W. Jin, and M. S. Demokan, "Sensitive, Multipoint Gas Detection using TDM and Wavelength Modulation Spectroscopy," Electronics Letters, Vol. 36, No. 14, pp 1191-1193, July 2000.

[2.20] H. L. Ho, W. Jin, H. B. Yu, K. C. Chan, C. C. Chan and M. S. Demokan, "Experimental Demonstration of a Fiber-Optic Gas Sensor Network Addressed by FMCW," IEEE Photonics Technology Letters, Vol. 12, No. 11, pp 1546-1548, November 2000.

[2.21] G. Jacobsen, H. Olesen, F, Birkedahl and B. Tromborg, "Current / Frequency – Modulation Characteristics for Directly Optical Frequency – Modulated Injection Lasers at 830 nm and 1.3 μm," Electronics Letters, Vol. 18, No. 20, pp 874 – 876, September 1982.

[2.22] W. Lenth, "High Frequency Heterodyne Spectroscopy with Current – Modulated Diode Lasers," IEEE Journal of Quantum Electronics, Vol. QE-20, No. 9, pp 1045-1050, September 1984.

[2.23] J. A. Silver, "Frequency – Modulation Spectroscopy for Trace Species Detection: Theory and Comparison among Experimental Methods," Applied Optics, Vol. 31, No. 6, pp 707-717, February 1992.

[2.24] R. Arndt, "Analytical Line Shapes for Lorentzian Signals Broadened by Modulation," Journal of Applied Physics, Vol. 36, No. 8, pp 2522-2524, August 1965.

[2.25] J. Reid and D. Labrie, "Second – Harmonic Detection with Tunable Diode Lasers – Comparison of Experiment and Theory," Applied Physics B: Lasers and Optics, Vol. 26, No. 3, pp 203-210, November 1981.

[2.26] J. M. Supplee, E. A Whittaker and W. Lenth, "Theoretical Description of Frequency Modulation and Wavelength Modulation Spectroscopy," Applied Optics, Vol. 33, No. 27, pp 6294-6302, September 1994.

[2.27] L. C. Philippe and R. K. Hanson, "Laser Diode Wavelength – Modulation Spectroscopy for Simultaneous Measurement of Temperature, Pressure and Velocity in Shock – Heated Oxygen Flows," Applied Optics, Vol. 32, No. 30, pp 6090-6103, October 1993.

[2.28] I. Linnerud, P. Kaspersen and T. Jaeger, "Gas Monitoring in the Process Industry using Diode Laser Spectroscopy," Applied Physics B: Lasers and Optics, Vol. 67, No. 3, pp 297-305, September1998.

[2.29] P. Kluczynski and O. Axner, "Theoretical Description based on Fourier Analysis of Wavelength – Modulation Spectrometry in terms of Analytical

and Background Signals," Applied Optics, Vol. 38, No. 27, pp 5803-5815, September 1999.

[2.30] P. Kluczynski, A. M. Lindberg and O. Axner, "Characterization of Background Signals in Wavelength – Modulation Spectrometry in terms of a Fourier based Formalism," Applied Optics, Vol. 40, No. 6, pp 770-782, February 2001.

[2.31] P. Kluczynski, A. M. Lindberg and O. Axner, "Background Signals in Wavelength Modulation Spectrometry with Frequency – Doubled Diode-Laser Light. I. Theory," Applied Optics, Vol. 40, No. 6, pp 783-793, February 2001.

[2.32] P. Kluczynski, A. M. Lindberg and O. Axner, "Background Signals in Wavelength Modulation Spectrometry by use of Frequency – Doubled Diode-Laser Light. II. Experiment," Applied Optics, Vol. 40, No. 6, pp 794-805, February 2001.

[2.33] S. Schilt, L. Thevenaz and P. Robert, "Wavelength Modulation Spectroscopy: Combined Frequency and Intensity Laser Modulation," Applied Optics, Vol. 42, No. 33, pp 6728-6738, November 2003.

[2.34] P. W. Werle, P. Mazzinghi, F. D'Amato, M. De Rosa, K. Maurer and F. Slemr, "Signal Processing and Calibration Procedures for In Situ Diode-Laser Absorption Spectroscopy," Spectrochimica Acta Part A, Vol. 60, pp 1685-1705, July 2004.

Chapter 3

Analytical Methodologies: Fundamentals of Molecular Spectroscopy

3.1 Introduction

This chapter gives a theoretical appreciation of molecular spectroscopy, describing in detail the formation of gas absorption line spectra and how concentration and pressure can influence and indeed be derived from these lineshapes. This discussion serves only to give the reader a fundamental background of molecular spectroscopy and is in no way comprehensive; for a more detailed review of the topics highlighted in this chapter the reader is directed towards the following excellent texts: [3.1 – 3.7]. The chapter also describes how these gas absorption lines were modelled in order to provide a comparison to experimentally measured signals.

3.2 Formation of Gas Absorption Line Spectra

When a gas molecule absorbs electromagnetic radiation there is a change in its internal energy. The energy transition familiar to most scientists is the transfer of electrons between allowed energy levels in an atom; however, molecules can also store energy in vibrations and rotations. Like the electronic transitions, vibrational and rotational transitions occur between discrete, allowed levels. Figure 3.1 shows an energy transition triggered by the absorption of electromagnetic energy. Note here that the figure could represent any of the above mentioned types of transition and that the numbers distinguishing the levels are actually quantum numbers. The quantum of electromagnetic energy required to make the jump from one energy level to another was defined by Planck and is given by:

$$\Delta E = h\nu = \frac{hc}{\lambda} \tag{3.1}$$

where h is Planck's constant (6.63×10^{-34} Js) and ν and λ are the frequency and wavelength of the electromagnetic radiation respectively.

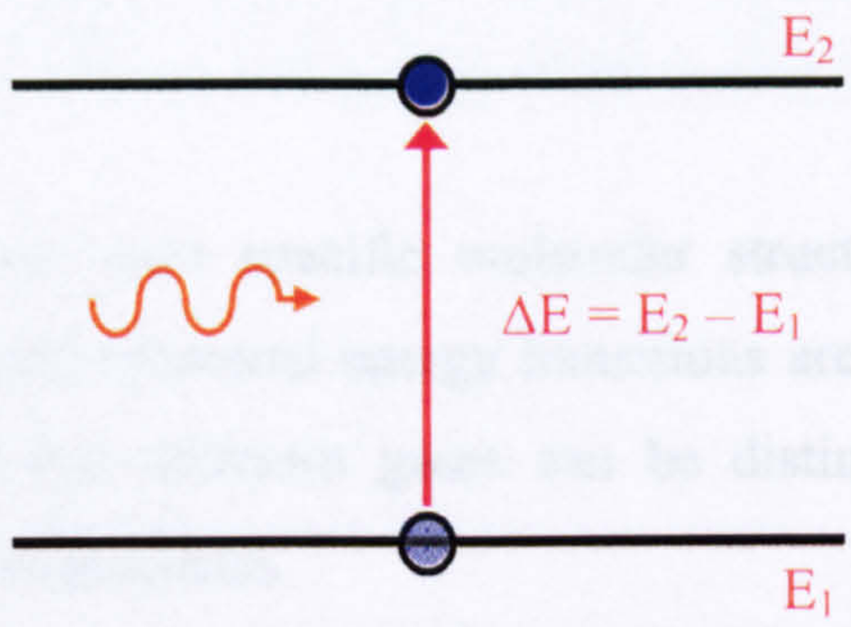

Figure 3.1: Absorption of electromagnetic radiation

The main point to take from this is of course that this absorption of electromagnetic energy, required to make the transition, is a function of the frequency / wavelength of the electromagnetic radiation. Therefore, if a single frequency source, such as a DFB laser operating at frequency ν, as defined by equation (3.1), is directed through a gas consisting of this molecule, the molecule will jump from state 1 to state 2 and the laser intensity will have decreased. If this laser source is scanned over a frequency range and the output intensity is plotted there will be a dip in intensity at frequency ν, as shown in figure 3.2.

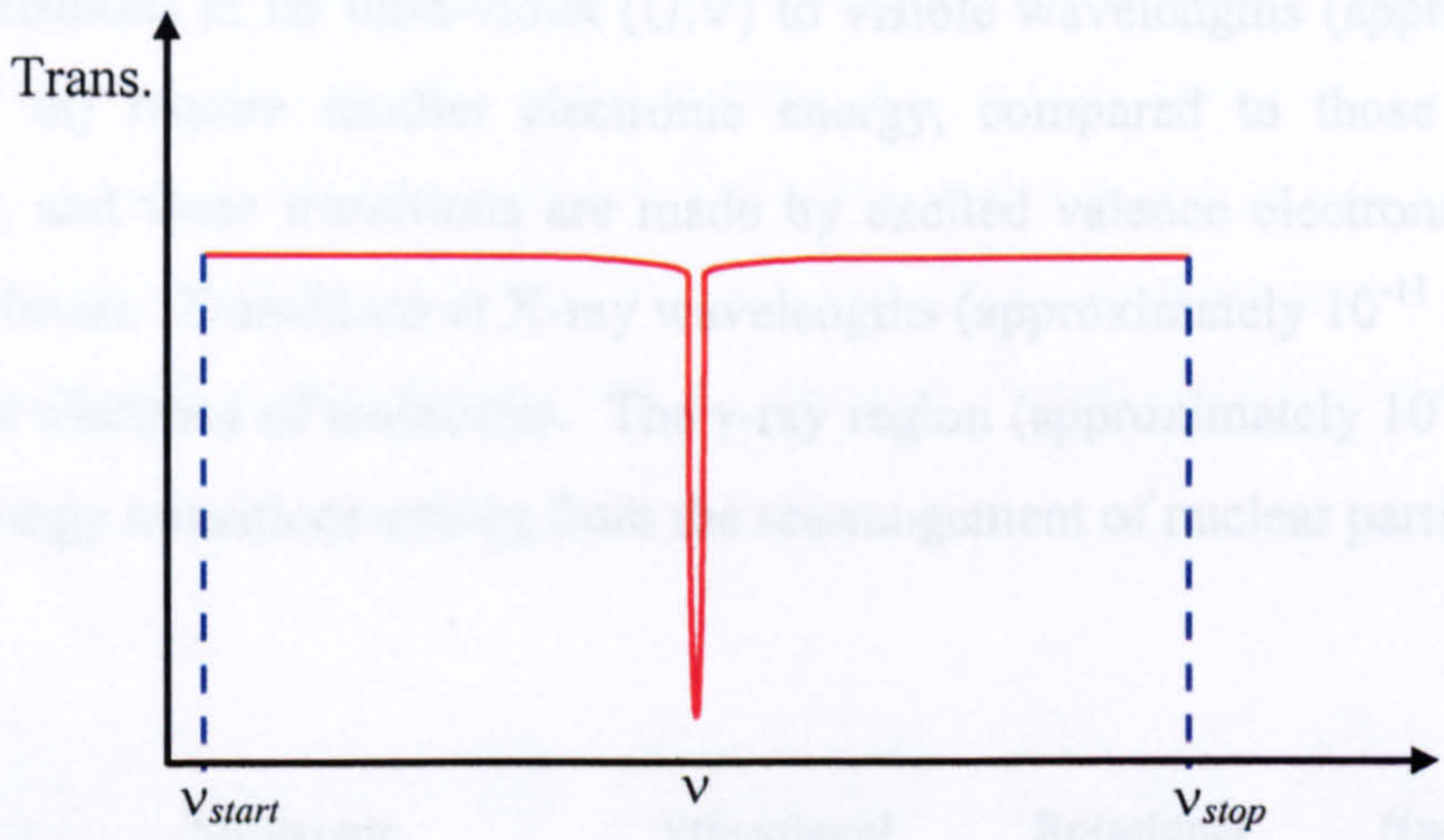

Figure 3.2: Absorption of laser intensity at ν

As molecules have their own specific molecular structure, the combination of electronic, vibrational and rotational energy transitions are unique to that molecule. This of course means that different gases can be distinguished by their unique absorption / transmission spectrum.

There are general regions in the electromagnetic spectrum into which molecular energy transition processes, including those mentioned above, can be categorised, as shown in figure 3.3. At radio wavelengths (from approximately 1 m upwards) the

energy change arises from the reversal of spin of a nucleus or of the electrons surrounding the nucleus. At microwave wavelengths (approximately 10^{-3} to 1 m) energy is stored in the form of molecular rotations. Rotation of a molecule gives rise to a periodic change in the dipole moment. The interaction of an electromagnetic field with this changing dipole moment gives rise to the absorption or emission of energy. The region of greatest interest is the infra-red (I.R) region where energy is stored in the form of vibrations. Again, it is the interaction of a changing dipole moment, brought about by molecular vibration, with electromagnetic radiation which leads to energy transitions and line spectra. Infra-red spectroscopy is discussed in greater detail in the following section. The infra-red wavelengths extend from 10^{-6} to 10^{-3} m. Transitions at far ultra-violet (U.V) to visible wavelengths (approximately 10^{-8} to 10^{-6} m) require smaller electronic energy, compared to those at X-ray wavelengths, and these transitions are made by excited valence electrons between molecular orbitals. Transitions at X-ray wavelengths (approximately 10^{-11} to 10^{-8} m) involve inner electrons of molecules. The γ-ray region (approximately 10^{-15} to 10^{-11} m) covers energy transitions arising from the rearrangement of nuclear particles.

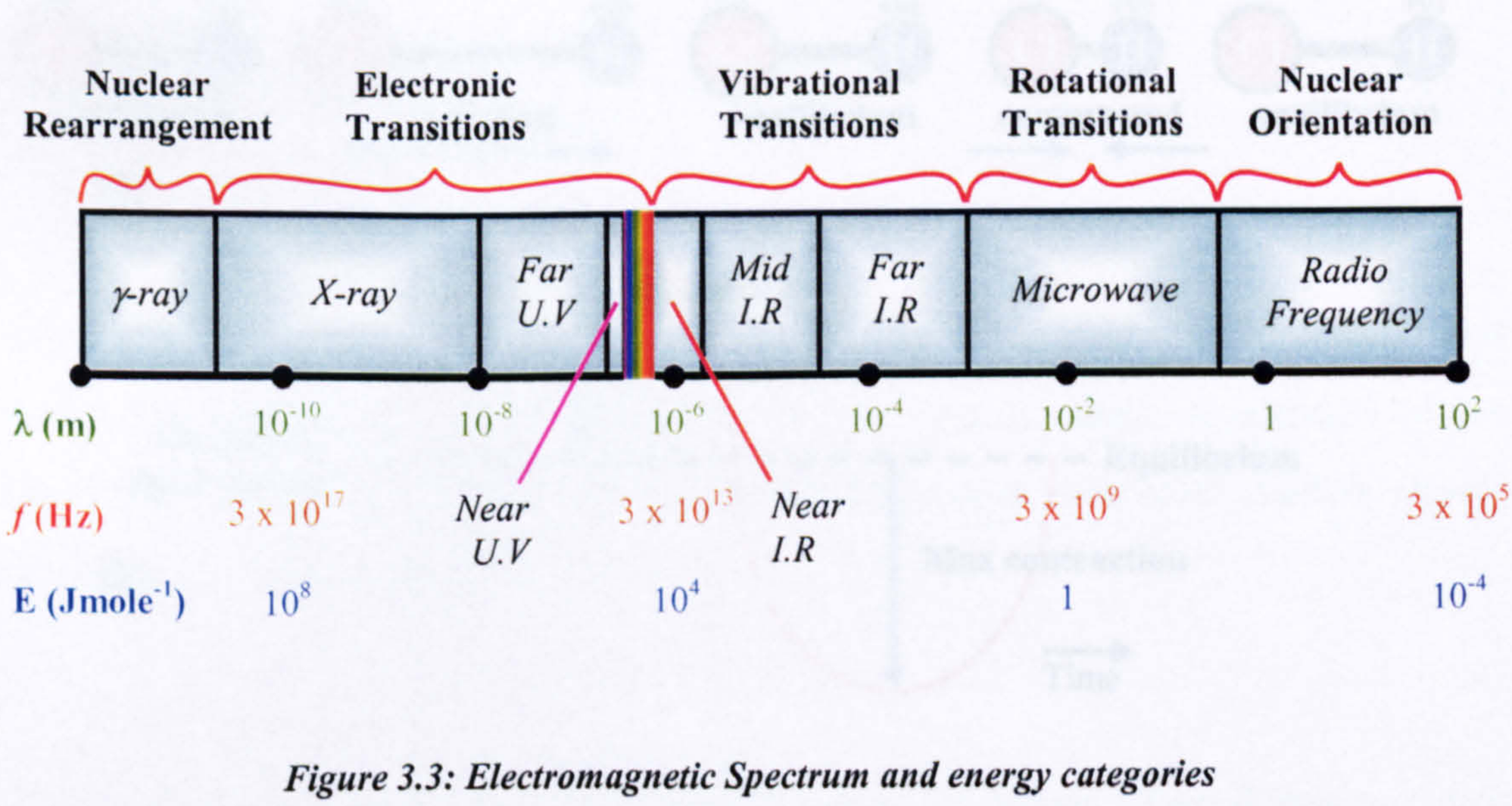

Figure 3.3: Electromagnetic Spectrum and energy categories

3.3 Vibrational Spectroscopy and Infra-red Spectra

As mentioned above, infra-red spectroscopy is the study of molecular vibrations. For ease of explanation it is best to start with the vibration in a diatomic molecule and to first consider the bond between the two atoms as being like a spring. This bond will remain in equilibrium until an input of energy changes the bond length. During a vibration, the bond (like a spring) between the two molecules is compressed and stretched at a certain frequency and this periodic change in the bond length can lead to a periodic fluctuation in the dipole moment. Figure 3.4 shows the stretching and contraction of the HCl molecule and the oscillating dipole moment as a consequence. A dipole moment is present here because there is a charge separation between the two atoms; the larger chlorine atom has a slightly negative charge and the smaller hydrogen atom has a slightly positive charge. The dipole moment is at a maximum when the bond length is at its longest and at a minimum when at its shortest.

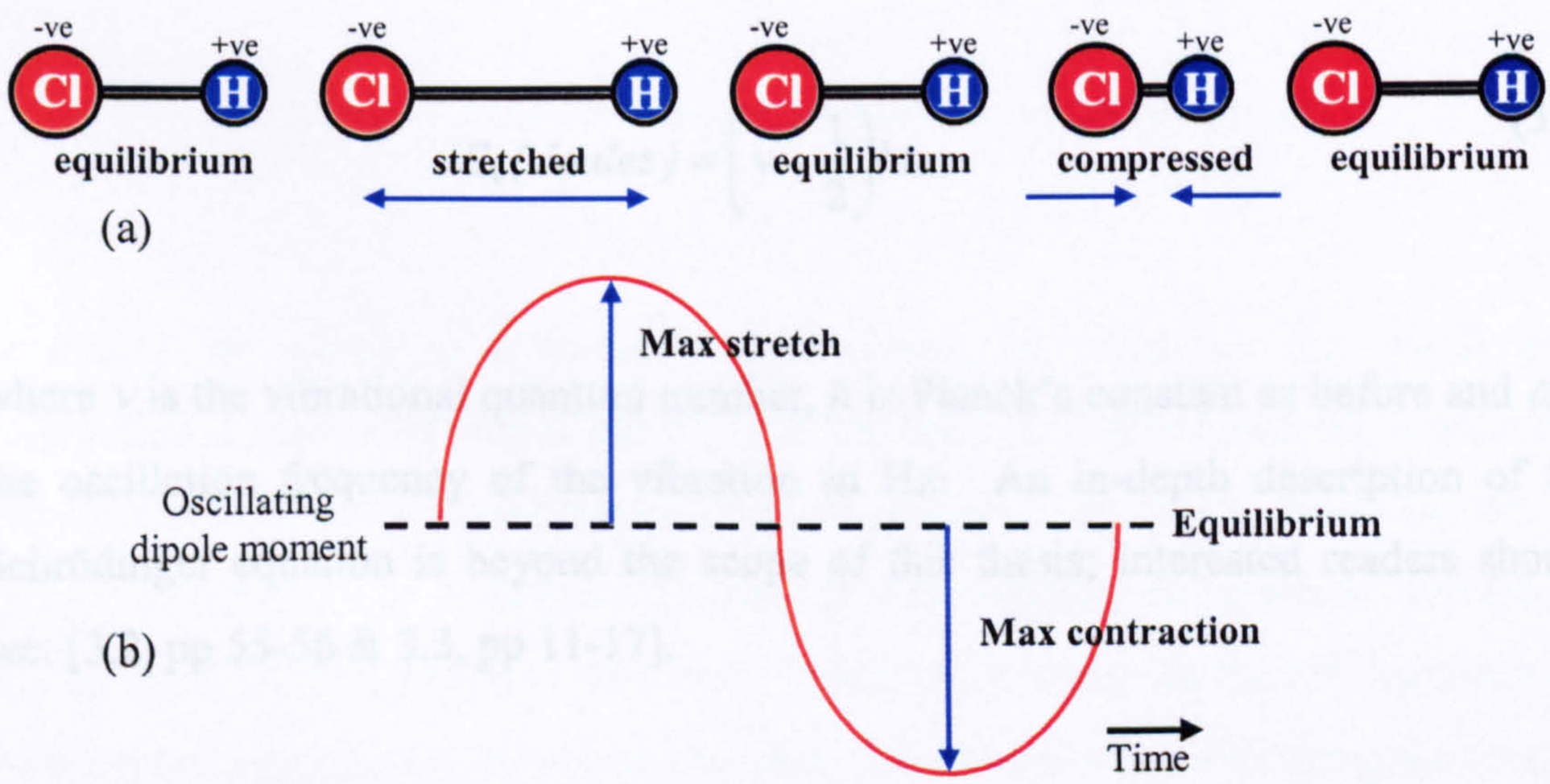

Figure 3.4: (a) Stretching and compression of the diatomic molecule HCl (b) Resulting change in dipole moment

Interaction of this changing dipole moment with electromagnetic radiation then leads to the absorption or emission of energy. Furthering the analogy of the bond behaving like a spring, it can be assumed the bond obeys Hooke's law[I]. Therefore, the greater the change in bond length (stretch or compression), the greater the input of energy required (restoring force). The equation describing the energy / bond length relationship is thus given by:

$$E = \frac{1}{2}k\left(l - l_{eq}\right)^2 \tag{3.2}$$

where k is the force constant (derived from Hooke's law), l is the bond length and l_{eq} is the bond length at which the bond is in equilibrium.

As previously mentioned, vibrational energies are quantised into allowed states and these are given by equation (3.3), which comes from the use of equation (3.2) in the Schrödinger equation[II].

$$E_v(Joules) = \left(v + \frac{1}{2}\right)h\omega \tag{3.3}$$

where v is the vibrational quantum number, h is Planck's constant as before and ω is the oscillation frequency of the vibration in Hz. An in-depth description of the Schrödinger equation is beyond the scope of this thesis; interested readers should see: [3.2, pp 55-56 & 3.3, pp 11-17].

This distribution of energies is illustrated in figure 3.5 below. Two things to notice from this diagram are that: firstly, the zero point energy is not actually zero but ($h\omega$/

[I] Hooke's law: F = -kX, an approximation declaring the linear relationship between a body's displacement, X, and the force, F, causing the displacement. k is the force constant.

[II] Schrödinger equation: $H\psi = E\psi$, describes the conservation of energy in quantum mechanics. H is the Hamiltonian operator, ψ is the wavefunction and E represents the energy levels.

2) and this agrees with equation (3.3); secondly, the energy levels are equally spaced by $h\omega$. This figure models an ideal harmonic oscillator which applies in the limit of small excursions in bond length.

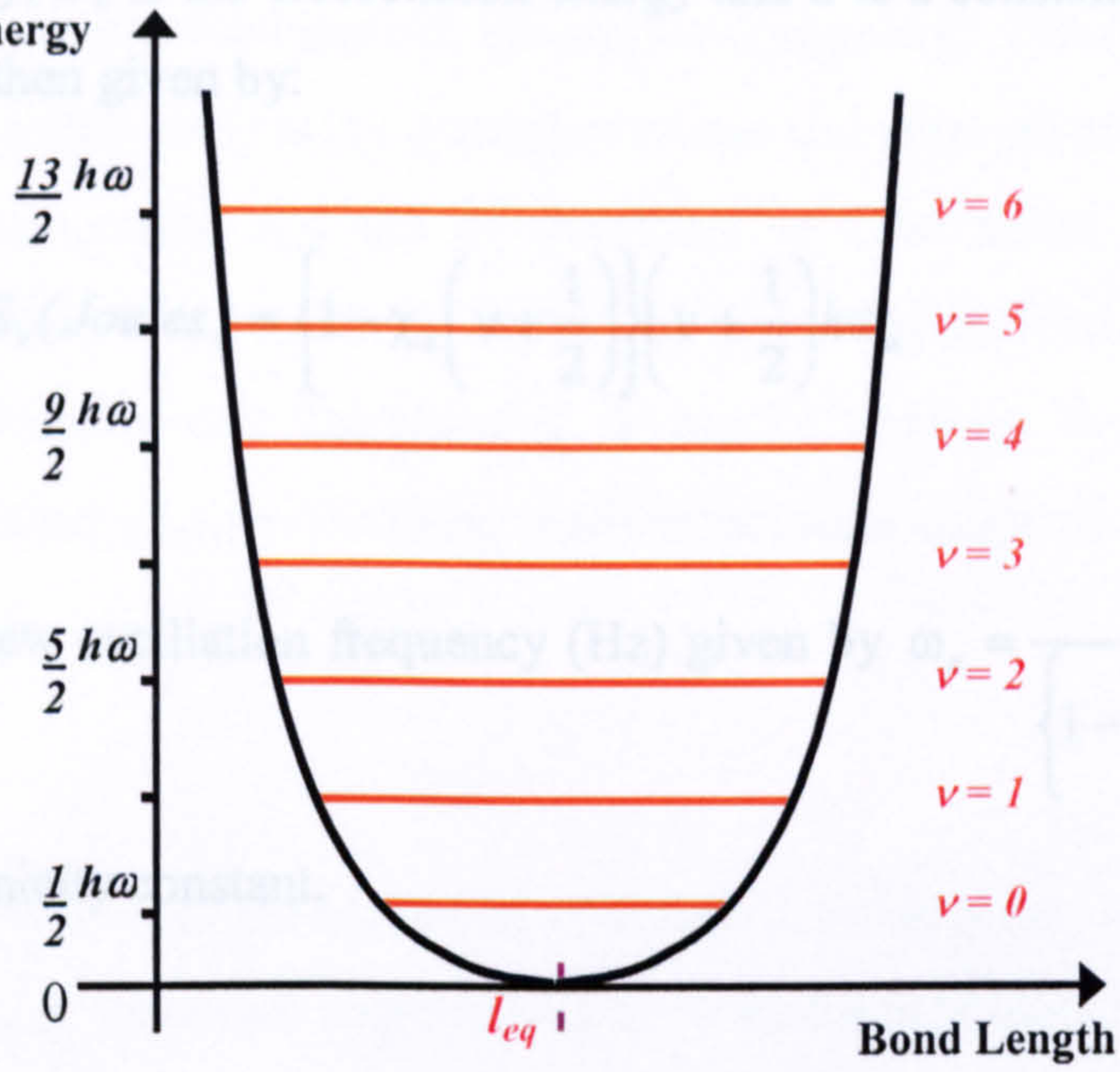

Figure 3.5: Ideal distribution of energies for a diatomic molecule

In reality the atoms in a molecule can experience vibrations that result in a contraction or stretch of a bond greater than the limit of simple harmonic motion and therefore a more complicated model must be devised. Figure 3.6 shows the typical energy distribution of a diatomic molecule experiencing anharmonic oscillation. Again, there are two points to take from figure 3.6. Firstly, on the left-hand-side of the diagram, representing short bond lengths, the curve is steep indicating the limit of further compression. On the right-hand-side, representing long bond lengths, a plateau develops indicating that further stretching leads to a weakening of the bond and eventually, dissociation. The second point is that the energy spacing is no longer equal; in fact the energy levels are determined by using the energy function equation (3.4) [3.1] below in the Schrödinger equation.

$$E = D_e\left[1 - exp\left\{-a\left(l - l_{eq}\right)\right\}\right]^2 \tag{3.4}$$

This is simply an expression that fits the anharmonic oscillation curve to a good degree of accuracy; D_e is the dissociation energy and a is a constant. The quantised energy levels are then given by:

$$E_v(Joules) = \left\{1 - \chi_e\left(\nu + \frac{1}{2}\right)\right\}\left(\nu + \frac{1}{2}\right)h\omega_e \tag{3.5}$$

where ω_e is the new oscillation frequency (Hz) given by $\omega_e = \dfrac{\omega}{\left\{1 - \chi_e\left(\nu + \frac{1}{2}\right)\right\}}$ and

χ_e is the anharmonicity constant.

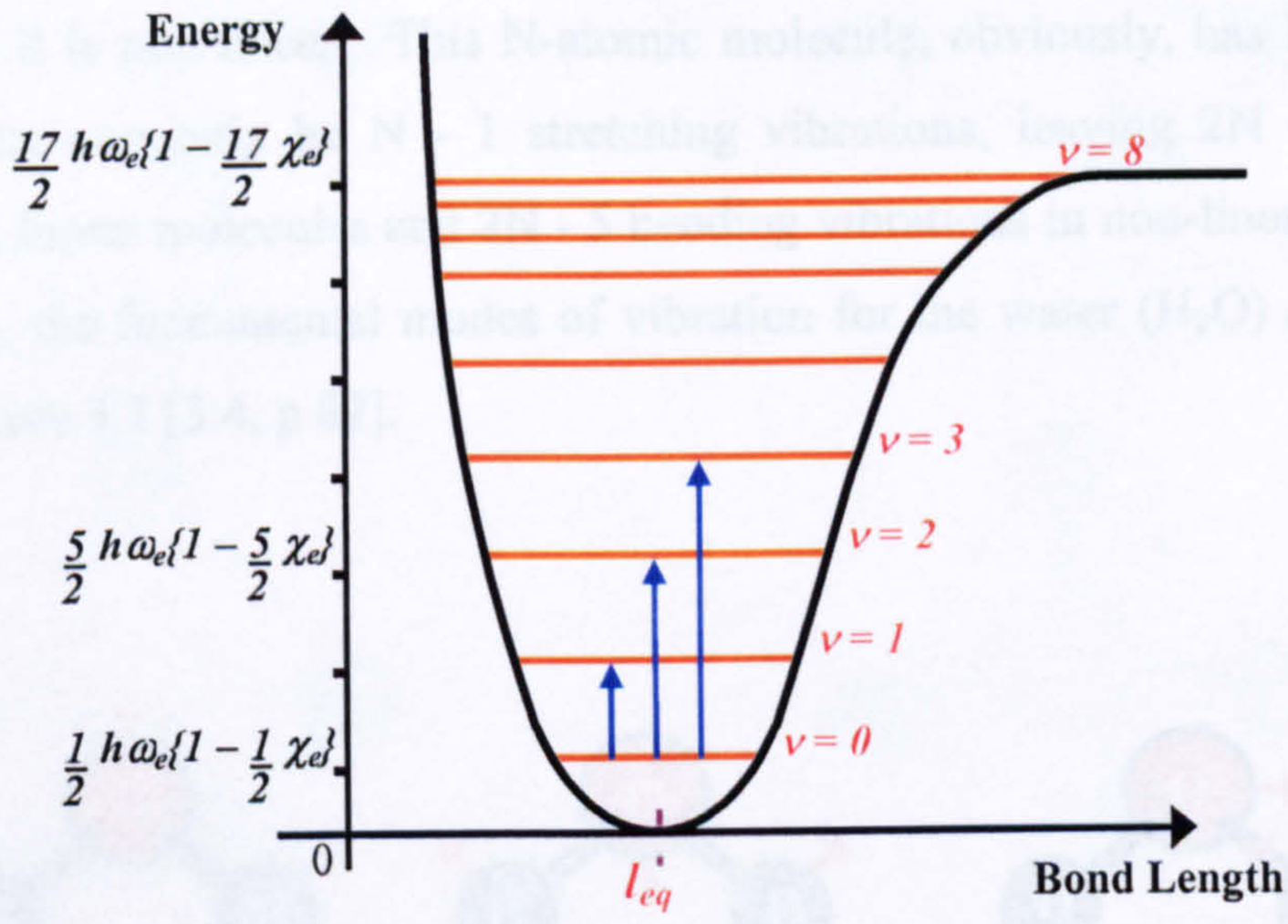

Figure 3.6: Realistic distribution of energies for a diatomic molecule

The anharmonicity in the oscillations gives rise to the possibility for energy transitions greater than $\Delta\nu = \pm 1$. Shown in figure 3.6 are three transitions marked by the blue arrows. The transition from $\nu = 0$ to $\nu = 1$ ($\Delta\nu = +1$) is known as the fundamental transition. The jump from $\nu = 0$ to $\nu = 2$ ($\Delta\nu = +2$) is known as the first overtone and when observing a spectrum, shows a weaker absorption than the fundamental at twice the fundamental absorption frequency. Finally, the transition from $\nu = 0$ to $\nu = 3$ ($\Delta\nu = +3$) is the second overtone and gives an absorption, weaker than both the fundamental and the 1st overtone, at three times the fundamental absorption frequency. The population density of higher states, relative to the ground state, decreases rapidly and therefore it is highly unlikely that there will be observable absorption spectra resulting from transitions originating at $\nu = 1$ and above.

The next stage is to discuss the modes of vibration in polyatomic molecules in order to finally realise the vibrations experienced by a methane molecule. An N-atomic molecule has 3N – 5 fundamental vibrations if it is linear, and 3N – 6 fundamental vibrations if it is non-linear. This N-atomic molecule, obviously, has N - 1 bonds, meaning there can only be N - 1 stretching vibrations, leaving 2N – 4 bending vibrations in linear molecules and 2N - 5 bending vibrations in non-linear molecules. To illustrate, the fundamental modes of vibration for the water (H_2O) molecule are shown in figure 3.7 [3.4, p 82].

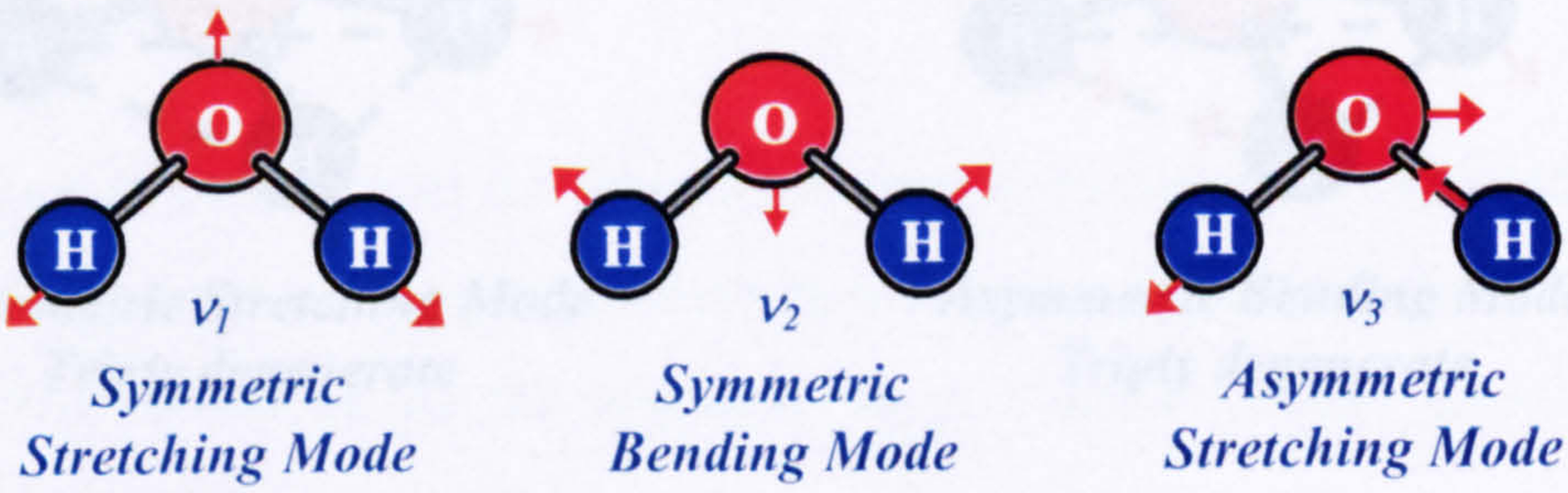

Figure 3.7: The fundamental modes of vibration for the H_2O molecule

H_2O is a non-linear, tri-atomic molecule so has 3(3) – 6 = 3 fundamental vibrations, two of which are stretching vibrations and the third is a bending vibration. Like the HCl molecule discussed earlier there is a charge separation (permanent dipole moment) and thus all three vibrations give rise to an oscillating dipole and produce infra-red spectra. All three modes are then said to be infra-red active.

Methane (CH_4) was chosen as the experimental gas for this research work and the reasons for such a choice are made clear in chapter 4. The fundamental vibrations of the CH_4 molecule are shown in figure 3.8 [3.2, p 198]. CH_4 is known as a non-linear, tetrahedral spherical-top molecule and thus has 3(5) – 6 = 9 vibrational modes, four of which are stretching vibrations and five are bending vibrations.

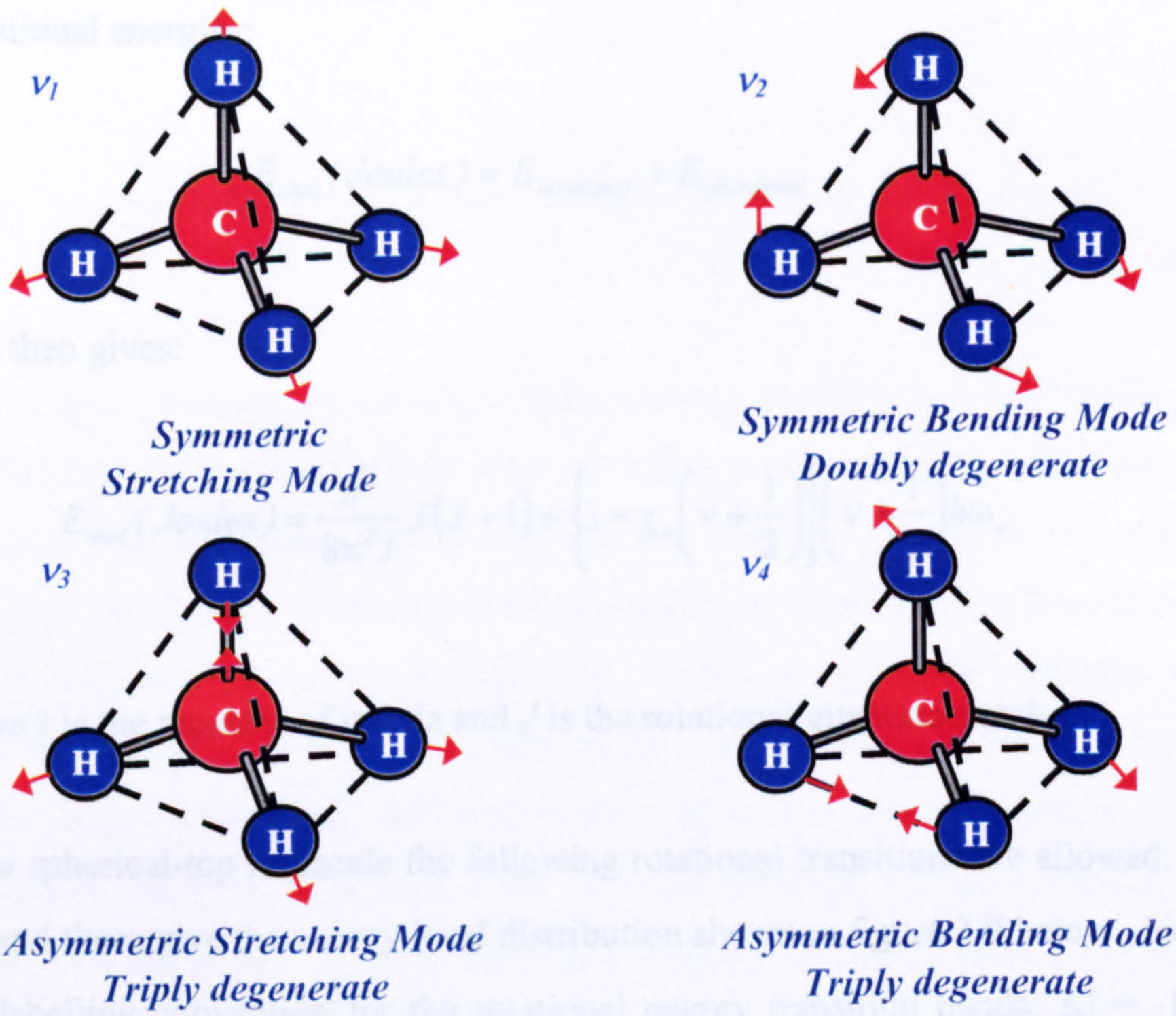

Figure 3.8: Fundamental vibrations of CH_4 molecule

Atoms in a vibration can experience more than one motion, in fact all the atoms in a molecule can move simultaneously at the same frequency but in several different planes. The motions are identical in all aspects except direction and are called degenerate. The ν_2 mode in figure 3.8 is doubly degenerate and modes ν_3 and ν_4 are triply degenerate, giving the nine vibrations in total. CH_4 does not possess a permanent dipole moment, thus only the asymmetric vibrations (ν_3 and ν_4) are infra-red active.

Molecular motions can be further complicated by the presence of rotations in addition to the discussed vibrations; however, the treatment of rotational-vibrational energies is simplified using the Born-Oppenheimer approximation, which assumes that the combined energy is simply the sum of the individual rotational and vibrational energies:

$$E_{total}(Joules) = E_{rotational} + E_{vibrational} \tag{3.6}$$

This then gives:

$$E_{total}(Joules) = \frac{h^2}{8\pi^2 I} J(J+1) + \left\{1 - \chi_e\left(\nu + \frac{1}{2}\right)\right\}\left(\nu + \frac{1}{2}\right) h\omega_e \tag{3.7}$$

where I is the moment of inertia and J is the rotational quantum number.

For a spherical-top molecule the following rotational transitions are allowed: $\Delta J = 0$, ± 1 and these give the energy level distribution shown in figure 3.9 below. Note here the labelling convention for the rotational energy transition bands; $\Delta J = -1, 0, +1$ denoted P, Q and R respectively.

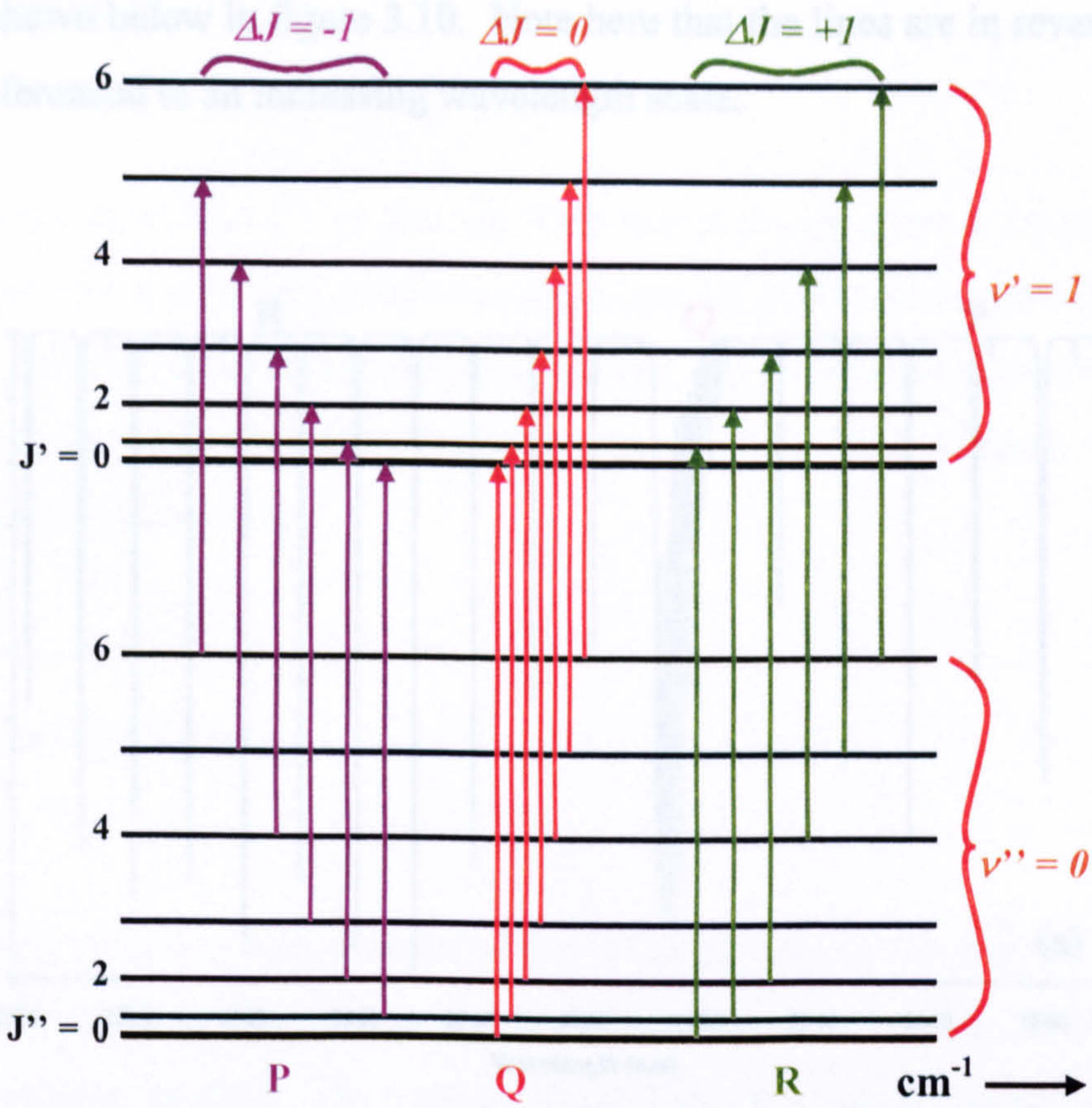

Figure 3.9: Rotational energy transitions between two vibrational states

The overall vibrations of molecules are extremely complex and their motion would be a superposition of all the individual stretching and bending vibrations pointed out thus far. As mentioned previously, the fact that the vibrations are not simple harmonic oscillations mean there is the possibility of overtone transitions at multiples of the fundamental absorption frequency. These are normally relatively weak in intensity but can, however, be enhanced by a phenomenon known as "accidental degeneracy", where two different vibrations in the same molecule can have frequencies very close to each other and one vibration can gain intensity at the expense of the other. There is also the possibility of combination ($\nu_n + \nu_{n+1}$) and difference ($\nu_n - \nu_{n+1}$) bands. All of these features lead to complex and unique absorption spectra for gas molecules. The P, Q and R branches for the fundamental, mid infra-red absorption band of methane, around 3.3 μm (~ 3030 cm^{-1}) and its accompanying near infra-red, 1st overtone absorption band, around 1650 nm (~ 6060

cm^{-1}) are shown below in figure 3.10. Note here that the lines are in reverse order as they are referenced to an increasing wavelength scale.

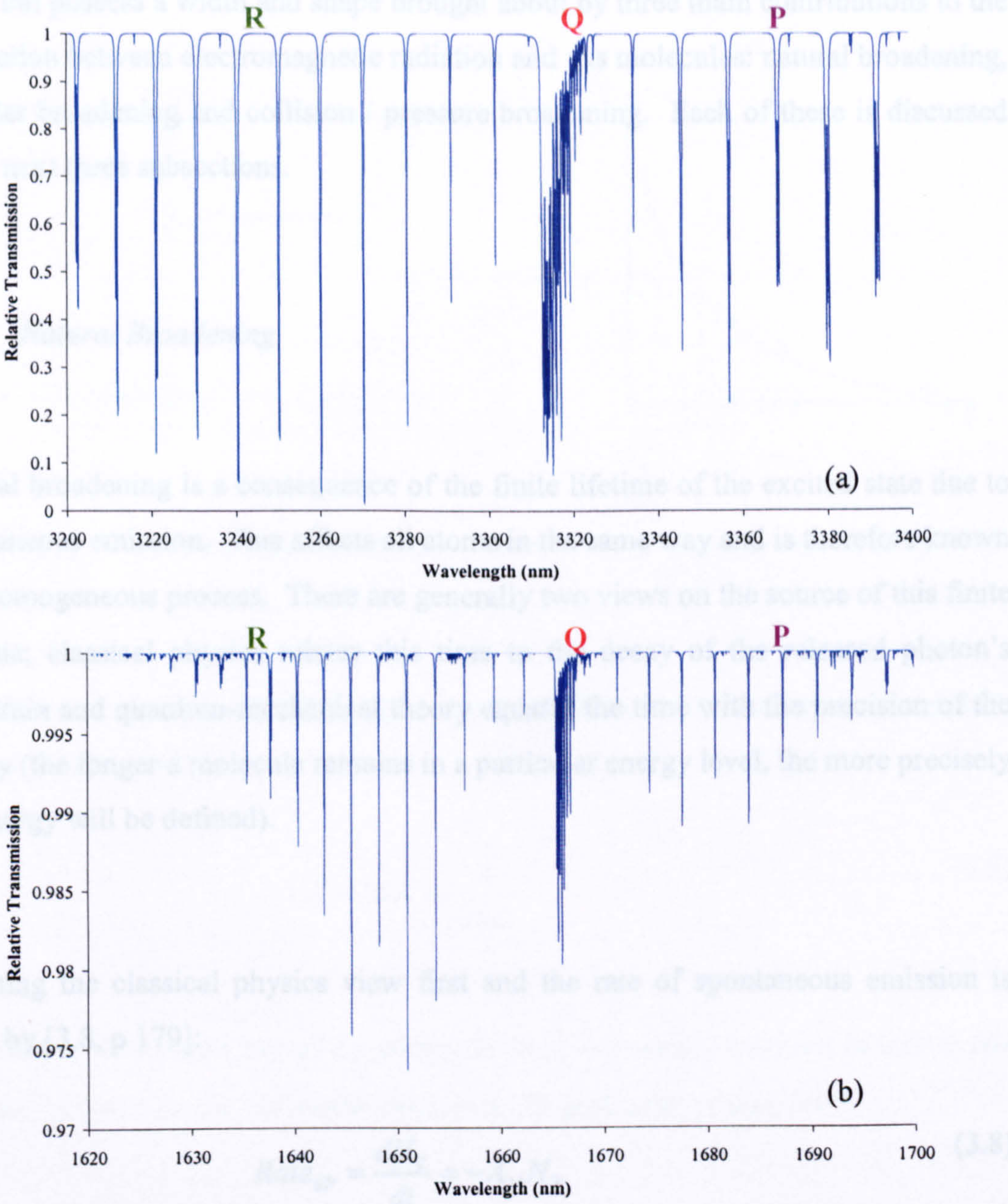

Figure 3.10: 1 % CH_4 at 22 ℃, 1 atm pressure; path length = 5.9 cm (a) Fundamental absorption spectrum (b) 1st overtone absorption spectrum – spectra modelled using Agilent VEE program (section 3.7) and HITRAN '04 data

3.4 Width of Line Spectra

It can be seen from figure 3.10 that the lines that make up spectra are not infinitely sharp but possess a width and shape brought about by three main contributions to the interaction between electromagnetic radiation and gas molecules: natural broadening, Doppler broadening and collision / pressure broadening. Each of these is discussed in the next three subsections.

3.4.1 Natural Broadening

Natural broadening is a consequence of the finite lifetime of the excited state due to spontaneous emission. This affects all atoms in the same way and is therefore known as a homogeneous process. There are generally two views on the source of this finite lifetime; classical physics relates this time to the decay of the released photon's wavetrain and quantum-mechanical theory equates the time with the precision of the energy (the longer a molecule remains in a particular energy level, the more precisely the energy will be defined).

Adopting the classical physics view first and the rate of spontaneous emission is given by [3.8, p 179]:

$$Rate_{SP} = \frac{dN_2}{dt} = -A_{21}N_2 \tag{3.8}$$

where N_2 is the density of atoms in the upper energy state and A_{21} is the Einstein decay coefficient.

3.4 Width of Line Spectra

It can be seen from figure 3.10 that the lines that make up spectra are not infinitely sharp but possess a width and shape brought about by three main contributions to the interaction between electromagnetic radiation and gas molecules: natural broadening, Doppler broadening and collision / pressure broadening. Each of these is discussed in the next three subsections.

3.4.1 Natural Broadening

Natural broadening is a consequence of the finite lifetime of the excited state due to spontaneous emission. This affects all atoms in the same way and is therefore known as a homogeneous process. There are generally two views on the source of this finite lifetime; classical physics relates this time to the decay of the released photon's wavetrain and quantum-mechanical theory equates the time with the precision of the energy (the longer a molecule remains in a particular energy level, the more precisely the energy will be defined).

Adopting the classical physics view first and the rate of spontaneous emission is given by [3.8, p 179]:

$$Rate_{SP} = \frac{dN_2}{dt} = -A_{21}N_2 \tag{3.8}$$

where N_2 is the density of atoms in the upper energy state and A_{21} is the Einstein decay coefficient.

3.4 Width of Line Spectra

It can be seen from figure 3.10 that the lines that make up spectra are not infinitely sharp but possess a width and shape brought about by three main contributions to the interaction between electromagnetic radiation and gas molecules: natural broadening, Doppler broadening and collision / pressure broadening. Each of these is discussed in the next three subsections.

3.4.1 Natural Broadening

Natural broadening is a consequence of the finite lifetime of the excited state due to spontaneous emission. This affects all atoms in the same way and is therefore known as a homogeneous process. There are generally two views on the source of this finite lifetime; classical physics relates this time to the decay of the released photon's wavetrain and quantum-mechanical theory equates the time with the precision of the energy (the longer a molecule remains in a particular energy level, the more precisely the energy will be defined).

Adopting the classical physics view first and the rate of spontaneous emission is given by [3.8, p 179]:

$$Rate_{SP} = \frac{dN_2}{dt} = -A_{21}N_2 \tag{3.8}$$

where N_2 is the density of atoms in the upper energy state and A_{21} is the Einstein decay coefficient.

The exponential decay in population of state 2 has a time constant, $\tau = (A_{21})^{-1}$ also known as the finite lifetime of the emitted wavetrain and is illustrated in figure 3.11 below.

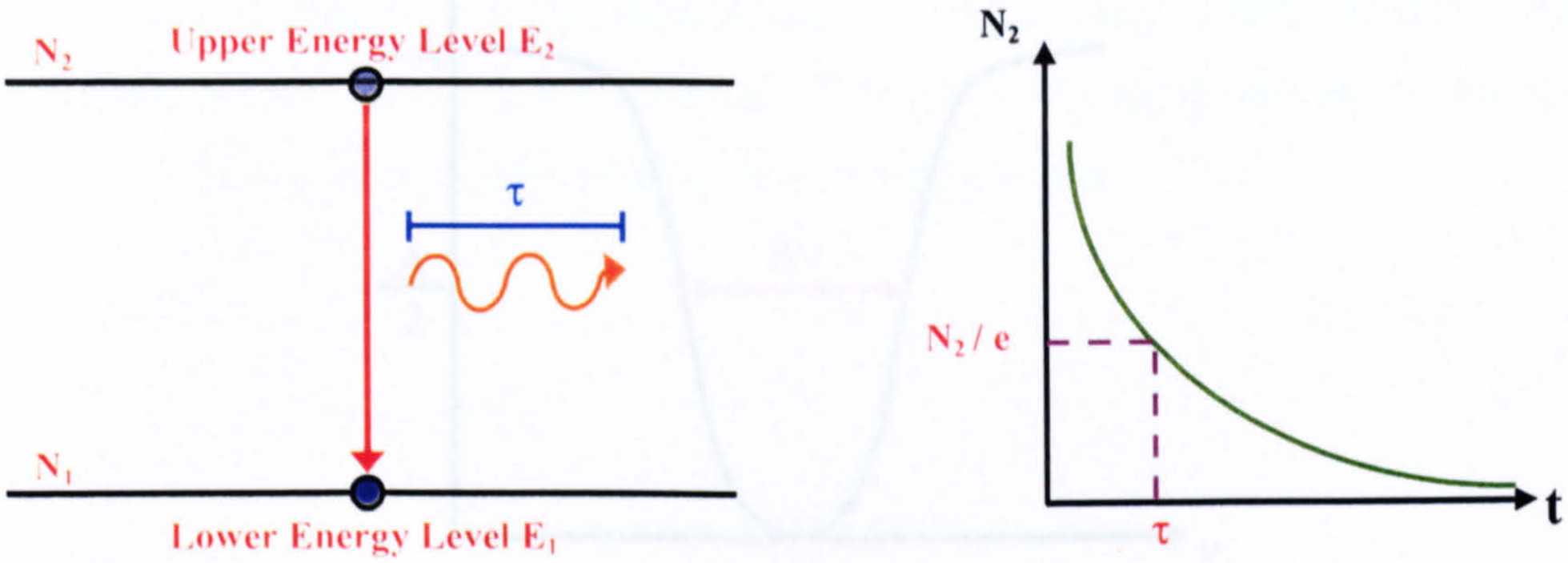

Figure 3.11: The exponential decay of a wavetrain induced by spontaneous emission

The quantum-mechanics relationship is known as Heisenberg's uncertainty principle, and can be given by:

$$\Delta E = h\Delta\nu \approx \frac{h}{2\pi\Delta t} \tag{3.9}$$

where ΔE is the uncertainty of the energy level, h is Planck's constant as before and Δt is the natural lifetime the molecule stays in the particular energy level.

If it is assumed that $\tau = \Delta t$, the frequency spread as a result of this uncertainty is given by equation (3.10) and is also illustrated in figure 3.12. The spread of frequencies, $\Delta\nu$, is also known as the full-width-half-maximum (FWHM) linewidth and is one of the most important parameters in gas line shape analysis.

$$\Delta\nu \geq \frac{1}{\tau} \tag{3.10}$$

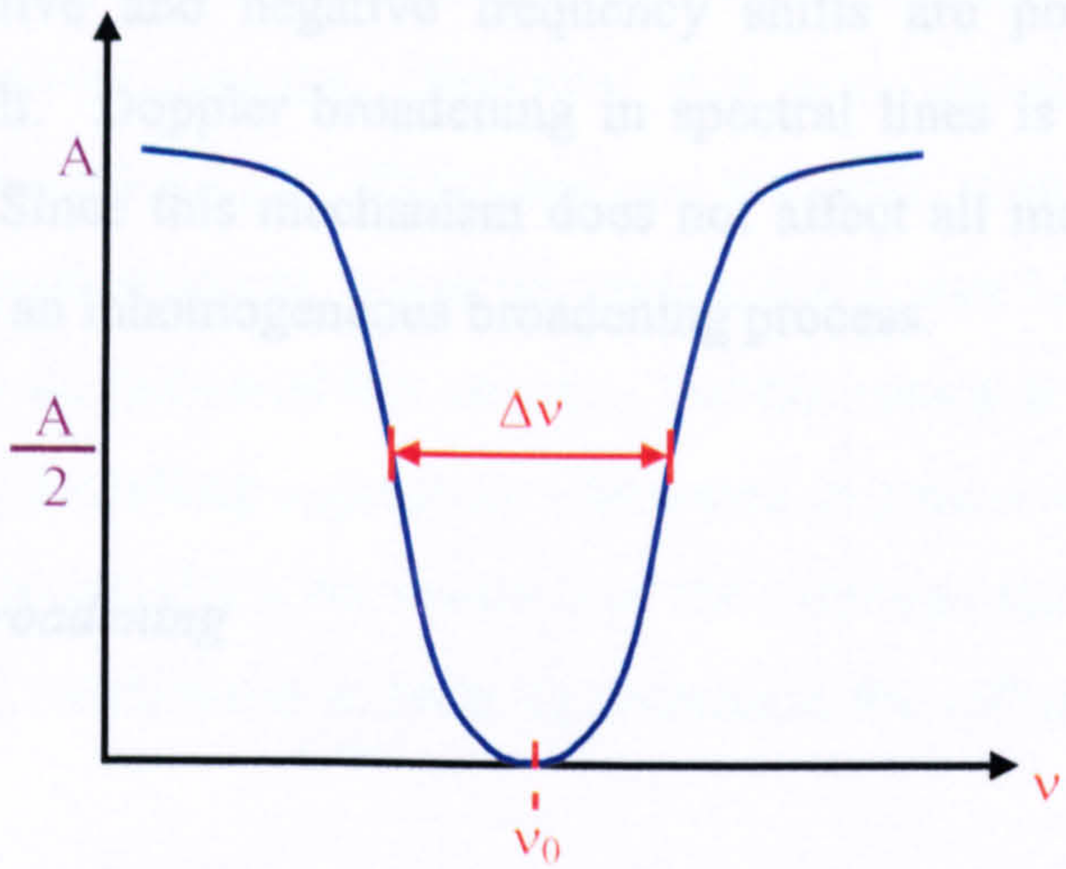

Figure 3.12: Natural linewidth of spectral line. ν_0 is the line centre

For natural broadening the spread in frequencies is usually modelled by a Lorentzian profile.

3.4.2 Doppler Broadening

Doppler broadening is the result of the Doppler Effect, which is the apparent shift in the frequency of a signal emitted or absorbed by a body in motion. The common analogy is a train's whistle getting higher in frequency as the train travels with constant velocity towards an observer, and lower in frequency as it travels away. In terms of spectroscopy, the frequency of the radiation absorbed during a transition differs according to the direction and velocity of motion of the gas molecule, relative to the source of radiation. As the molecule moves with constant velocity towards the electromagnetic radiation, the frequency appears higher (blue shifted); consequently

the frequency at which the absorption occurs is lower. As the molecule moves away from the electromagnetic radiation, the frequency appears lower (red shifted), giving rise to absorption at a higher frequency. When the molecules are travelling with greater velocity the red and blue shifts are greater. Since the molecular motions are random both positive and negative frequency shifts are possible and a broad lineshape can result. Doppler broadening in spectral lines is best modelled by a Gaussian profile. Since this mechanism does not affect all molecules in the same way, it is known as an inhomogeneous broadening process.

3.4.3 Collision Broadening

Collision broadening, also known as pressure broadening, dominates at atmospheric pressure (~ 1 atm). Due to the increased pressure there is an increase in the likelihood of molecules colliding with each other. These collisions between molecules give rise to a shorter lifetime of the wavetrain, or from a quantum-mechanics view point, an increased blurring of the energy levels, and result in a larger spread of frequencies. In reference to equation (3.10) then, the formula for the frequency spread is now:

$$\Delta\nu \geq \frac{1}{\tau_C} \tag{3.11}$$

where $\tau_C = (A_{21} + K)^{-1}$ and K is the probability of a collision.

Since it is an extension of the natural broadening phenomena, the lineshape used to model the gas absorption is, again, Lorentzian and the process is also termed a homogeneous broadening mechanism.

3.4.4 The Voigt Profile

It is generally accepted that at pressures greater than 200 mbar, collision broadening begins to dominate; therefore, a Lorentzian profile becomes increasingly more accurate with increasing pressure. However, this work investigated gas pressures over the range of 200 mbar up to 2000 mbar and therefore, with the exception of the high-end pressure measurements, it was not certain that a pure Lorentzian profile was a suitable model for all measured line spectra. For this reason it was decided to use a Voigt profile in the modelling algorithms (discussed in greater detail in section 3.7). A Voigt profile is essentially a convolution of the Gaussian and Lorentzian profiles and has dampening coefficients in order to determine the influence each has on the overall profile.

3.5 Intensity of Line Spectra

There are two main contributors to the intensity of a spectral line and these are: transition probability and population of states. Each is discussed in the following sub-sections.

3.5.1 Transition Probability

This was touched on previously when discussing the selection rules for the rotational (ΔJ) and vibrational ($\Delta \nu$) energy transitions in sections 3.2 and 3.3 and is simply the likelihood of a molecule making a transition from one energy level to another. For example, when discussing the methane molecule it was mentioned that the selection rule for the rotational energy transitions was $\Delta J = 0, \pm 1$; meaning transitions outside of this have zero intensity and consequently have no observable spectra.

3.5.2 Population of States

Again, this was touched upon in section 3.3 when discussing transitions originating from $\nu = 1$ and above. These transitions and spectra are considerably weaker than transitions from $\nu = 0$ due to the fact that with increasing energy levels, the population density rapidly decreases. This is modelled effectively by the Boltzmann distribution given in equation (3.12) below, describing the ratio of the population of the upper energy state to the lower energy state as:

$$\frac{N_{Upper}}{N_{Lower}} = e^{\left(\frac{-\Delta E}{kT}\right)} \tag{3.12}$$

where ΔE is the difference between energy states as before, k is the Boltzmann constant (1.38×10^{-23} JK^{-1}) and T is the temperature in Kelvin.

3.5.3 The Beer – Lambert Law

The Beer – Lambert law simply describes the logarithmic relationship between intensity at the input, I_{in}, to an absorbing medium and the intensity at the output, I_{out}, and is given by:

$$I_{out} = I_{in} e^{-\alpha Cl} \approx I_{in}(1 - \alpha Cl) \tag{3.13}$$

where α is the molar absorption coefficient of the absorbing medium (in this case the gas), C is the concentration of the gas and l is the length of the absorbing path (in this case the micro - optic cell). The approximation: $(1 - \alpha Cl)$ is only accurate in the limit of $\alpha Cl \ll 1$. The concentration is normally expressed as a mole fraction or

percentage, leaving the units of length and absorption coefficient to be the reciprocal of each other i.e. cm and cm^{-1} respectively. Equation (3.13) states that the strongest absorption signals are achieved with gases at high concentrations, measured over long path lengths (as highlighted in chapter 2).

3.6 Extracting Concentration and Pressure from Line Spectra

In order to determine the concentration and pressure of a gas from the recovered absorption line transmission function or its corresponding derivatives, further analysis is required of the Beer – Lambert law in equation (3.13).

3.6.1 Concentration and Absolute and Derivative Signals

For gas monitoring at atmospheric pressure the gas absorption line, as a function of frequency, can be described by a Lorentzian profile, given by equation (3.14) below [3.9].

$$\alpha(\nu) = \frac{N_0 S}{\pi\gamma\left\{\left(\frac{\nu-\nu_0}{\gamma}\right)^2 + 1\right\}} = \frac{\alpha_0}{(\Delta^2 + 1)} \tag{3.14}$$

where N_0 is the number of molecules at STP[III], S is the linestrength (cm.molecule^{-1}),γ is the half-width-half-maximum (HWHM) linewidth (cm^{-1}) and ν_0 and α_0 are the frequency and absorption coefficient at line centre respectively. Therefore, the recovered absolute gas transmission function is given by:

[III] 1 mole (6.02×10^{23} molecules) occupies 22.4 litres at STP, giving $N_0 \approx 2.5 \times 10^{19}$ molecules cm^{-3} at 25 °C and 1atm pressure.

$$1 - \frac{I_{out}}{I_{in}} = \frac{N_0 S}{\pi\gamma\left\{\Delta^2 + 1\right\}} Cl = \left\{\frac{\alpha_0}{\left(\Delta^2 + 1\right)} Cl\right\} \tag{3.15}$$

Rearranging (3.15) for C and setting $\Delta = 0$, the concentration at line centre is given by:

$$C = \frac{\left(1 - \frac{I_{out}}{I_{in}}\right)}{\alpha_0 l} \tag{3.16}$$

which simply states that the concentration is proportional to the depth of the relative transmission function, as illustrated in figure 3.13 below.

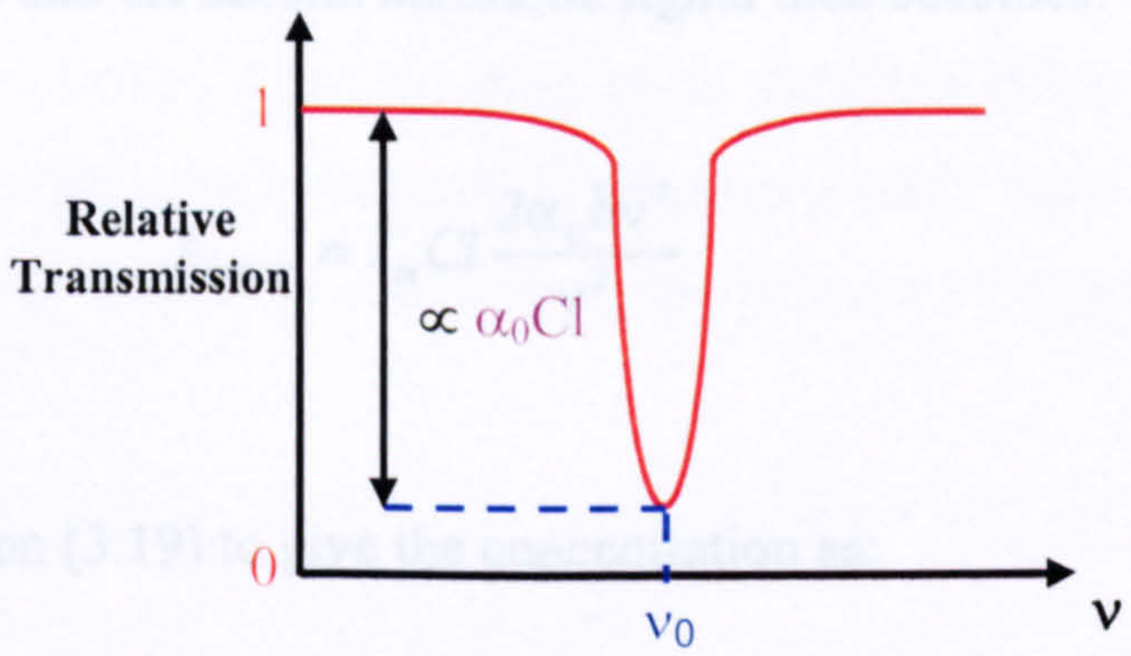

Figure 3.13: Concentration from transmission function, scaled to path length and absorption coefficient

In WMS / derivative measurements, the extraction of concentration is a little more complex. As mentioned in chapters 1 and 2, the amplitude of the 2nd derivative is proportional to the slope of the 1st derivative, in turn proportional to the depth of the absolute transmission function at line centre. The simplest way to determine concentration in derivative spectroscopy is then to measure the amplitude of the 2nd derivative signal at line centre. Measured harmonic signals are proportional to the

derivative signals in the limit of small modulation index ($m = \delta\nu/\gamma << 1$), and the signals for the first two harmonics are given by equations (3.17) and (3.18) below.

$$I_{out\,f} = -I_{in}Cl\frac{d\alpha(\nu)}{d\nu}\delta\nu = I_{in}Cl\frac{2N_0S\Delta\delta\nu}{\pi\gamma^2(\Delta^2+1)^2} = I_{in}Cl\frac{2\alpha_0\Delta\delta\nu}{\gamma(\Delta^2+1)^2} \tag{3.17}$$

It can be seen then that the amplitude of the first harmonic has a dependency on $\delta\nu / \gamma$. This dependency becomes stronger with increasing order of harmonic and the second harmonic is then:

$$I_{out\,2f} = -I_{in}Cl\frac{2N_0S(3\Delta^2-1)\delta\nu^2}{\pi\gamma^3(\Delta^2+1)^3} = -I_{in}Cl\frac{2\alpha_0(3\Delta^2-1)\delta\nu^2}{\gamma^2(\Delta^2+1)^3} \tag{3.18}$$

At line centre $\Delta = 0$ and the second harmonic signal then becomes:

$$I_{out\,2f} = I_{in}Cl\frac{2\alpha_0\delta\nu^2}{\gamma^2} \tag{3.19}$$

Rearranging equation (3.19) to give the concentration as:

$$C = \frac{\gamma^2 I_{out\,2f}}{2I_{in}l\alpha_0\delta\nu^2} \tag{3.20}$$

Therefore, as expected, the concentration is proportional to the amplitude of the 2nd harmonic signal ($I_{out\ 2f}$) at line centre, scaled by the input power, the absorption coefficient, the absorption path length, the gas absorption linewidth and the amplitude of the sinusoidal modulation. The 1st and 2nd harmonic signals are shown, along with their relationship to concentration, in figure 3.14.

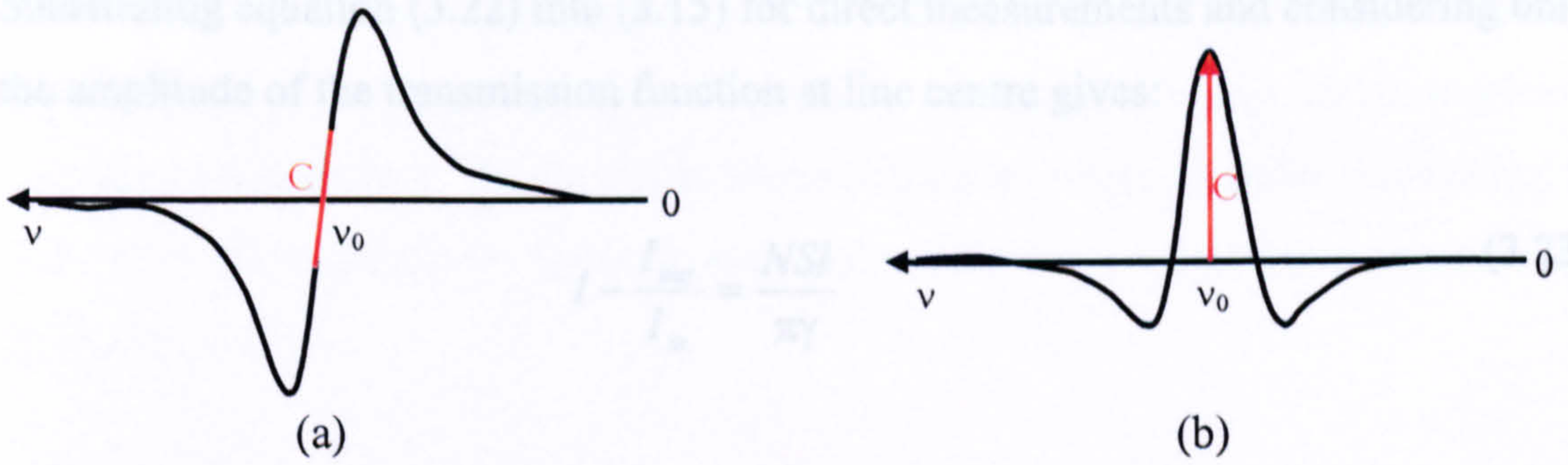

Figure 3.14: Concentration from (a) 1st harmonic / derivative and (b) 2nd harmonic / derivative of transmission function, scaled to path length, absorption coefficient and input power

3.6.2 Pressure and Absolute and Derivative Signals

If we consider pressures at which collision broadening dominates and concentrations at which the Beer – Lambert approximation holds, the relationship between pressure and linewidth for a pressure-broadened Lorentzian profile (and consequently for directly measured line-shapes) is well known and is given by equation (3.21) below [3.10, p 245].

$$\gamma = \gamma_0 \left(\frac{P}{P_0} \right) \left(\frac{T_0}{T} \right)^{\frac{1}{2}} \tag{3.21}$$

where γ_0 is the HWHM linewidth at pressure $P_0 = 1$ atm and temperature $T_0 = 300°K$. The gas concentration, C, can be expressed as the number of gas molecules per unit volume (N), relative to the number of gas molecules at STP per unit volume (N_0):

$$C = \frac{N}{N_0} \tag{3.22}$$

Substituting equation (3.22) into (3.15) for direct measurements and considering only the amplitude of the transmission function at line centre gives:

$$1-\frac{I_{out}}{I_{in}}=\frac{NSl}{\pi\gamma} \tag{3.23}$$

Substituting equation (3.21) into (3.23) gives:

$$1-\frac{I_{out}}{I_{in}}=\frac{NSl}{\pi\gamma_0\left(\frac{P}{P_0}\right)\left(\frac{T_0}{T}\right)^{\frac{1}{2}}} \tag{3.24}$$

At constant temperature equation (3.24) can be simplified to:

$$1-\frac{I_{out}}{I_{in}}=\frac{NSl}{\pi\gamma_0\left(\frac{P}{P_0}\right)}=\frac{P_0NSl}{\pi\gamma_0P}=\frac{NKl}{P} \tag{3.25}$$

where K is a constant given by $(P_0S / \pi\gamma_0)$. The Ideal Gas Law is given by:

$$P=\frac{nRT}{V}=NRT \tag{3.26}$$

where P is the pressure (atm), n is the number of moles, R is the universal gas constant (82.0575 atm.cm^3/mol.° K), T is the temperature (° K), V is the volume (cm^3) and N is the number of gas molecules per unit volume, as before. Rearranging equation (3.26) for N and substituting into equation (3.25) gives:

$$1-\frac{I_{out}}{I_{in}}=\frac{PKl}{PRT}=\frac{Kl}{RT} \tag{3.27}$$

From the above analysis, the amplitude of the absolute absorption line transmission function appears to be independent of pressure / linewidth change for atmospheric pressure measurements. However, at lower pressures, where Doppler broadening is influential, the transmission function amplitude will show a small dependence on the linewidth.

In TDLS / WMS measurements determining the linewidth is, again, a little more complex. Returning to equations (3.17) and (3.18) and the relationships between 1st and 2nd harmonics / derivatives, it is obvious that the peaks of the 1st harmonic / derivative are located at the points when the second harmonic / derivative is equal to zero. Therefore, removing the vertical scaling constants from equation (3.18) and setting to zero gives:

$$\frac{2\left(3\Delta^2 - 1\right)\delta\nu^2}{\gamma^2\left(\Delta^2 + 1\right)^3} = 0 \tag{3.28}$$

The solution to this equation is $\Delta^2 = (1/3)$, which, when solved for ν, gives two absolute frequency locations of $\nu = \nu_0 \pm (\gamma/\sqrt{3})$ as illustrated in figure 3.15 below.

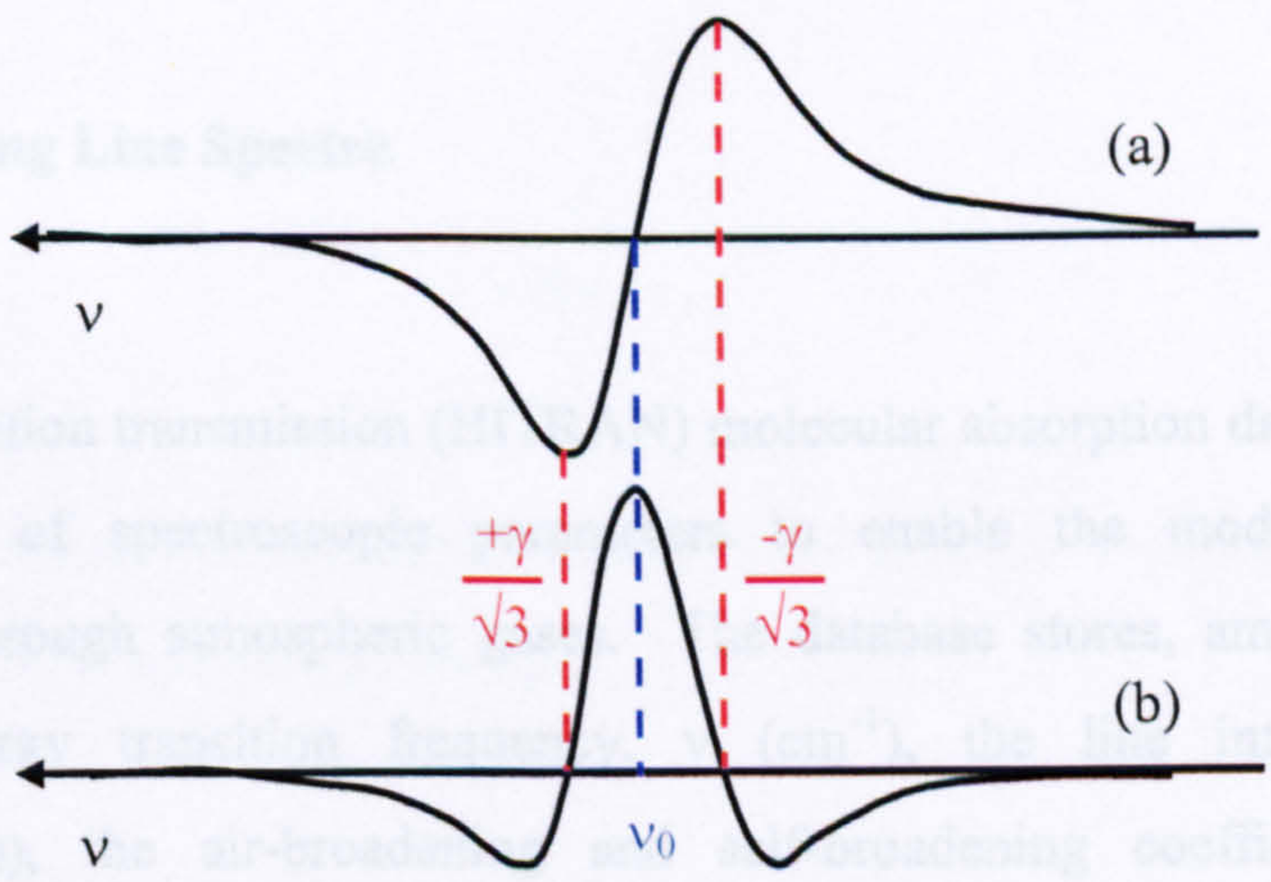

Figure 3.15: Linewidth relationship between (a) 1st and (b) 2nd derivatives of transmission function

Therefore, it is possible, in principle, to extract linewidth information from harmonic / derivative traces.

From the above analysis then, several conclusions can be drawn:

1. For TDLS with direct detection gas concentration can be determined directly from the amplitude of the gas absorption line transmission function and, to a reasonable approximation, signal amplitude is independent of pressure / linewidth change at atmospheric pressures.
2. For TDLS / WMS detection the gas concentration can no longer be regarded as independent of pressure / linewidth and derivative signal amplitudes depend upon the system scaling factor $\delta\nu / \gamma$. However, it is in principle, possible to extract the linewidth from the recovered harmonic / derivative signals.
3. As well as measuring the concentration and pressure directly from the recovered signal amplitude and linewidth respectively, the parameters can be determined from curve fitting procedures, matching theoretical predictions to the recovered signals. Section 3.7 describes the modelling of atmospheric gas absorption line transmission functions.

3.7 Modelling Line Spectra

The high-resolution transmission (HITRAN) molecular absorption database [3.11] is a compilation of spectroscopic parameters to enable the modelling of light transmission through atmospheric gases. The database stores, among others, the molecular energy transition frequency, ν (cm^{-1}), the line intensity (cm^{-1} / ($molecule.cm^{-2}$)), the air-broadening and self-broadening coefficients and the pressure shift. The information is for transitions at 296 °K. Obviously, in industrial applications the gas pressure and temperature varies from STP and the gas

composition can vary from target gas / air mix; therefore, a program using the Agilent VEE runtime environment was developed by industrial collaborators OptoSci Ltd.[IV]. As mentioned previously, the program uses a Voigt profile, which is a convolution of the Gaussian (Doppler broadening) and Lorentzian (collision broadening) profiles. Traditionally the generation of a Voigt profile, by a process of numerical integration, was time consuming; however, recent progress in the development of very accurate approximation methods [3.12] has allowed the VEE program to model atmospheric absorption profiles over a range of pressures. The process of convolution is mathematically represented by the following classic equation:

$$(G * L)(\nu) = \int_{-\infty}^{+\infty} G(\nu')L(\nu - \nu')d\nu' \tag{3.29}$$

In [3.12] the Gaussian profile, G(ν), is given by:

$$G(\nu) = \frac{1}{\sigma\sqrt{2\pi}} exp\left(\frac{-\nu^2}{2\sigma^2}\right) \tag{3.30}$$

where σ is the standard deviation. Likewise, the Lorentzian profile, L(ν), is given by:

$$L(\nu) = \frac{a_L}{1 + 4(\nu/\gamma_L)^2} \tag{3.31}$$

where a_L is the absorption coefficient as before and γ_L is the HWHM linewidth. The resulting Voigt profile is then given by:

[IV] OptoSci Ltd: 141 St James Road, Glasgow, G4 0LT, Scotland.
Tel: +44(0)141 552 7020, Email: info@optosci.com

$$I(\nu) = \frac{\gamma_L}{\gamma_G} a_L \sqrt{\pi ln(2)} V(X,Y) \tag{3.32}$$

where γ_G is the HWHM linewidth of the Gaussian profile. $V(X,Y)$ is given by:

$$V(X,Y) = \sum_{i=1}^{4} \frac{C_i(Y - A_i) + D_i(X - B_i)}{(Y - A_i)^2 + (X - B_i)^2} \tag{3.33}$$

where *Ai* through to *Di* are a set of pre-defined constants shown in table 3.1. X and Y in both equations (3.32) and (3.33) are given by:

$$X = \frac{2\sqrt{ln(2)}}{\gamma_G} \nu \tag{3.34}$$

and

$$Y = \frac{\gamma_L}{\gamma_G} \sqrt{ln(2)} \tag{3.35}$$

I	A_i	B_i	C_i	D_i
1	-1.2150	1.2359	-0.3085	0.0210
2	-1.3509	0.3786	0.5906	-1.1858
3	-1.2150	-1.2359	-0.3085	-0.0210
4	-1.3509	-0.3786	0.5906	1.1858

Table 3.1: Parameters used in generation of Voigt profile

By using the Voigt profile and adhering to the Beer-Lambert law, the program developed by OptoSci Ltd. is capable of modelling gas absorption spectra for a wide

range of concentrations, pressures, temperatures and absorption path lengths. Fine adjustment of the broadening coefficients also permits the modelling of target gas absorption in host / balance gases other than air.

These theoretical predictions are compared to the measured absolute transmission functions, recovered either directly or through derivative methods. The curve fitting procedure requires only some fine adjustments over the pressure and concentration variables to provide the best match.

3.8 Conclusions

A theoretical treatment of gas molecules and molecular absorption spectra has been presented. The relationships between pressure, linewidth and concentration in direct absolute absorption line transmission profiles and their derivatives have been described in detail. Finally a general description of the novel software designed by industrial collaborators OptoSci Ltd. to model the absorption of light through various atmospheric gas compositions was given. With this background it is now possible to recognise the important parameters which define unique gas absorption line spectra and how to extract quantitative gas concentration and pressure measurements from these spectra.

3.9 References

[3.1] C. N. Banwell and E. M. McCash, "Fundamentals of Molecular Spectroscopy: Fourth Edition," McGraw – Hill, 1994.

[3.2] B. P. Straughan and S. Walker, "Spectroscopy Volume Two: Molecular, Microwave, Infrared, Far-infrared and Raman Spectroscopy, Force Constants, Group Theory, and Thermodynamic Functions," Chapman and Hall Ltd., 1976.

[3.3] G. M. Barrow, "Introduction to Molecular Spectroscopy, International Student Edition," McGraw – Hill Kogakusha Ltd., 1962.

[3.4] J. M. Hollas, "Basic Atomic and Molecular Spectroscopy, Tutorial Chemistry Texts: 11," The Royal Society of Chemistry, 2002.

[3.5] J. M. Hollas, "High Resolution Spectroscopy," Butterworth and Co. Ltd., 1982.

[3.6] E. D. Hinkley, "Laser Monitoring of the Atmosphere: Topics in Applied Optics, Volume 14," Springer – Verlag Berlin Heidelberg New York, 1976.

[3.7] A. Thorne, U. Litzen and S. Johansson, "Spectrophysics: Principles and Applications," Springer – Verlag Berlin Heidelberg New York, 1999.

[3.8] J. T. Verdeyen, "Laser Electronics: Third Edition," Prentice – Hall Inc., 1995.

[3.9] G. Stewart, C. Tandy, D. Moodie, M. A. Morante and F. Dong, "Design of a Fibre Optic Multi-Point Sensor for Gas Detection," Sensors and Actuators B: Chemical, Vol. 51, pp 227-232, April 1998.

[3.10] E. D. Hinkley, "Topics in Applied Physics, Volume 14: Laser Monitoring of the Atmosphere," Springer – Verlag Berlin Heidelberg New York, 1976.

[3.11] L. S. Rothman et al., "The HITRAN 2004 molecular spectroscopic database," Journal of Quantitative Spectroscopy and Radiative Transfer, Vol. 96, pp 139-204, 2005.

[3.12] A. B. McLean, C. E. J. Mitchell and D. M. Swanston, "Implementation of an Efficient Analytical Approximation to the Voigt Function for Photoemission Lineshape Analysis," Journal of Electron Spectroscopy and Related Phenomena, Vol. 69, No. 2, pp 125 – 132, September 1994.

Chapter 4

Experimental Methodologies: Systems and Procedures

4.1 Introduction

This chapter describes the experimental systems and methodologies used to implement both direct TDLS and TDLS / WMS detection schemes, reflecting the state-of-the-art for industrial gas monitoring. It is important to note here that the systems described in this chapter were assembled and tested by the author. As well as discussing parameter choice and the normalisation methods key to providing immunity to calibration drift and system loss variations, the chapter also describes the construction of a fibre ring-resonator and the development of novel signal processing techniques for wavelength referencing.

Methane (CH_4) gas was chosen for these investigations for two reasons. The first is the high demand for methane measurement in industrial applications, ranging from safety monitoring in oil and gas exploration plants, to environmental concerns in landfill sites. The second reason is that it has relatively strong absorption at near infra-red wavelengths, allowing for accurate analysis of lineshapes. In the 1600 – 1700 nm range, methane absorption lines fall within P-, Q- and R- branches, which categorise rotational / vibrational states. One of the most commonly addressed lines is the Q6 line around 1665 nm, shown below in figure 4.1. However, as can be seen from the figure, the lines in the Q- branch are closely packed together and with increasing pressure these lines begin to merge, making accurate lineshape analysis extremely difficult.

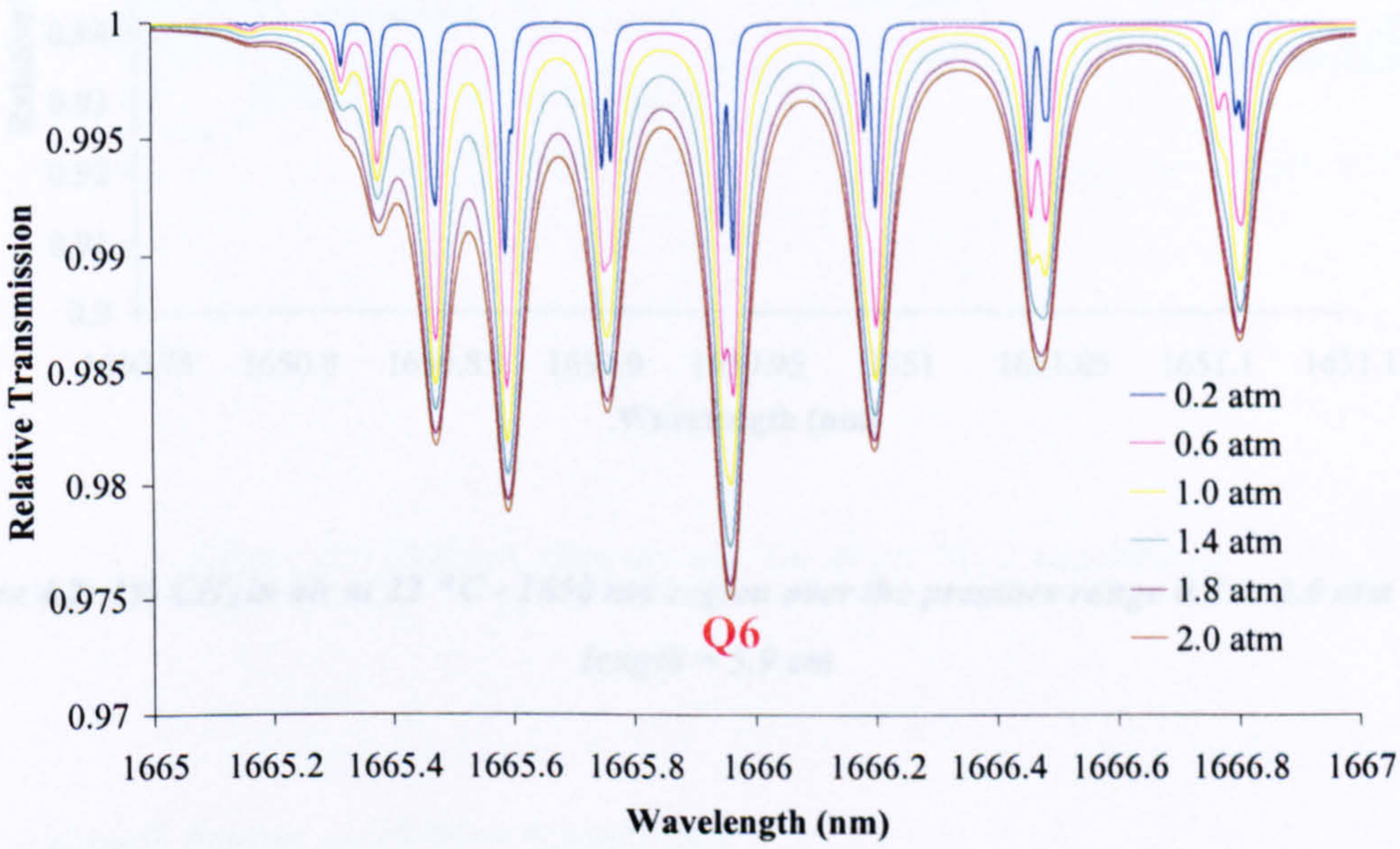

Figure 4.1: 1 % CH_4 in air at 22 °C - Q branch region over the pressure range 0.2 to 2.0 atm – path length = 5.9 cm

In the interests of achieving accurate lineshapes and pressure measurements, the R - branch combination line at 1650.956 nm was a better choice. As can be seen from figure 4.2, although this line is a combination of two transitions resolvable at low

pressure, the combination line remains symmetrical at high pressure and permits an off-line measurement to be made. The linestrength is also comparable to the Q6 line. Through personal communication with Dr Moodie of OptoSci Ltd. the line was confirmed to be free of interference from overlapping lines arising from other known atmospheric gases. For these reasons, the TDLS detection techniques described in this chapter were used to interrogate the CH_4 *line* at 1650.956 nm.

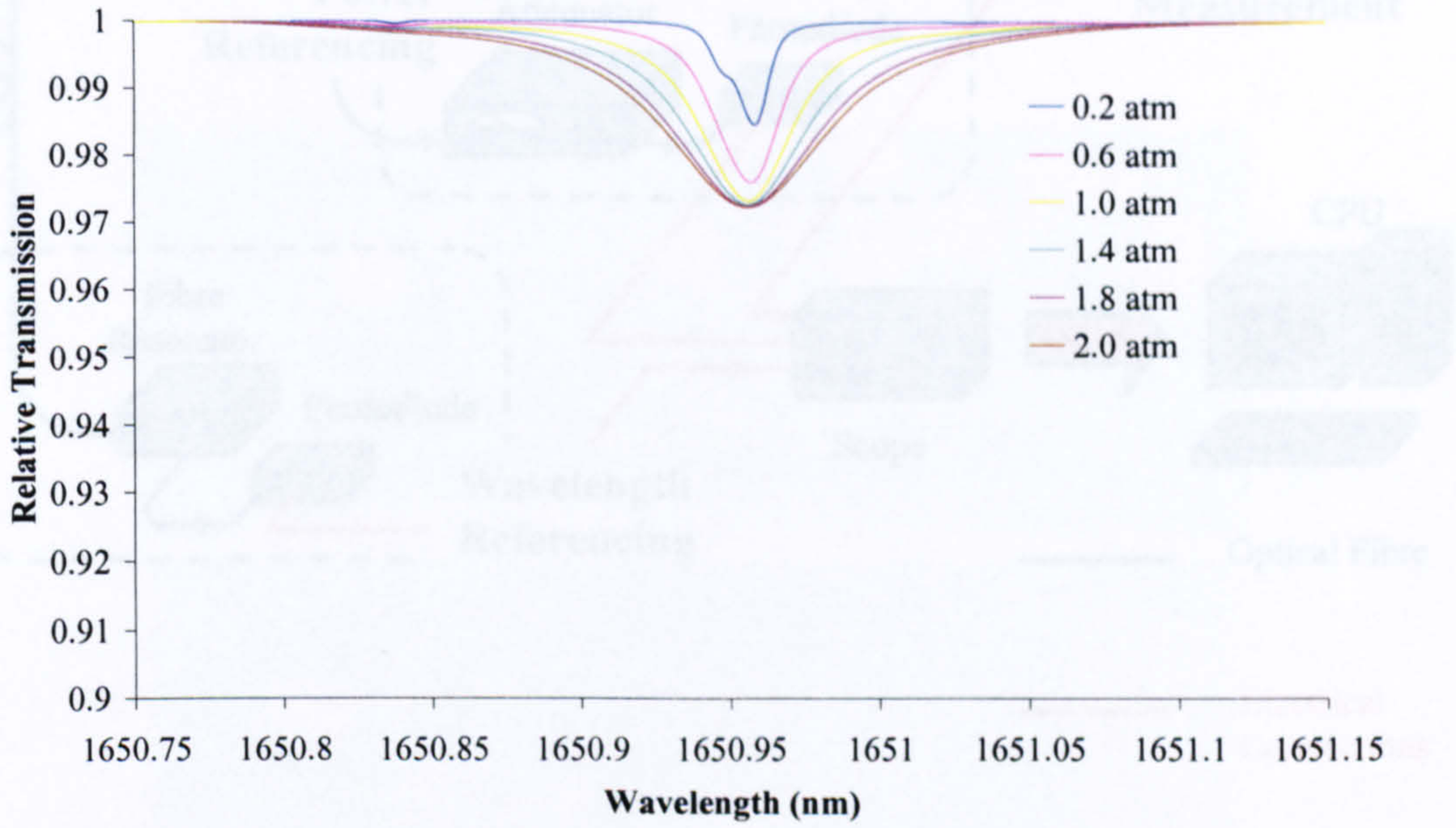

Figure 4.2: 1% CH_4 in air at 22 °C - 1650 nm region over the pressure range 0.2 to 2.0 atm – path length = 5.9 cm

4.2 Tunable Diode Laser Spectroscopy with Direct Detection

The general principles of operation for TDLS with direct detection were described in detail in chapter 2 and figure 4.3 illustrates the experimental set up used to implement these principles. In the figure, the system is broken down into four major areas: signal source and drive electronics; gas measurement; power referencing and wavelength referencing.

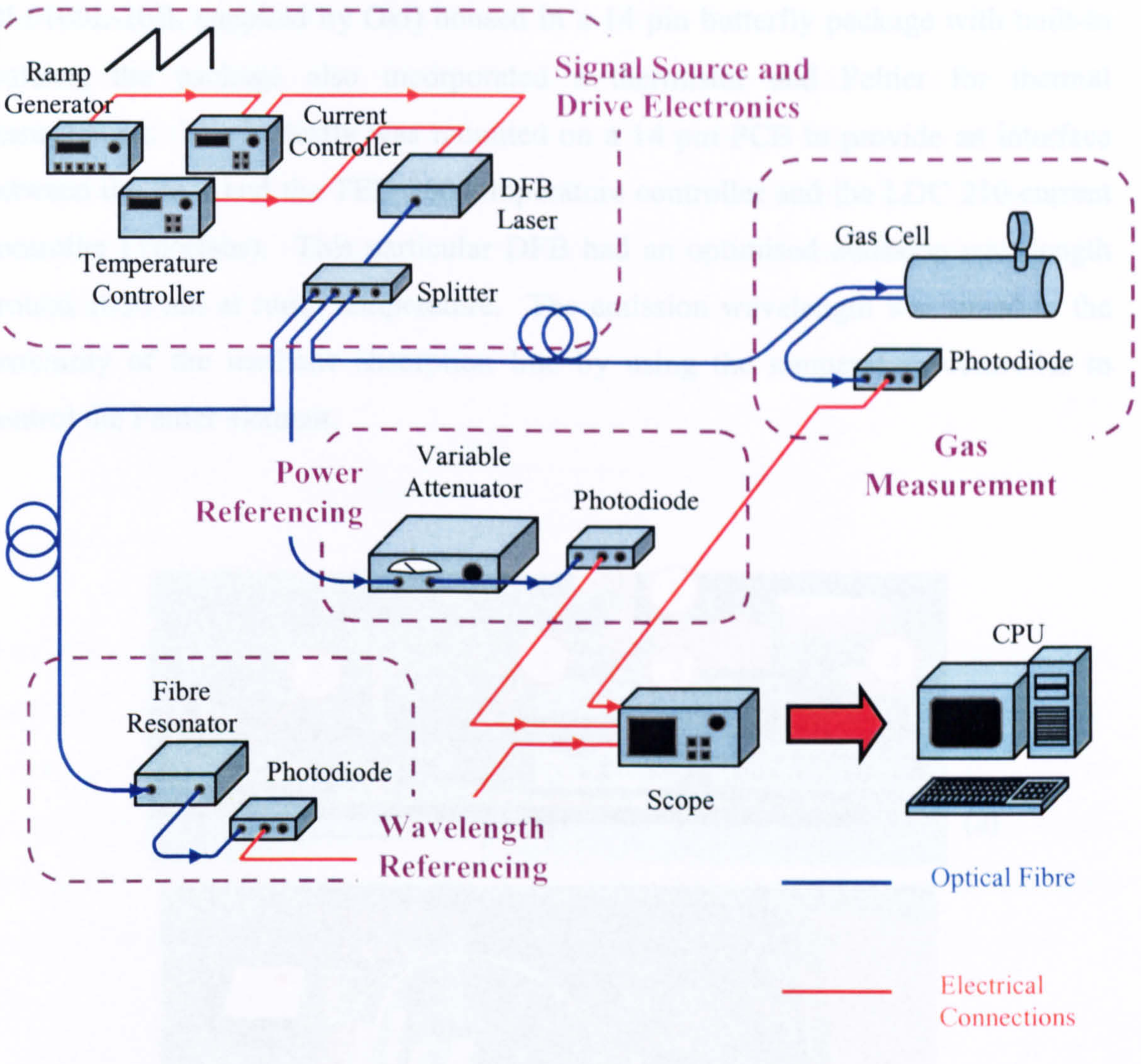

Figure 4.3: Diagram of set up used for direct TDLS experiments

4.2.1 Signal Source and Drive Electronics

The signal source and drive electronics essentially includes all the components and their associated parameters that were necessary to provide a high power density, single wavelength source, tunable over the entire wavelength range of the chosen methane gas absorption line. Pictured below in figure 4.4(a) is the actual laboratory equipment used and figure 4.4(b) shows a detailed photograph of the laser source. The source comprised a distributed feedback (DFB) laser diode (model number:

OL6109L-10B, supplied by Oki) housed in a 14 pin butterfly package with built-in isolator; the package also incorporated a thermistor and Peltier for thermal management. The butterfly was mounted on a 14 pin PCB to provide an interface between the laser and the TED 200 temperature controller and the LDC 210 current controller (Thorlabs). This particular DFB had an optimised emission wavelength around 1650 nm at room temperature. The emission wavelength was tuned to the proximity of the methane absorption line by using the temperature controller to control the Peltier element.

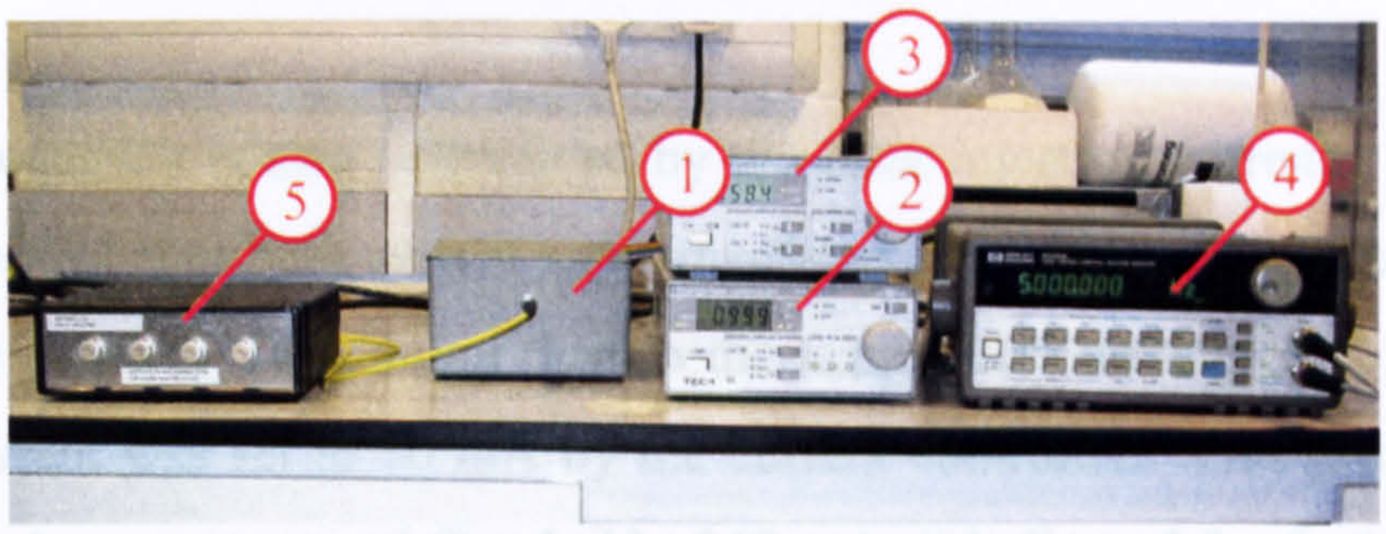

(a)

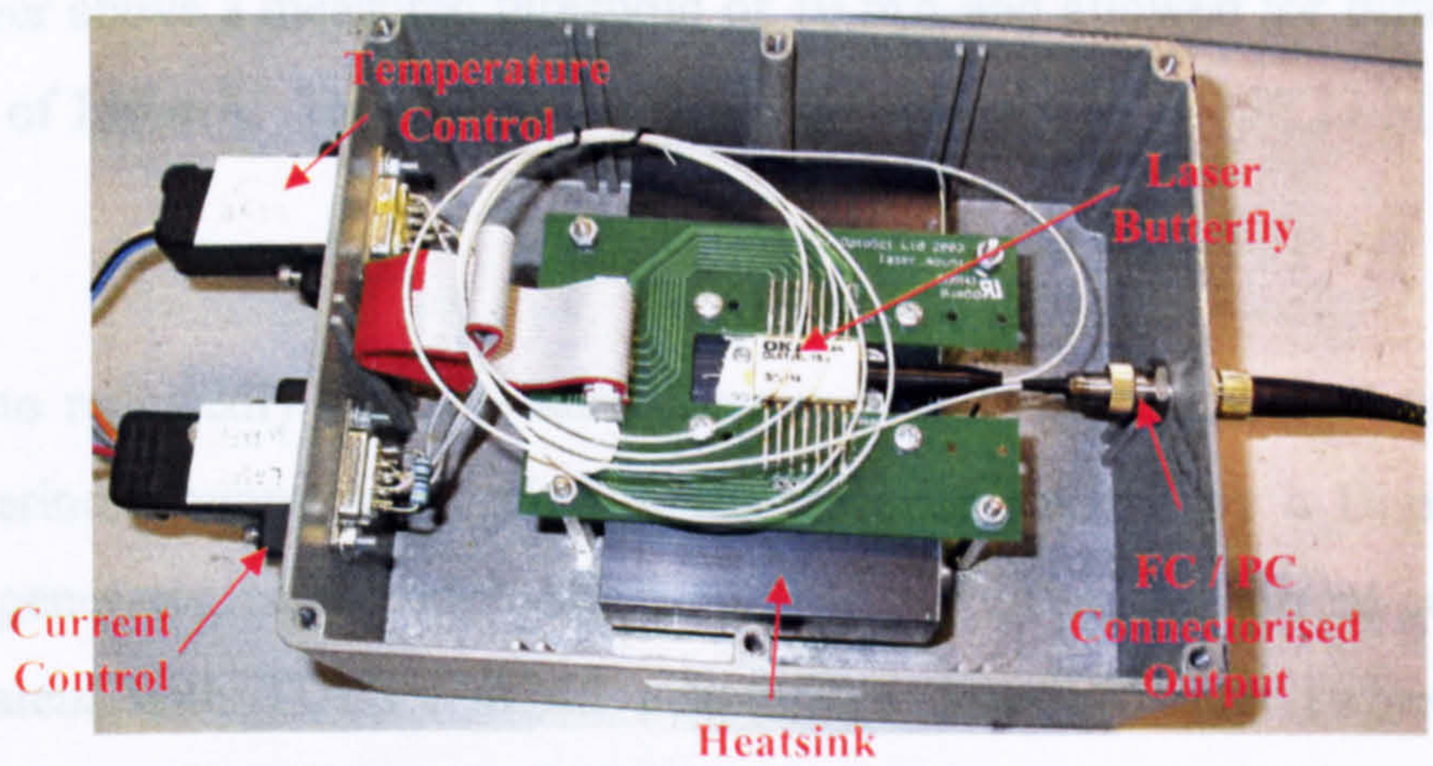

(b)

Figure 4.4: (a) Laboratory set up for laser source and drive electronics: 1. Laser Source, 2. Temperature Control, 3. Current Control, 4. Ramp Generator and 5. Fibre Splitter (b) Detailed photograph of laser diode and peripherals

Thermal tuning provides a wider tuning rate compared to current tuning but at the expense of reduced precision. Once a desired wavelength is reached, the temperature controller employs a feedback control loop to keep the temperature and laser output stabilised. From some earlier characterisation experiments, an interferometer was

used to determine the DC tuning rate at 10.51 GHz / ° C. The thermistor measures the temperature of the laser and the thermistor resistance measurement is displayed on the temperature controller; this allows feedback to the user. Thermistor resistance, R, is related to the temperature, T, by equation (4.1) [4.1]. To tune to the centre of the gas absorption line at 1650.956 nm the temperature of the laser was increased to 35.346 °C (6.455 kΩ).

$$T(°C) = \left\{ \frac{3892}{\ln\left(R(k\Omega) / 2.142 \times 10^{-5} \right)} \right\} - 273.15 \qquad (4.1)$$

The laser frequency is also determined by the laser injection current. Indeed, it is only with control over both current and temperature, that the laser's centre frequency can be truly defined. In addition then to the temperature setting of 35.346 °C, the injection current was set to 70 mA by the current controller. This provided ample laser power above a measured threshold of 10 mA and allowed for further tuning up to a limit of 150 mA. The DC tuning rate was measured to be 756.23 MHz / mA.

In order to repeatedly scan the laser frequency over the entire methane absorption line, a periodic ramp was applied to the injection current by a Digimess FG100 function generator, connected to the modulation input on the current controller. To be consistent with TDLS / WMS adaptations described later (where the sweep frequency has to be kept relatively low) the ramp modulation frequency was set to 5 Hz. The ramp modulation amplitude depends on the width of the line and as these experiments were intended for a large pressure range (0.2 to 2.0 atm); the modulation amplitude was made large enough to cover the widest absorption line. This was measured to be 80 mA peak-to-peak (800 mV on the ramp generator as the modulation coefficient on the current controller is 100 mA / V). In addition to frequency modulation, modulation of the injection current also leads to a change in power. The current vs. power characteristic of this particular DFB laser is shown in figure 4.5.

Tunable diode laser spectroscopy requires a narrow source in order to accurately interrogate lineshapes. It is typical for any given gas line to have a linewidth of approximately 3 GHz at atmospheric pressure. Therefore, to achieve a sensitive and discriminate gas measurement over the range of 0.2 atm to 2.0 atm, it was necessary that the source linewidth be much narrower than this. Typical DFB sources are around 10 MHz. Again, using an interferometer, the linewidth of this particular laser source was measured to be 3.4 MHz; three orders of magnitude less than the gas line.

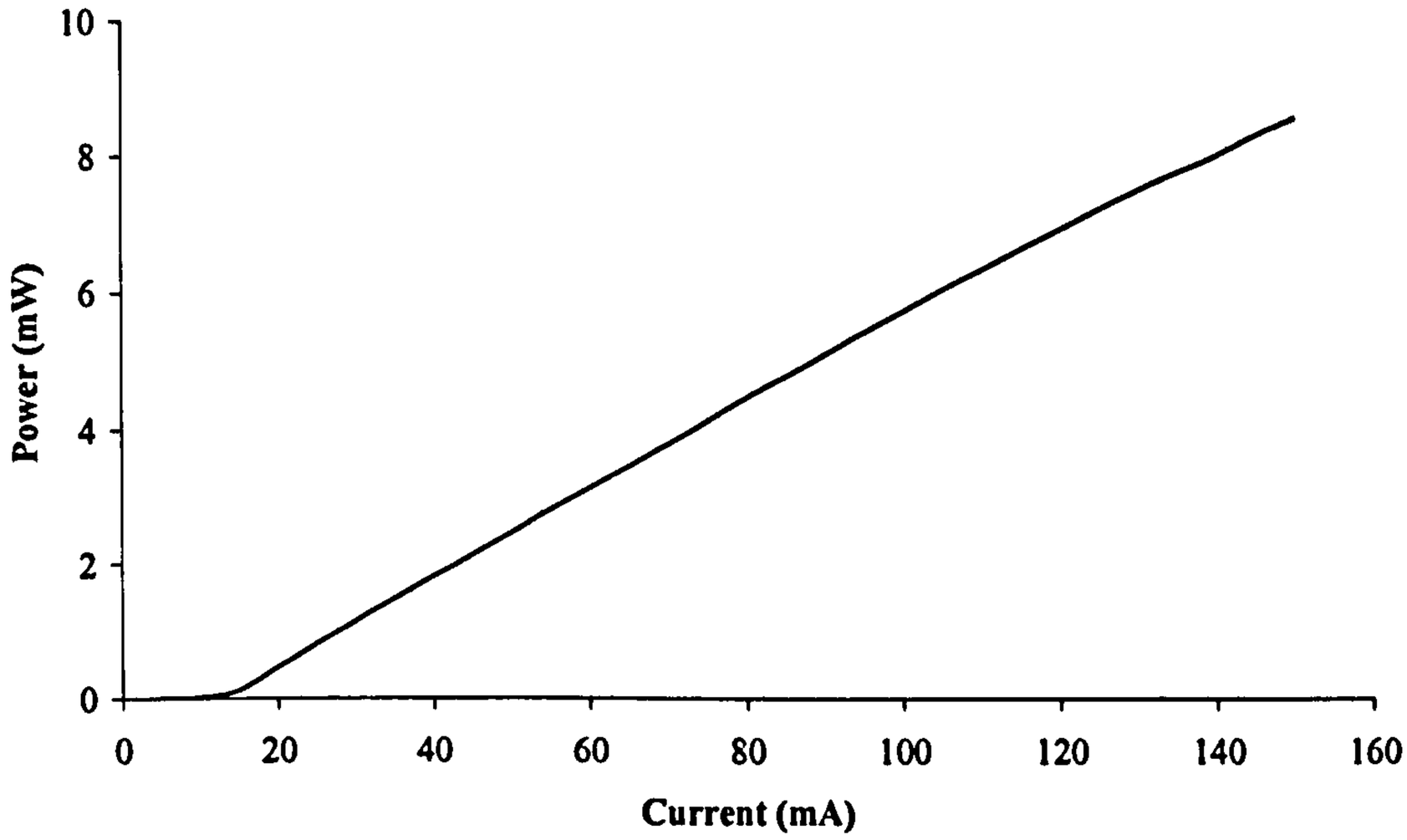

Figure 4.5: Plot of current vs. power for the 1650 nm Oki DFB laser module

To enable the signal processing and normalisation procedures, described later in section 4.2.6, the laser signal was split into three channels: a gas measurement channel; a power referencing channel and a wavelength referencing channel. The laser butterfly was PC connectorised permitting light transmission, over optical fibre, to a standard comms 4-way, 1550 nm fibre splitter. Although the split ratio between

each output was not exactly even, any discrepancies were normalised out, again as described in section 4.2.6.

4.2.2 Gas Measurement

A schematic of the gas cell housing is provided in figure 4.6. The housing consisted of a 37.5 cm long tube and two end caps, each with a diameter of 9 cm. There was a rubber gasket between each end cap and the tube to provide an air-tight seal. The volume of the cell housing was approximately 2384 cm^3 (2.384 Litres). At one end cap there were three Swagelok valves to control the gas in and out of the cell housing. The valves were self tapping and were inserted into the housing by drilling holes in the end cap, slightly smaller than the diameter of the valves, and then screwing the valves in. There were two inlet valves; one for the desired gas mixture, in this case CH_4:N_2, and the second for an inert purge gas, in this case N_2. The outlet valve was connected to a vacuum pump, which had its outlet pipe passed to a fume cupboard for safe removal of the gas. A more detailed description of the gas handling procedure is given in section 4.2.6. At the opposite end cap there were two fibre insertion points and a digital pressure gauge. Fibre insertion was achieved by drilling a hole into the end cap, passing the fibre through, splicing a pigtail to the end of the fibre and then gluing and sealing up the splice protector half-way through the hole. As for the pressure gauge, it was inserted into the cell in the same way as the Swagelok valves. The LEO-2 digital pressure gauge (from Omni Instruments) measures an absolute pressure range from 0 to 3 bar, with a resolution of 3 decimal places (1 millibar). The relationship between atmospheres and bars is: 1 bar = 0.986923266 atm. Inserted into the side of the housing was a thermocouple, which in turn was connected to a TES thermistor unit, for accurate (to 1 °C) measurement of the temperature. All holes and joins were sealed and tested to ensure the measurement cell sustained a gas mixture above 2.0 bar for a sufficient period.

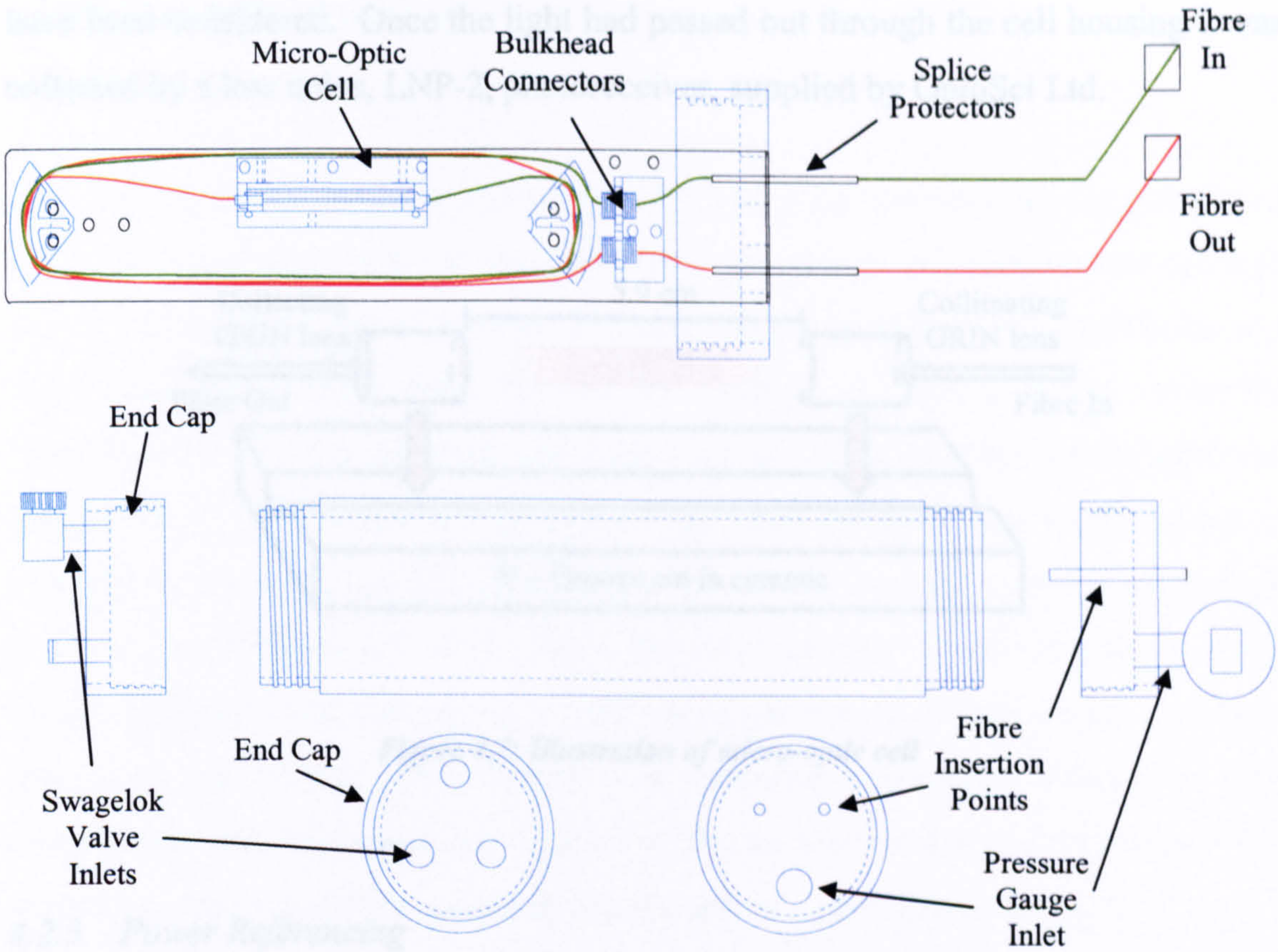

Figure 4.6: Schematic of gas cell housing

Within the cell housing was a micro-optic cell, which consisted of two gradient-index (GRIN) lenses, aligned in a ceramic v–groove, with an open path of 5.9 cm, as shown in figure 4.7. The lenses were secured in the v–groove by ultra-violet curing glue. Both the glue and v – groove are insensitive to changes in temperature, making them ideal for maintaining lens alignment in extreme environments. At the fibre input to the cell the first GRIN lens collimates the light across the open path, where the target gas would normally be present. The light is then collected by the second GRIN lens and travels through the fibre back out of the cell. The lenses had standard anti-reflection coatings to suppress interferometric noise[I] by approximately 30 dB. This level of suppression was acceptable for the gas concentration levels that were under primary investigation; however, for low ppm level detection, the more expensive 60 dB suppression coatings or a focusing GRIN lens design would have to

[I] Interferometric noise is the result of back reflections from the surfaces of the lenses [4.2 – 4.5]

have been considered. Once the light had passed out through the cell housing it was collected by a low noise, LNP-2, photoreceiver, supplied by OptoSci Ltd.

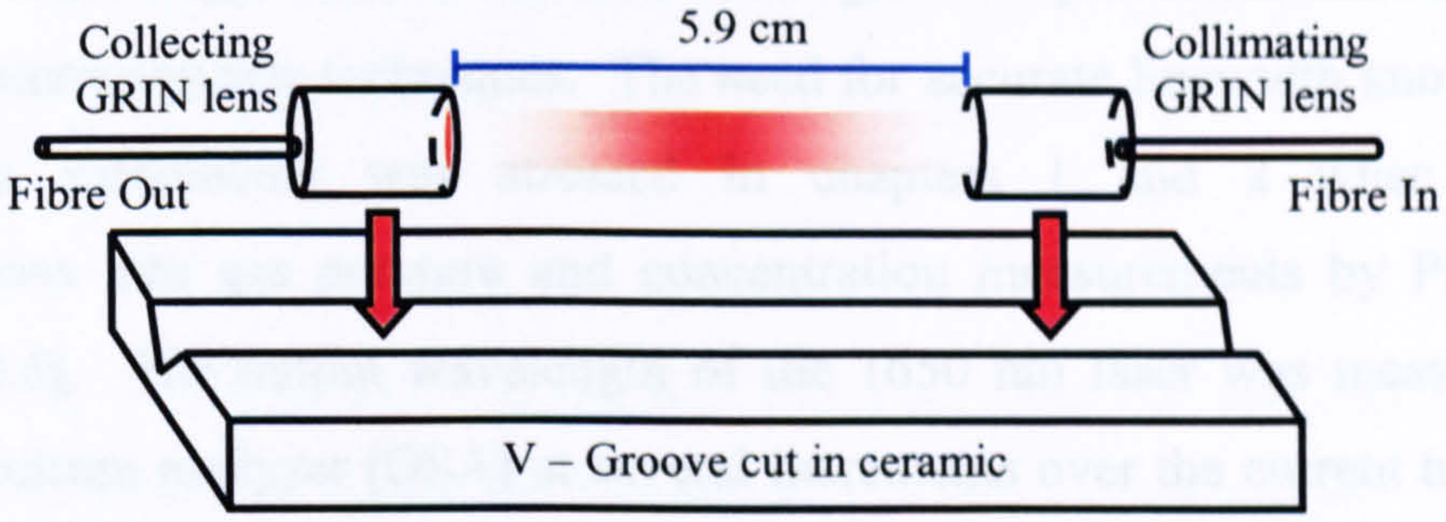

Figure 4.7: Illustration of micro-optic cell

4.2.3 Power Referencing

In order to monitor and normalise to the change in power as the laser injection current was ramped, the second channel served as a power reference. This fraction of the main laser beam was attenuated via a variable attenuator to match the off-line power of the signal coming from the gas cell. The losses through the gas cell and housing essentially came from the splices, bulkhead connectors and the open path. The attenuation of the second channel also accounted for any disparity in the splitting ratio between both channels. The power referencing signal was also monitored on a LNP-2 photoreceiver. It is worth noting at this point that the gain settings on all the LNPs were the same; they were set at the lowest gain of 1 k for two reasons. The first being that the DFB laser supplied ample signal and amplification was not required. The second reason was to maximise the available bandwidth (1 MHz). The bandwidth issue was not crucial to the direct implementation of TDLS but it maintained consistency with the TDLS / WMS schemes described later.

4.2.4 Wavelength Referencing

This section reports on the development of a fibre ring-resonator for the purpose of applying a wavelength scale to our time-based gas absorption measurements through standard interferometric techniques. The need for accurate linewidth knowledge and wavelength referencing was stressed in chapters 1 and 2 when reviewing investigations into gas pressure and concentration measurements by Philippe and Hanson [4.6]. The output wavelength of the 1650 nm laser was measured on an optical spectrum analyser (OSA) at several increments over the current tuning range and is shown in figure 4.8. It is evident from this current vs. wavelength plot that a linear mapping of wavelength on to time-based gas measurements would have been inaccurate, particularly when tuning over extended wavelength ranges for high pressure gas lines. Repeatability of scans is also an issue as it is widely accepted that over the course of time the operation wavelength of a laser source drifts.

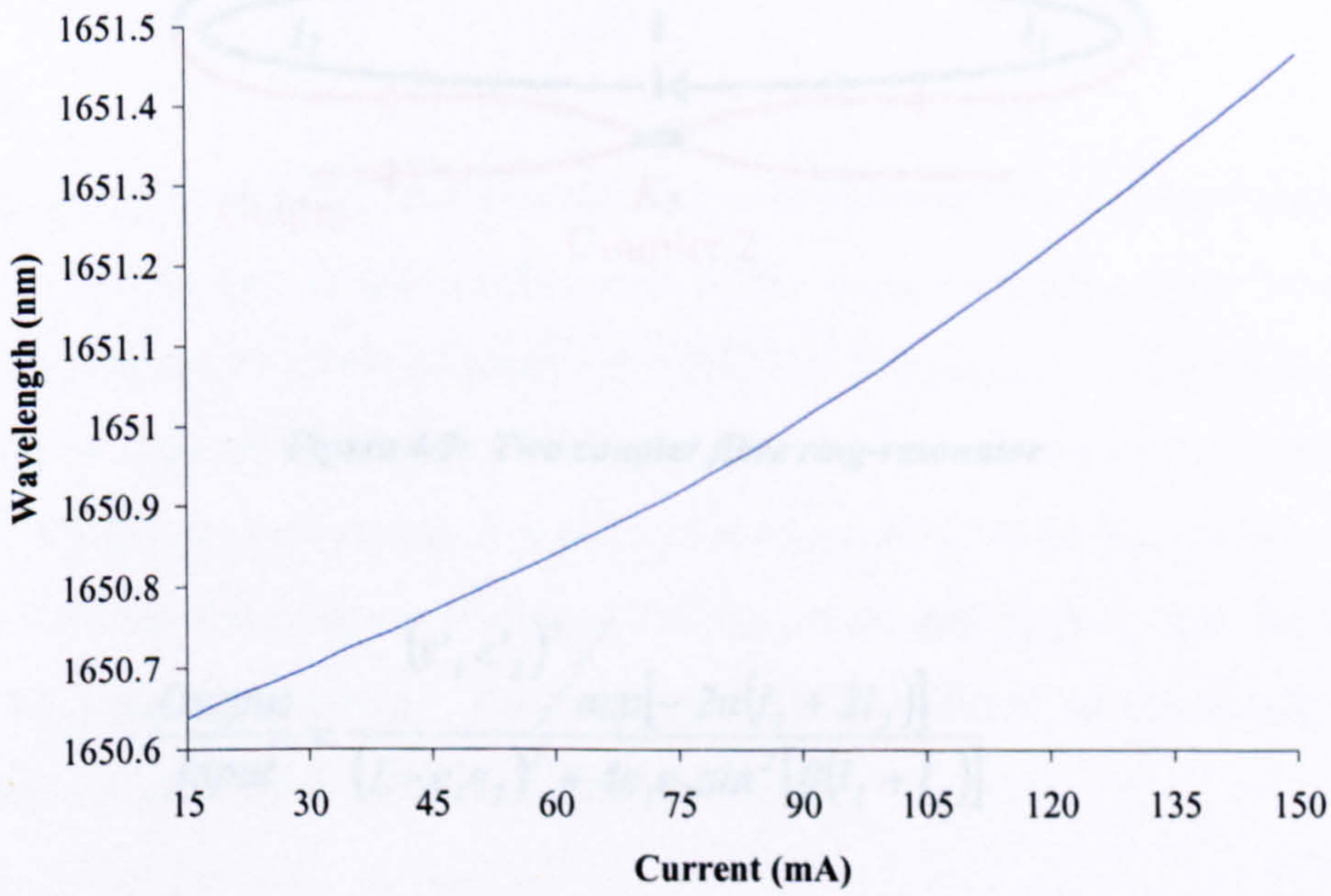

Figure 4.8: Current vs. wavelength relationship for 1650 nm laser module

A bulk optics approach described in [4.6] monitors the laser's relative wavelength / frequency change as it is tuned across the gas line. An absolute scale is then determined by comparing the gas measurements to theoretical predictions. A similar approach is described here using a fibre ring-resonator. This fibre-based approach provides a solution to the interference, alignment and maintenance issues incurred when using a bulk-optics system in industrial environments.

The fibre ring-resonator was constructed from two 1550 nm couplers fused in the configuration shown in figure 4.9 below. It is known from Urquhart [4.7 and 4.8] that the channel passing output provides the classic Fabry-Perot response. This response can be modelled using Urquhart's equations (4.2) to (4.5) below:

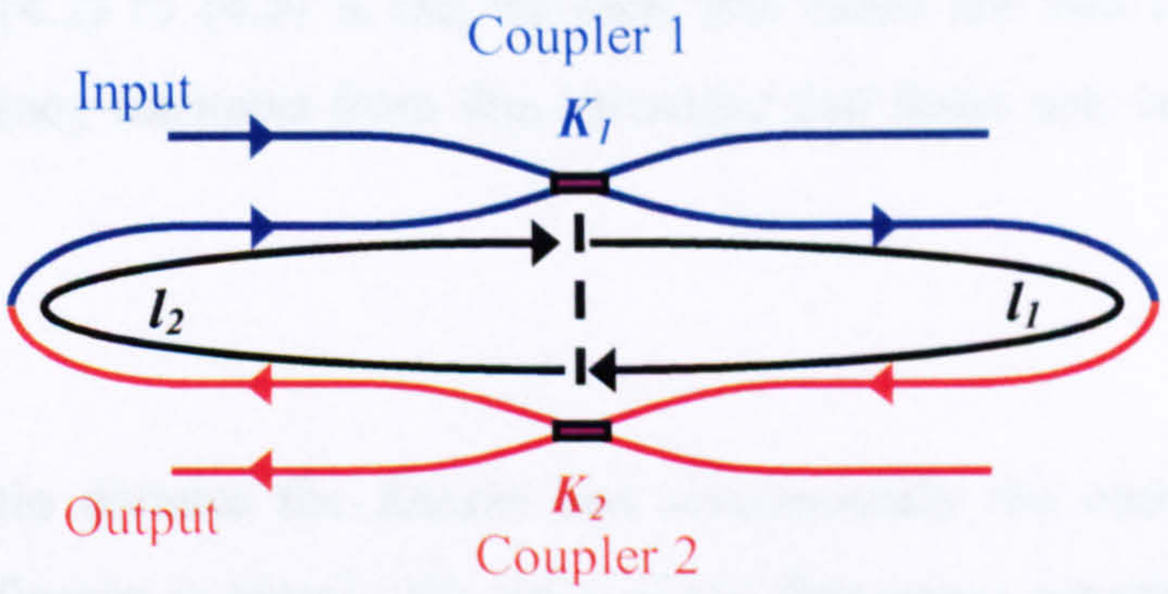

Figure 4.9: Two coupler fibre ring-resonator

$$\frac{Output}{Input} = \frac{\left(\varepsilon'_1 \varepsilon'_2\right)^2 \Big/ exp\left[-2\alpha\left(l_1 + 2l_2\right)\right]}{\left(1 - \varepsilon_1 \varepsilon_2\right)^2 + 4\varepsilon_1 \varepsilon_2 sin^2\left[\beta\left(l_1 + l_2\right)\right]} \tag{4.2}$$

where:

$$\varepsilon_j = \left(1 - K_j\right)^{\frac{1}{2}} \left(1 - \gamma_j\right)^{\frac{1}{2}} exp\left(-2\alpha l_j\right),\ j = 1,\ 2. \tag{4.3}$$

and

$$\varepsilon'_j = K_j^{\frac{1}{2}}\left(1-\gamma_j\right)^{\frac{1}{2}} exp\left(-2\alpha l_j\right),\ j = 1,\ 2. \tag{4.4}$$

α is the field loss in the fibre (typically 0.22 dB / km for standard single mode fibre), $l_1 + l_2$ is the length of the ring, and K_1 and K_2 and γ_1 and γ_2 are the coupling ratios and excess losses of couplers 1 and 2 respectively. β is the propagation constant and is given by:

$$\beta = \left(\frac{2\pi}{\lambda}\right)n \tag{4.5}$$

where n is the refractive index of the fibre (typically 1.45) and λ is the wavelength.

From equations (4.2) to (4.5) it can be seen that there are two main factors that dictate the frequency response from this resonator and those are: coupling ratio and ring length.

The coupling ratio dictates the finesse and consequently the contrast ratio of the resonator. The finesse is simply the ratio of the frequency separation between the peaks to the full-width-half-maximum (FWHM) of the peaks; the higher the finesse, the sharper the transmission peak. Since the accuracy of this wavelength referencing technique hinged on the accurate location of the transmission peaks, there had to be a trade-off between the finesse (sharpness) of the transmission peak and the precision of the data logging software. The contrast ratio is defined as the amplitude of a transmission peak relative to the minimum intensity.

The ring length of the fibre resonator dictates the frequency separation between transmission peaks, also known as the free spectral range (FSR). The relationship between finesse and FSR is given below in equation (4.6):

$$Finesse = \frac{FSR}{FWHM} \tag{4.6}$$

For a fixed frequency scan, the longer the fibre ring is, the greater the number of transmission peaks supported. Again, there had to be a trade-off here between the number of transmission peaks and the precision of the data logger. There was also a practical limitation imposed on the fibre ring length. Due to the physical constraints of splicing two small bodied couplers together, the shortest ring size achievable was approximately 47 cm.

With the above limitations in mind a MATLAB program was devised by the author to model Urquhart's equations and is detailed in Appendix B. Figure 4.10 shows the fibre ring-resonator response for three readily available pairs of couplers; 20:80; 40:60 and 50:50. Since either arm can be coupled into the ring this provided five possible coupling ratios.

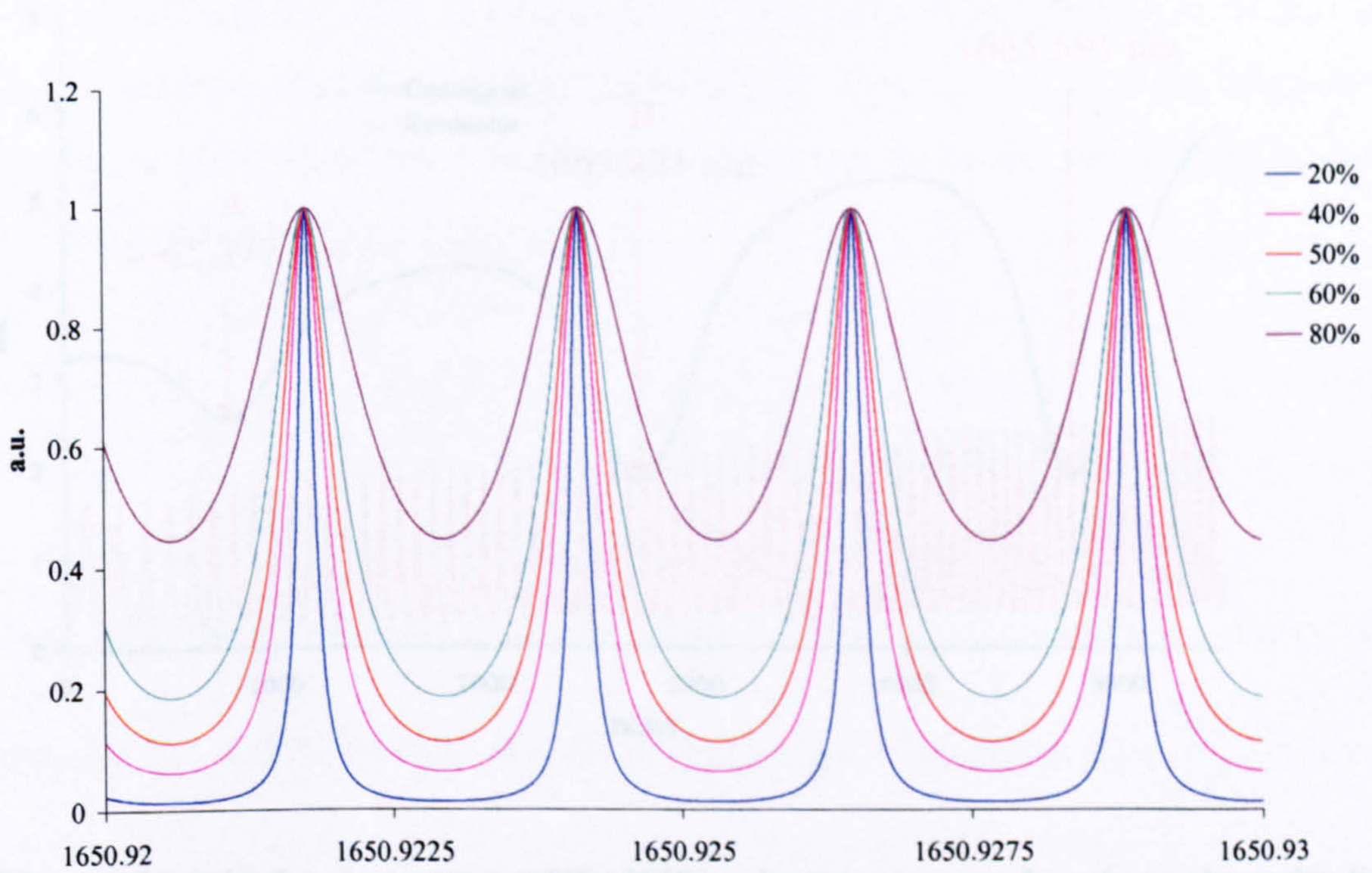

Figure 4.10: Plot of fibre ring-resonator response for five different coupling ratios

It can be seen from figure 4.10 that with increasing coupling ratio comes decreasing finesse and contrast ratio. From this analysis it was decided to use two 40:60 couplers and to tap 40 % into the ring. This offered acceptable finesse and contrast ratio, allowing for accurate location of the peaks, whilst requiring only modest precision in data logging. The output of the resonator was measured on a LNP-2 photoreceiver.

To characterise the resonator's frequency response, measured gas lines were used as absolute frequency references. As mentioned previously, the Q- branch of methane has many lines tightly packed together; this permitted three lines to be addressed in one scan of the laser injection current. Although the lines merge, the peak absorption wavelengths are well documented in the HITRAN database. The scan of the three methane gas absorption lines in the Q- branch and the corresponding resonator output for the scan are shown below in figure 4.11.

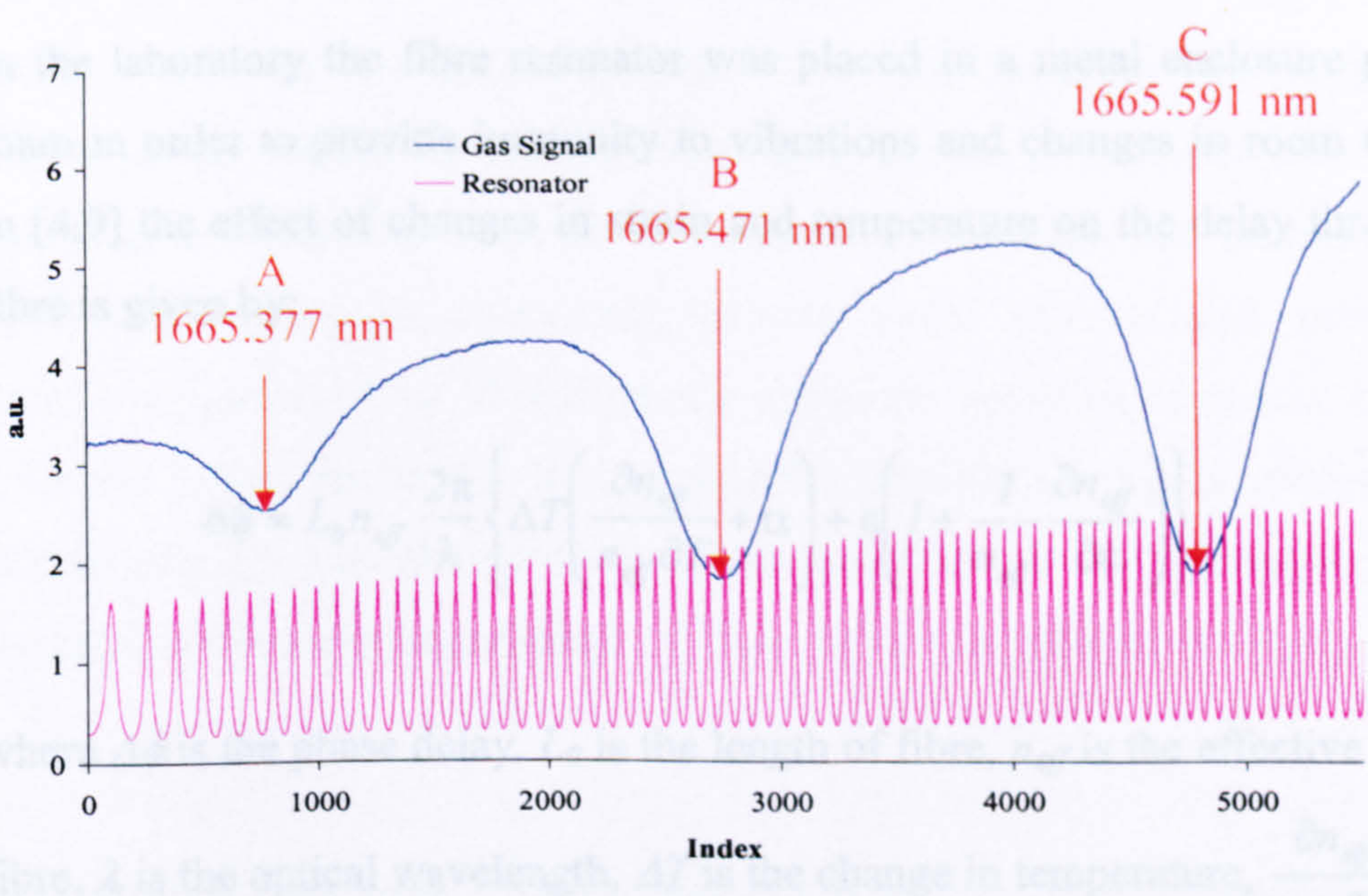

Figure 4.11: Injection current scan of the 1665 nm laser source over 3 methane absorption lines and the corresponding resonator output

Three lines provided two sets of absolute wavelength references, allowing two calculations of the resonator frequency spacing (or FSR) to be made. Closer inspection between points A and B showed 24 transmission peaks over a frequency increment of 10.1675 GHz, giving a FSR of 0.4236 GHz. The frequency increment between points B and C was 12.9392 GHz and supported 30 transmission peaks, giving a FSR of 0.4313 GHz. The average of these two gave the most accurate measurement, that being a fibre ring-resonator FSR of 0.4275 GHz. The FSR of any resonator is given by equation (4.7):

$$FSR = \frac{c}{n_{eff} L_0} \tag{4.7}$$

where c is the speed of light in a vacuum, n_{eff} is the effective refractive index of the medium (in this case standard single mode fibre ~ 1.45) and L_0 is the length of the optical path (in this case the fibre ring ~ 0.47 m).

In the laboratory the fibre resonator was placed in a metal enclosure packed with foam in order to provide immunity to vibrations and changes in room temperature. In [4.9] the effect of changes in strain and temperature on the delay through optical fibre is given by:

$$\Delta\phi = L_0 n_{eff} \frac{2\pi}{\lambda}\left\{\Delta T\left(\frac{\partial n_{eff}}{n_{eff}\partial T} + \alpha\right) + \varepsilon\left(1 + \frac{1}{n_{eff}}\frac{\partial n_{eff}}{\partial \varepsilon}\right)\right\} \tag{4.8}$$

where $\Delta\phi$ is the phase delay, L_0 is the length of fibre, n_{eff} is the effective index of the fibre, λ is the optical wavelength, ΔT is the change in temperature, $\frac{\partial n_{eff}}{n_{eff}\partial T}$ is the rate of change of effective refractive index with temperature (~ 10^{-5} °C $^{-1}$ for silica), α is the linear temperature coefficient of expansion (0.5×10^{-6} °C $^{-1}$ for silica) and ε is the

strain. Converting the phase delay to a change in fibre path length by multiplying $\Delta\phi$ by $\lambda / 2\pi$ and ignoring the effects of strain gives:

$$\Delta L = L_0 n_{eff} \left\{ \Delta T \left(\frac{\partial n_{eff}}{n_{eff} \partial T} + \alpha \right) \right\} \tag{4.9}$$

Therefore, the combined effects of refractive index change and path length change (as a result of a change in temperature) on the frequency response of the fibre ring-resonator can be determined from equations (4.9) and (4.7). The error in FSR as a result of these effects is thus given by:

$$FSR_{error} = \frac{c}{n_{eff}(L_0 - \frac{1}{2}\Delta L)} - \frac{c}{n_{eff}(L_0 + \frac{1}{2}\Delta L)} \tag{4.10}$$

For a room temperature variation of approximately 5 °C the error in ring length can be $\Delta L = 3.577875 \times 10^{-5}$ m for n_{eff}=1.45 and $L_0 = 0.47$ m. From equation (4.10) this results in an error of $\sim 3.4 \times 10^{-5}$ GHz. Therefore, for room temperature variations the inaccuracy of the wavelength referencing technique is negligible. However, in industrial environments large scale temperature variations are commonplace so to ensure the wavelength referencing scheme would remain valid, some means of thermo-regulation of the fibre resonator enclosure would be required. Alternatively, from the above analysis it is, in principle, possible to employ scaling factors to compensate for the change in resonator path length and consequent frequency response with temperature change.

Another important point to note is that the refractive index of standard single mode silica optical fibre is a function of the wavelength of the transmitted light. The variation in refractive index of silica as a function of wavelength is well known and in [4.10, p 108] the plot of this variation is used to quantify material dispersion (where different wavelengths travel through the material at different velocities

causing a pulse spread). From this well-known relationship it is apparent that, in the wavelength range of 1000 nm to 2000 nm, the refractive index of silica can vary by approximately 0.01. Also, in [4.10, p. 58] the normalised propagation constant for linearly polarised modes in optical fibre as a function of frequency is given. It is used to describe waveguide dispersion in optical fibre, which arises due to the 20 % of light propagating through the cladding travelling faster than the 80 % of light propagating through the core. The normalised propagation constant is given by:

$$b = \frac{\left[\left(\frac{\beta}{k}\right) - n_2\right]}{(n_1 - n_2)} \tag{4.11}$$

where β / k is the effective refractive index (n_{eff}) of the waveguide, β is the propagation constant as given in equation (4.5), k is the constant: 2π / λ and n_1 (typically 1.452) and n_2 (typically 1.477) are the refractive indexes of the fibre core and cladding respectively. The normalised frequency is given by:

$$V = \frac{2\pi a}{\lambda}\left(n_1^2 - n_2^2\right)^{\frac{1}{2}} \tag{4.12}$$

where a is the fibre core radius (typically 4.1 μm). Rearranging equation (4.11) for β / k and equation (4.12) for λ, the axes of the figure in [4.10, p. 58] can be changed to give effective index vs. wavelength. Considering only the LP 01 mode, the change in effective index in single mode silica fibre for the wavelength range of interest is approximately 0.004. Therefore, the total change in effective refractive index in the 1000 to 2000 nm range is 0.014. This gives rise to an error in FSR of $\sim 4.1 \times 10^{-3}$ GHz, which falls within experimental error for determining the fringe spacing in the first place. Therefore, it can be concluded that errors induced by variations in refractive index, as seen by different source wavelengths, have a negligible affect on the accuracy of the wavelength referencing procedure.

For each measurement the relative frequency increment was used to change time-based gas absorption signals into wavelength- / frequency- based signals. This process was achieved through a MATLAB program devised by both Andrew McGettrick and the author. The program is located in Appendix C: 1 and an accompanying description of the frequency / wavelength mapping procedure is provided here.

Firstly, the program assumes all the signals are captured at the same time, so both the normalised gas signal and the resonator signal have the same time-indexed axis. This essentially means that the gas signal is incremented by the resonator transmission peaks with a fixed Δf, as shown below in figure 4.12.

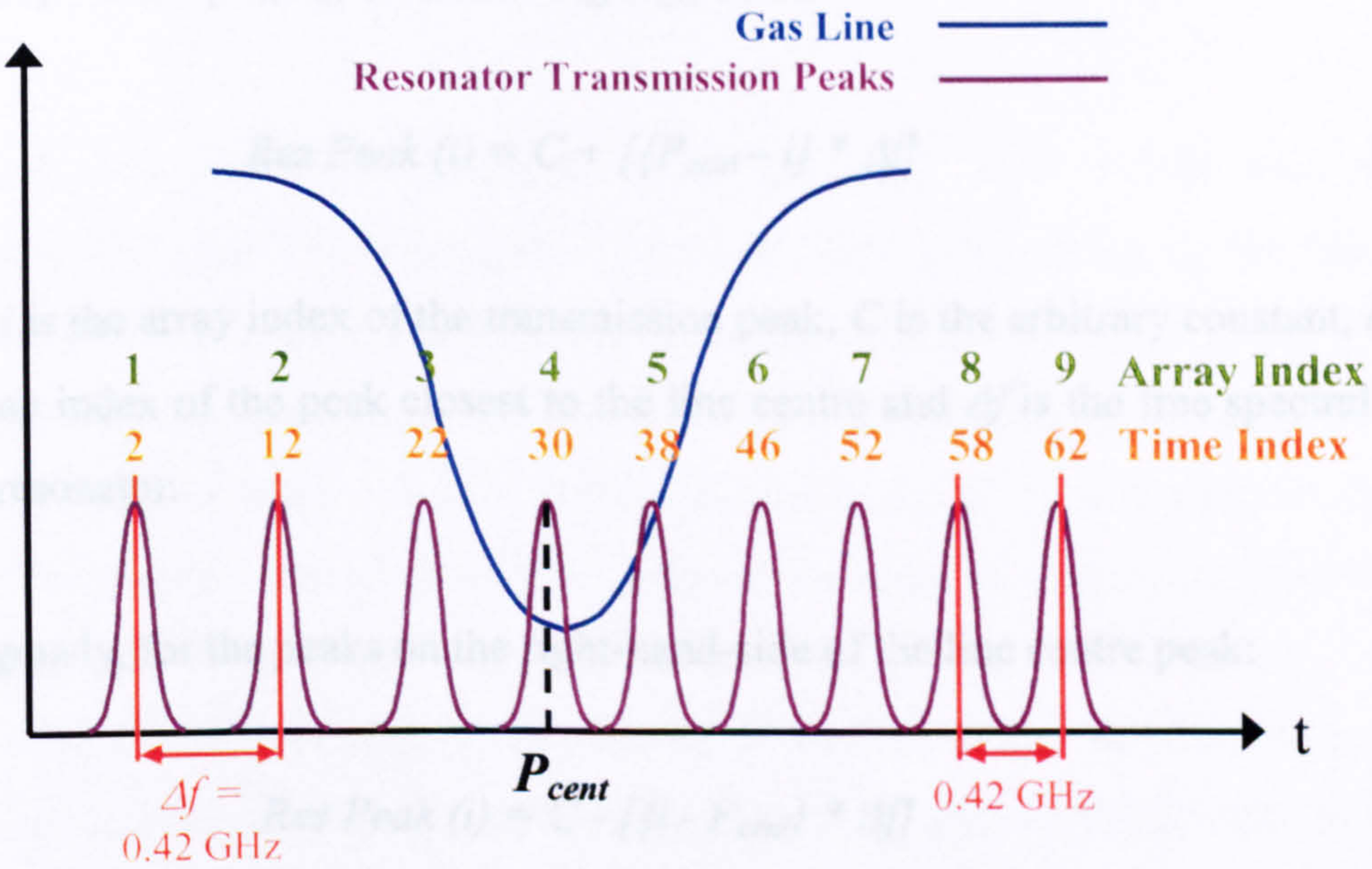

Figure 4.12: Illustration of wavelength mapping process showing example time and array indexing

Note that in practice there were many more transmission peaks than the number shown in figure 4.12, meaning smaller intervals, over which it was reasonably accurate to assume a linear relationship between time index and frequency /

wavelength. The number of peaks has been decreased in figure 4.12 in order to illustrate the mapping process more clearly. As can be seen from figure 4.12, although the time difference between the peaks differs, the frequency separation remains the same. The MATLAB program uses a "FINDPEAK" algorithm devised by Julian Andrew de Marchi [4.11] (located in Appendix C: 2), to scan through the measured resonator values, comparing each successive value to the previous for points of inflection (maxima or minima). The time-indexed locations of the maxima are stored in one array and the minima locations are stored in another. In this case only the maxima (peaks) are of interest. The array entries are then indexed; to illustrate, example indexing of the peaks is shown in figure 4.12. The program identifies the time index value of the gas absorption line centre and then finds the resonator transmission peak closest to that line centre. This peak is then labelled with an arbitrary constant to begin the relative frequency scale. The peaks on the left-hand-side of the line centre peak (labelled P_{cent} in figure 4.12) are assigned a frequency value by using the following algorithm:

$$Res\ Peak\ (i) = C + [\{P_{cent} - i\} * \Delta f] \tag{4.13}$$

where i is the array index of the transmission peak, C is the arbitrary constant, P_{cent} is the array index of the peak closest to the line centre and Δf is the free spectral range of the resonator.

Analogously, for the peaks on the right-hand-side of the line centre peak:

$$Res\ Peak\ (i) = C - [\{i - P_{cent}\} * \Delta f] \tag{4.14}$$

This then corresponds with the laser characteristic by having the gas absorption signal mapped onto decreasing frequency increments, with a scan of increasing injection current. To increase accuracy, a polynomial curve fit is made to the series of discrete frequency values. The scale is also converted to wavelength using the following well-known equation:

$$\lambda = \frac{c}{f} \tag{4.15}$$

where λ is wavelength, c is the speed of light in a vacuum and f is frequency.

An absolute scale is made by shifting the relative frequency / wavelength curve to a known reference point; in this case, the peak absorption frequency / wavelength of the target gas line. Therefore, the MATLAB program also reads in a theoretical model of the gas absorption transmission function for the measured gas composition and shifts the frequency curve to the measured peak absorption frequency of 1.81713 x 10^{14} Hz and the wavelength curve to the measured peak absorption wavelength of 1650.956 nm.

4.2.5 Data Collection

All three channels were measured on a Tektronix TDS 3014B oscilloscope, automated via a LabVIEW program. The LabVIEW program set up the triggering from the power reference channel; the time-base setting of 200 ms (1 / 5 Hz); the vertical resolution (maximum 512 samples) and the number of averages collected (set to 64). The scope offers a horizontal resolution of 10,000 samples and the LabVIEW program stored these time-indexed voltages in comma-separated-values (CSV) format with a precision of 10 decimal points. This meant the gas measurement and wavelength referencing procedure could be carried out with complete confidence. Figure 4.13 shows an example of an experimentally measured gas signal and accompanying power and wavelength referencing signals. As can be seen the resonator transmission peaks are completely resolved and follow the trend of increasing power. Note, in the figure the gas absorption line is normalised to the increasing power (as detailed in the next section) as the location of the peak absorption may be distorted by changing power, leading to wavelength referencing errors. The horizontal location of each of the resonator transmission peaks is not a function of the laser power and so remains un-normalised.

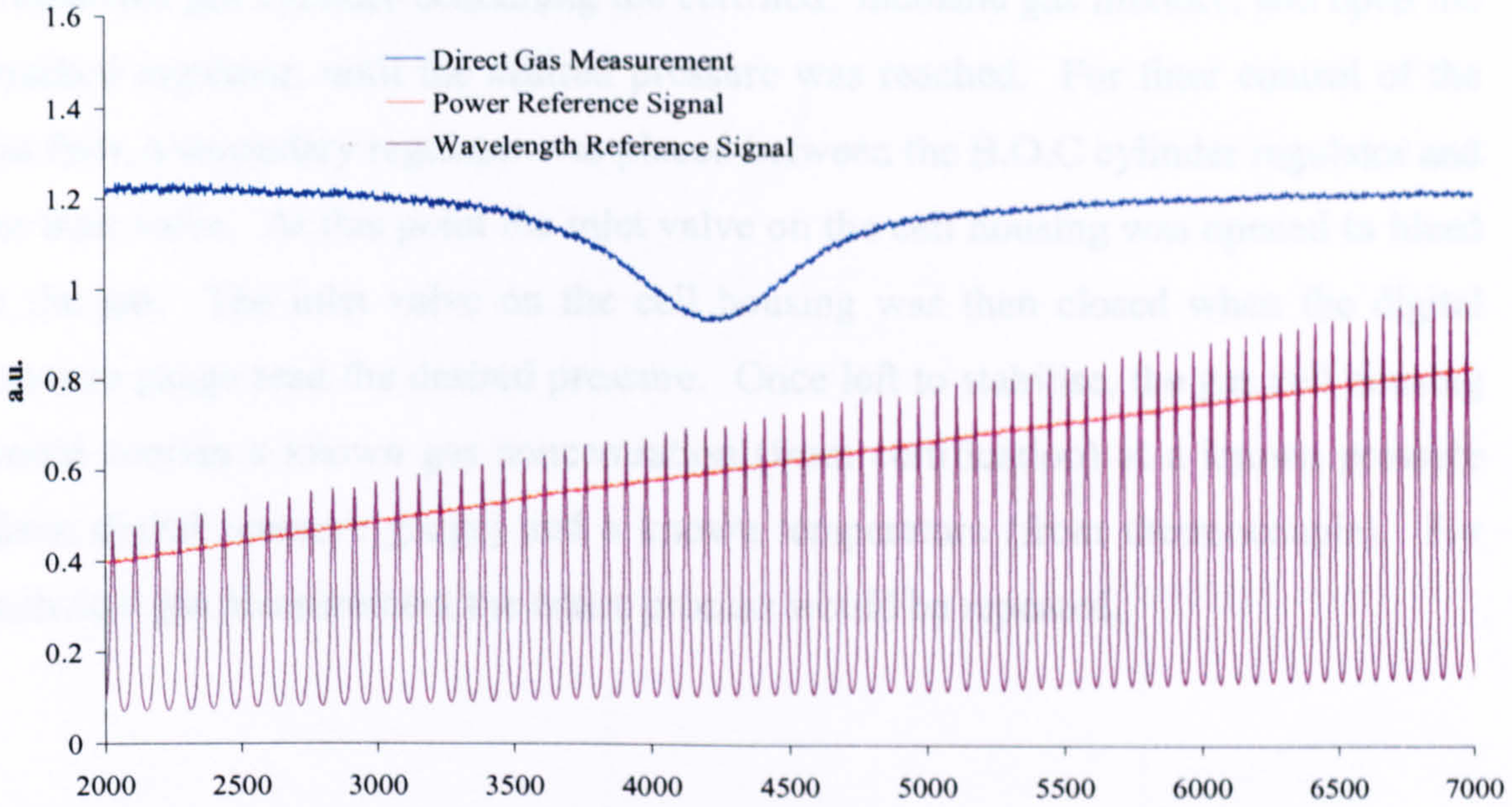

Figure 4.13: Example measurement of 10 % methane and corresponding signals

4.2.6 Measurement Procedure and Signal Processing

This section describes the procedure used for taking one direct measurement using the experimental apparatus documented above.

The first step was to prime the gas measurement cell and housing. Before evacuating, the cell was purged with nitrogen. This was because the vacuum pump used here was an oil-based rotary pump and to use it with flammable gases such as methane would have been extremely dangerous. Once the cell, cell housing and connecting pipes were completely purged of methane, only the exhaust valve was left open and the housing was vacuumed down to 0.000 bar (as read on the digital pressure gauge). At this point the exhaust valve was closed off and then the vacuum pump was switched off. The next step was to fully open the valve of the B.O.C

pressurised gas cylinder containing the certified[II] methane gas mixture, and open the attached regulator, until the desired pressure was reached. For finer control of the gas flow, a secondary regulator was placed between the B.O.C cylinder regulator and the inlet valve. At this point the inlet valve on the cell housing was opened to bleed in the gas. The inlet valve on the cell housing was then closed when the digital pressure gauge read the desired pressure. Once left to stabilise, the gas cell housing would contain a known gas concentration (from certification) at a known pressure (from digital pressure gauge) and a known temperature (from thermocouple). For each new gas measurement the entire process would be repeated.

Figure 4.14 illustrates the calibration and signal processing procedures used in the direct TDLS experiments. The power reference was attenuated to match the off-line power of the gas signal. A ratio was also taken between the gas signal and power reference at corresponding values off-line to provide a zero-point reference (denoted *C* in figure 4.14). The gas signal was normalised firstly to the increasing power signal and then to the zero-point reference. The resonator response provided the wavelength reference to map a reliable absolute wavelength scale on to the time-based measurements, as described in section 4.2.4. The resulting gas absorption line transmission functions allowed for measurement of the gas concentrations and pressures, via direct measurement of the depths and linewidths respectively, or by curve fitting theoretical predictions (based on the known pressure, concentration and temperature parameters) to these experimental signals. Results taken using this approach are discussed in chapter 5.

[II] Gas mixtures are supplied by B.O.C with a certification accurate to within +/- 5 %

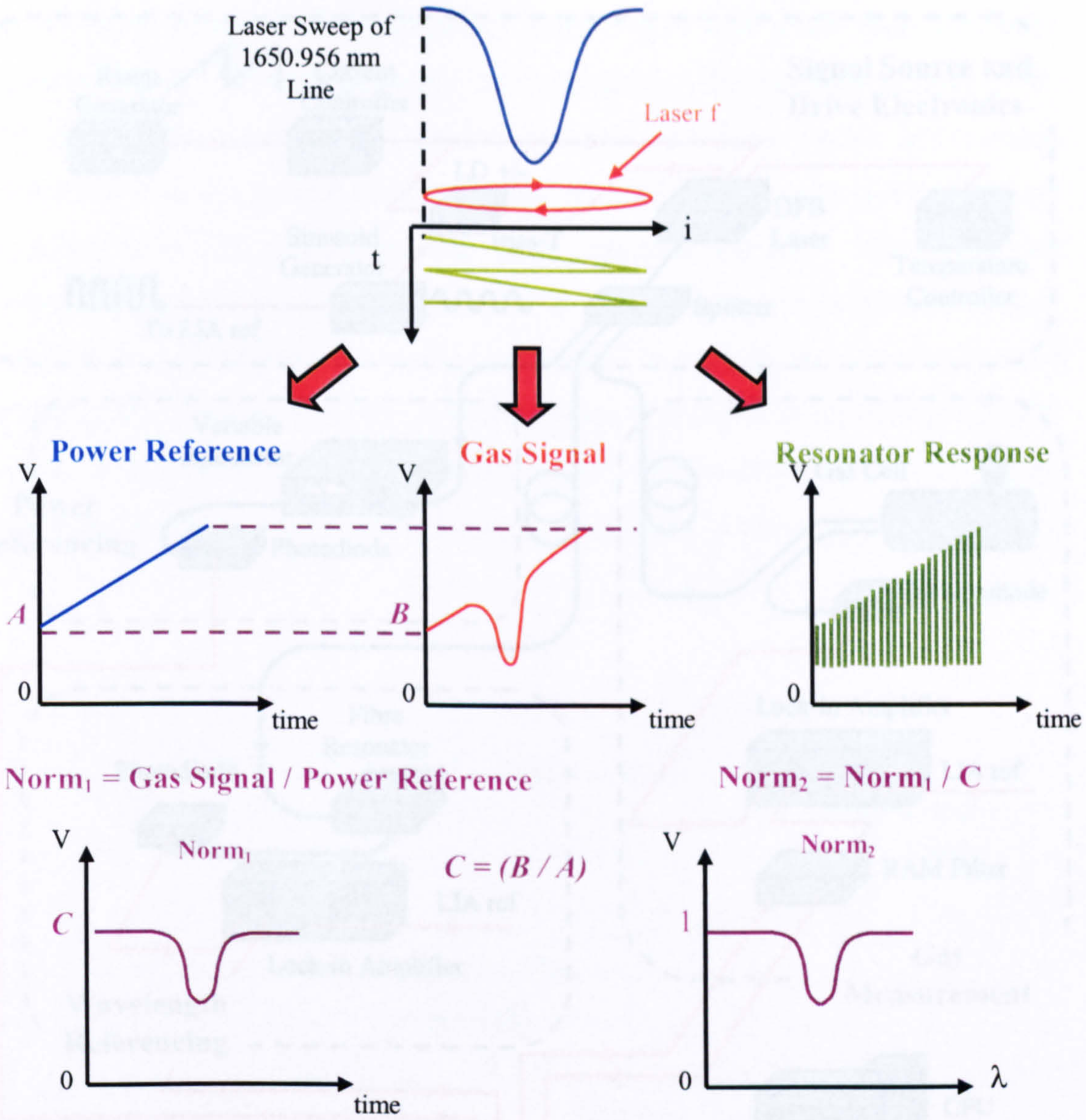

Figure 4.14: Example of calibration and signal processing procedures for direct TDLS

4.3 Tunable Diode Laser Spectroscopy with Wavelength Modulation Spectroscopy

The laboratory system architecture was modified slightly compared to the direct implementation and is illustrated below in figure 4.15.

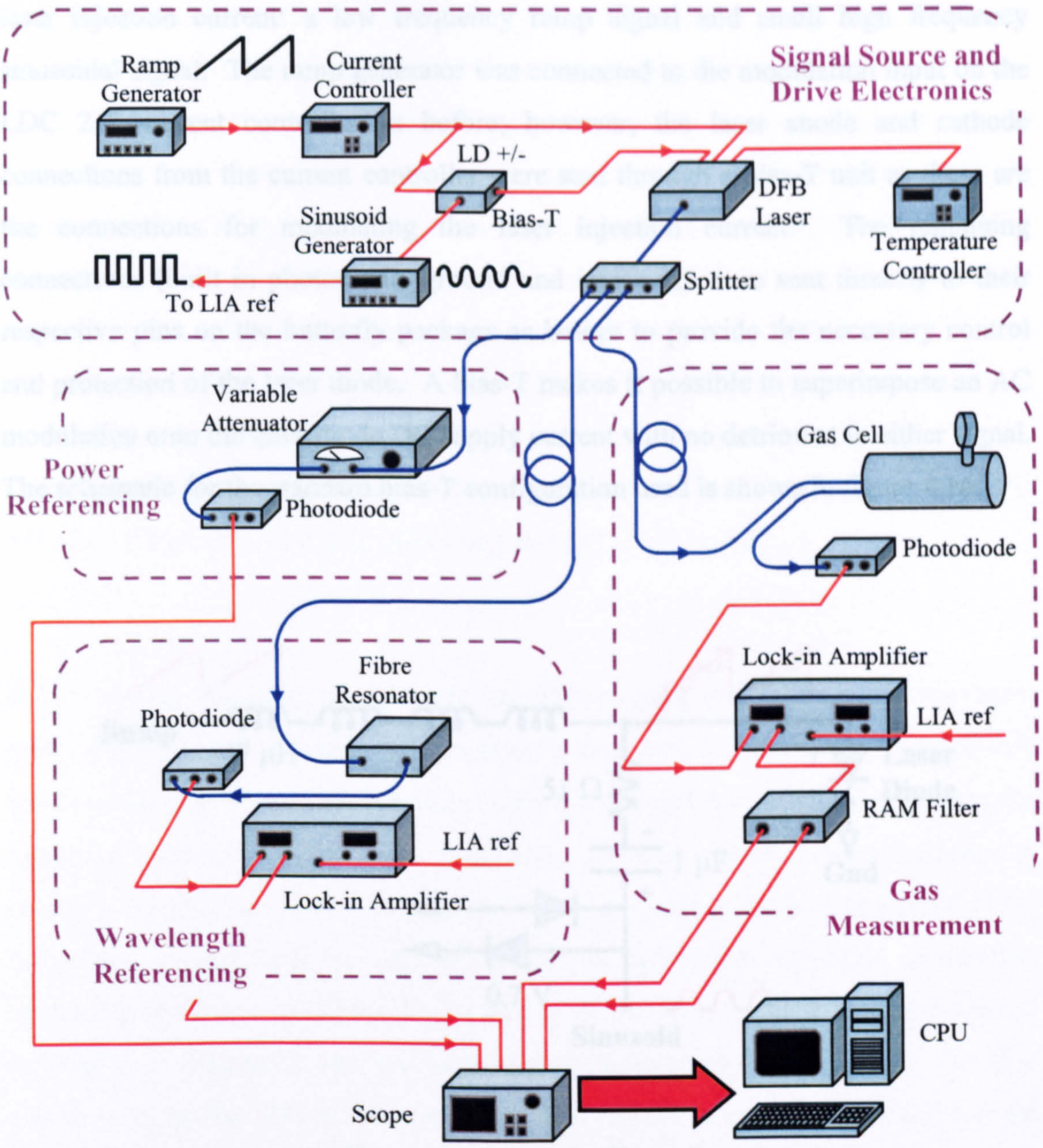

Figure 4.15: System architecture for TDLS / WMS detection

4.3.1 Signal Source and Drive Electronics

The DFB laser was tuned to the proximity of the gas absorption line at 1650.956 nm using the same current and temperature values as before: 70 mA and 6.455 kΩ (35.346 °C). As was mentioned in chapter 2, there was a double modulation on the

laser injection current: a low frequency ramp signal and small high frequency sinusoidal signal. The ramp generator was connected to the modulation input on the LDC 210 current controller as before; however, the laser anode and cathode connections from the current controller were sent through a bias-T unit as these are the connections for modulating the laser injection current. The remaining connections (built in photodiode, ground and interlock) were sent directly to their respective pins on the butterfly package as before to provide the necessary control and protection of the laser diode. A bias-T makes it possible to superimpose an AC modulation onto the laser diode DC supply current with no detriment to either signal. The schematic for the standard bias-T configuration used is shown in figure 4.16.

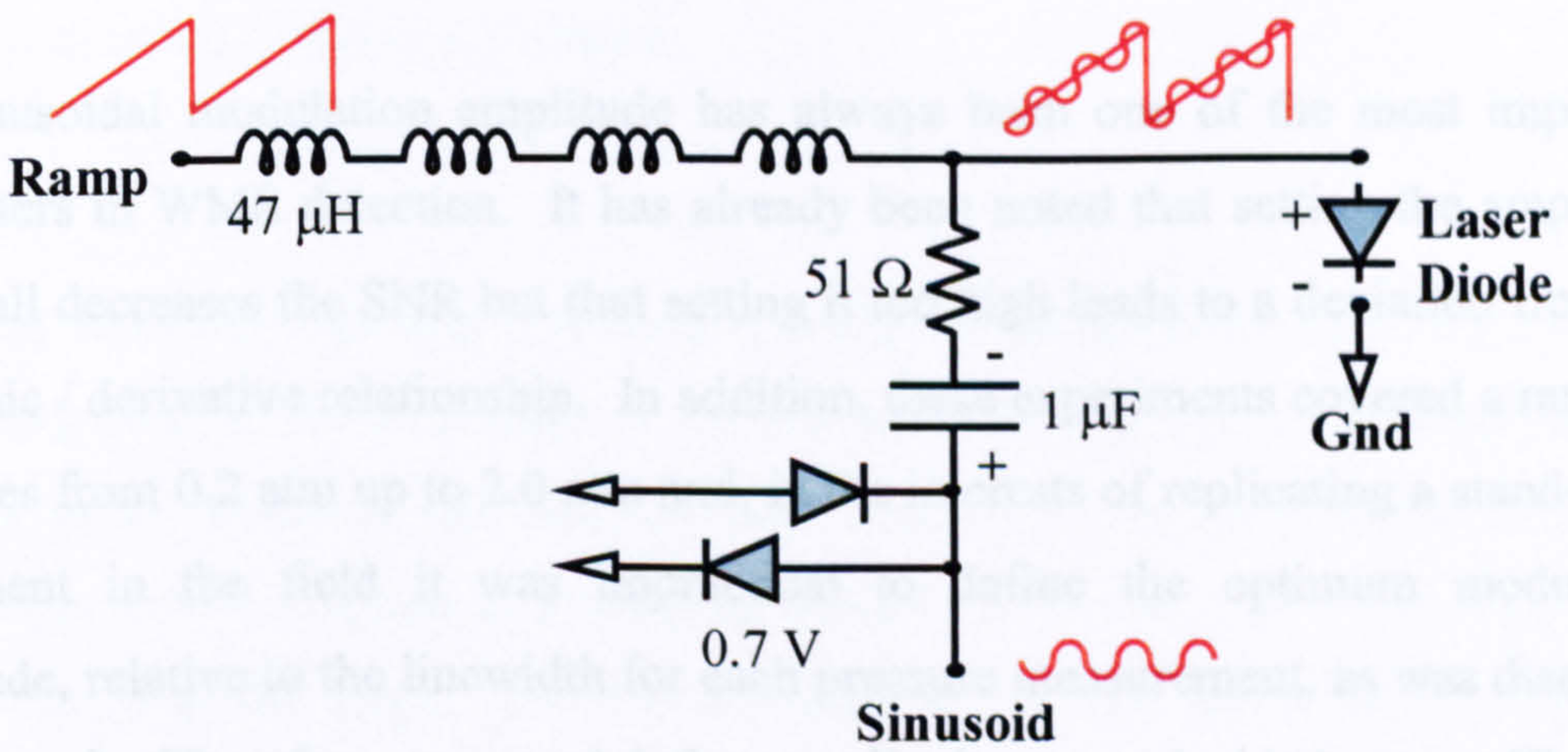

Figure 4.16: Schematic of bias – T

The series connection of 4 × 47 µH inductors presents the ramp voltage with zero resistance at low frequencies (cut off ~ 1 kHz); therefore, the DC bias (+ 70 mA) and 5 Hz ramp signal (± 40 mA) supplied by a Digimess FG100 function generator remained unchanged from the direct set up. If the amplitude of the sinusoidal modulation input goes higher than ± 0.7 V the diodes conduct sending the excess signal to ground, providing adequate protection of the laser diode from excessive voltages and negative biasing. The 1 µF capacitor blocks DC signals up to a cut-off

frequency of ~ 3 kHz. The ~ 50 Ω resistor provides impedance matching of the coax output from the Hewlett Packard 33120A function generator providing the sine wave. Therefore, the output signal directly modulating the laser injection current was a large, low frequency ramp signal with a smaller high frequency sinusoid superimposed. The typical modulation frequency of the sinusoid can lie anywhere between 10 kHz and 100 KHz [4.12] but to remain consistent with the successful work of fellow researchers within the group at Strathclyde [4.13 and 4.14], 10 kHz was chosen initially. The 3dB bandwidth of the LDC 210 current controller is stated at 100 kHz. Although this is suitable for primary investigations at 10 kHz, higher modulation frequencies were investigated later and the bias-T used here permitted AC modulation up to 250MHz (switching limit of diode is 4 ns).

The sinusoidal modulation amplitude has always been one of the most important parameters in WMS detection. It has already been noted that setting the amplitude too small decreases the SNR but that setting it too high leads to a deviation from the harmonic / derivative relationship. In addition, these experiments covered a range of pressures from 0.2 atm up to 2.0 atm and, in the interests of replicating a stand-alone instrument in the field it was impractical to define the optimum modulation amplitude, relative to the linewidth for each pressure measurement, as was discussed in chapter 2. Therefore, two modulation amplitudes were decided upon. The first was dictated by the FSR of the resonator peaks (details in section 4.3.4) and was set to 35 mV peak-to-peak (δV = 17.5 mV). The second was determined by the optimum $\delta\nu \sim 2*\gamma$ (m = 2.0, mentioned previously in chapter 2) relationship for atmospheric methane. In [4.6, 4.15 & 4.16] it was stated that the optimum modulation index, that is the modulation index that gives rise to a maximum FM 1st harmonic signal, is $\delta\nu \sim 2*\gamma$; therefore, the TDLS / WMS system was set up to measure 1.0 atmosphere of methane and the modulation amplitude was increased until a maximum FM 1st harmonic signal was reached. This optimum amplitude was 600 mV peak-to-peak (δV = 300 mV). Having two modulation amplitudes permitted analysis of TDLS / WMS lineshapes at two extremes of the harmonic / derivative relationship.

The modulated laser light was then split into three channels, as with the direct TDLS set up, for gas measurement and calibrations to frequency and power change.

4.3.2 Gas Measurement

From figure 4.15 it can be seen that the initial gas measurement procedure remained unchanged from the direct adaptation, with the light travelling through optical fibre, in and out of the gas measurement cell and into the LNP-2 photoreceiver. The electronic signal was then passed over a BNC lead to a Perkin Elmer 7280 DSP lock-in amplifier. The basic principles of operation for lock-in amplification are shown in the block diagram in figure 4.17 below.

A lock-in amplifier's general operation is designed for detecting small signals on a zero background so the first stage of the process is to amplify the input signal such that any small deviation will become large relative to the zero background. To remove any spurious signals as a result of mains interference, a 50 Hz rejection filter follows the amplifier stage. The AC components are then amplified using an AC gain stage; this further enhances the desired signal relative to the background, as it is usually considered good practice, for optimum demodulator performance, that as large a signal as possible is presented to the analogue-to-digital converter (ADC). Linked to the AC gain is the full scale sensitivity and this describes the lock-in amplifier's limit in resolving small changes from the background. The optimum scenario is to have as small a sensitivity value as possible, whilst achieving as large a gain as possible. Without the correct balance the lock-in amplifier overloads. The ADC has a sampling rate of 7.5 MHz for high rate conversion and to prevent aliasing.

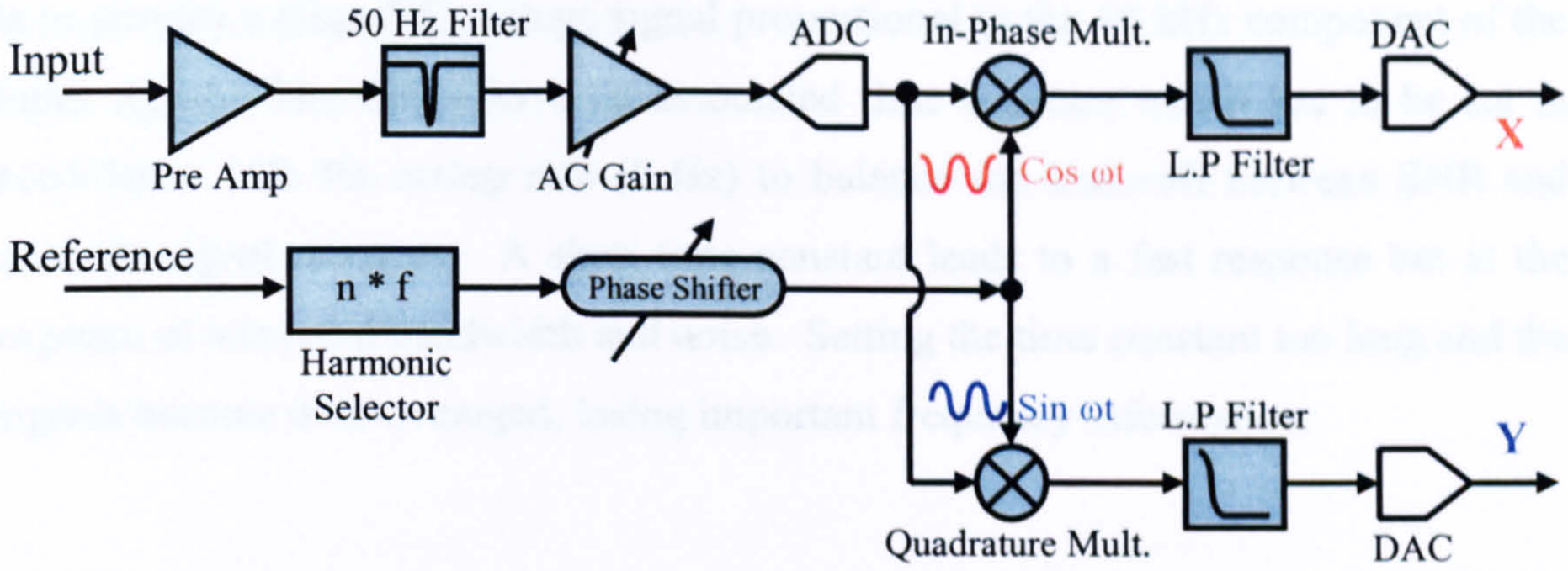

Figure 4.17: Block diagram for the Perkin Elmer 7280 DSP lock-in amplifier

The reference signal to the lock-in can be generated internally or measured externally. External reference mode is better suited to industrial application as any changes in the injection current modulation are reflected in the reference. The reference signal in our case was a TTL-logic level interpretation of the sinusoid modulation from the HP33120A function generator. With the harmonic selector set to the first harmonic (n =1), the lock-in amplifier measures the input signal at 10 kHz. This external reference is passed to a digital phase-locked loop (PLL), allowing the lock-in amplifier to continuously track the period / frequency of the signal. The lock-in amplifier's processor then generates a series of phase values, and consequently a sinusoid at 10 kHz, to multiply with the digitised input signal. This dual-phase lock-in amplifier produces two demodulation functions: in-phase and quadrature or X and Y vectors respectively; intuitively, Y lags X by 90 °. In addition, the lock-in amplifier employs a phase shifter at the input to the reference channel. The reference phase is regarded as the phase of the X vector, relative to the input signal. A common technique employed in industrial based spectroscopy is to adjust the phase to maximise the signal on the X channel, consequently, minimising the signal on the Y channel.

The final stages of the lock-in detection process are low-pass filtering of the digital X and Y signals and digital-to-analogue conversion. The aim of these two procedures

is to provide a clean DC voltage signal proportional to the 10 kHz component of the input signal. The filters have an associated time constant which has to be set in accordance with the sweep rate (5 Hz) to balance the trade-off between SNR and accurate signal recovery. A short time constant leads to a fast response but at the expense of increased bandwidth and noise. Setting the time constant too long and the signals become over-averaged, losing important frequency information.

In-keeping with the industrial viewpoint of maximising signal-to-noise ratio (SNR), the lock-in amplifier detection phase is set to optimise the output amplitude. The most consistent approximation[III] to this is to align the phase with the RAM component when the gas cell is free from the target gas. The desired AM component (resulting from the interaction between the gas absorption line and the frequency modulated light) is at the same frequency and thus is recovered along with the RAM. The 1st harmonic output signal shows the signal generated by the FM superimposed on the large background signal generated by the RAM. The RAM component is then traditionally removed by a DC RAM filter or a DC offset. Figure 4.18 illustrates the recovery of a 1st harmonic signal by lock-in detection. As the laser centre frequency is scanned across the gas absorption line, the dither signal interrogates the slope / gradient. At the start of the sweep (a), before any absorption, there is zero intensity modulation induced by the FM. Gradually the slope of the absorption profile increases negatively (b); thus, intensity modulation induced by the FM increases in magnitude but is 180 ° out of phase, relative to the FM induced signal on the right-hand-side of the gas absorption line. This is reflected in the negatively increasing portion of the 1st harmonic. The gradient of the absorption line is at its peak at point (c), giving rise to the maximum negative point (c) on the 1st harmonic. From this point the gradient decreases again and momentarily returns to being flat (e), where the harmonic signal shows a crossing through zero. After peak absorption the gradient of the absorption line increases positively to a maximum at point (f). As the gradient is positive the intensity modulation shifts 180 °. At the end of the scan the

---

[III] Measuring the resultant of the RAM and FM induced AM signal would increase the output signal amplitude but the optimisation parameters would require readjustment for each new gas composition

gradient of the absorption line and consequently the FM induced intensity modulation returns to zero (g). The 1st harmonic signal mapped out by the lock-in amplifier is then mathematically related to the 1st derivative of the gas absorption line transmission function.

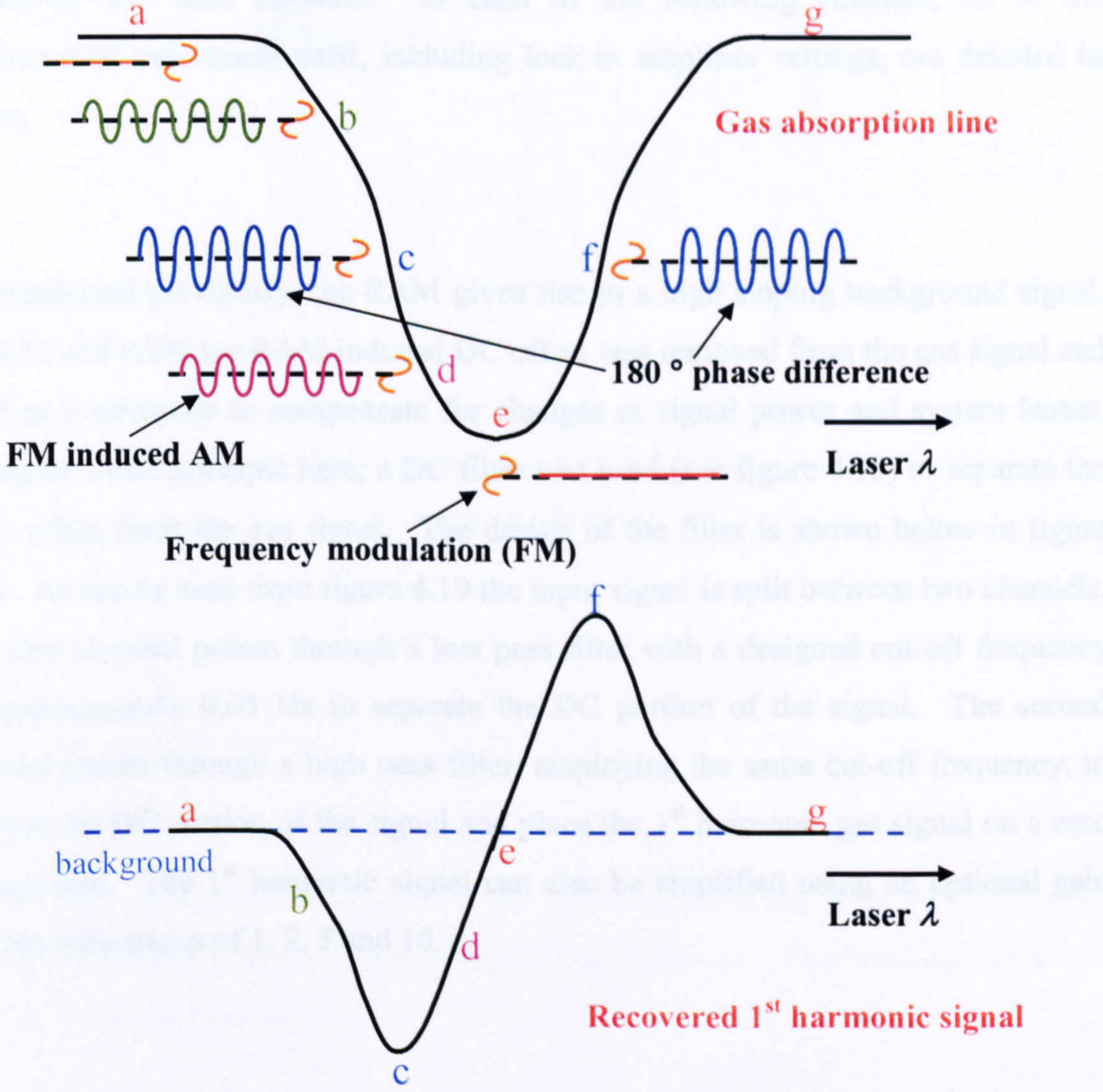

Figure 4.18: Illustration of lock-in detection process: labelled points on gas absorption line correspond to labelled points on 1st harmonic signal

In figure 4.18 the dither signal and induced modulation signals are shown relatively large for clarity. The problems associated with a large dither signal are discussed in chapter 5.

The parameters in determining optimum lock-in detection are thus: AC gain, sensitivity and time constant. In each of the following chapters, all of the experimental parameters used, including lock-in amplifier settings, are detailed in tables.

As mentioned previously, the RAM gives rise to a high sloping background signal. In [4.13 and 4.14] the RAM induced DC offset was removed from the gas signal and used as a reference to compensate for changes in signal power and system losses. Using the same principle here, a DC filter was used (see figure 4.15) to separate the large offset from the gas signal. The design of the filter is shown below in figure 4.19. As can be seen from figure 4.19 the input signal is split between two channels. The first channel passes through a low pass filter with a designed cut-off frequency of approximately 0.03 Hz to separate the DC portion of the signal. The second channel passes through a high pass filter, employing the same cut-off frequency, to remove the DC portion of the signal and place the 1^{st} harmonic gas signal on a zero background. The 1^{st} harmonic signal can also be amplified using an optional gain section with stages of 1, 2, 5 and 10.

To remove the sloping background from experimentally measured signals a second scan was taken with the gas cell completely purged of any target gas.

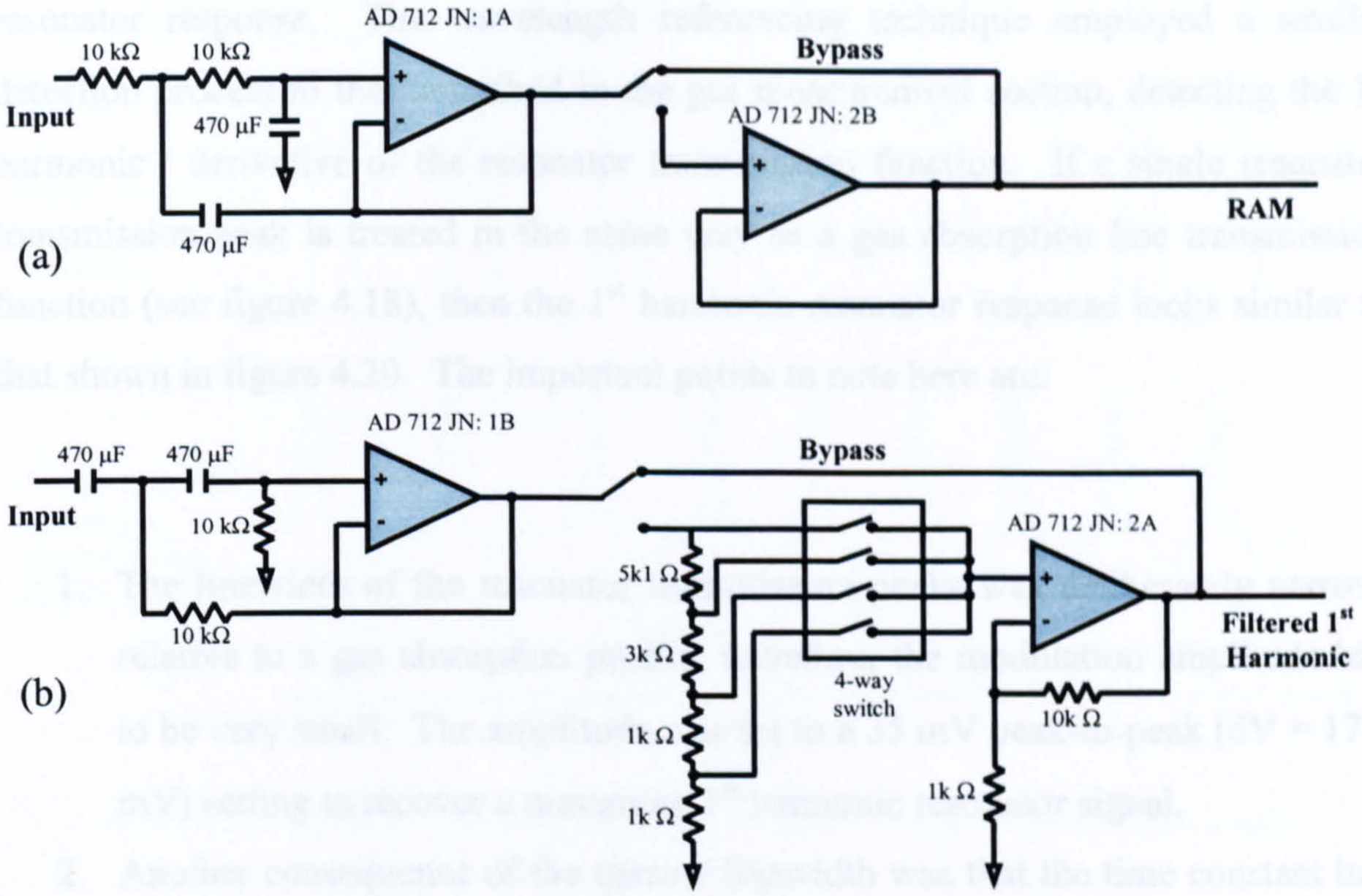

Figure 4.19: Schematic for DC RAM filter: (a) RAM measurement channel, (b) Filtered 1st harmonic channel

4.3.3 Power Referencing

As can be seen from figure 4.15, the power referencing procedure remained unchanged from the direct TDLS measurement technique. The level of attenuation remained unchanged also.

4.3.4 Wavelength Referencing

Wavelength referencing for TDLS / WMS signals was a little more complex than in the direct version. The addition to the process was the presence of a SR 850 DSP lock-in amplifier to lock into the 10 kHz dither signal superimposed on the direct

resonator response. The wavelength referencing technique employed a similar detection process to that described in the gas measurement section, detecting the 1st harmonic / derivative of the resonator transmission function. If a single resonator transmission peak is treated in the same way as a gas absorption line transmission function (see figure 4.18), then the 1st harmonic resonator response looks similar to that shown in figure 4.20. The important points to note here are:

1. The linewidth of the resonator transmission peaks was deliberately narrow, relative to a gas absorption profile; therefore, the modulation amplitude had to be very small. The amplitude was set to a 35 mV peak-to-peak (δV = 17.5 mV) setting to recover a maximum 1st harmonic resonator signal.
2. Another consequence of the narrow linewidth was that the time constant had to be set much smaller than that for the gas measurement, so as not to average over the high frequency content of the signal.
3. There was a much smaller loss over the fibre path through the resonator to the photodiode (compared to the gas measurement path); therefore, the magnitude of the signal at the front end of the lock-in amplifier was much larger. For that reason, the sensitivity / AC gain balance had to be re-optimised, with both levels dropping to prevent overload.

It can be seen from figure 4.20 that the frequency increment of 0.42 GHz, defined by the peak positions on the direct resonator response, is defined by the zero-crossings in the 1st harmonic response. Therefore, a MATLAB program, again devised by Andrew McGettrick and the author, was developed to use this relationship to map the time-based derivative absorption measurement onto an absolute wavelength / frequency scale. The MATLAB program is detailed in Appendix C: 3 and again a description is provided here.

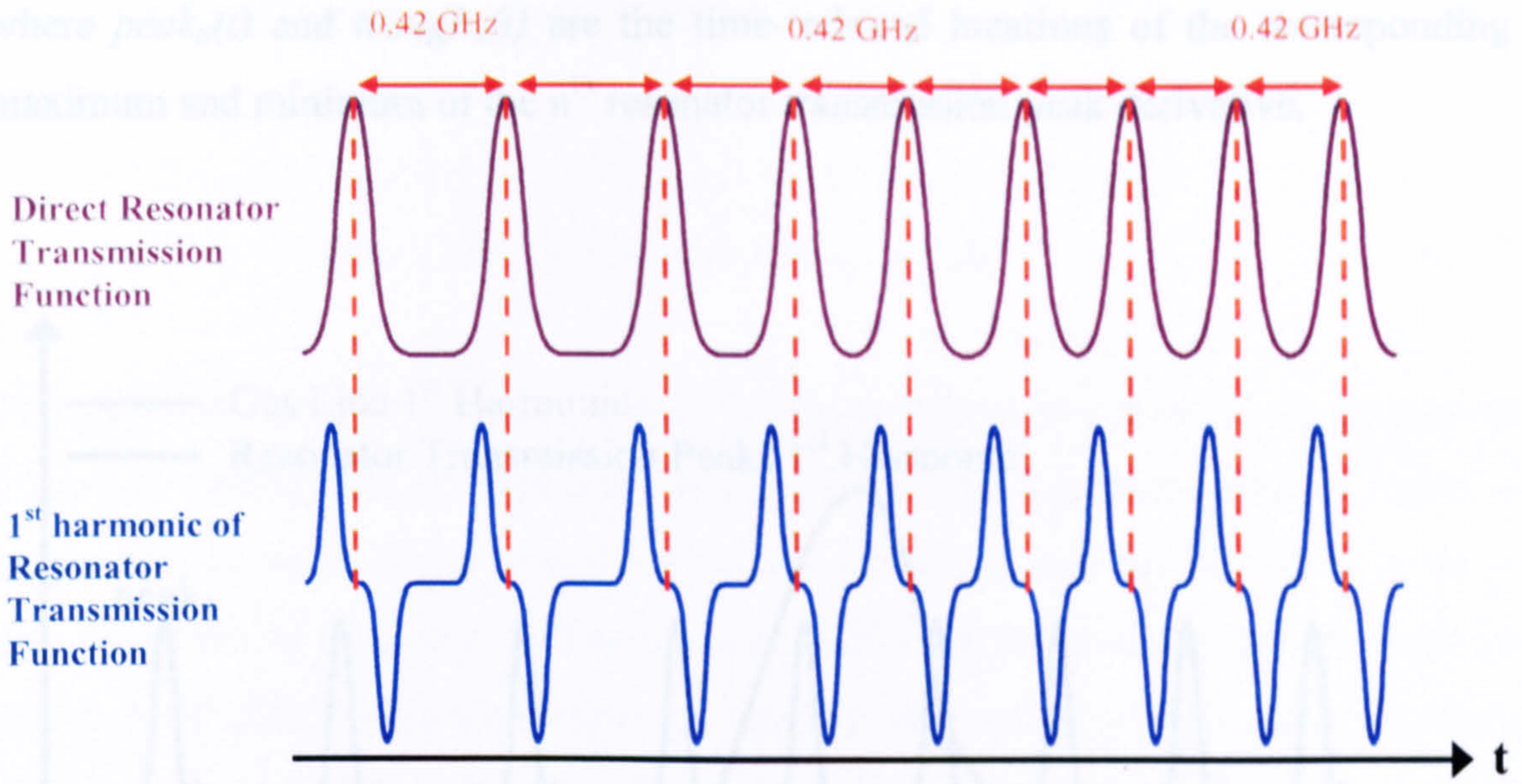

Figure 4.20: Typical 1st harmonic response of the fibre resonator transmission profile

Again, as with the direct TDLS experimental set up, all the signals were captured at the same time and were thus all on the same time-indexed axis. Therefore, the 1st harmonic of the gas absorption line transmission function can be regarded as being incremented by the peaks and troughs of the 1st harmonic resonator response, as illustrated in figure 4.21. Note, that in practice there were many more transmission peaks than the amount shown in figure 4.21 and consequently, many more 1st harmonic zero-crossings, meaning smaller intervals over which it was safe to assume a linear time-index / frequency relationship.

Again, the MATLAB program uses the "FINDPEAK" algorithm to generate an array of peaks and an array of troughs. As the transmission peaks can be assumed symmetrical, the time-indexed location of zero-crossing, *n*, can be defined as:

$$zerocross_n(t) = \frac{trough_n(t) + peak_n(t)}{2} \tag{4.16}$$

where $peak_n(t)$ and $trough_n(t)$ are the time-indexed locations of the corresponding maximum and minimum of the n^{th} resonator transmission peak derivative.

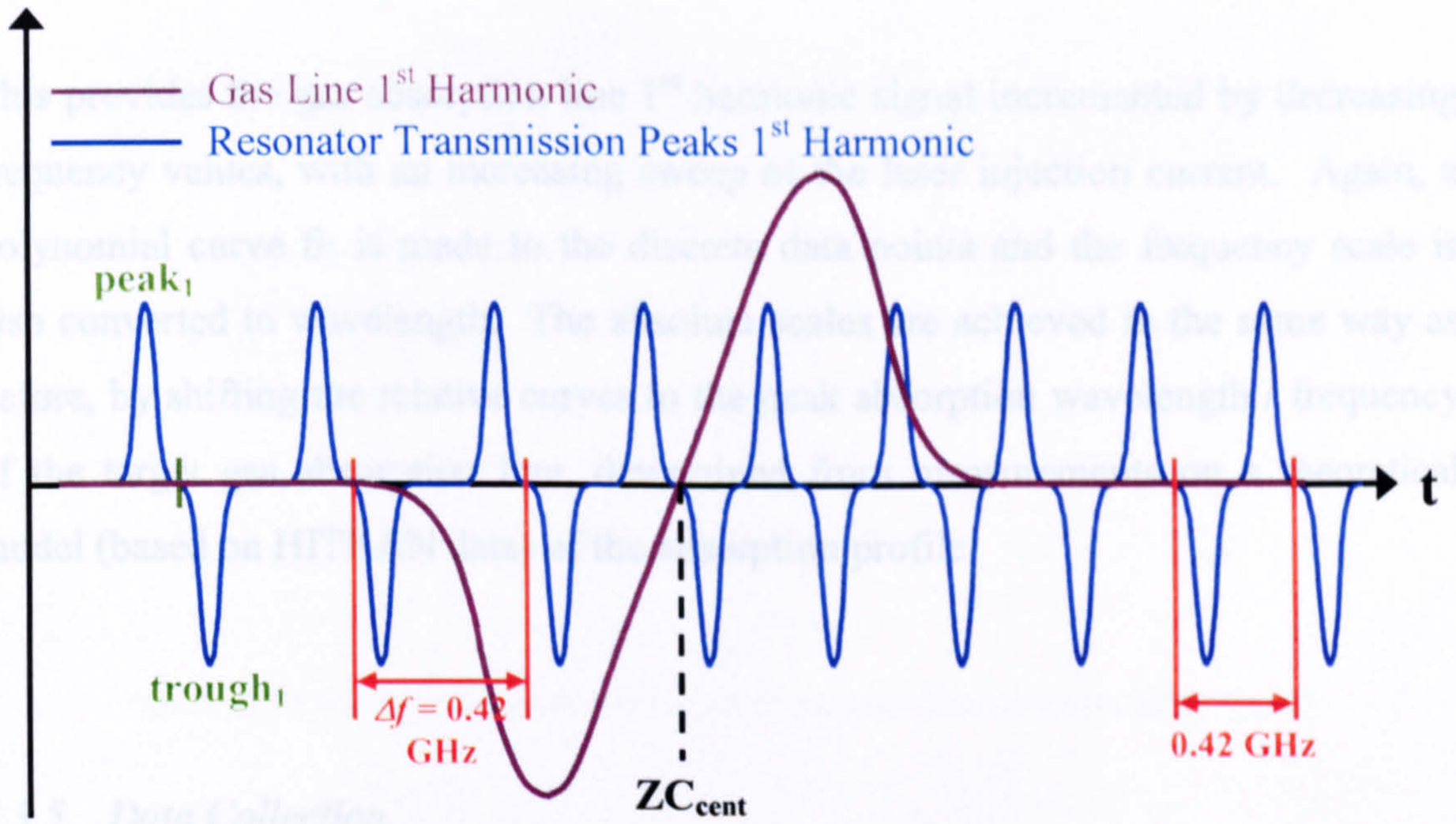

Figure 4.21: Illustration of wavelength / frequency mapping process for TDLS / WMS signals

Now there is an indexed array of zero-crossings. The MATLAB program locates the zero-crossing of the 1st harmonic of the gas absorption line (line centre of absolute transmission function) and also locates the resonator zero-crossing closest to that point (labelled ZC_{cent} in figure 4.21). Analogous to the direct wavelength referencing scheme, this resonator zero-crossing is given an arbitrary value to initiate the relative frequency scale. The zero-crossings on the left-hand-side of the line centre zero-crossing are assigned a frequency value by using the following algorithm:

$$Zero\ Cross\ (i) = C + [\{ZC_{cent} - i\} * \Delta f] \tag{4.17}$$

where i is the array index of the zero-crossing, C is the arbitrary constant, ZC_{cent} is the array index of the zero-crossing closest to the line centre and Δf is the free spectral range of the resonator.

Analogously, for the zero-crossings on the right-hand-side of the line centre zero-crossing:

$$Zero\ Cross\ (i) = C - [\{i - ZC_{cent}\} * \Delta f] \tag{4.18}$$

This provides the gas absorption line 1st harmonic signal incremented by decreasing frequency values, with an increasing sweep of the laser injection current. Again, a polynomial curve fit is made to the discrete data points and the frequency scale is also converted to wavelength. The absolute scales are achieved in the same way as before, by shifting the relative curves to the peak absorption wavelength / frequency of the target gas absorption line, determined from measurements on a theoretical model (based on HITRAN data) of the absorption profile.

4.3.5 Data Collection

All the electronic signals were captured as detailed in section 4.2.5 and figure 4.22 shows an example of an experimentally measured 1st harmonic of the gas absorption line transmission function and accompanying power and wavelength referencing signals. The points to note here are that, again as with the direct TDLS signal, the gas measurement has been normalised (as detailed in section 4.3.6) to ensure the positive and negative peaks and zero-crossing locations are not distorted by the changing laser power. The 1st harmonic resonator response is not normalised to the power but is decreased in magnitude for image clarity. Also shown is the filtered DC signal, representing the RAM contribution to the lock-in amplifier measurement.

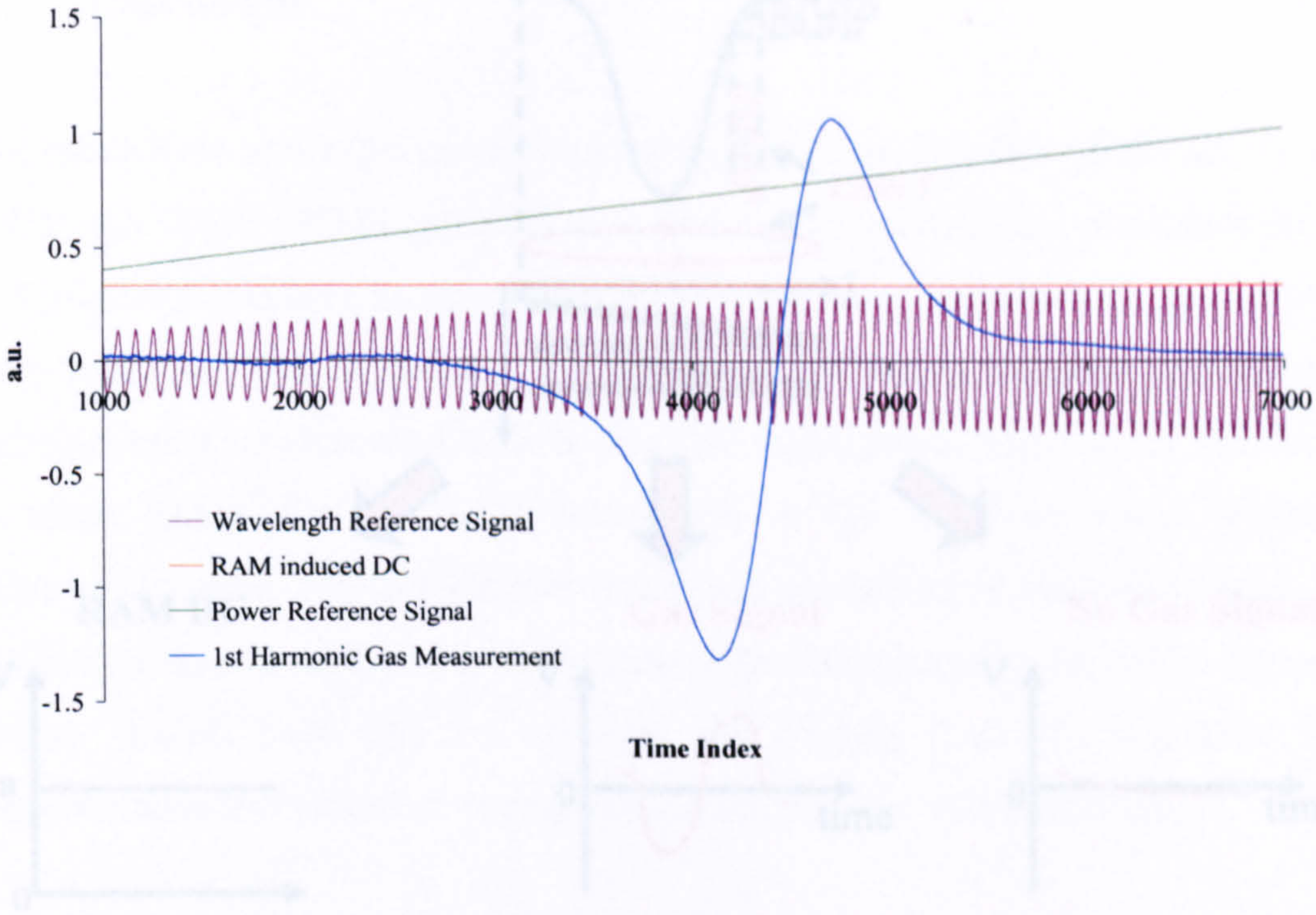

Figure 4.22: Example measurement of 10 % methane and corresponding signals

4.3.6 Measurement Procedure and Signal Processing

Figure 4.23 illustrates the calibration and signal processing procedures used in the TDLS / WMS experiments. As all the signals were triggered and captured at the same time, they were all measured on the same time-indexed axis. The "no gas signal" was then simply subtracted from the gas signal to place the 1st harmonic / derivative on a zero background. To normalise to the increasing laser power as the centre frequency is swept across the gas line, the zeroed signal was divided directly by the power reference. If the sinusoidal modulation was large it could be seen on the power reference signal; however, as the signals were triggered to the ramp signal and not to the sinusoid, signal averaging removed this. Finally, to compensate for changes in signal power and any losses in the system, the signal was divided by the average value of (or a single point on) the RAM induced DC signal. The results of this approach are discussed in detail in chapter 5.

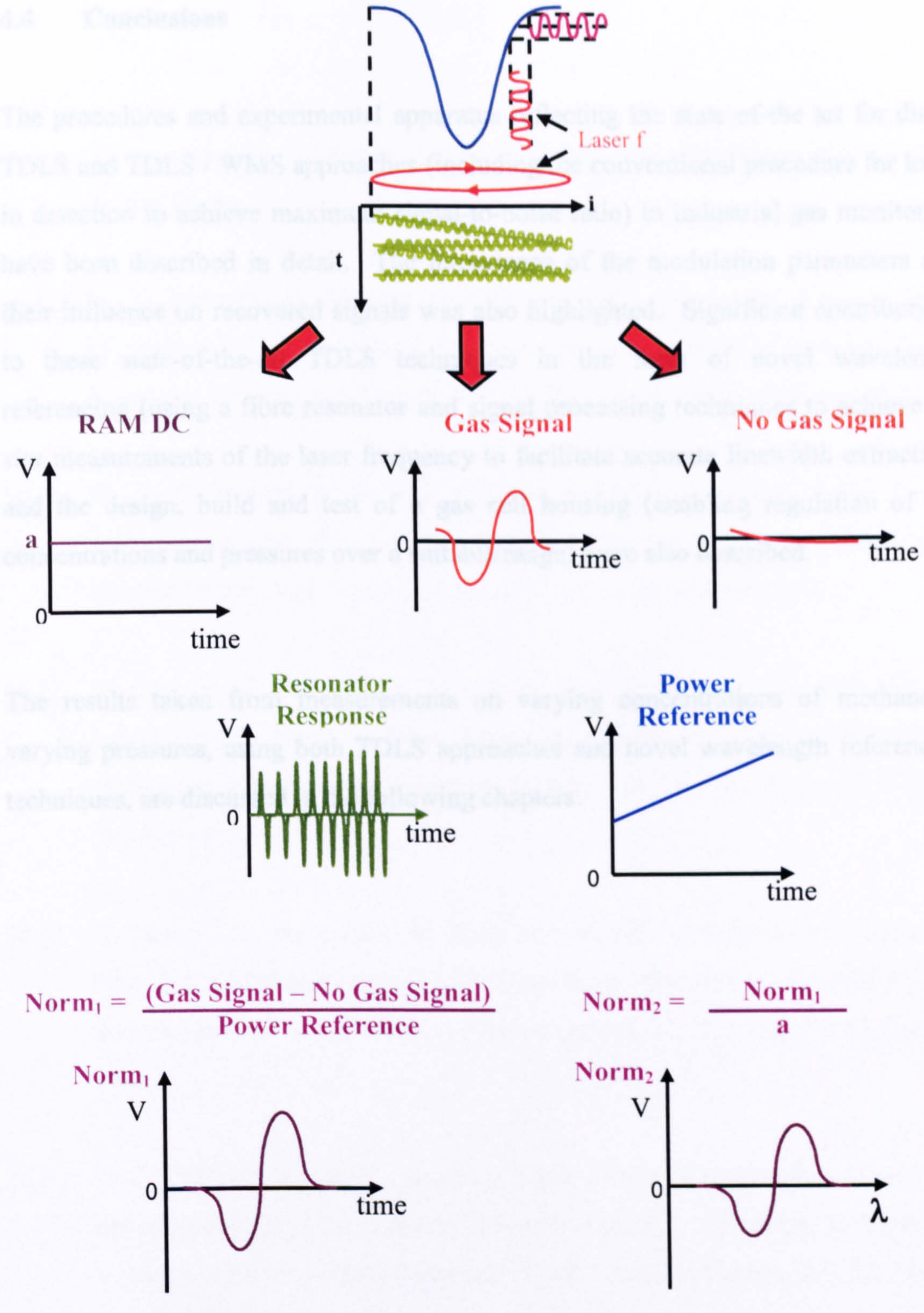

Figure 4.23: Example of signal processing and calibration procedures for TDLS / WMS

4.4 Conclusions

The procedures and experimental apparatus reflecting the state-of-the art for direct TDLS and TDLS / WMS approaches (including the conventional procedure for lock-in detection to achieve maximum signal-to-noise ratio) in industrial gas monitoring have been described in detail. The importance of the modulation parameters and their influence on recovered signals was also highlighted. Significant contributions to these state-of-the-art TDLS techniques in the form of novel wavelength referencing (using a fibre resonator and signal processing techniques to achieve *in-situ* measurements of the laser frequency to facilitate accurate linewidth extraction) and the design, build and test of a gas cell housing (enabling regulation of gas concentrations and pressures over a suitable range) were also described.

The results taken from measurements on varying concentrations of methane at varying pressures, using both TDLS approaches and novel wavelength referencing techniques, are discussed in the following chapters.

4.5 References

[4.1] JDS Uniphase, "Butterfly Laser Modules: DC Operating Instructions," August 2000.

[4.2] M. A. Morante, G. Stewart, B. Culshaw and J. M. Lopez-Higuera, "New Micro-Optic Cell for Optical Fibre Gas Sensors with Interferometric Noise Reduction," Electronics Letters, Vol. 33, No. 16, pp 1407-1409, July 1997.

[4.3] W. Jin, G. Stewart, W. Philp, B. Culshaw and M. S. Demokan, "Limitation of Absorption-Based Fiber Optic Gas Sensors by Coherent Reflections," Applied Optics, Vol. 36, No. 25, pp 6251-6255, September 1997.

[4.4] W. Jin, Y. Z. Xu, M. S. Demokan and G. Stewart, "Investigation of Interferometric Noise in Fiber-Optic Gas Sensors with use of Wavelength Modulation Spectroscopy," Applied Optics, Vol. 36, No. 28, pp 7239-7246, October 1997.

[4.5] G. Stewart, A. Mencaglia, W. Philp and W. Jin, "Interferometric Signals in Fiber Optic Methane Sensors with Wavelength Modulation of the DFB Laser Source," Journal of Lightwave Technology, Vol. 16, No. 1, pp 43-53, January 1998.

[4.6] L. C. Philippe and R. K. Hanson, "Laser Diode Wavelength – Modulation Spectroscopy for Simultaneous Measurement of Temperature, Pressure and Velocity in Shock – Heated Oxygen Flows," Applied Optics, Vol. 32, No. 30, pp 6090-6103, October 1993.

[4.7] P. Urquhart, "Compound Optical - Fiber based Resonators," Journal of the Optical Society of America, Vol. 5, No. 6, pp 803-812, June 1988.

[4.8] P. Urquhart, "Transversely Coupled Fiber Fabry-Perot Resonator: Theory," Applied Optics, Vol. 26, No. 3, pp 456-463, February 1987.

[4.9] B. Culshaw, "Measuring Strain using Optical Fibres," Strain 2000, Vol. 36, No.3, pp 105-113.

[4.10] G. Keiser, "Optical Fiber Communications – Third Edition," McGraw-Hill, 2000.

[4.11] J. A. De Marchi: julian@matlinks.net

[4.12] P. Werle, "A Review of Recent Advances in Semiconductor Laser based Gas Monitors," Spectrochimica Acta Part A: Molecular and Biomolecular Spectroscopy, Vol. 54, No. 2, pp 197-236, February 1998.

[4.13] B. Culshaw, G. Stewart, F. Dong, C. Tandy and D. Moodie, "Fibre Optic Techniques for Remote Spectroscopic Methane Detection – from Concept to System Realisation," Sensors and Actuators B: Chemical, Vol. 51, pp 25-37, May 1998.

[4.14] G. Stewart, C. Tandy, D. Moodie, M. A. Morante and F. Dong, "Design of a Fibre Optic Multi-Point Sensor for Gas Detection," Sensors and Actuators B: Chemical, Vol. 51, pp 227-232, August 1998.

[4.15] P. Kluczynski and O. Axner, "Theoretical Description based on Fourier Analysis of Wavelength – Modulation Spectrometry in terms of Analytical and Background Signals," Applied Optics, Vol. 38, No. 27, pp 5803-5815, September 1999.

[4.16] S. Schilt, L. Thevenaz and P. Robert, "Wavelength Modulation Spectroscopy: Combined Frequency and Intensity Laser Modulation," Applied Optics, Vol. 42, No. 33, pp 6728-6738, November 2003.

Chapter 5

Results and Analysis

5.1 Introduction

The chapter reports on accurate and simultaneous measurements of gas concentration and pressure using both TDLS with direct detection and a new approach to TDLS with wavelength modulation spectroscopy.

The initial objective was to extract concentration and pressure under varying conditions using the conventional approaches to TDLS with direct detection and TDLS / WMS detection. Attempts were made at recovering linewidths and accurate absorption depths from which to extract the pressure and concentration respectively. Numerical integration of recovered 1st harmonic signals was also attempted with a view to recovering the absolute absorption line transmission function. In this chapter

we discuss and illustrate the reasons why conventional approaches to TDLS with WMS are fundamentally flawed in terms of achieving accurate gas composition measurements in a stand-alone instrument. As will be seen, issues arise from complications in the signal analysis process, which requires accurate knowledge of system and target gas parameters. Errors in the determination of these parameters accumulate, making the final determination of concentration and pressure inaccurate. Through careful signal and theoretical analysis the sources of these errors are identified and removed. The analysis also introduces a means of recovering the absolute absorption line transmission function, which is then validated through promising experimental results.

5.2 TDLS with Direct Detection

5.2.1 Introduction

TDLS with direct detection has been well researched in the past but achieving accurate and simultaneous measurements of gas concentration and pressure in stand-alone, field-deployable instruments has been difficult due to issues regarding accurate and reliable *in-situ* wavelength referencing.

As was illustrated in figure 1.2 in chapter 1 and as was proved in chapter 3, the signal amplitudes of the recovered absolute transmission functions have negligible, if any, dependence on pressure / linewidth change at pressures above 1 atmosphere (from pressure broadened Lorentzian lineshape analysis). In addition, recovery of the gas line transmission signals leads to simple, accurate analysis and the technique can be absolute with no need for calibration. For these two reasons, signals recovered using TDLS with direct detection serve as an ideal starting point for determining the accuracy of our proposed wavelength referencing technique and curve fitting

procedure before the more complex analysis of the TDLS / WMS signals. As the HITRAN database details the transmission of light through gases in the atmosphere, the host gas is always air. In order to model the transmission of light through various concentrations of methane in nitrogen, the HITRAN air-broadening coefficient has to be manipulated. Therefore, curve fitting theoretical profiles to directly recovered gas absorption line transmission signals over a range of pressures will determine the most accurate coefficient for N_2 broadening.

This section (5.2) reports on the process of curve fitting theoretical absorption profiles (based on HITRAN data) to directly recovered methane (CH_4) transmission signals, proving that simultaneous measurements of gas concentration and pressure are possible. The accuracy and reliability of the novel wavelength referencing technique and the determination of the N_2 broadening coefficient are also discussed.

5.2.2 The Need for Accurate Wavelength Referencing

The importance of accurate and reliable wavelength referencing has been highlighted many times throughout this thesis and figure 5.1 serves to emphasise the point. The blue line in figure 5.1 shows an experimentally measured gas absorption line transmission profile for 10.13 % CH_4 in N_2 balance at 1.000 bar, 20.5 °C in the 1650 nm region. The wavelength scale applied to the experimental signal was determined from the DC current / wavelength tuning relationship for the 1650 nm laser (~ 0.006 nm / mA, measured as described in chapter 4). In order to scan the width of the line a sweep of 80 mA peak-to-peak was applied to the laser injection current. This translates, according to the tuning relationship, as a sweep of approximately 0.5 nm. The absolute scale was achieved by shifting the relative scale to the known peak absorption wavelength at 1650.956 nm.

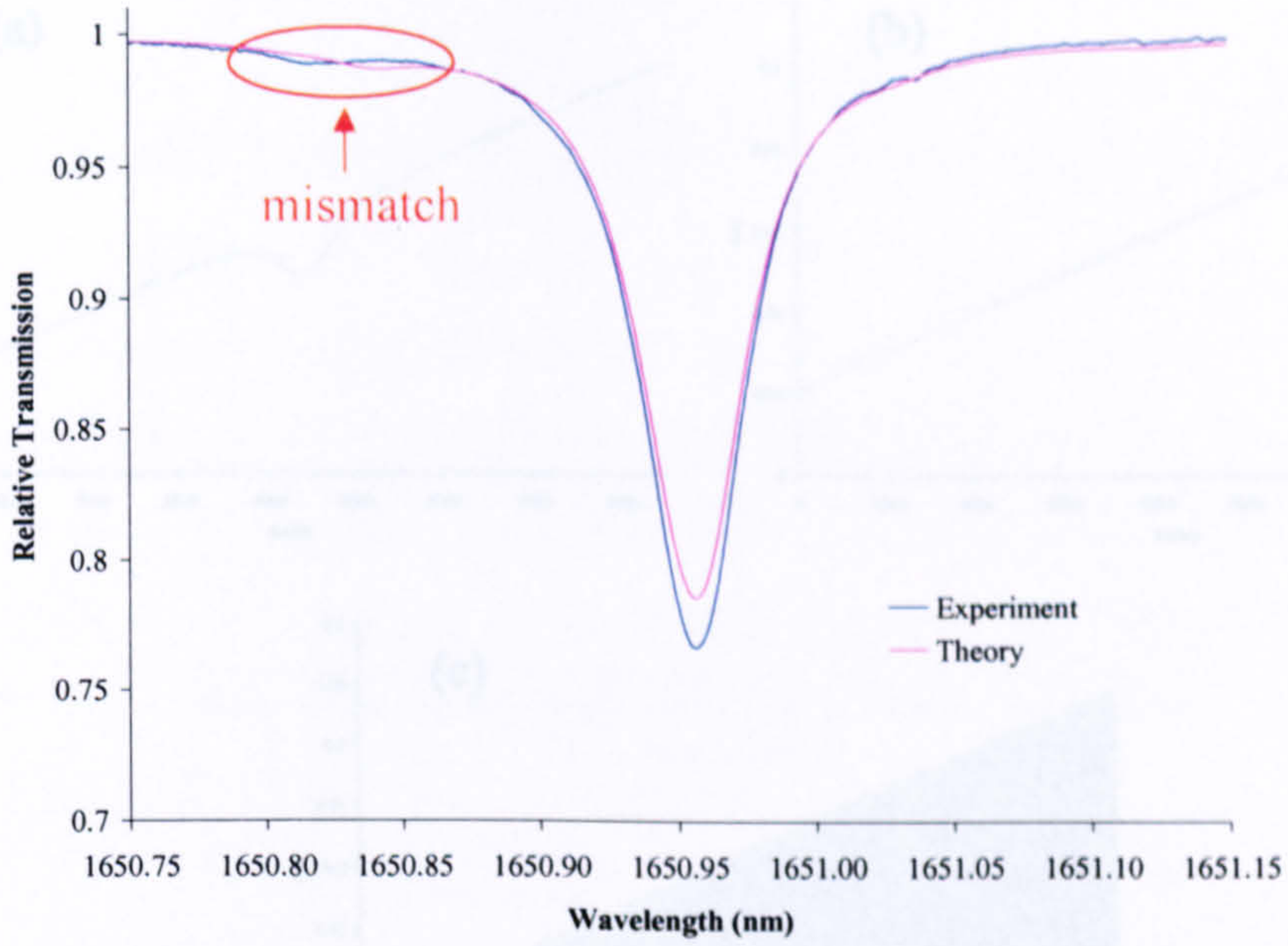

Figure 5.1: 10.13 % CH_4 : N_2 balance at 20.5 °C and 1.000 bar pressure – Comparison of experimental signal (referenced to DC current tuning coefficient) to theoretical prediction

It can be seen that there is reasonable agreement between the converted time-based signal and theory (based on the HITRAN transmission data for CH_4 in air at the known pressure, concentration and temperature) immediately around the absorption line centre at 1650.956 nm, but that there is a noticeable mismatch at a second, smaller absorption feature at 1650.83 nm. The peak absorption wavelength of this smaller feature is well documented in spectroscopic databases such as HITRAN and therefore, the mismatch can only be attributed to the inaccuracy associated with the linear mapping of the wavelength with the sweep of the injection current. This hypothesis is backed up by the current vs. wavelength relationship shown in figure 4.8.

All further signals shown in this section (5.2) were measured using the experimental system and methodologies described in section 4.2 of chapter 4. Figure 5.2 shows the experimentally measured signals from the gas measurement, power referencing and wavelength referencing channels.

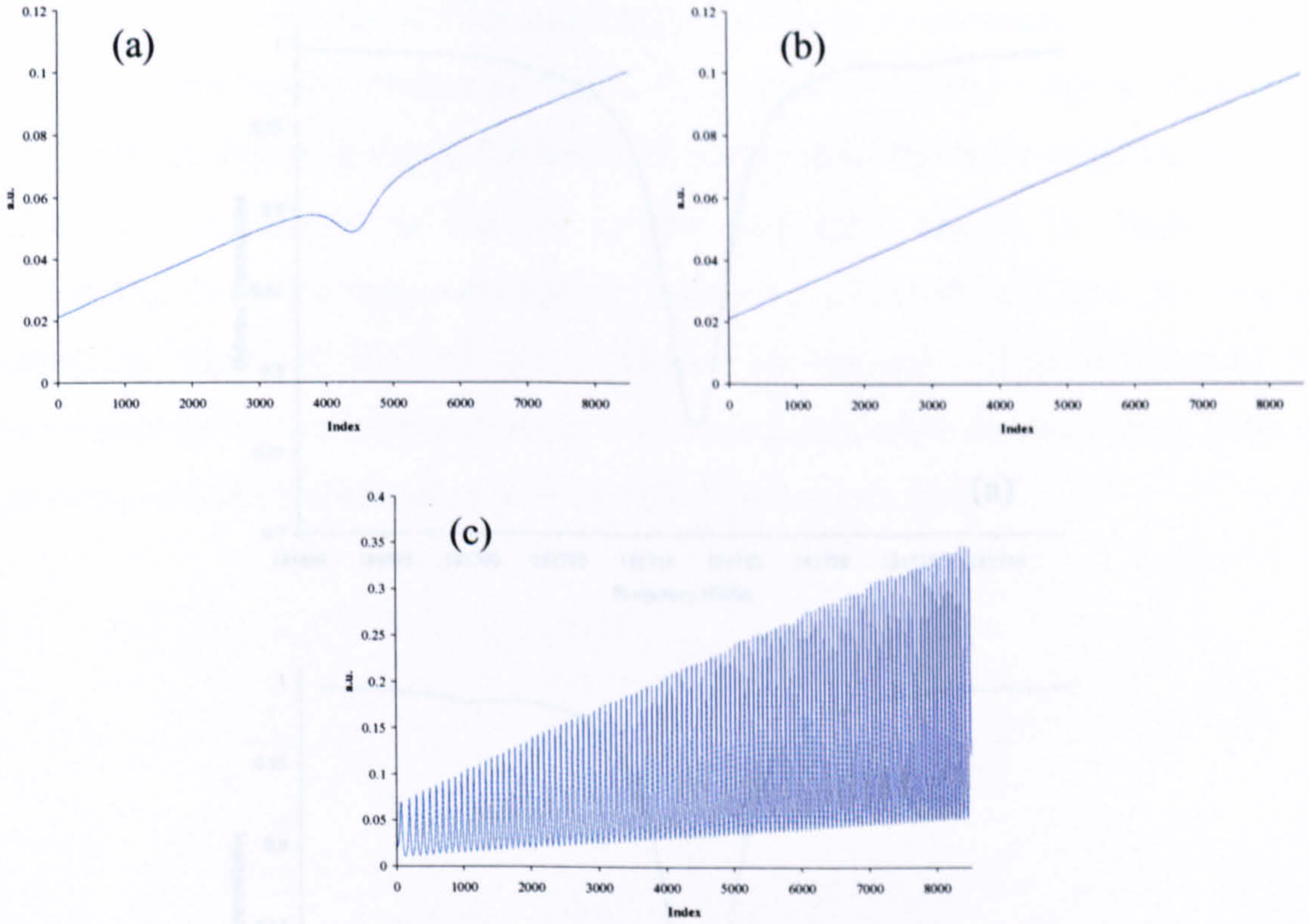

Figure 5.2: 10.13 % CH_4 : N_2 balance at 20.5 °C and 1.000 bar pressure – Experimentally measured output signals: (a) trimmed gas signal, (b) trimmed power reference signal, (c) trimmed resonator response

The LabVIEW program triggers all the received signals to a threshold voltage on the power reference signal. The recovered gas signal (a) is normalised to the increasing power (b) as the laser centre frequency is swept across the gas line, by dividing (a) by (b). The result of (a) divided by (b) is the signal shown in figure 5.1; this time, however, the novel wavelength referencing approach is applied. Using the normalised gas signal and the received resonator trace (c) in the wavelength referencing MATLAB program (described in section 4.2 of chapter 4), we obtain absolute frequency and wavelength referenced plots, shown below in figure 5.3.

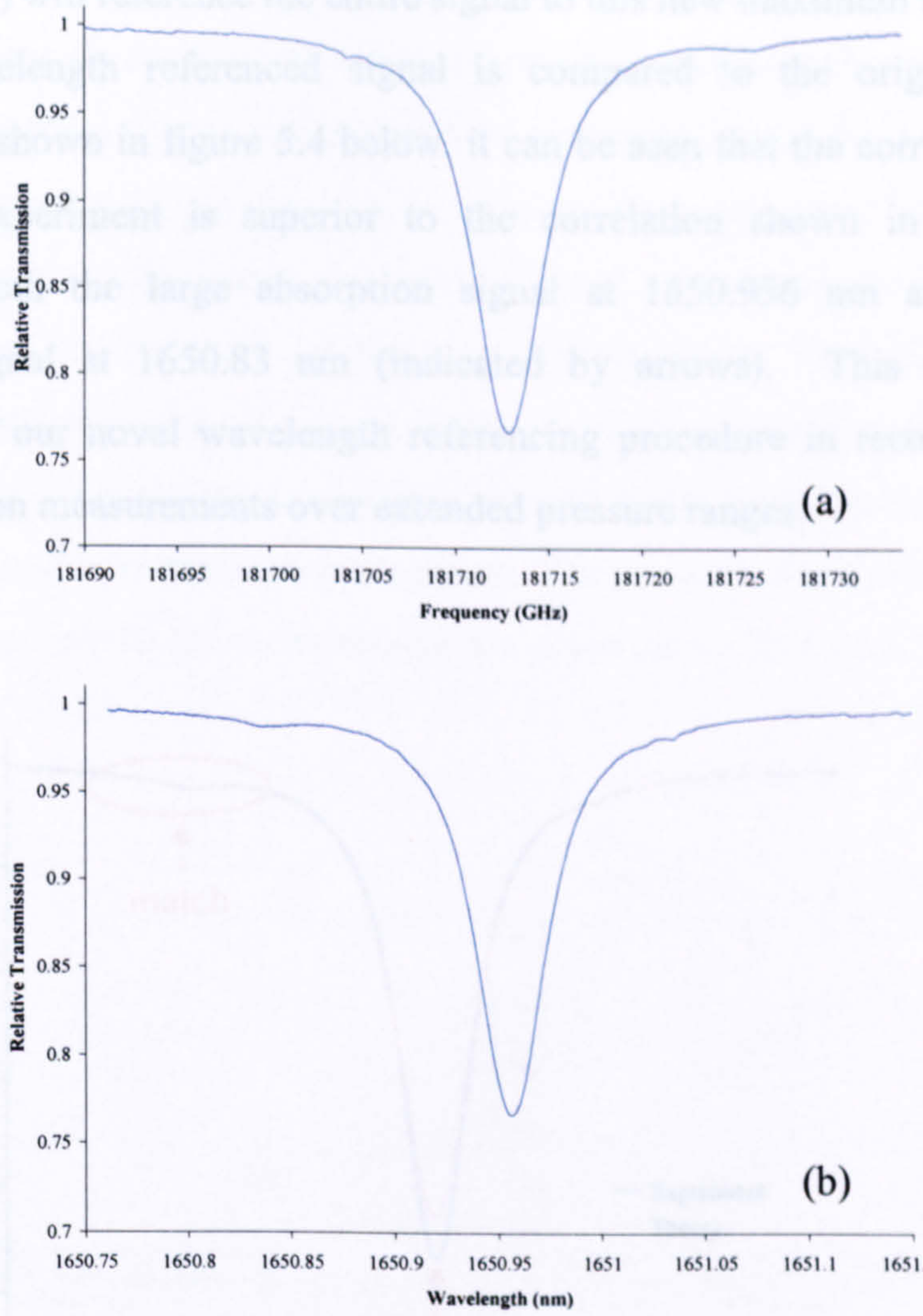

Figure 5.3: 10.13 % CH_4 : N_2 balance at 20.5 °C and 1.000 bar pressure – Recovered normalised (a) frequency and (b) wavelength referenced gas absorption line transmission signals

Finally, to account for any difference between the off-line amplitude of the gas signal (figure 5.2 (a)) and the off-line amplitude of the power reference signal (figure 5.2 (b)), due to uneven split ratios or system losses, the normalised gas signal (figure 5.3) is divided by a zero-point reference. In this case the zero-point reference was taken from the amplitude of the normalised signal at 1650.77 nm. Dividing all the amplitudes in the signal by this amplitude references the entire signal to a maximum transmission of 1. If the signal is not truly off-line; for example, if neighbouring lines merge with the line of interest and the signal is no longer 1, multiplying the fractional transmission amplitude by the amplitude of the theoretical prediction (at

the same point) will reference the entire signal to this new maximum transmission. If the new wavelength referenced signal is compared to the original theoretical prediction, as shown in figure 5.4 below, it can be seen that the correlation between theory and experiment is superior to the correlation shown in figure 5.1 by referencing both the large absorption signal at 1650.956 nm and the smaller absorption signal at 1650.83 nm (indicated by arrows). This emphasises the importance of our novel wavelength referencing procedure in recovering accurate gas composition measurements over extended pressure ranges.

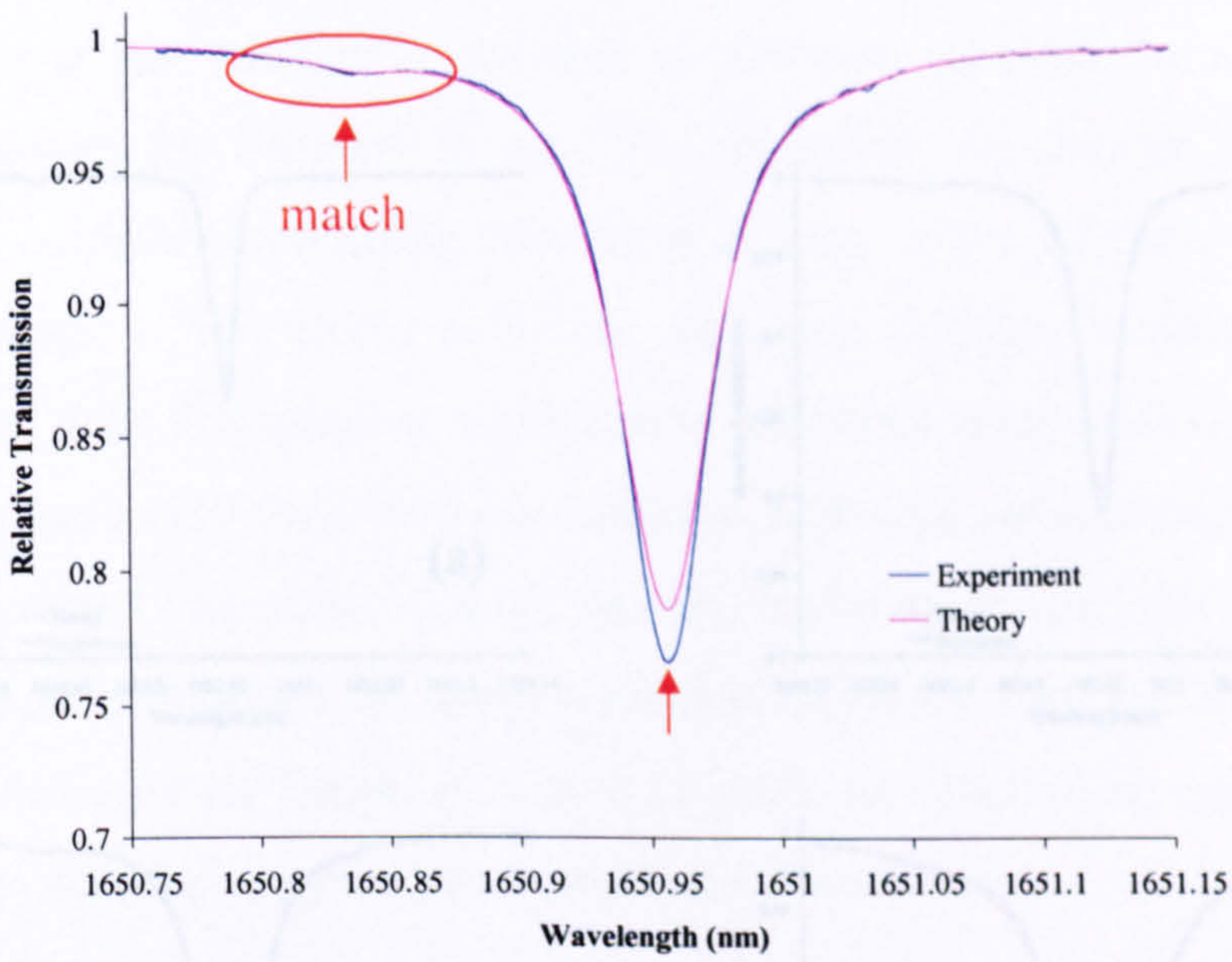

Figure 5.4: 10.13 % CH_4 : N_2 balance at 20.5 °C and 1.000 bar pressure – New wavelength referenced absorption line transmission function compared to the theoretical prediction

5.2.3 Determining the N_2 Broadening Coefficient

It can be seen from figure 5.4 above that there is a noticeable discrepancy between the theoretical prediction of peak absorption depth and that measured experimentally. Indeed, when examining the correlation between experimental and theoretical

absolute transmission profiles for a range of pressures, shown in figure 5.5 below, it can be seen that, although the absorption linewidth increases with pressure, the error in the depth between theory and experiment increases and as the linewidth of any profile is measured at half-maximum, there is an increasing error in linewidth. As mentioned throughout this thesis, the depth of the absolute transmission function is a measure of the concentration of the gas; therefore, the error in concentration increases with pressure also. To quantify the errors, theoretical transmission profiles were matched to the experimental results shown in figure 5.5 by successive iterations of the pressure and concentration parameters. The pressure and concentration values giving the line of best fit for each pressure are noted below in table 5.1.

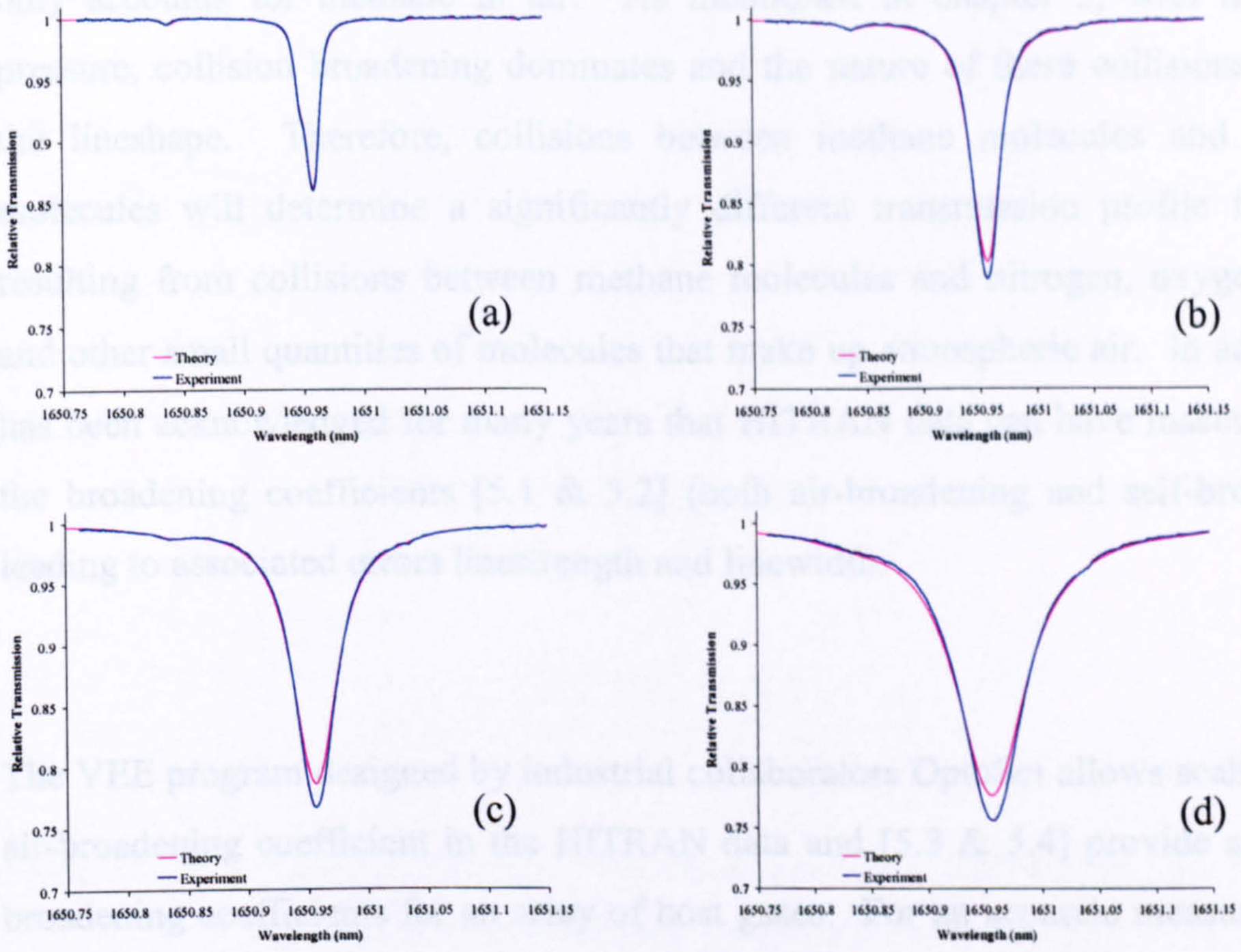

Figure 5.5: 10.13 % CH_4 : N_2 balance at room temperature and (a) 0.209 bar, (b) 0.615 bar, (c) 1.000 bar and (d) 1.805 bar pressure – increasing error with pressure

Digital Gauge Pressure (bar) Accuracy ± 0.1 %	TDLS Recovered Pressure (bar)	Pressure Error (bar)	Cylinder Conc. (%) Accuracy ± 5 %	TDLS Recovered Conc. (%)	Conc. Error (%)
(a) 0.209	0.209	0	10.13	10.3	1.7
(b) 0.615	0.580	0.035	10.13	11.2	10.6
(c) 1.000	0.920	0.08	10.13	11.4	12.5
(d)1.805	1.620	0.185	10.13	11.3	11.5

Table 5.1: Error in pressure and concentration between theoretical predictions and experiment

The lineshape errors can be attributed to host gas broadening effects: the experimental gas mixture is methane in nitrogen, whereas the HITRAN database only accounts for methane in air. As mentioned in chapter 3, with increasing pressure, collision broadening dominates and the nature of these collisions dictates the lineshape. Therefore, collisions between methane molecules and nitrogen molecules will determine a significantly different transmission profile from one resulting from collisions between methane molecules and nitrogen, oxygen, argon and other small quantities of molecules that make up atmospheric air. In addition, it has been acknowledged for many years that HITRAN data can have inaccuracies in the broadening coefficients [5.1 & 5.2] (both air-broadening and self-broadening) leading to associated errors linestrength and linewidth.

The VEE program designed by industrial collaborators OptoSci allows scaling of the air-broadening coefficient in the HITRAN data and [5.3 & 5.4] provide a range of broadening coefficients for an array of host gases. For an accurate measurement of concentration and pressure, the broadening coefficient must be manipulated in order to account for pure nitrogen broadening of the HITRAN methane transmission data. As nitrogen (14.00674 amu) has a smaller atomic mass than both oxygen (15.9994 amu) and argon (39.948 amu), this intuitively suggests the air-broadening coefficient must be scaled downwards. This is backed up by the fact that for a fixed pressure, concentration and temperature, the linestrength (area under the curve) must remain

constant and that for an increase in absorption depth, there must be a decrease in absorption linewidth due to broadening effects only.

Figure 5.6 below shows the three experimentally measured methane gas absorption line transmission signals shown in figure 5.5 (a), (c) and (d) above compared to theory, where the air-broadening coefficient has been scaled by 0.9.

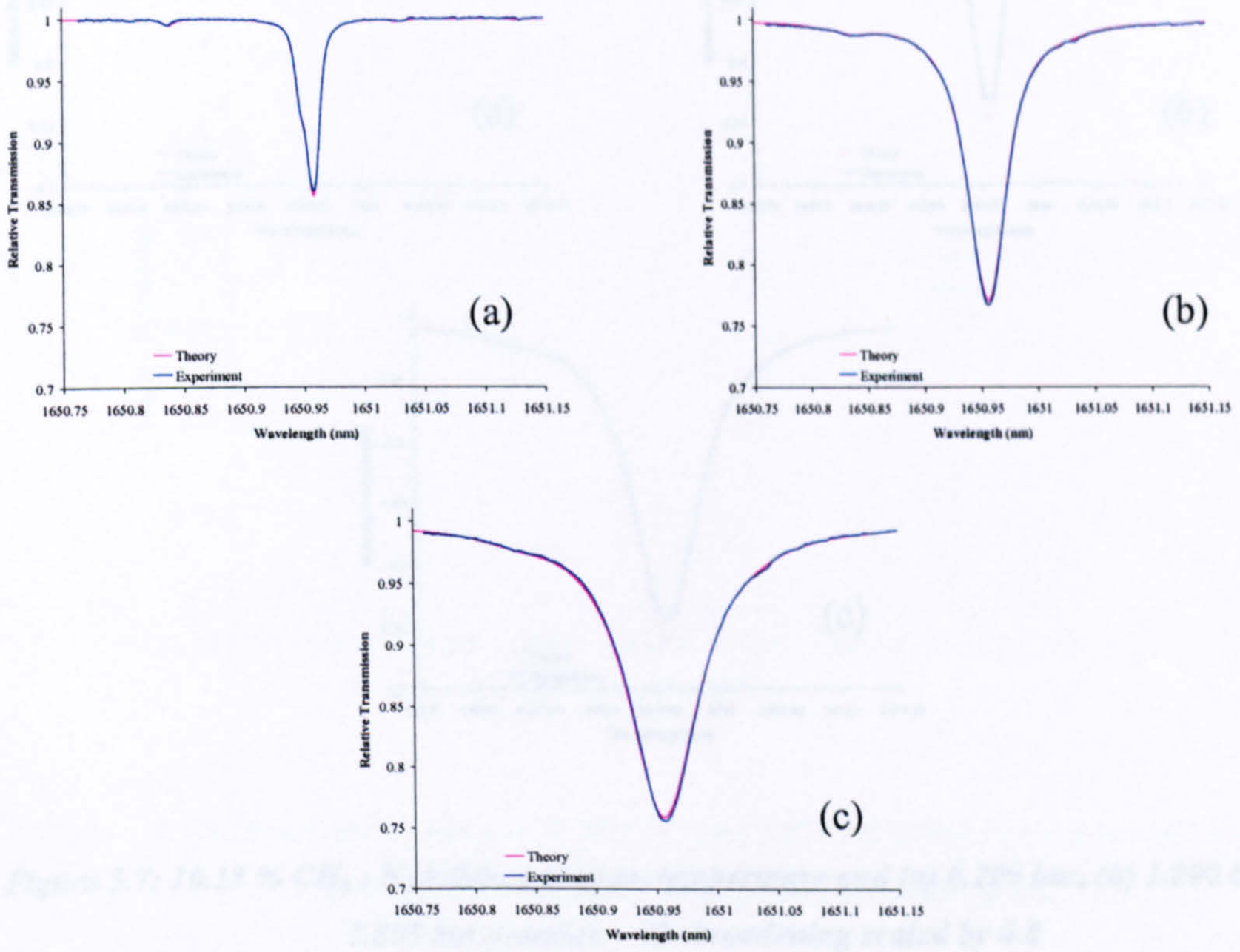

Figure 5.6: 10.13 % CH_4 : N_2 balance at room temperature and (a) 0.209 bar, (b) 1.000 bar and (c) 1.805 bar pressure - air-broadening scaled by 0.9

Figure 5.7 shows the three methane gas absorption line transmission signals shown in figure 5.5 (a), (c) and (d) above compared to theory, where the air-broadening coefficient has been scaled by 0.8. From figures 5.6 and 5.7 it can be seen that the scaling factor for the broadening coefficient lies somewhere between 0.9 and 0.8 and

that it lies closer to 0.9. Indeed, after several more iterations, it can be found that the theoretical predictions match experiment to a high degree of accuracy (as far as can be determined visually) over the full range of pressures when the air-broadening coefficient is scaled by 0.87.

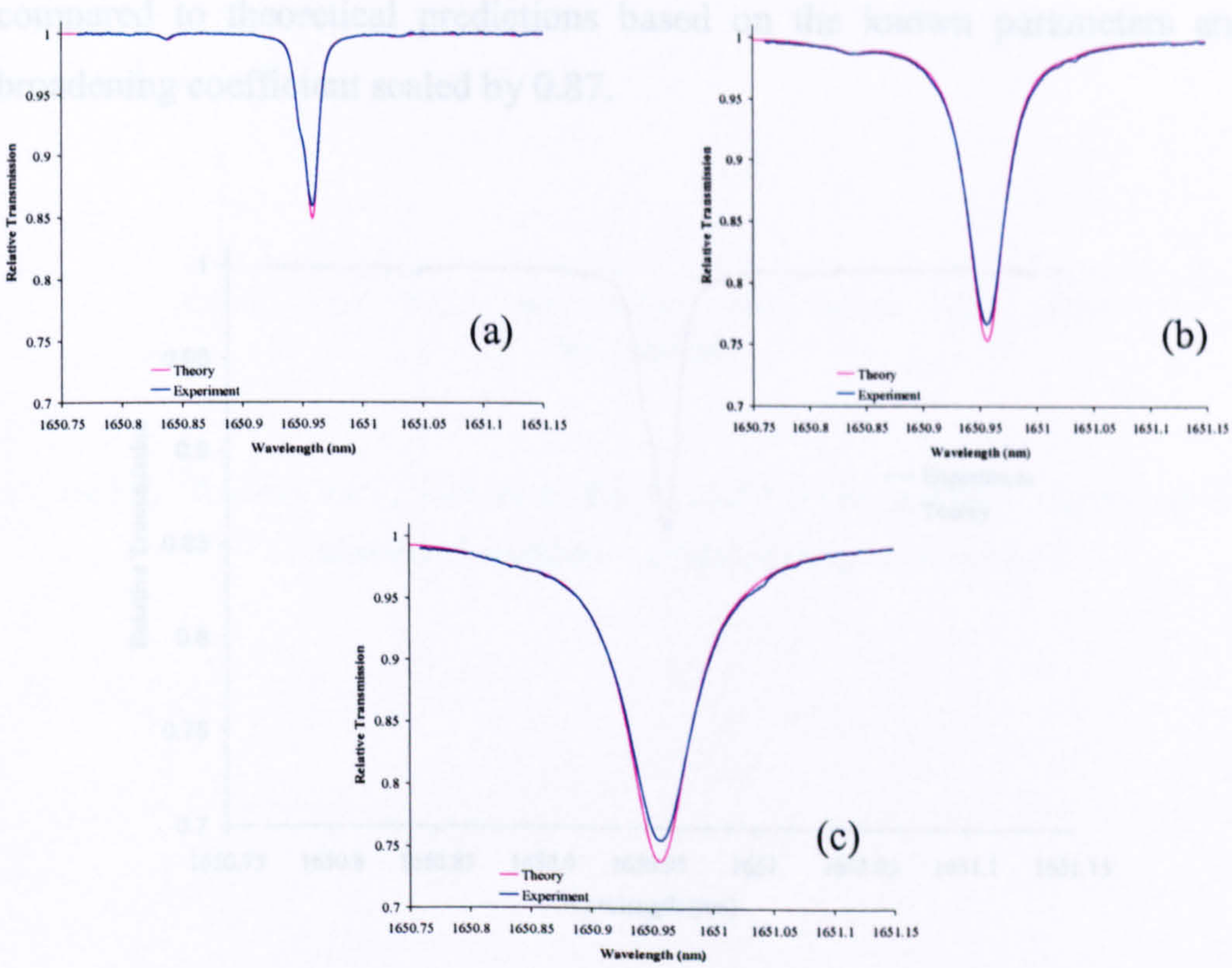

Figure 5.7: 10.13 % CH_4 : N_2 balance at room temperature and (a) 0.209 bar, (b) 1.000 bar and (c) 1.805 bar pressure - air-broadening scaled by 0.8

5.2.4 Accurate and Simultaneous Measurement of Gas Concentration and Pressure using Curve Fitting

Figures 5.8 to 5.12 and 5.13 to 5.17 show experimental signals for an extended pressure set (0.2 to 1.8 bar) and an ambient[1] pressure set (0.9 to 1.1 bar) respectively, compared to theoretical predictions based on the known parameters and an air-broadening coefficient scaled by 0.87.

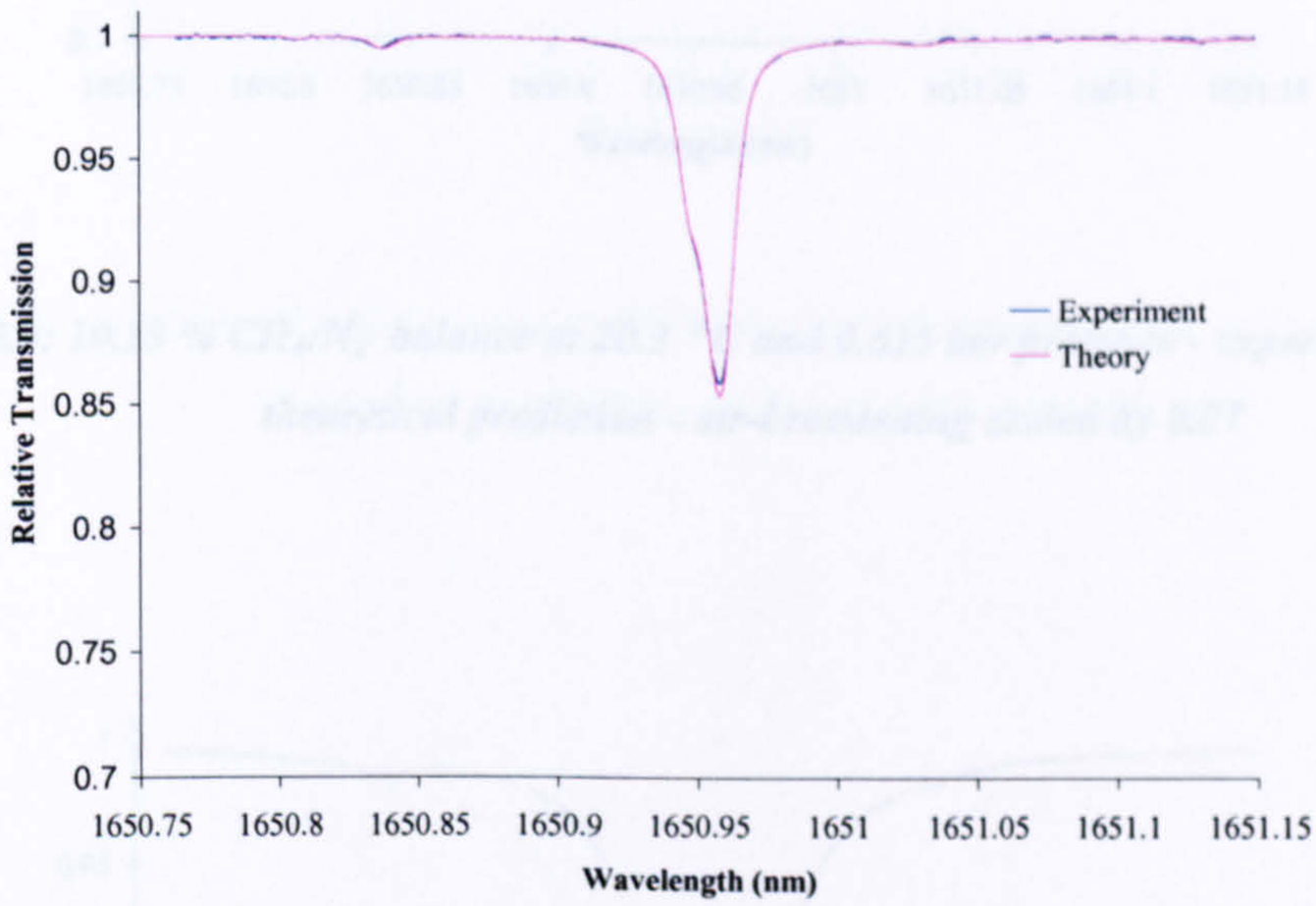

Figure 5.8: 10.13 % CH_4:N_2 balance at 20.1 °C and 0.209 bar pressure - experiment compared to theoretical prediction - air-broadening scaled by 0.87

[1] Atmospheric air pressure is known to fluctuate by approximately ± 10 % around the common estimate of 1 atmosphere

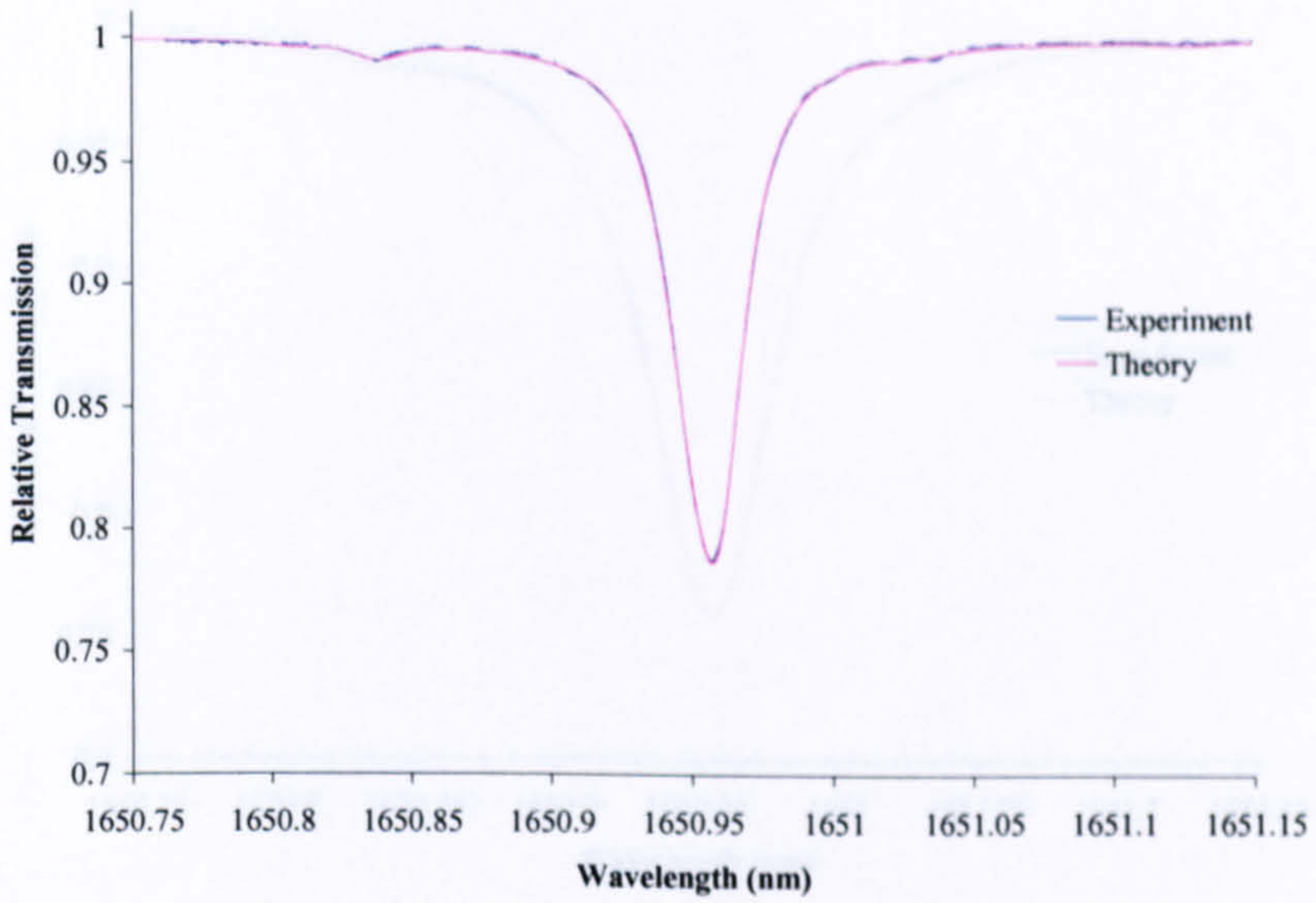

Figure 5.9: 10.13 % CH_4:N_2 balance at 20.3 °C and 0.615 bar pressure - experiment compared to theoretical prediction - air-broadening scaled by 0.87

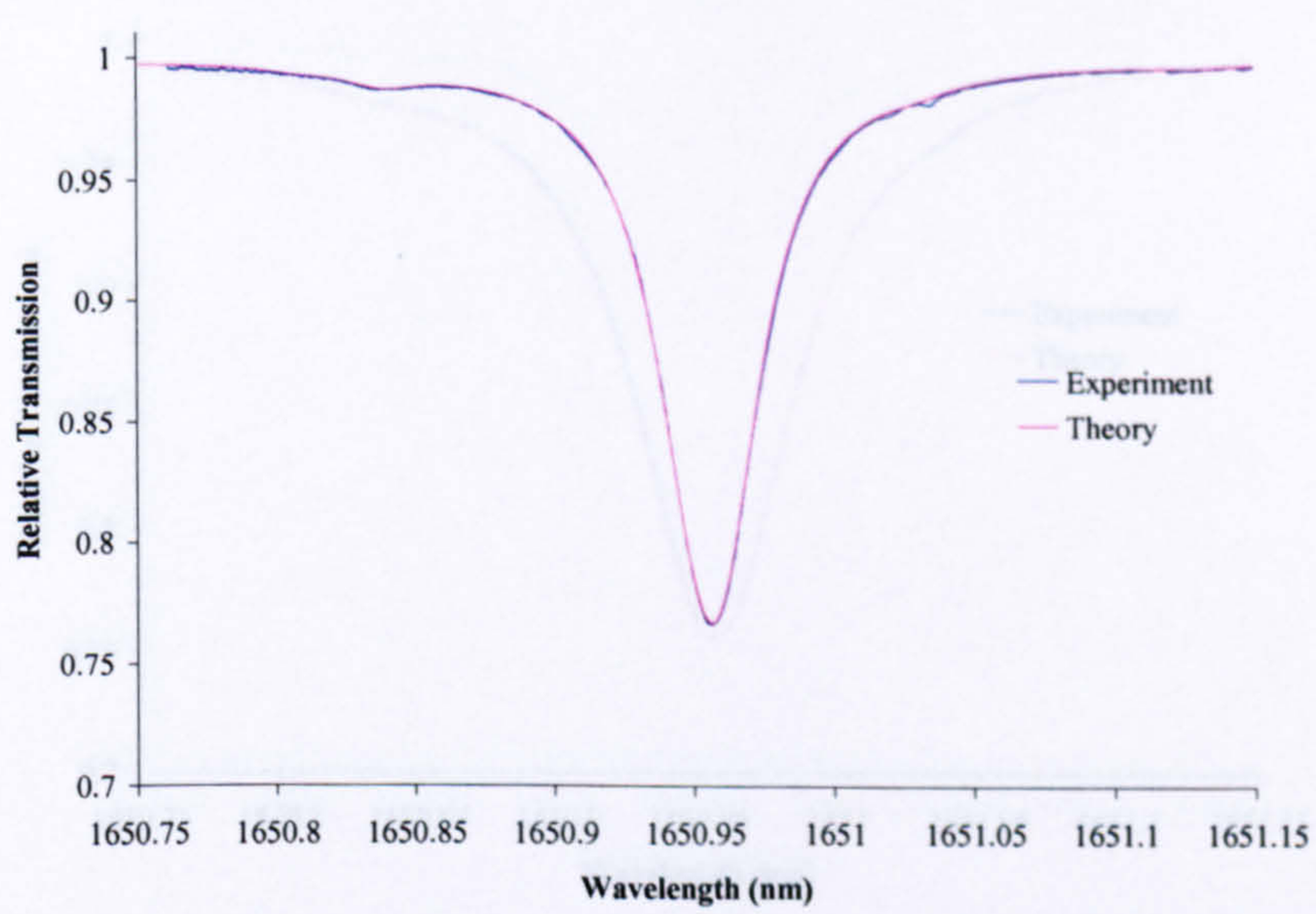

Figure 5.10: 10.13 % CH_4:N_2 balance at 20.5 °C and 1.000 bar pressure - experiment compared to theoretical prediction - air-broadening scaled by 0.87

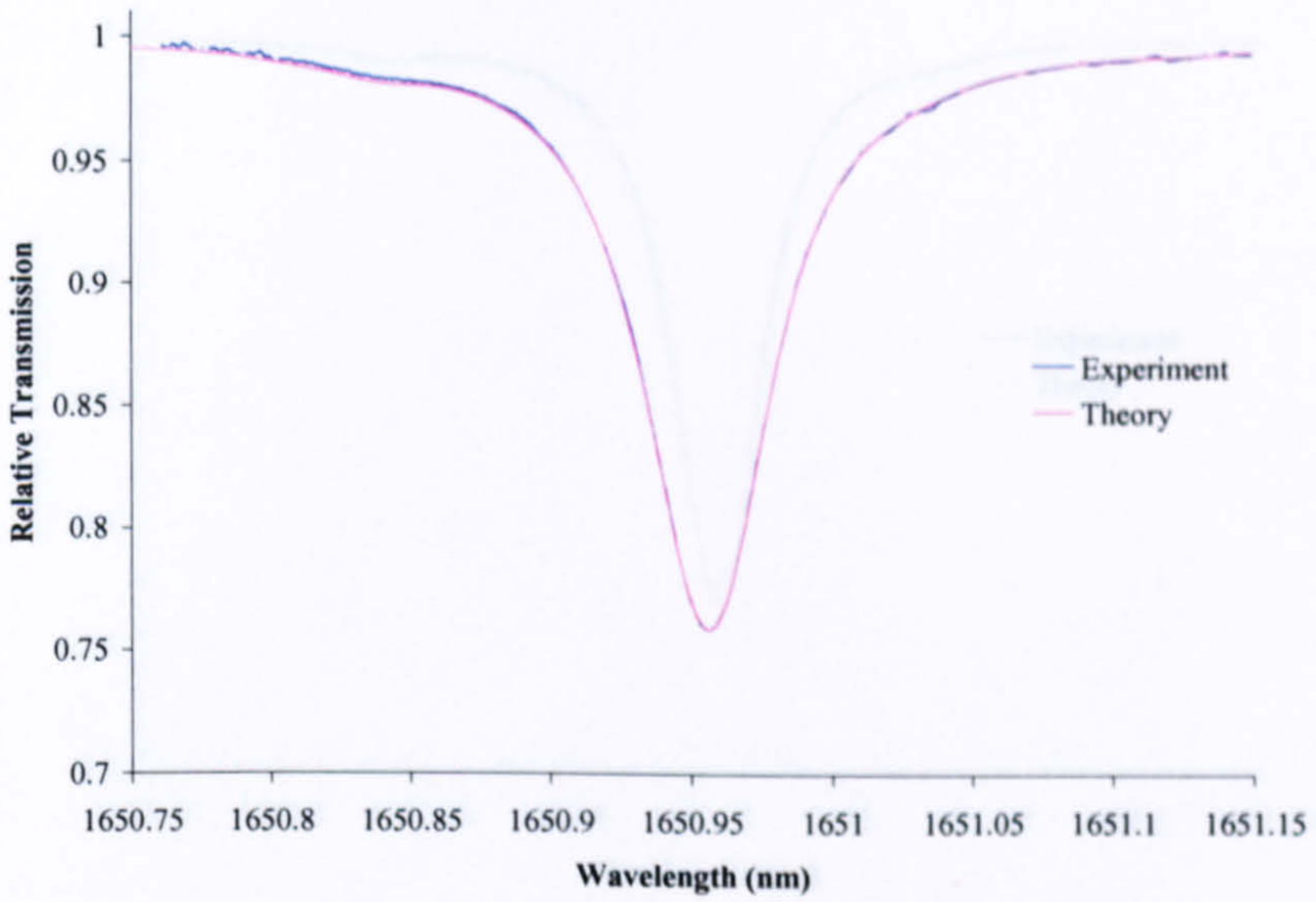

Figure 5.11: 10.13 % CH_4: N_2 balance at 20.7 °C and 1.397 bar pressure - experiment compared to theoretical prediction - air-broadening scaled by 0.87

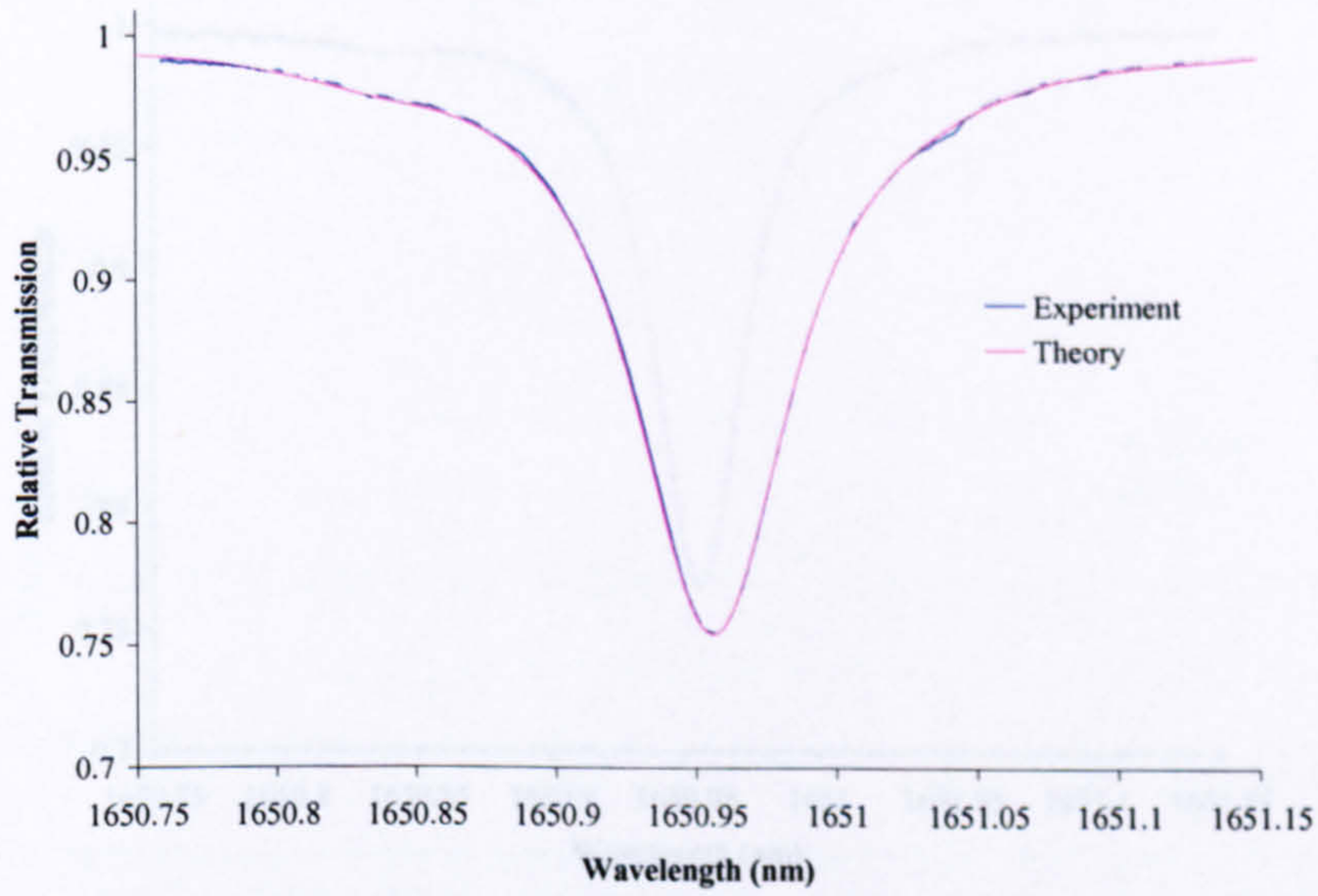

Figure 5.12: 10.13 % CH_4:N_2 balance at 20.5 °C and 1.805 bar pressure - experiment compared to theoretical prediction - air-broadening scaled by 0.87

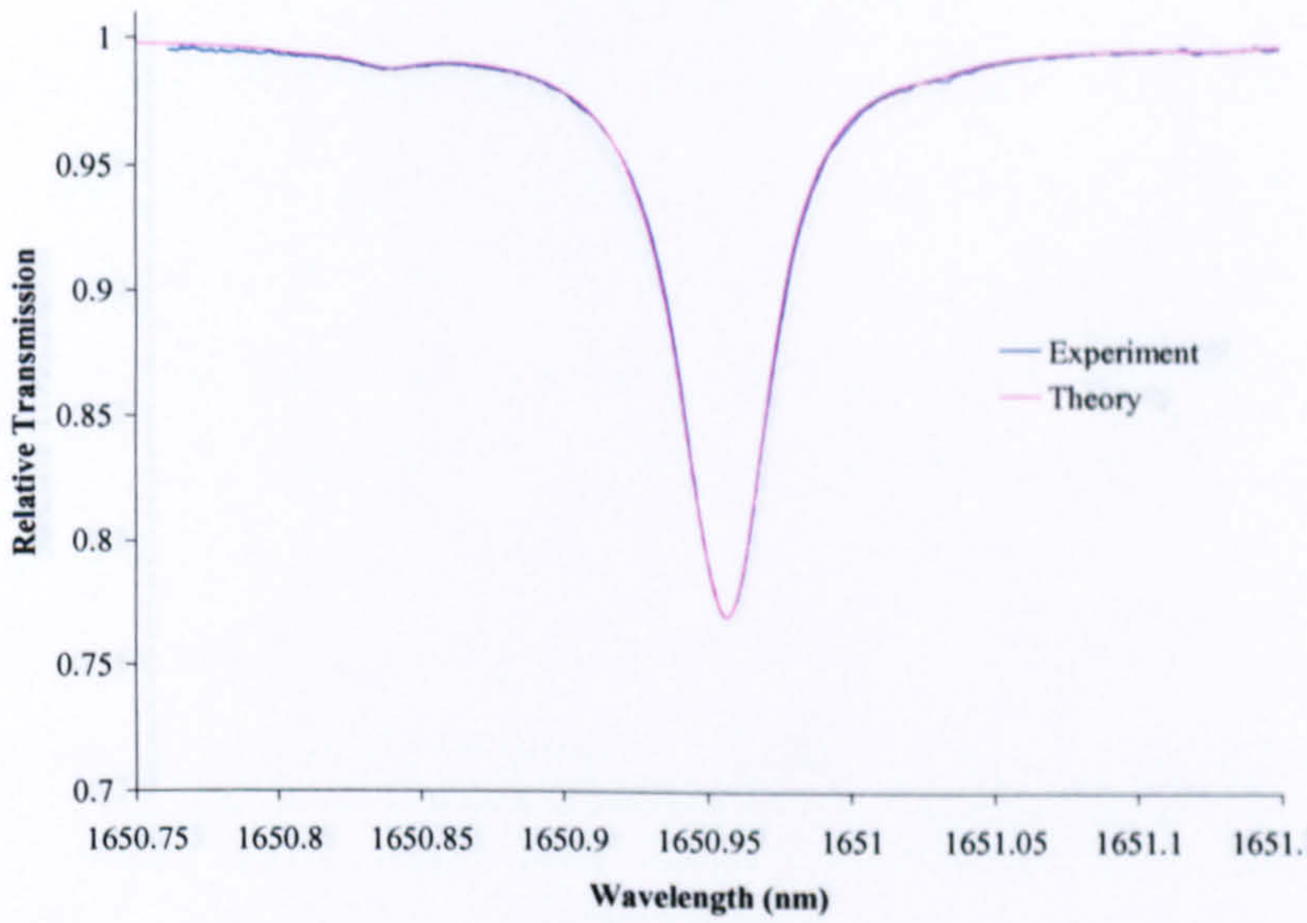

Figure 5.13: 10.13 % CH_4:N_2 balance at 21 °C and 0.902 bar pressure - experiment compared to theoretical prediction - air-broadening scaled by 0.87

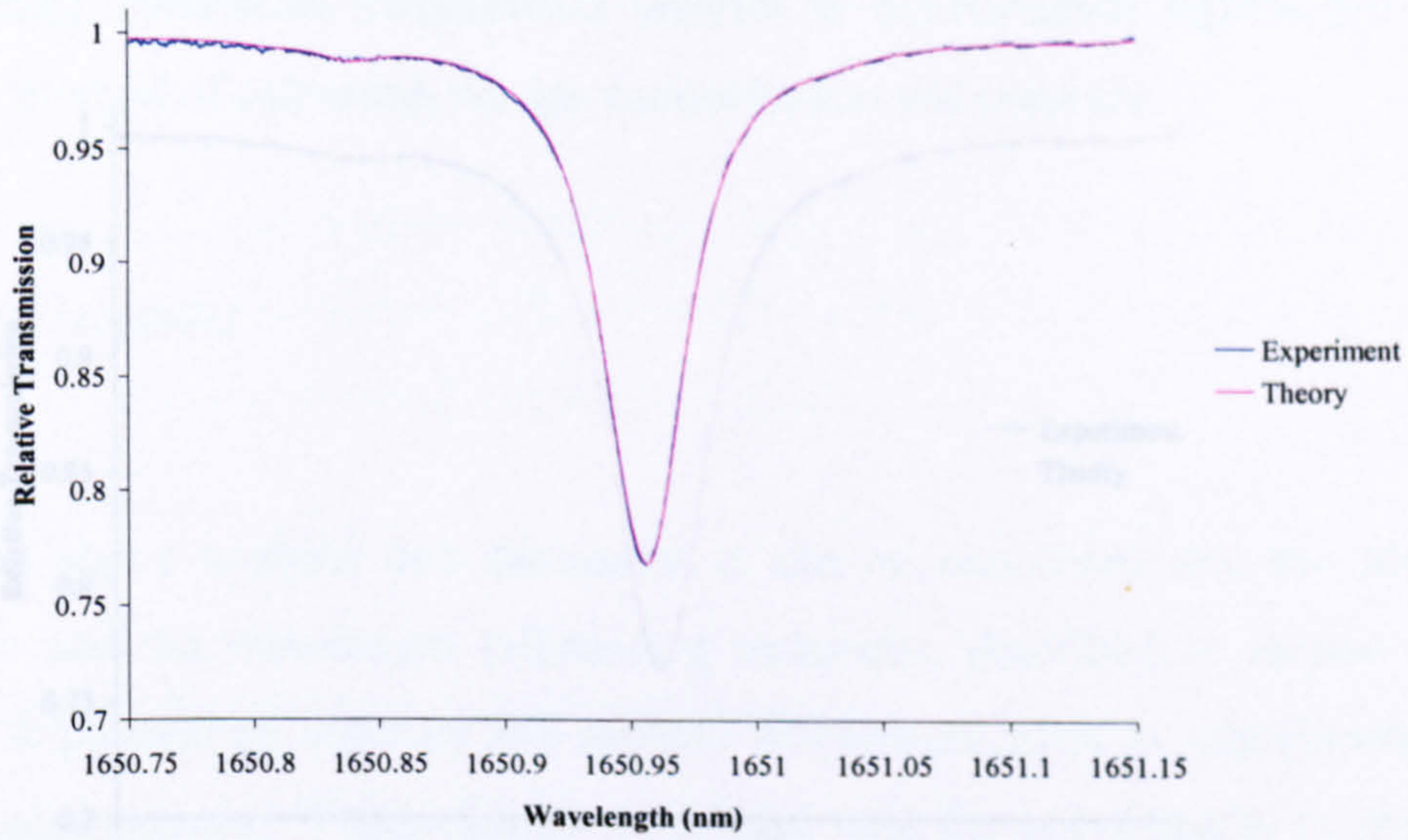

Figure 5.14: 10.13 % CH_4:N_2 balance at 20.2 °C and 0.953 bar pressure - experiment compared to theoretical prediction - air-broadening scaled by 0.87

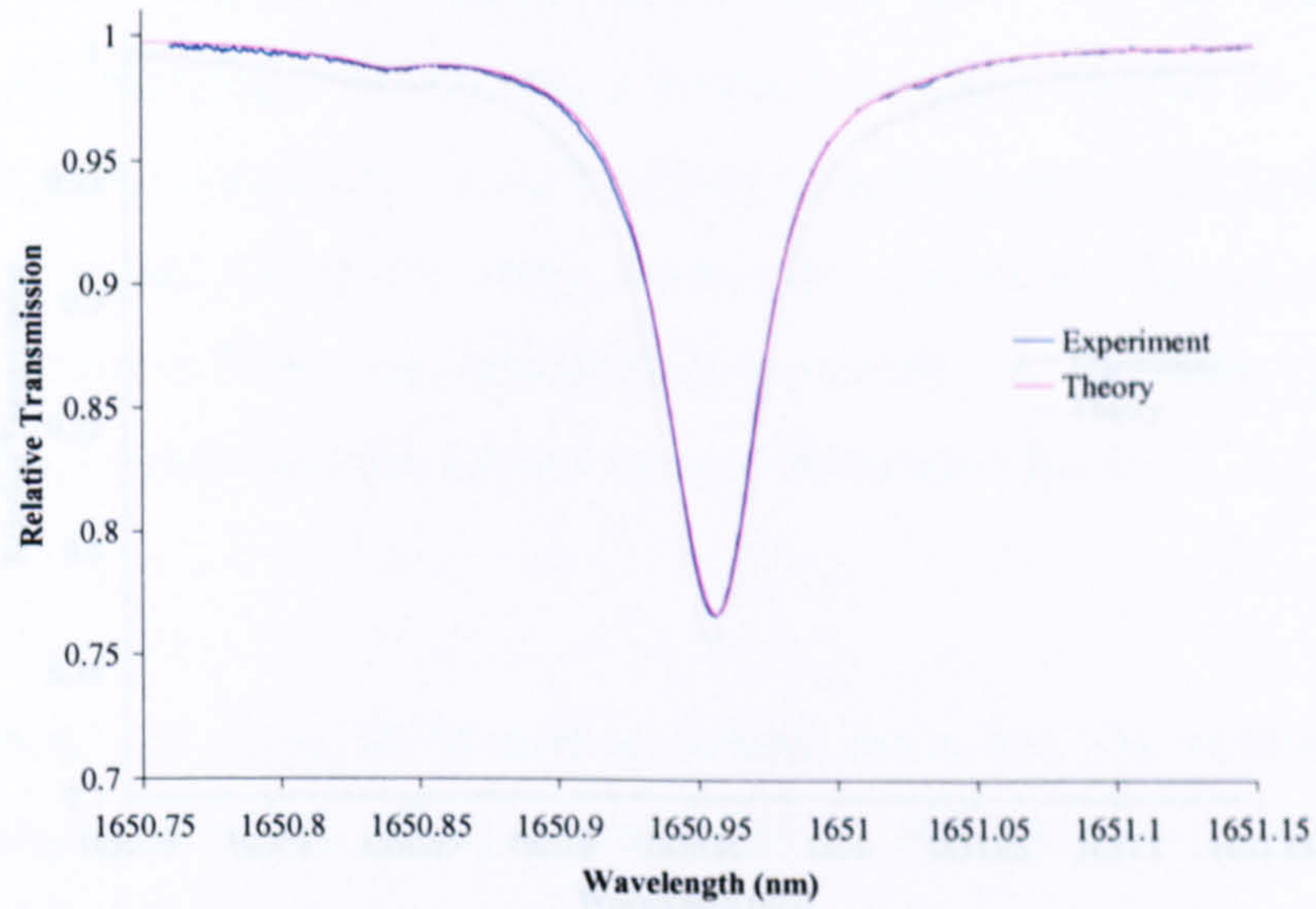

Figure 5.15: 10.13 % CH_4:N_2 balance at 20.3 °C and 1.011 bar pressure - experiment compared to theoretical prediction - air-broadening scaled by 0.87

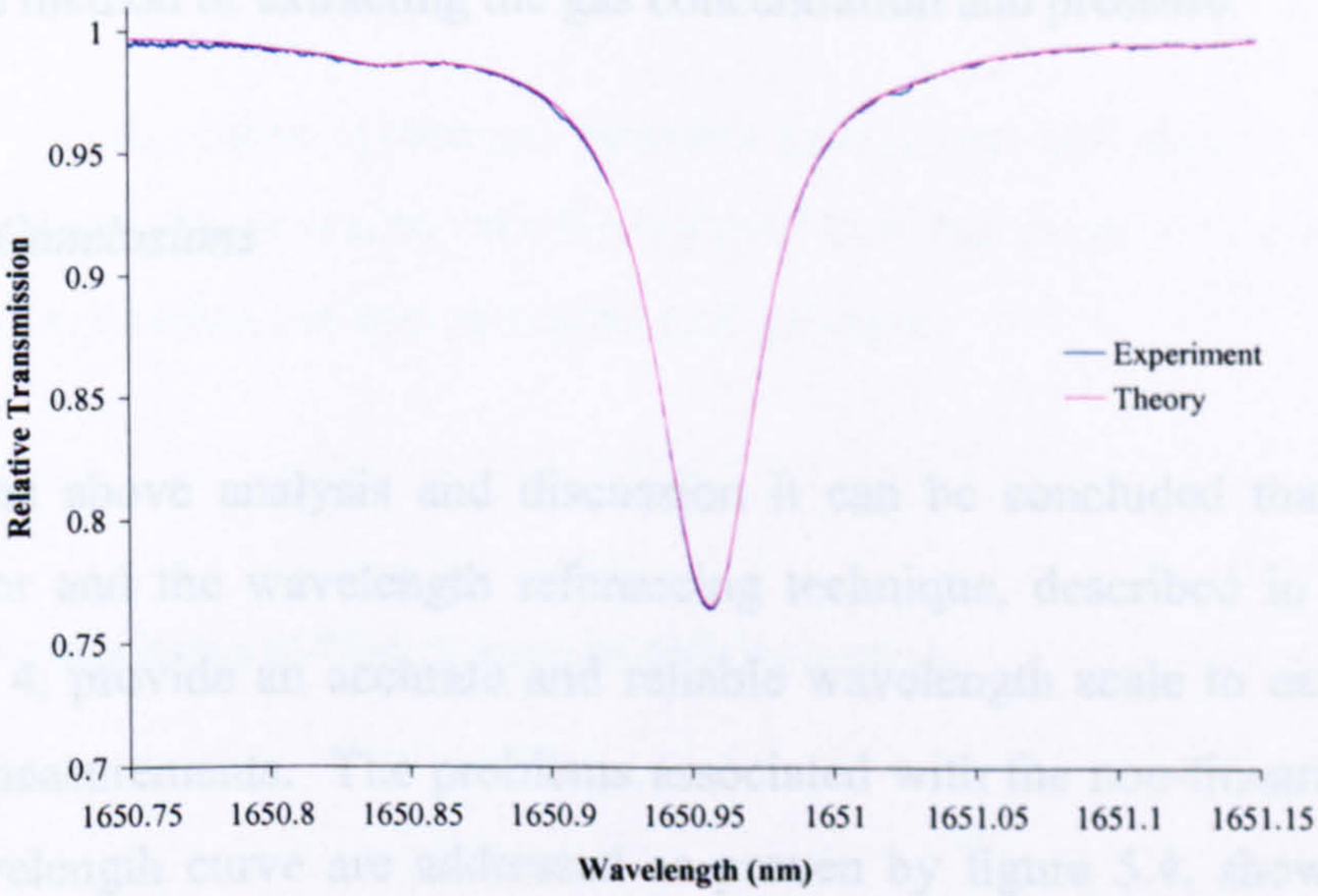

Figure 5.16: 10.13 % CH_4:N_2 balance at 20.2 °C and 1.061 bar pressure - experiment compared to theoretical prediction - air-broadening scaled by 0.87

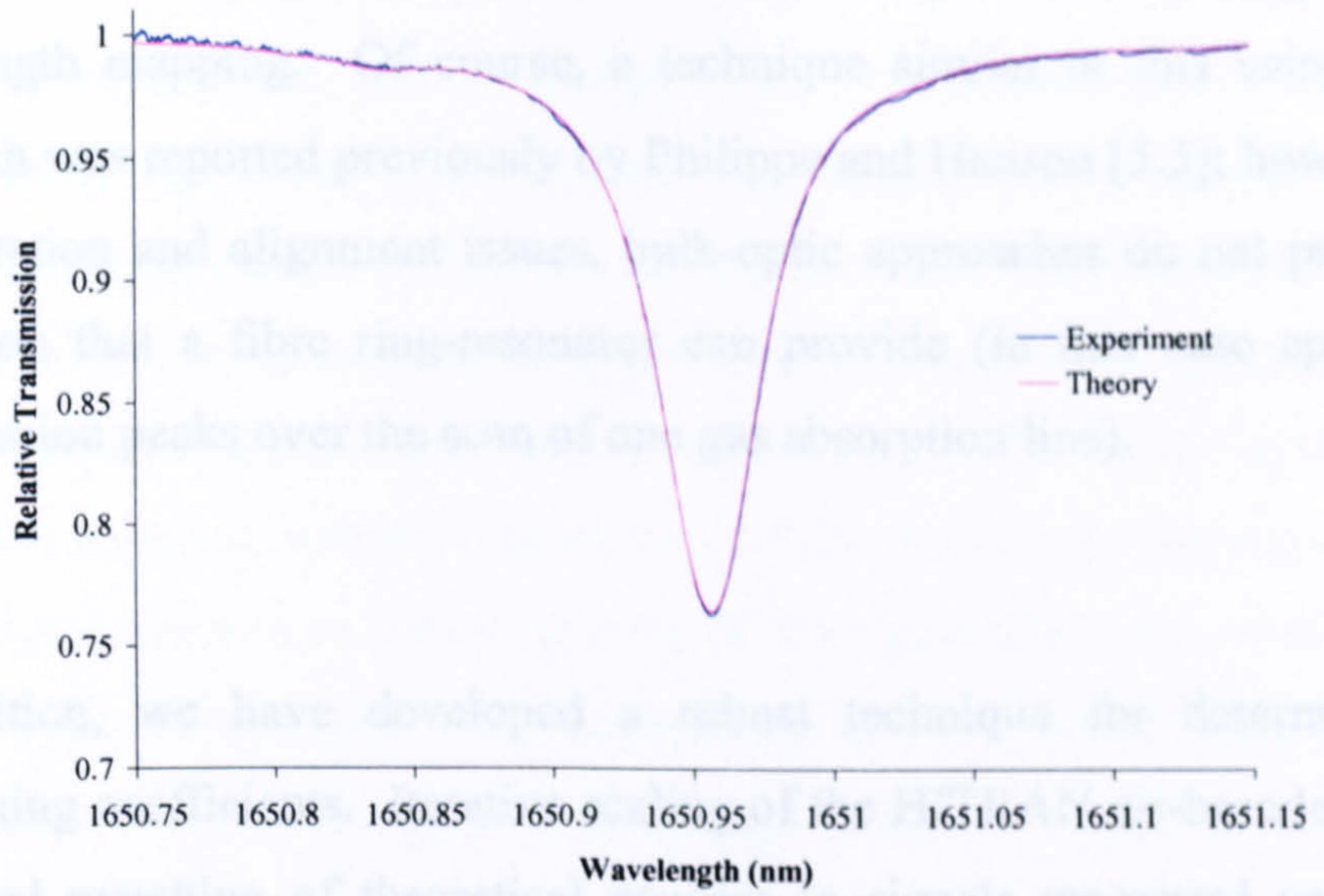

Figure 5.17: 10.13 % CH_4:N_2 balance at 20.3 °C and 1.101 bar pressure - experiment compared to theoretical prediction - air-broadening scaled by 0.87

As can be seen, the excellent agreement between experiment and theory shows that curve fitting theoretical transmission profiles to experimental signals provides an accurate method of extracting the gas concentration and pressure.

5.2.5 Conclusions

From the above analysis and discussion it can be concluded that the fibre ring-resonator and the wavelength referencing technique, described in section 4.2.4 of chapter 4, provide an accurate and reliable wavelength scale to experimental time-based measurements. The problems associated with the non-linearity in the current vs. wavelength curve are addressed as proven by figure 5.4, showing matching at both absorption feature wavelengths (1650.83 nm and 1650.956 nm). Laser wavelength drift and the non-repeatability of the current vs. wavelength curve are also addressed by taking continuous, *in-situ* measurements of the wavelength for each scan. Mathematical approximations to the current vs. wavelength curve could be made but determining the absolute location of the gas absorption line centre

wavelength on the curve would be difficult, and only a small error in determining the location on a highly non-linear curve would give rise to large errors in the wavelength mapping. Of course, a technique similar to this using a bulk-optics approach was reported previously by Philippe and Hanson [5.5]; however, as well as the vibration and alignment issues, bulk-optic approaches do not provide the same resolution that a fibre ring-resonator can provide (in this case approximately 80 transmission peaks over the scan of one gas absorption line).

In addition, we have developed a robust technique for determining host gas broadening coefficients. Iterative scaling of the HITRAN air-broadening coefficient permitted matching of theoretical profiles to signals recovered using TDLS with direct detection. Multiplying the HITRAN air-broadening coefficient by 0.87 provided accurate linewidth and linestrength scaling for N_2 broadening of CH_4, giving close agreement between experiment and theory over an extended pressure range (shown in figures 5.8 to 5.17). This also further proved the validity of the wavelength referencing technique.

Finally, this excellent agreement between experiment and theory, illustrated in the figures above, also provides satisfactory evidence that curve fitting provides accurate means of extracting gas concentration and pressure.

5.3 Conventional TDLS with WMS Detection

5.3.1 Introduction

TDLS with wavelength modulation spectroscopy enables AC detection at relatively high frequencies where laser and 1/f noise is reduced; this, coupled with lock-in

detection, provides one to two orders of magnitude improvement on direct detection. Increased sensitivity is usually required when measuring low absorption linestrengths; however, WMS techniques may be required in many modern industrial applications, regardless of absorption linestrength, where optical access and low received powers can be a problem. In addition, the WMS approach eliminates the high infra-red background noise signals experienced by DC detection schemes in high temperature applications. However, the penalty for using conventional TDLS / WMS techniques in industrial processes, where pressure is varying and unknown, is a significant increase in the complexity of the signal analysis. As was mentioned in chapter 2, the critical issue is the dependence of the 1st and 2nd harmonic / derivative signal amplitudes on the systematic scaling factor $\delta\nu$ / γ and errors in determining these parameters accumulate to determine the overall error on the extracted concentration and / or pressure. As the dependence of derivative signal amplitude on the scaling factor and hence the scope for error in determining the scaling factor increases with order of derivative, it was decided that we focus on detection at the 1st harmonic. Likewise, it is much simpler to recover the fundamental absorption line transmission function from the 1st harmonic than it is from higher order signals.

5.3.2 Signal Analysis: Identification of Problems

The signals shown in this section (5.3) were measured using the experimental system and methodologies described in section 4.3 of chapter 4 and figures 5.18 to 5.21 show the experimentally measured and normalised 1st harmonic signals, taken using a low sinusoidal modulation index and a high modulation index. As mentioned in chapter 4, the low modulation index was determined by the linewidth of the fibre resonator transmission peaks. If we assume the HWHM linewidth of a gas absorption line at 1 atm pressure is approximately 3 GHz and the FWHM linewidth ($2*\gamma$) of a resonator transmission peak is 0.08 GHz[II], the low modulation index was

[II] The FSR of the resonator is ~ 0.4 GHz and the Finesse of the resonator is ~ 5; therefore, FWHM ~ 0.08 GHz

set to recover the maximum 1st harmonic signal (i.e. when $\delta\nu = 2*\gamma$) of the resonator and is consequently m ~ 0.03 (0.08 GHz / 3 GHz). The high modulation index was set at m ~ 2.0 (or $\delta\nu/\gamma \sim 2$) for the 1650 nm methane absorption line at 1 atm pressure, again, as reported in chapter 4. The lock-in amplifier settings for this particular experiment, including the reference phase to align with the RAM signal, are noted in table 5.2. The time constant for the resonator 1st harmonic measurement was 100 μS.

	Low Modulation Index	High Modulation Index
AC Gain	20 dB, Dynamic Range:15	14 dB, Dynamic Range:13
Sensitivity	20 mV	50 mV
Time Constant	1 ms	1 ms
Reference Harmonic	1st	1st
Reference Phase	+ 11.700 °	+ 11.700 °

Table 5.2: Settings for Perkin Elmer DSP lock-in amplifier

For the signals taken using the low modulation index, shown in figure 5.18, the signal recovered when the gas cell was empty (b) is subtracted from the gas signal (a) in order to remove any small residual background. This signal (a – b) is then normalised to the increasing power (c) as the laser centre frequency is swept across the gas line. Finally, in order to account for changes in signal power and system losses, the signal is normalised to the average value of (or a single point on) the RAM induced DC signal (d).

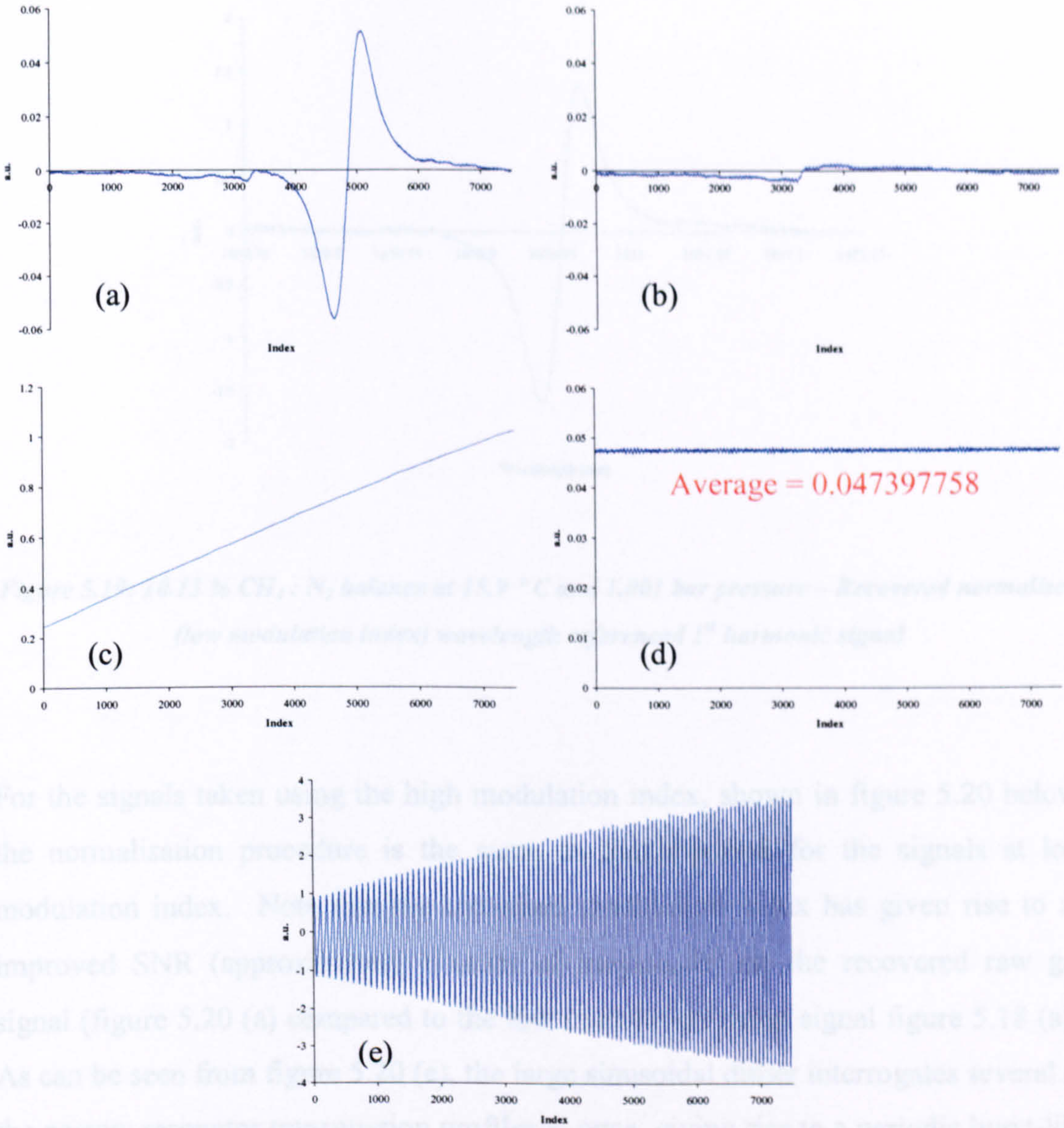

Figure 5.18: 10.13 % CH_4 : N_2 balance at 15.9 °C and 1.001 bar pressure – Experimentally measured signals using low modulation index: trimmed (a) gas signal, (b) no gas signal, (c) power reference signal, (d) DC RAM signal, (e) 1st harmonic resonator response

The normalised 1st harmonic signal is then wavelength referenced using the 1st harmonic resonator response (e) in the MATLAB program described in section 4.3.4 of chapter 4. The resulting wavelength referenced plot is shown in figure 5.19.

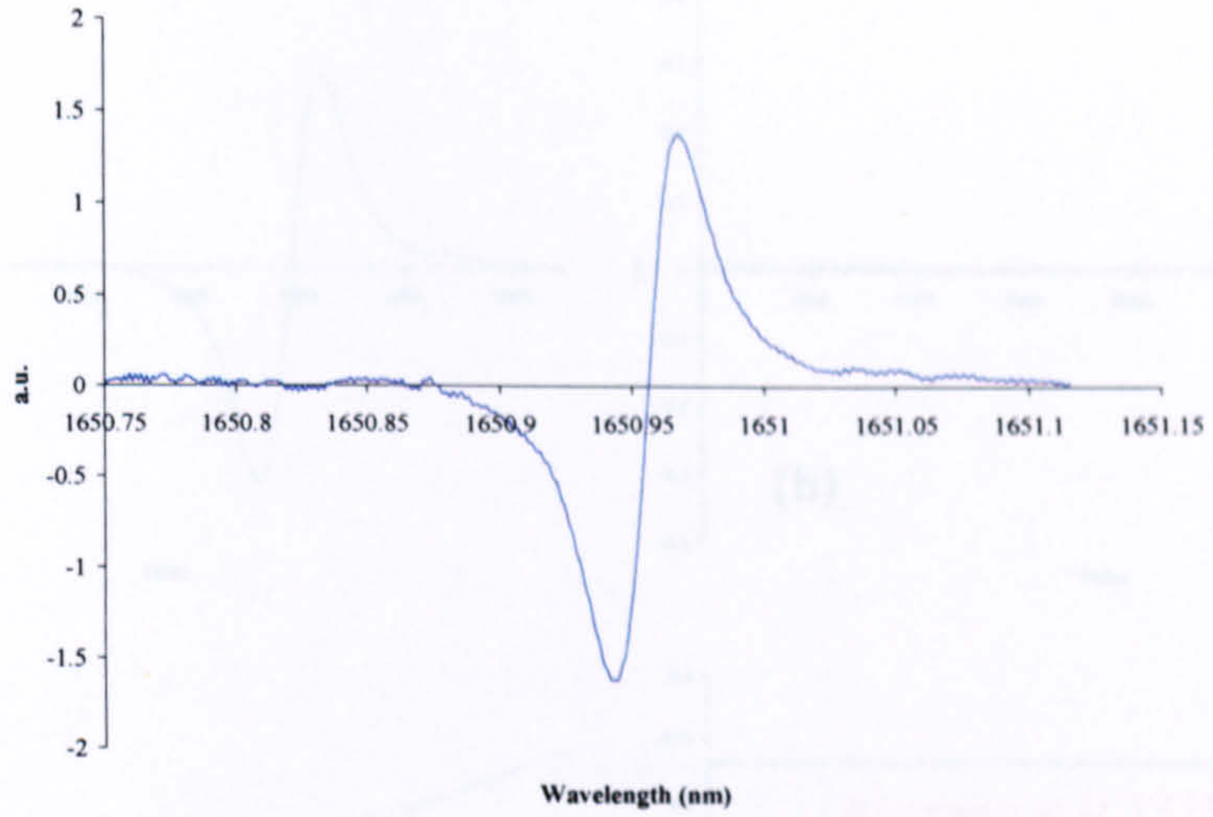

Figure 5.19: 10.13 % CH_4 : N_2 balance at 15.9 °C and 1.001 bar pressure – Recovered normalised (low modulation index) wavelength referenced 1st harmonic signal

For the signals taken using the high modulation index, shown in figure 5.20 below, the normalisation procedure is the same as that reported for the signals at low modulation index. Note that the increased modulation index has given rise to an improved SNR (approximately 1 order of magnitude) on the recovered raw gas signal (figure 5.20 (a) compared to the low modulation index signal figure 5.18 (a)). As can be seen from figure 5.20 (e), the large sinusoidal dither interrogates several of the narrow resonator transmission profiles at once, giving rise to a periodic burst-like signal. It is, in principle, possible to relate this signal mathematically to the original direct resonator transmission profile and thus extract the frequency / wavelength mapping intervals between the peaks; however, as both the high modulation index and low modulation index signals were measured in quick succession of each other, it is valid to use the signal in figure 5.18 (e) to wavelength reference the high modulation index signal.

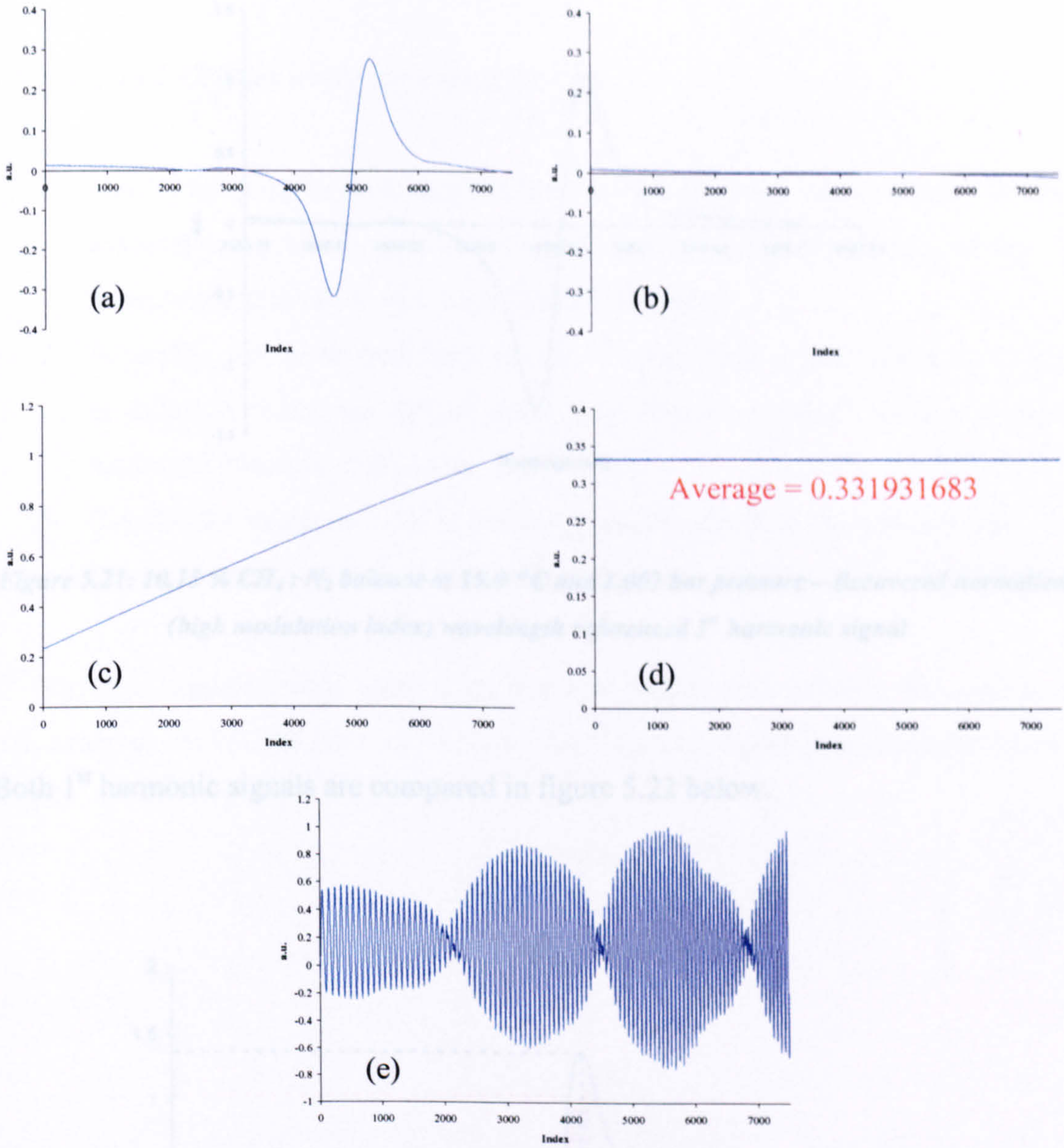

Figure 5.20: 10.13 % CH_4 : N_2 balance at 15.9 °C and 1.001 bar pressure – Experimentally measured signals using high modulation index: trimmed (a) gas signal, (b) no gas signal, (c) power reference signal, (d) DC RAM signal (e) 1st harmonic resonator response

The resulting wavelength referenced plot is shown in figure 5.21 below.

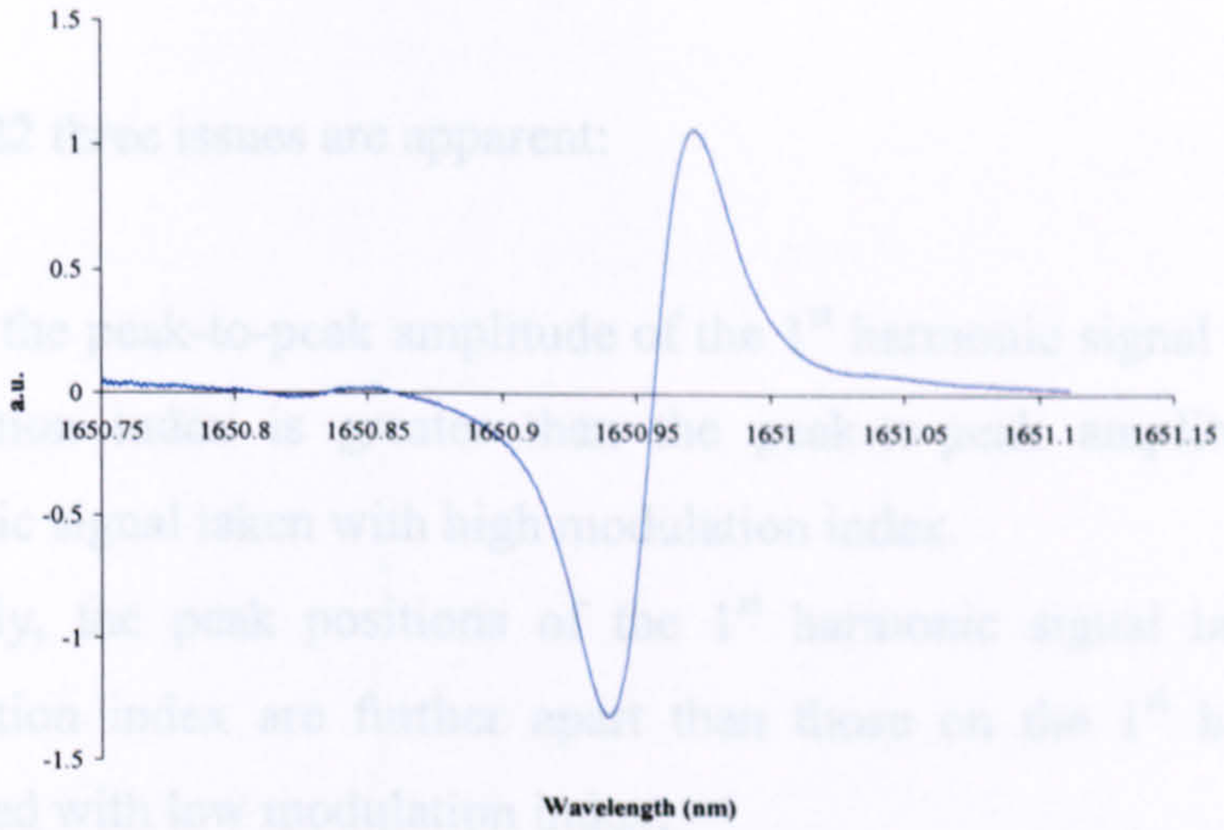

Figure 5.21: 10.13 % CH_4 : N_2 balance at 15.9 °C and 1.001 bar pressure – Recovered normalised (high modulation index) wavelength referenced 1st harmonic signal

Both 1st harmonic signals are compared in figure 5.22 below.

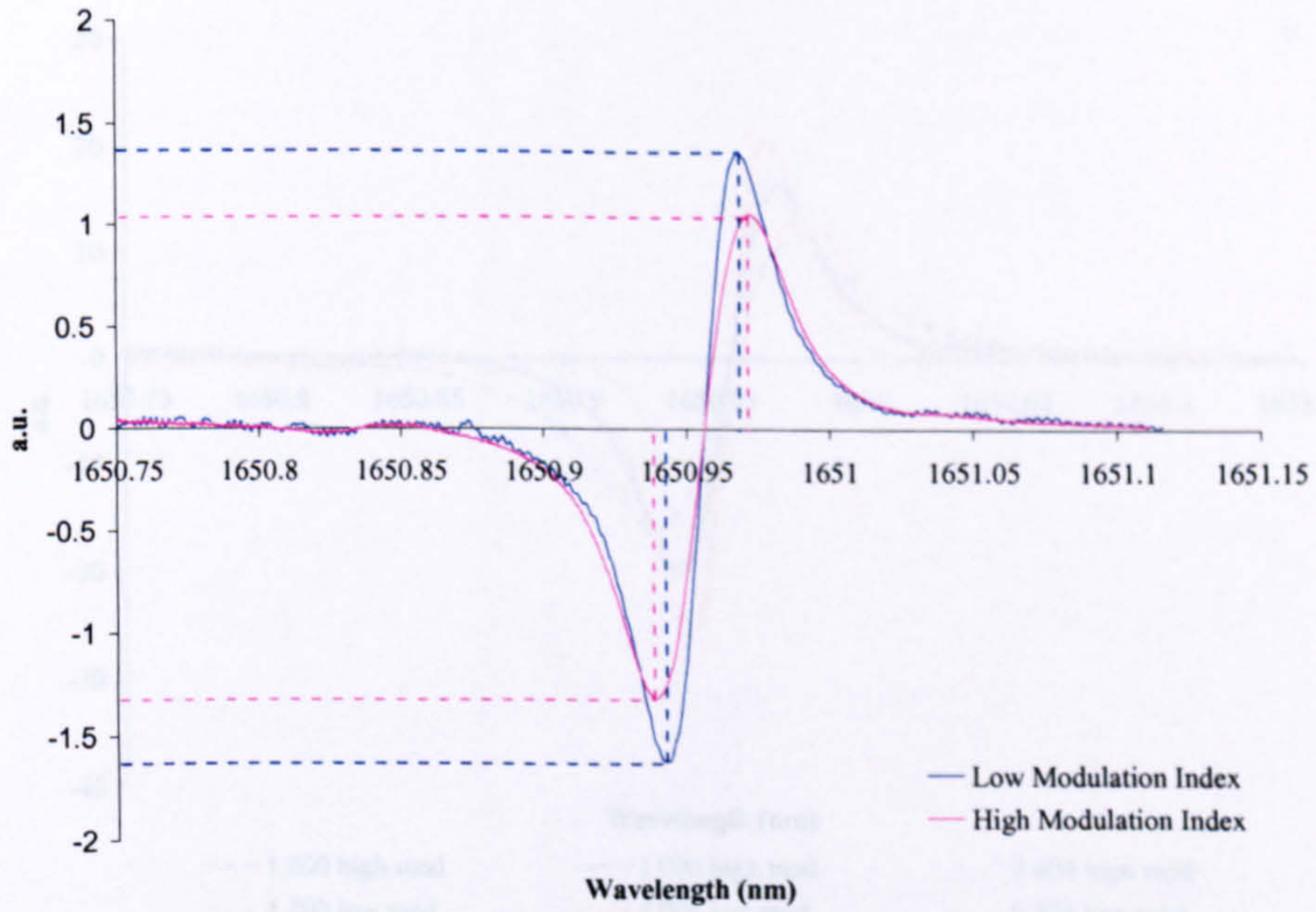

Figure 5.22: 10.13 % CH_4 : N_2 balance at 15.9 °C and 1.001 bar pressure – Comparison between 1st harmonic signals taken with low and high modulation index

From figure 5.22 three issues are apparent:

1. Firstly, the peak-to-peak amplitude of the 1st harmonic signal taken with low modulation index is greater than the peak-to-peak amplitude of the 1st harmonic signal taken with high modulation index.
2. Secondly, the peak positions of the 1st harmonic signal taken with high modulation index are further apart than those on the 1st harmonic signal measured with low modulation index.
3. Finally, the negative peak is greater in amplitude than the positive peak and the asymmetry is present for both the low and high modulation index signals.

1st harmonic signals, taken using high and low modulation indexes, for a range of pressures are shown in figure 5.23 below. An expanded figure is also shown over the page.

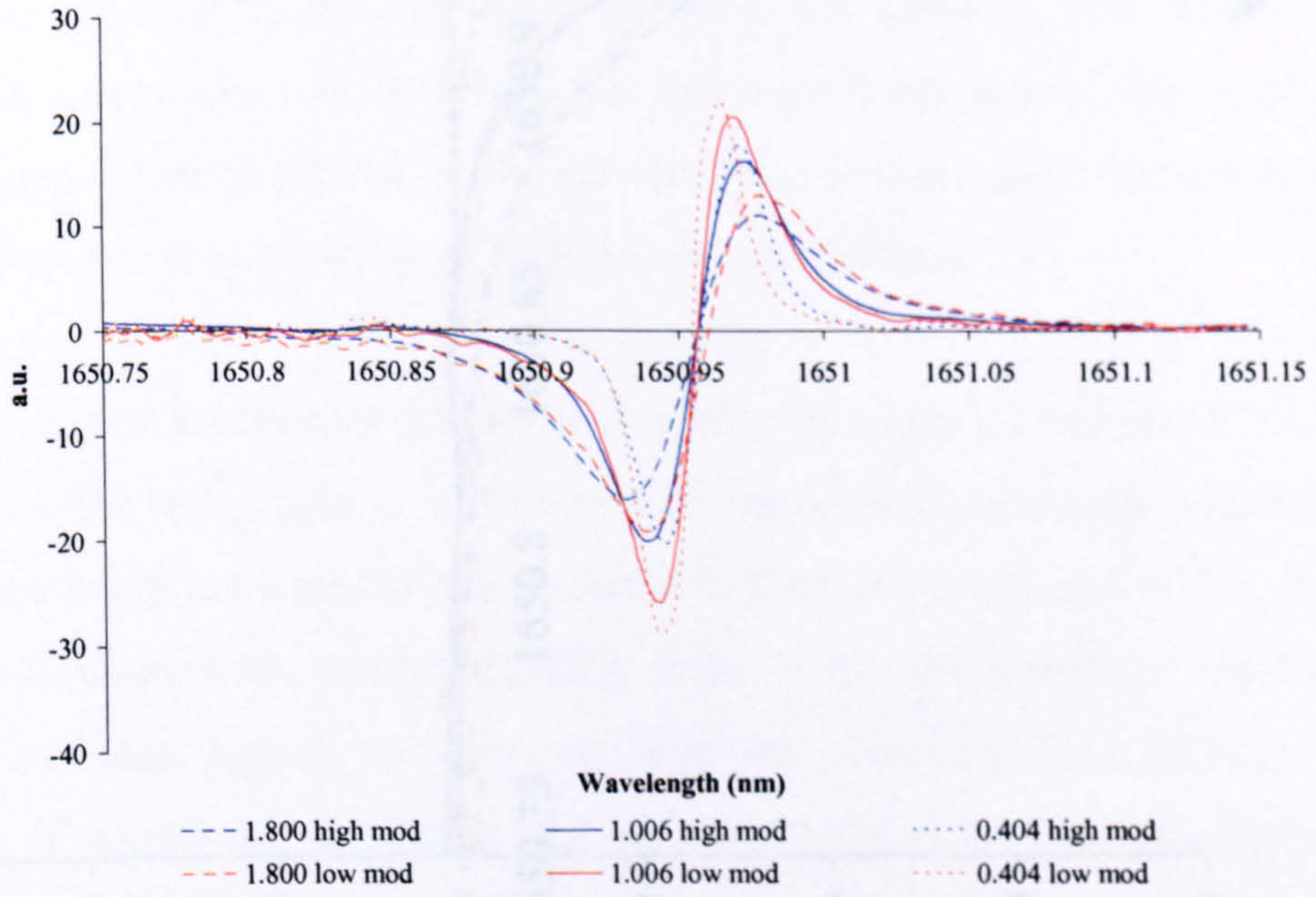

Figure 5.23: 10.13 % CH_4 : N_2 balance at 20.3 °C over pressure range 0.404 bar to 1.800 bar – Comparison between 1st harmonic signals taken with low and high modulation index

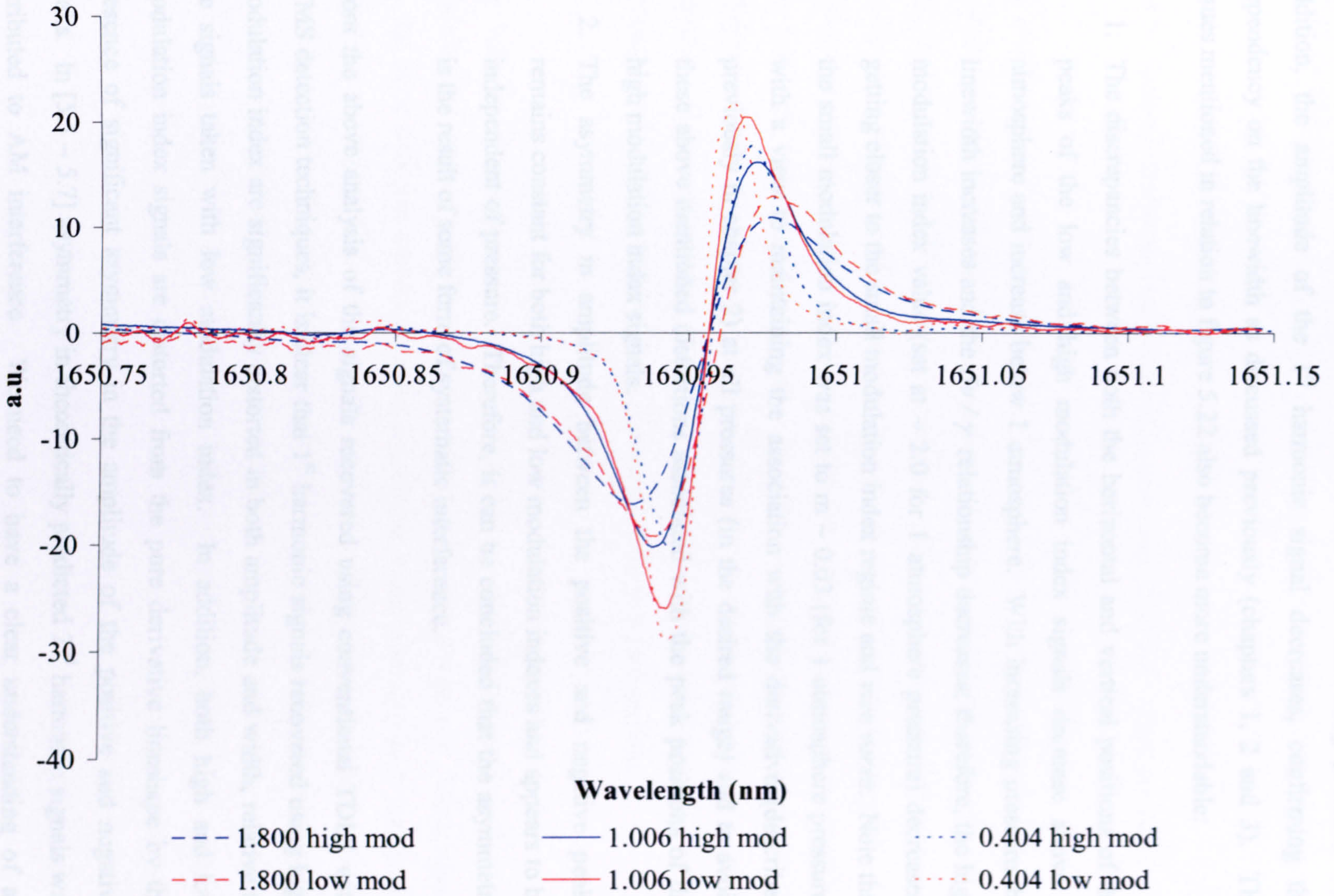
30
20
10
0
-10
-20
-30
-40
a.u.
1650.75
1650.8
1650.85
1650.9
1650.95
1651
1651.05
1651.1
1651.15
Wavelength (nm)
1.800 high mod
1.800 low mod
1.006 high mod
1.006 low mod
0.404 high mod
0.404 low mod

From figure 5.23 it can be seen that the horizontal positions of the peaks move further apart indicating the increase in linewidth with increasing pressure. In addition, the amplitude of the 1st harmonic signal decreases, confirming the dependency on the linewidth as discussed previously (chapters 1, 2 and 3). The issues mentioned in relation to figure 5.22 also become more understandable:

1. The discrepancies between both the horizontal and vertical positions of the peaks of the low and high modulation index signals decrease above 1 atmosphere and increase below 1 atmosphere. With increasing pressure the linewidth increases and the $\delta\nu / \gamma$ relationship decreases; therefore, the high modulation index value (set at ~ 2.0 for 1 atmosphere pressure) decreases, getting closer to the small modulation index regime and *vice versa*. Note that the small modulation index was set to m ~ 0.03 (for 1 atmosphere pressure) with a view to maintaining the association with the derivative (described previously in chapter 2) at all pressures (in the desired range) and to avoid these above mentioned distortions associated with the peak positions of the high modulation index signals.
2. The asymmetry in amplitude between the positive and negative peaks remains constant for both high and low modulation indexes and appears to be independent of pressure. Therefore, it can be concluded that the asymmetry is the result of some form of systematic interference.

From the above analysis of the signals recovered using conventional TDLS with WMS detection techniques, it is clear that 1st harmonic signals recovered using high modulation index are significantly distorted in both amplitude and width, relative to the signals taken with low modulation index. In addition, both high and low modulation index signals are distorted from the pure derivative lineshape by the presence of significant asymmetry in the amplitude of the positive and negative peaks. In [5.5 – 5.7] asymmetry in theoretically predicted 2nd harmonic signals was attributed to AM interference. We need to have a clear understanding of all contributions to the total signal and of the sources of distortion and errors in the analytical process. Section 5.3.3 discusses a revised analytical treatment of the

signals in conventional TDLS with WMS, which provides this. Here we have experimentally demonstrated some of the difficulties with conventional TDLS / WMS detection.

5.3.3 Revised Analytical Treatment of Conventional TDLS with WMS detection

As mentioned previously, the theoretical models in [5.5 – 5.7] use complex Fourier analysis to account for the distortion effects of large modulation index and RAM interference on 1st and 2nd harmonic lineshapes. Here a simpler analysis based on a Taylor series expansion of a Lorentzian broadened absorption line is reported. The theory assumes only a small modulation index ($m << 1$) with a view to maintaining the harmonic / derivative relationship in order to eventually extract linewidth information from measured derivatives. As will be shown, this simple analysis provides a clear understanding of all the contributions to the total signal, including the sources of distortion and the errors illustrated in the previous section.

As well as frequency modulation and scan, the applied sinusoid and ramp modulations produce a double modulation on the laser output power. Modulations on the laser injection current in a semiconductor laser modulate both the carrier density, resulting in AM, and the refractive index in the semiconductor material, resulting in FM. The degree of coupling of both modulations depends on the structure, the operating point of the laser and the frequency of the applied signal [5.8]. The intensity (I) of the laser source at a particular frequency (ν_1) is therefore given by:

$$I = I(\nu_1) + \Delta I(\nu_1)\cos(\omega t) \tag{5.1}$$

where ΔI is the amplitude of the small intensity modulation varying at the modulation frequency, ω. Recalling equation (3.13) from chapter 3 and substituting equation (5.1) for I, the output intensity from an absorbing medium is now given by:

$$I_{out} \approx [I(\nu_1) + \Delta I(\nu_1)cos(\omega t)](1 - \alpha(\nu)Cl) \tag{5.2}$$

A scan of the pressure broadened Lorentzian lineshape $\alpha(\nu)$ (showing both frequency and intensity modulation), is illustrated in figure 5.24 and all the signals generated and the significant features associated with them may be found from a Taylor series expansion of the lineshape around ν_1, as follows:

$$\alpha(\nu) = \alpha(\nu_1) + \frac{d\alpha(\nu_1)}{d\nu}.[\nu - \nu_1] + \frac{1}{2}.\frac{d^2\alpha(\nu_1)}{d\nu^2}.[\nu - \nu_1]^2 + \ldots \tag{5.3}$$

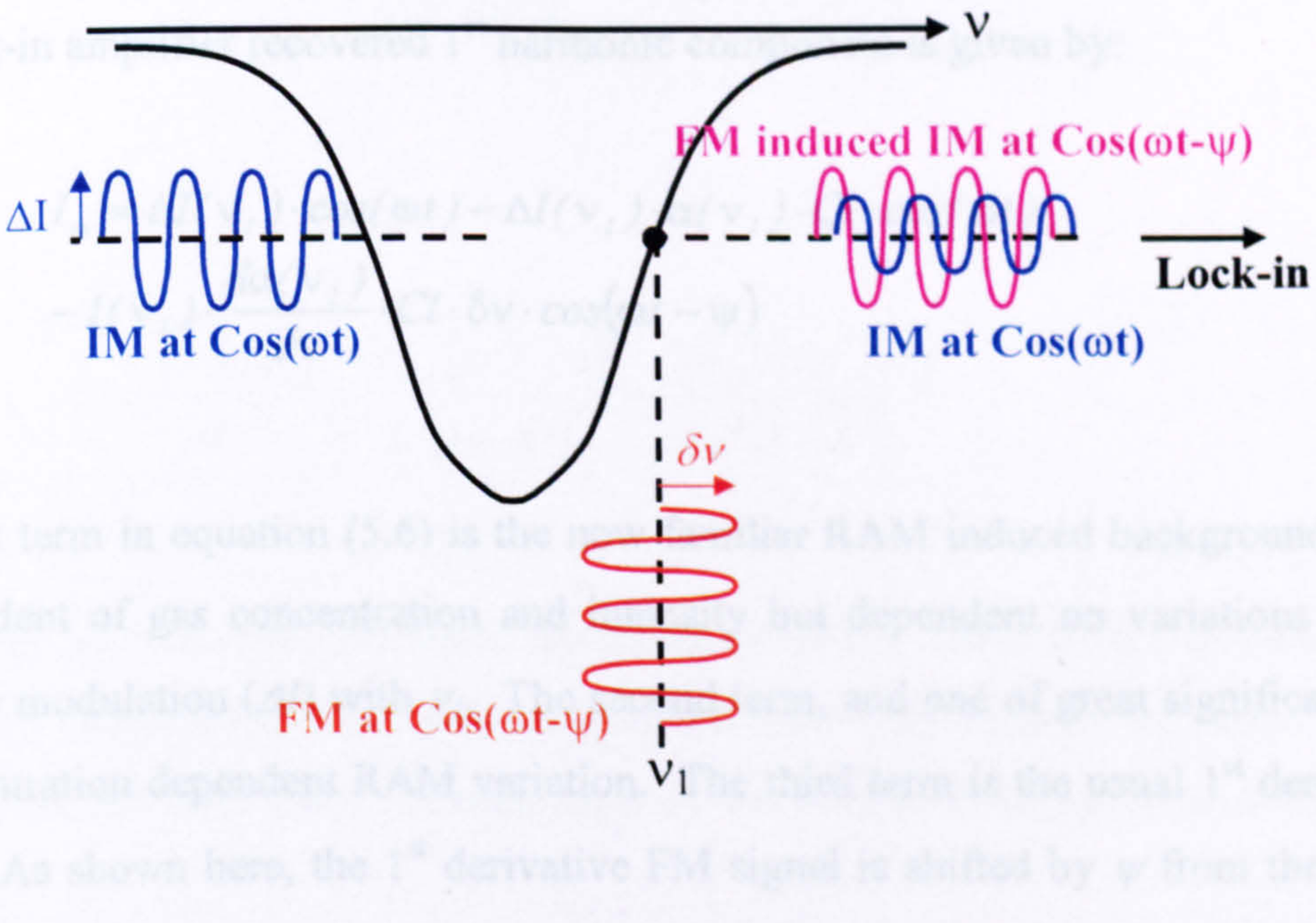

Figure 5.24: Frequency and intensity scan of pressure broadened absorption line

Substituting equation (5.3) into equation (5.2) and considering only a second order approximation, the output intensity now becomes:

$$I_{out} \approx [I(\nu_1)+\Delta I(\nu_1)cos(\omega t)]\times \left(1-\alpha(\nu_1)Cl-\frac{d\alpha(\nu_1)}{d\nu}.Cl.\delta\nu.cos(\omega t-\psi)-\frac{d^2\alpha(\nu_1)}{2d\nu^2}.Cl.\delta\nu^2.cos^2(\omega t-\psi)\right) \quad (5.4)$$

where $\delta\nu.cos(\omega t - \psi) = [\nu - \nu_1]$, $\delta\nu$ is the amplitude of the sinusoidal frequency modulation, as shown in figure 5.24 above, and ψ is the phase shift between the intensity and the frequency modulation. Multiplying out the bracketed terms in equation (5.4) gives rise to a number of direct and mixed components (full multiplication of the bracketed terms and all of the subsequent components are shown in Appendix D). The first key component is the DC term, given by:

$$I_{DC} = I(\nu_1)\cdot\{1-\alpha(\nu_1)Cl\} \quad (5.5)$$

The lock-in amplifier recovered 1st harmonic component is given by:

$$I_{\omega} = \Delta I(\nu_1)\cdot cos(\omega t)-\Delta I(\nu_1)\cdot\alpha(\nu_1)\cdot Cl\cdot cos(\omega t) - I(\nu_1)\cdot\frac{d\alpha(\nu_1)}{d\nu}\cdot Cl\cdot\delta\nu\cdot cos(\omega t-\psi) \quad (5.6)$$

The first term in equation (5.6) is the now familiar RAM induced background term, independent of gas concentration and intensity but dependent on variations in the intensity modulation (ΔI) with ν_1. The second term, and one of great significance, is a concentration dependent RAM variation. The third term is the usual 1st derivative signal. As shown here, the 1st derivative FM signal is shifted by ψ from the RAM variation. It is important to note here that even with small modulation amplitude, $\delta\nu$, the recovered 1st harmonic signal is not a true 1st derivative but is distorted by the presence of the RAM variation; this agrees well with the results and hypothesis reported in section 5.3.2.

The lock-in recovered 2nd harmonic component is given by:

$$I_{2\omega} = -\frac{1}{2}\cdot\Delta I(\nu_1)\cdot\frac{d\alpha(\nu_1)}{d\nu}\cdot Cl\cdot\delta\nu\cdot\cos(2\omega t-\psi) \qquad (5.7)$$
$$-\frac{1}{4}\cdot I(\nu_1)\cdot\frac{d^2\alpha(\nu_1)}{d\nu^2}\cdot Cl\cdot\delta\nu^2\cdot\cos 2(\omega t-\psi)$$

The first term in equation (5.7) shows a signal proportional to the 1st derivative arising from the RAM and the second term shows the usual 2nd derivative signal. Again, the derivative is separated from the RAM variation by ψ and the recovered 2nd harmonic is not a true second derivative of the lineshape, even with small $\delta\nu$. The treatment of the 1st and 2nd derivatives of the gas absorption lineshape remains the same as in chapter 3:

$$\frac{d\alpha(\nu_1)}{d\nu} = -\frac{2\alpha_0\Delta}{\gamma\left(1+\Delta^2\right)^2} = -\frac{2N_0S\Delta}{\pi\gamma^2\left(1+\Delta^2\right)^2} \qquad (5.8)$$

and

$$\frac{d^2\alpha(\nu_1)}{d\nu^2} = \frac{2\alpha_0\left(3\Delta^2-1\right)}{\gamma^2\left(1+\Delta^2\right)^3} = \frac{2N_0S\left(3\Delta^2-1\right)}{\pi\gamma^3\left(1+\Delta^2\right)^3} \qquad (5.9)$$

Therefore, the theoretical principles for extraction of the concentration and linewidth / pressure information from derivative lineshapes also remain the same. The components left over from multiplication of the bracketed terms in equation (5.4) are:

$$I_{negligible} = -\frac{1}{2}\Delta I(\nu_1).\frac{d\alpha(\nu_1)}{d\nu}.Cl.\delta\nu.(cos(\psi)) \qquad (5.10)$$
$$-\frac{1}{4}I(\nu_1).\frac{d^2\alpha(\nu_1)}{d\nu^2}.Cl.\delta\nu^2$$
$$-\frac{1}{4}\Delta I(\nu_1).\frac{d^2\alpha(\nu_1)}{d\nu^2}.Cl.\delta\nu^2.\left[cos(\omega t)+\frac{1}{2}\{cos(3\omega t-2\psi)+cos(2\psi-\omega t)\}\right]$$

Through cross product terms in the demodulation process, the RAM signal gives rise to distortion at higher and lower harmonic frequencies (3rd and 1st harmonic interference shown in bottom line of equation (5.10)). Since a lock-in amplifier only measures a particular harmonic, the 3rd harmonic interference shown here does not interfere with the lock-in recovered 1st and 2nd harmonic signals. Lower harmonic contributions (1st harmonic interference proportional to the 2nd derivative, shown in the bottom line of equation (5.10)) can be ignored for small modulation index (small $\delta\nu$). For high modulation index (large $\delta\nu$), the terms have a greater influence and this explains the discrepancies between high and low modulation index signals in figures 5.22 and 5.23.

5.3.4 Conclusions

Equations (5.6) to (5.9) give a theoretical description of the expected 1st and 2nd harmonic signals under conditions of varying detection phase and concentrations. It is clear from the above analysis that the n^{th} derivative signal associated with the n^{th} harmonic is significantly distorted by contributions from the RAM signal to an extent determined by the AM amplitude, ΔI, the relative phase of the laser AM and FM, ψ, and the detection phase set on the lock-in amplifier. The practical implications of this analysis are:

1. Under conventional TDLS / WMS detection conditions, a convenient method to approximately maximise the signal output, is to set the detection phase of the lock-in amplifier to align the large RAM component along the X axis (described in chapter 4). When gas is added to the measurement cell, the FM

induced AM component is separated from the RAM by some phase ψ, as illustrated in the phasor plot in figure 5.25. When set to the 1st harmonic, the lock-in amplifier then recovers the 1st harmonic component of the RAM signal (both the concentration dependent and independent contributions) and a FM induced AM contribution dictated by projection onto the measurement (X) axis. The RAM contribution independent of the gas concentration appears as the large background signal shown in figures 5.18 (d) and 5.20 (d) and is removed as described in chapter 4. The RAM contribution dependent on the gas concentration is reflected in the asymmetry shown in figures 5.22 and 5.23 and is not removed by the filtering / subtraction process.

2. The fact that the FM signal and hence the FM induced AM signal both lag the RAM signal by ψ means that the RAM contribution to the recovered FM 1st harmonic signal can be nulled, by appropriate selection of the lock-in amplifier detection phase. That is to say that we can set the phase to measure the FM component along the Y axis, at quadrature to the RAM signal. The principles and application of this technique are discussed in the following section.

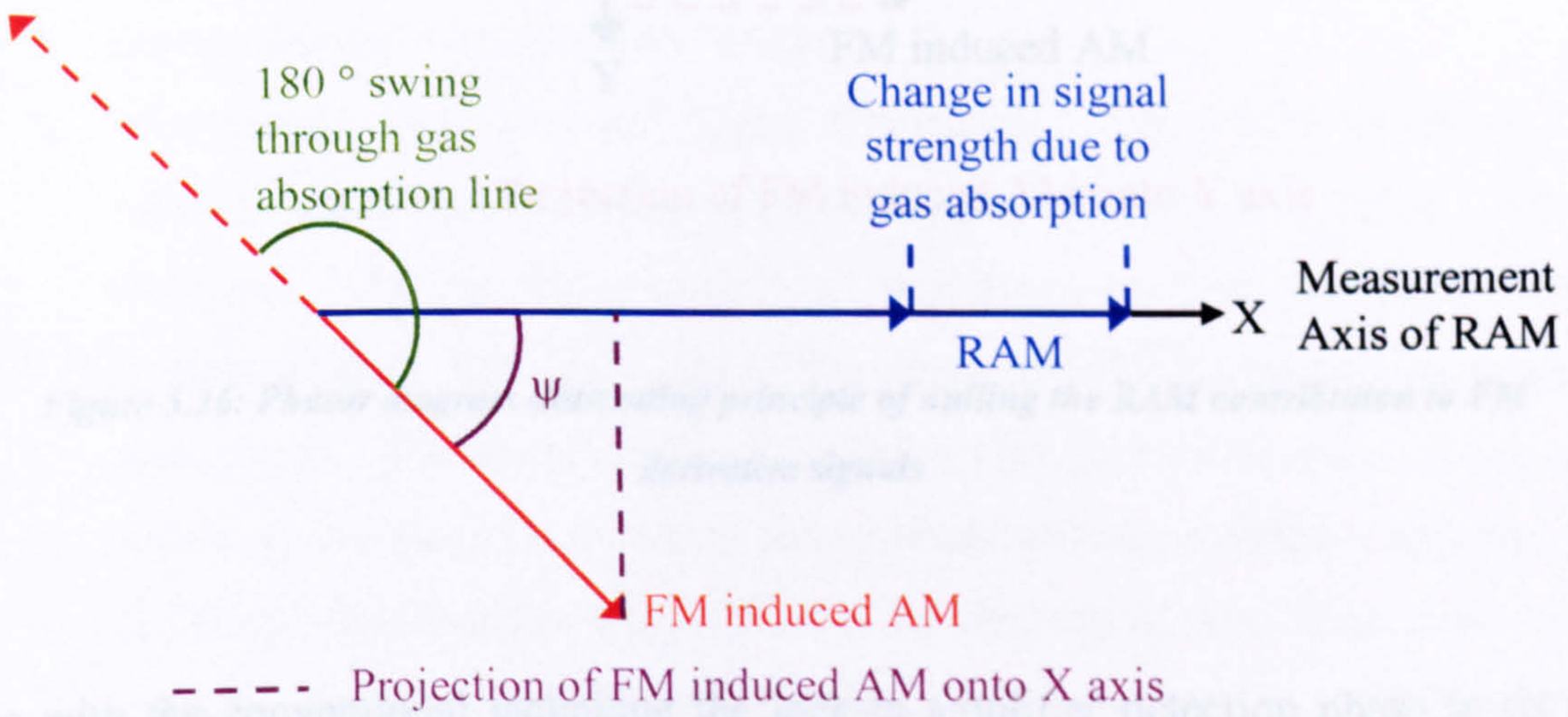

Figure 5.25: Phasor diagram illustrating AM – FM phase relationships in conventional TDLS / WMS

5.4 Novel Approach to Removing Systematic RAM Interference

5.4.1 Theoretical Principle

As mentioned above, an alternative approach to the conventional TDLS / WMS technique is to set the lock-in amplifier detection phase to null the RAM contribution and the principle is illustrated below in the phasor diagram in figure 5.26.

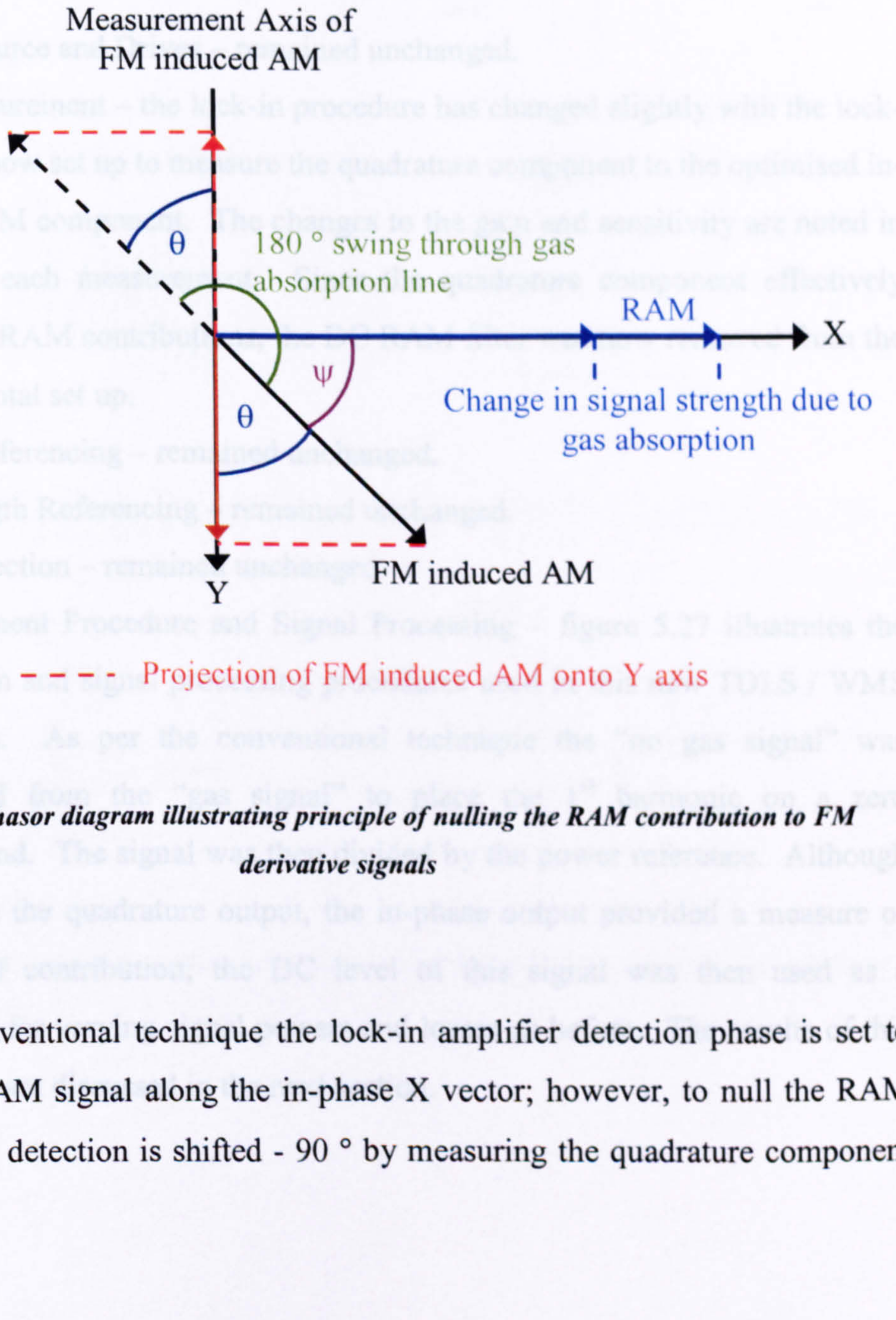

Figure 5.26: Phasor diagram illustrating principle of nulling the RAM contribution to FM derivative signals

As with the conventional technique the lock-in amplifier detection phase is set to maximise the RAM signal along the in-phase X vector; however, to null the RAM contribution, the detection is shifted - 90 ° by measuring the quadrature component

on the Y vector output. As can be seen from figure 5.26, the Y component of the FM induced AM signal is reduced by cos*(θ)* or sin*(ψ)*, where *θ* is the compliment angle (90 - *ψ*) °. Implementation of this principle is described in the following section.

5.4.2 Revised Experimental System and Procedure

The changes that were made to the original experimental system and procedure, described in chapter 4, are noted below:

1. Signal Source and Drives – remained unchanged.
2. Gas Measurement – the lock-in procedure has changed slightly with the lock-in phase now set up to measure the quadrature component to the optimised in-phase RAM component. The changes to the gain and sensitivity are noted in tables at each measurement. Since the quadrature component effectively nulls any RAM contributions, the DC RAM filter was now removed from the experimental set up.
3. Power Referencing – remained unchanged.
4. Wavelength Referencing – remained unchanged.
5. Data collection – remained unchanged.
6. Measurement Procedure and Signal Processing – figure 5.27 illustrates the calibration and signal processing procedures used in this new TDLS / WMS technique. As per the conventional technique the "no gas signal" was subtracted from the "gas signal" to place the 1st harmonic on a zero background. The signal was then divided by the power reference. Although nulled on the quadrature output, the in-phase output provided a measure of the RAM contribution; the DC level of this signal was then used as a reference for varying signal powers and losses as before. The results of this approach are discussed in the next section.

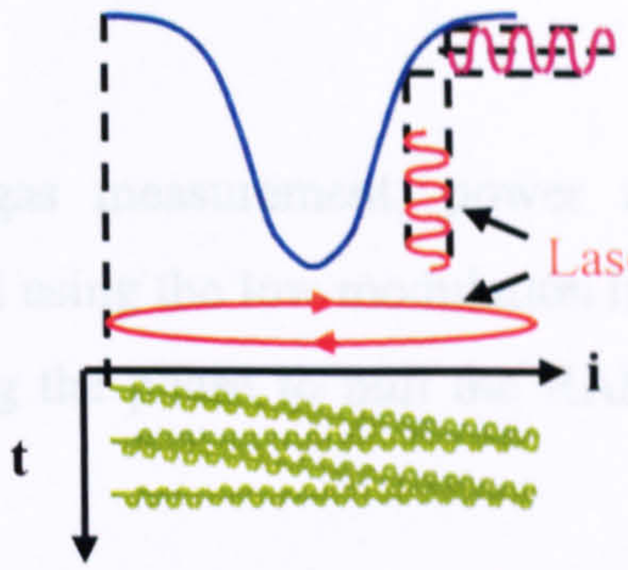

$$Norm_1 = \frac{(\text{Gas Signal} - \text{No Gas Signal})}{\text{Power Reference}}$$

$$Norm_2 = \frac{Norm_1}{a}$$

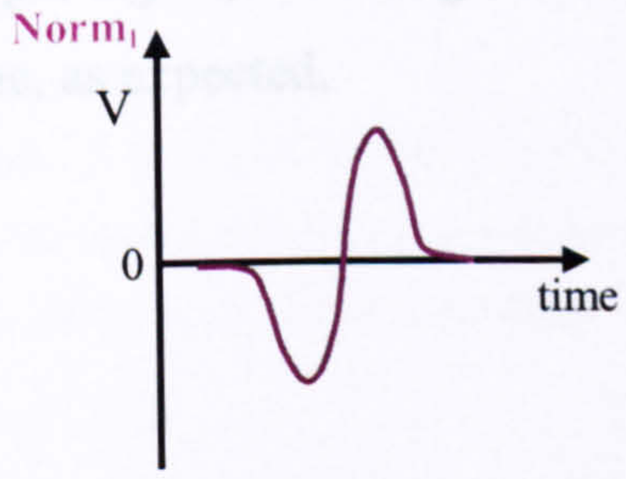

Figure 5.27: Normalisation procedure for signals in new TDLS / WMS measurement technique

5.4.3 Results and Discussion

Figure 5.28, shows the gas measurement, power referencing and wavelength referencing signals acquired using the low modulation index (m ~ 0.03). The lock-in amplifier settings, including the phase to null the RAM signal, are shown in table 5.3.

	Low Modulation Index	High Modulation Index
AC Gain	20 dB, Dynamic Range:15	14 dB, Dynamic Range:13
Sensitivity	20 mV	50 mV
Time Constant	1 ms	1 ms
Reference Harmonic	1st	1st
Phase to Maximise RAM	+ 11.700 °	+ 11.700 °
Phase to Null RAM	- 78.300 °	- 78.300 °

Table 5.3: Settings for Perkin Elmer DSP lock-in amplifier

The point to note from analysis of the signals shown in figure 5.28 is the asymmetry in the gas signal, reflecting the increase in signal power as the laser is swept over the gas line, as expected.

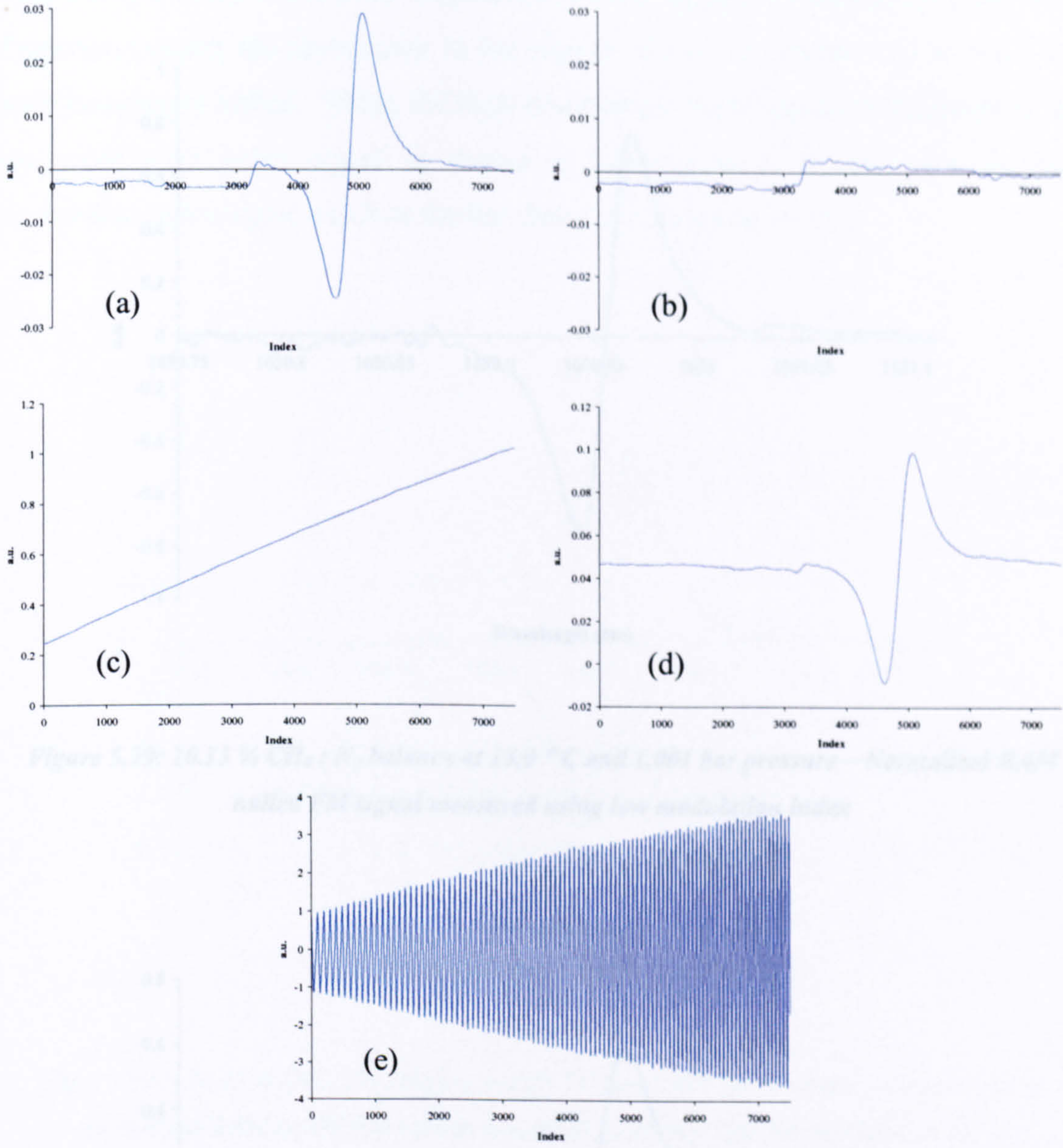

Figure 5.28: 10.13 % CH_4 : N_2 balance at 15.9 °C and 1.001 bar pressure – Experimentally measured signals using low modulation index: trimmed (a) gas signal, (b) no gas signal, (c) power reference signal, (d) Combined AM – FM signal, (e) 1st harmonic resonator response

When the gas signal is normalised, as discussed above, and used in conjunction with the resonator signal in the wavelength referencing MATLAB program, described in chapter 4, the wavelength referenced plot shown in figure 5.29 below is returned. Using the same process, the normalised and wavelength referenced high modulation index signal is shown below in figure 5.30.

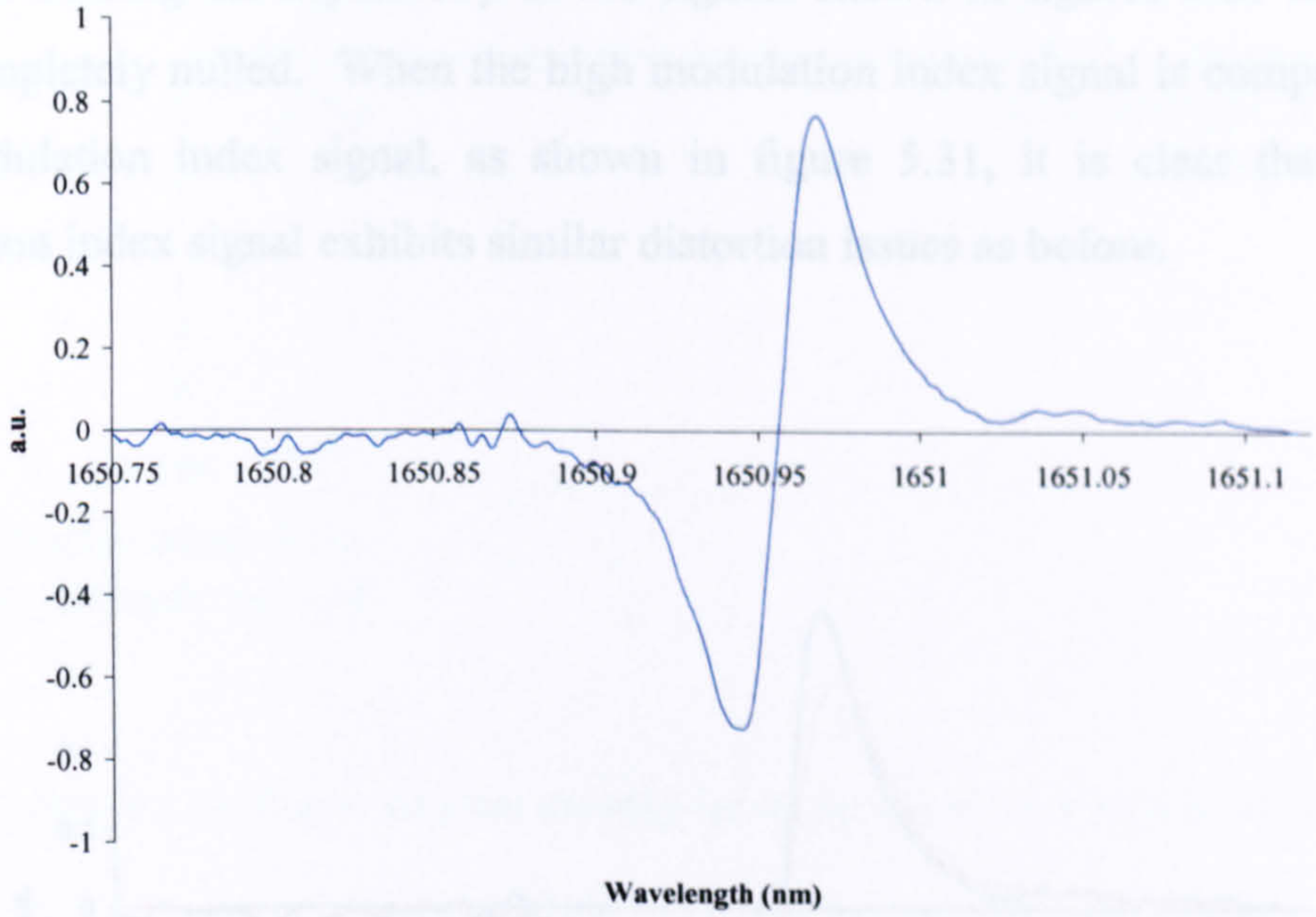

Figure 5.29: 10.13 % CH_4 : N_2 balance at 15.9 °C and 1.001 bar pressure – Normalised RAM nulled FM signal measured using low modulation index

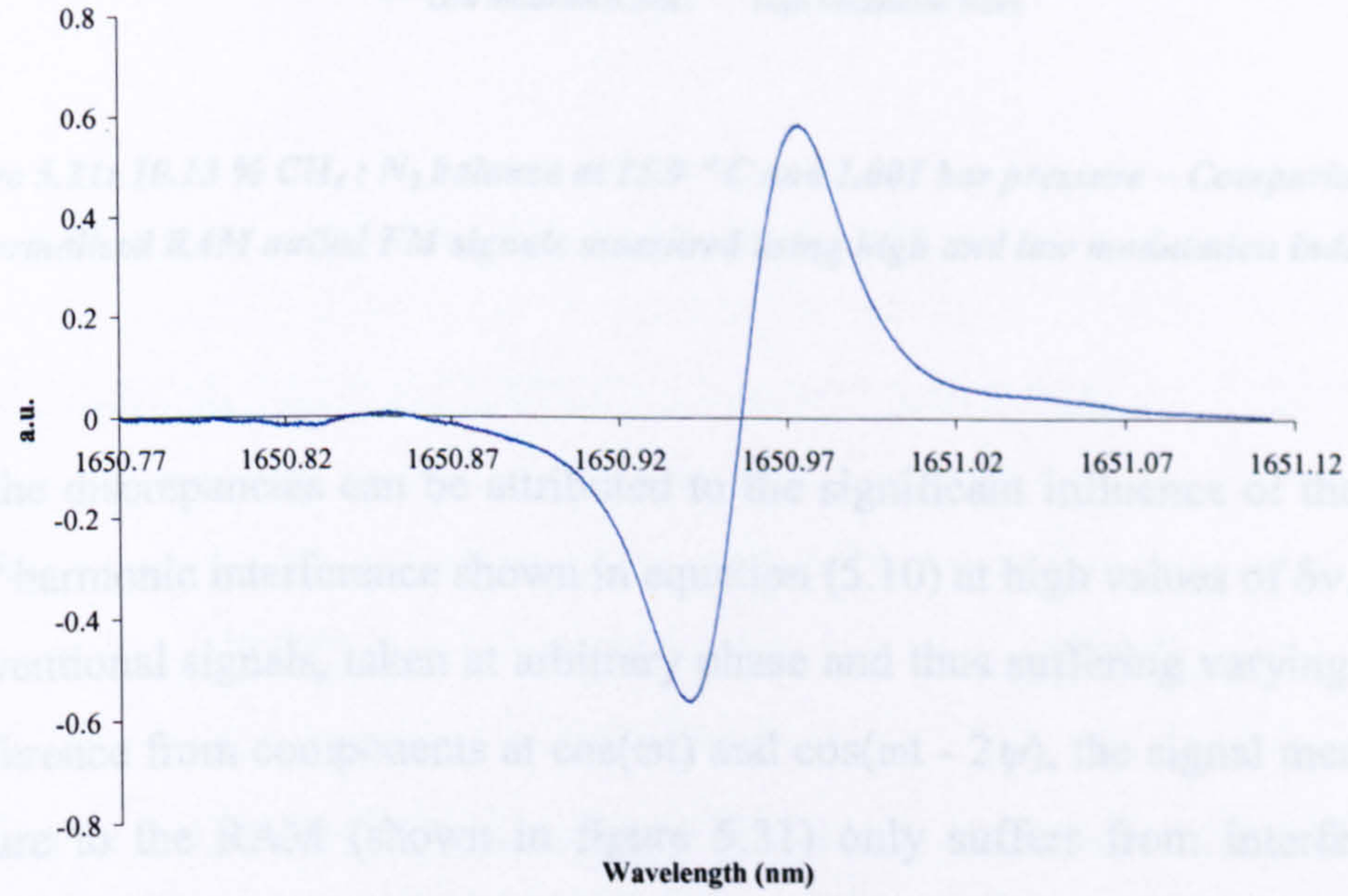

Figure 5.30: 10.13 % CH_4 : N_2 balance at 15.9 °C and 1.001 bar pressure – Normalised RAM nulled FM signal measured using high modulation index

Note the symmetry of the peak amplitudes in both signals, indicating that the RAM distortion causing the asymmetry in the signals shown in figures 5.21 to 5.23, has been completely nulled. When the high modulation index signal is compared to the low modulation index signal, as shown in figure 5.31, it is clear that the high modulation index signal exhibits similar distortion issues as before.

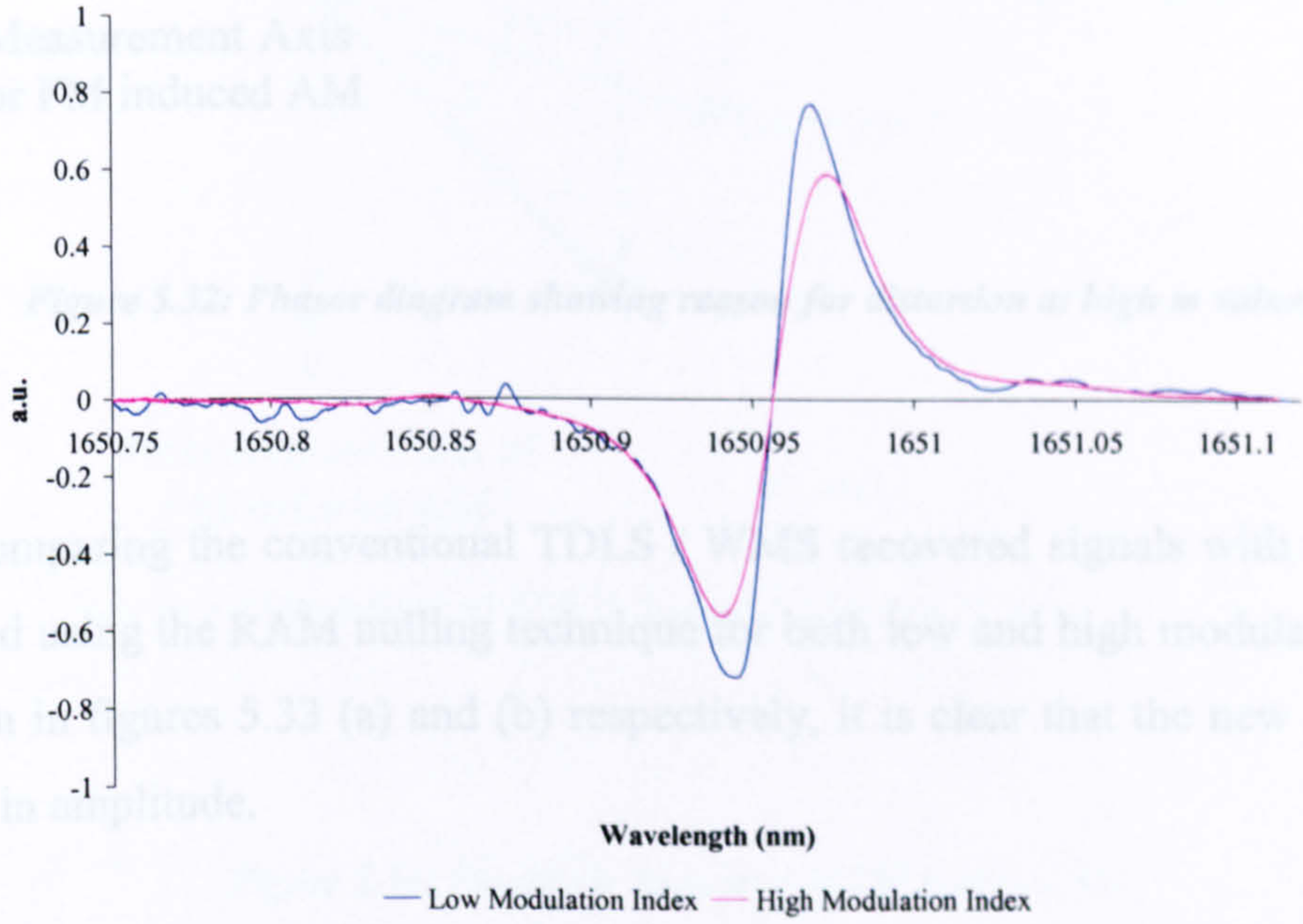

Figure 5.31: 10.13 % CH_4 : N_2 balance at 15.9 °C and 1.001 bar pressure – Comparison of normalised RAM nulled FM signals measured using high and low modulation index

Again, the discrepancies can be attributed to the significant influence of the second order 1st harmonic interference shown in equation (5.10) at high values of $\delta\nu$. Unlike the conventional signals, taken at arbitrary phase and thus suffering varying degrees of interference from components at $\cos(\omega t)$ and $\cos(\omega t - 2\psi)$, the signal measured at quadrature to the RAM (shown in figure 5.31) only suffers from interference at $\cos(\omega t - 2\psi)$, as shown in figure 5.32 below.

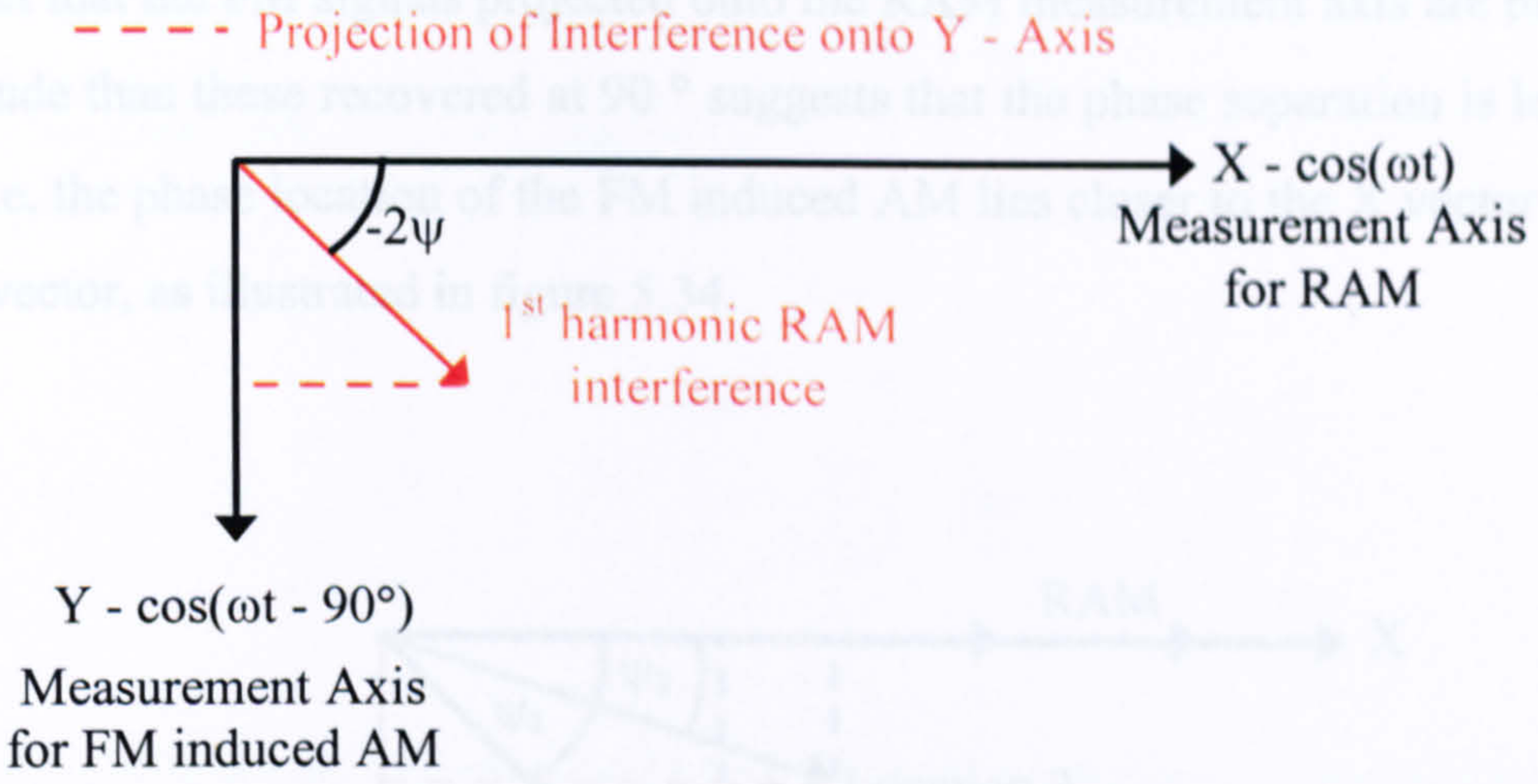

Figure 5.32: Phasor diagram showing reason for distortion at high m values

When comparing the conventional TDLS / WMS recovered signals with the signals recovered using the RAM nulling technique for both low and high modulation index, as shown in figures 5.33 (a) and (b) respectively, it is clear that the new signals are reduced in amplitude.

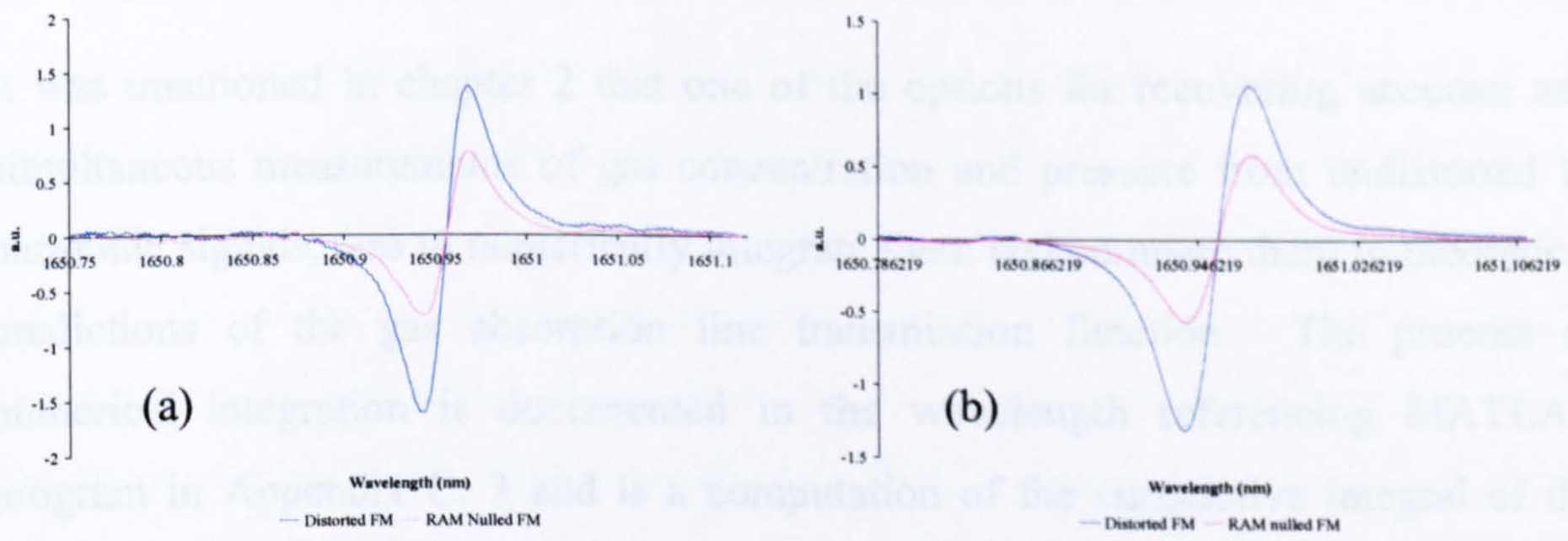

Figure 5.33: 10.13 % CH_4 : N_2 balance at 15.9 °C and 1.001 bar pressure – Comparison of distorted FM to RAM nulled FM signal, both measured using (a) low and (b) high modulation index

The fact that the FM signals projected onto the RAM measurement axis are bigger in amplitude than those recovered at 90 ° suggests that the phase separation is less than 45 °. i.e. the phase location of the FM induced AM lies closer to the X vector than to the Y vector, as illustrated in figure 5.34.

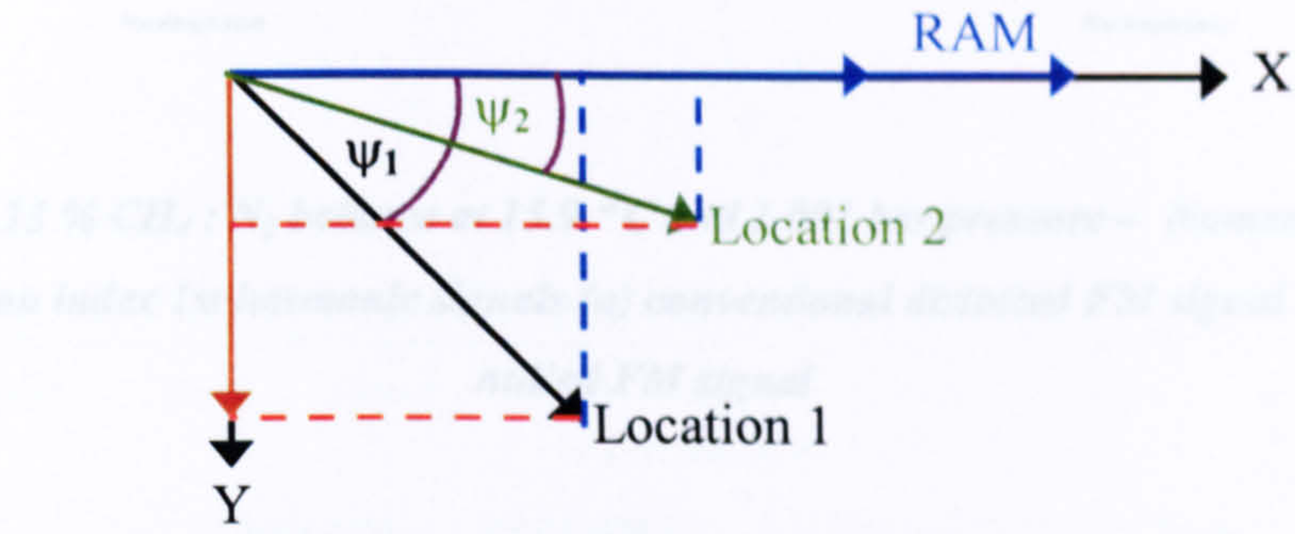

Figure 5.34: Possible ψ locations of FM induced AM

It was mentioned in chapter 2 that one of the options for recovering accurate and simultaneous measurements of gas concentration and pressure from undistorted 1st harmonic signals, was to numerically integrate them and compare them to theoretical predictions of the gas absorption line transmission function. The process of numerical integration is documented in the wavelength referencing MATLAB program in Appendix C: 3 and is a computation of the cumulative integral of the signal amplitudes, with respect to wavelength using trapezoidal integration. The integrals of the conventional and the RAM nulled 1st harmonic signals at low modulation index are shown below in figure 5.35. The high modulation index signals are ignored due to the distortion issues discussed above.

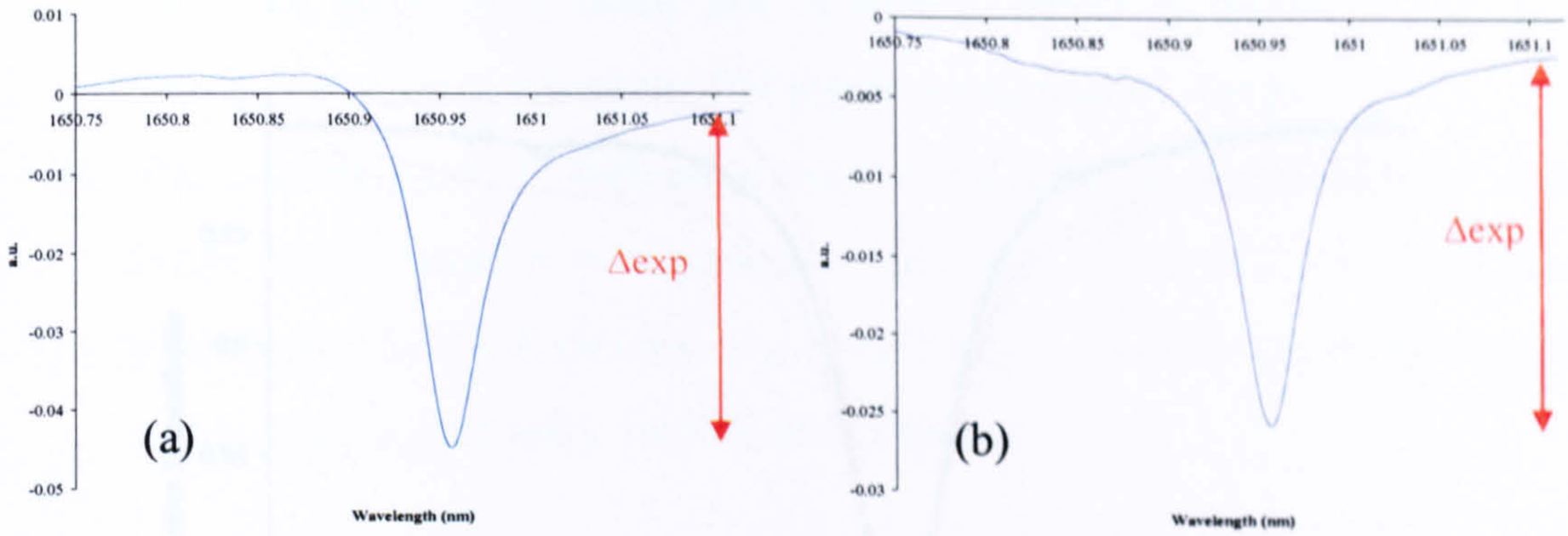

Figure 5.35: 10.13 % CH_4 : N_2 balance at 15.9 °C and 1.001 bar pressure – Numerical integrals of low modulation index 1st harmonic signals (a) conventional distorted FM signal and (b) RAM nulled FM signal

From figure 5.35 two issues are apparent: (i) due to the nature of derivative analysis the integrated signals are not referenced to an absolute transmission level and (ii) the asymmetry in the conventional 1st harmonic signal is manifest in an asymmetry in the wings of the integral signal. The amplitudes of the integrals are scaled to an absolute transmission level of 1 by multiplying them by Δtheory / Δexp, where Δtheory is the depth of the theoretical prediction (based on the known gas composition) and Δexp is the depth of the measured integral. The comparison of the scaled numerical integrals of both the conventionally recovered 1st harmonic signal and the RAM nulled 1st harmonic signal to theory are shown in figure 5.36 below. The direct signal for the same gas composition is also shown. As can be seen from the figure, although the RAM nulled 1st harmonic integral provides a better comparison to theory than the conventional 1st harmonic signal, there is still a significant error in the signal amplitude and linewidth. Unfortunately, this TDLS / WMS technique of recovering FM derivative signals is, inherently, not absolute and information relating to the absolute absorption line transmission function is lost. Straightforward integration of the derivatives with respect to wavelength, followed by a linear scaling of the integral amplitudes does not provide accurate recovery of the absolute transmission signals, hence the errors visible in figure 5.36.

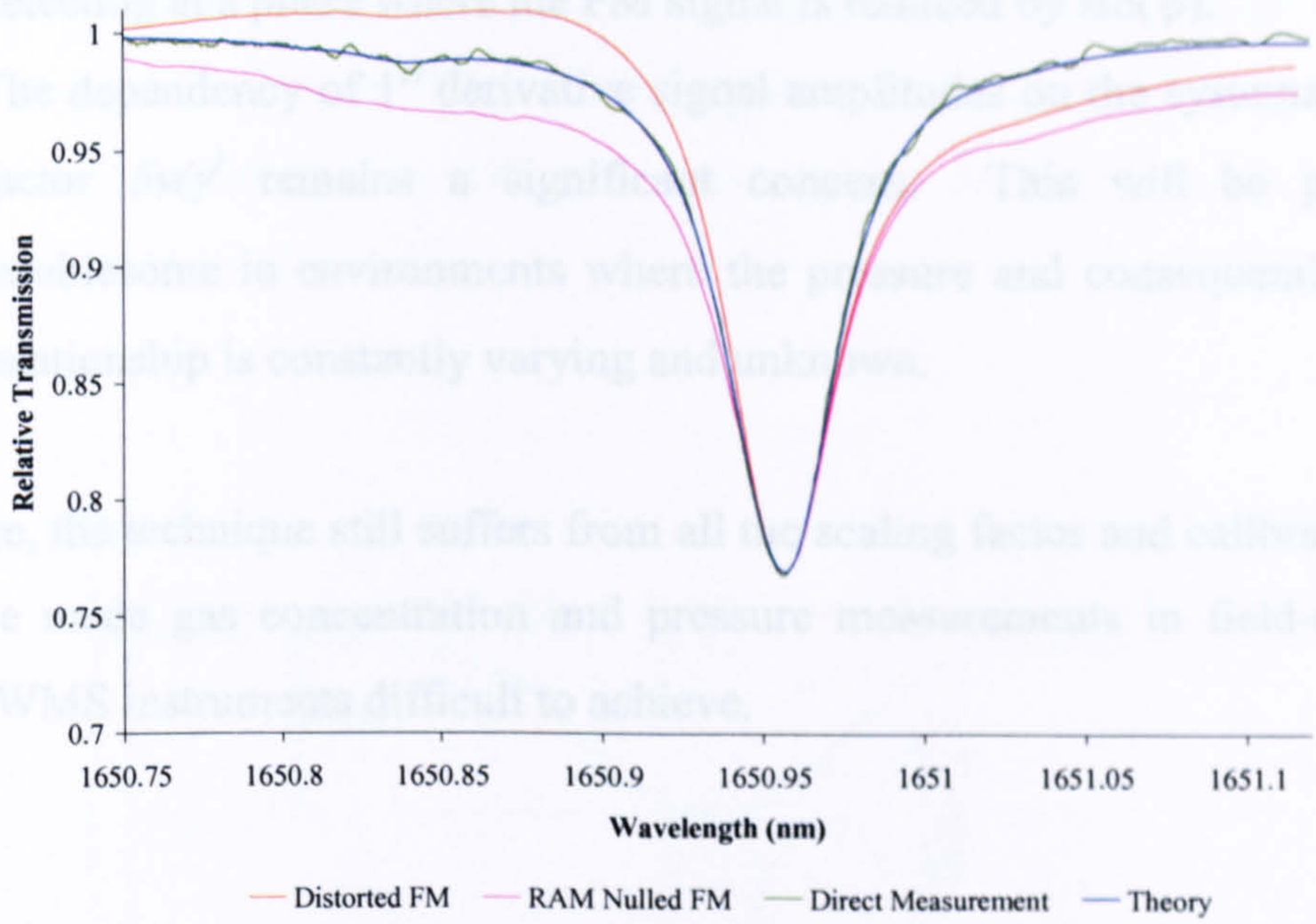

Figure 5.36: 10.13 % CH_4 : N_2 balance at 15.9 °C and 1.001 bar pressure – Comparison of integrated distorted FM and RAM nulled FM signals, taken at low modulation index, to theory

5.4.4 Conclusions

It is apparent then from equations (5.1) to (5.10) and the analysis of measured 1st harmonic signals that:

1. When attempting to recover an accurate derivative signal from the associated harmonic, low modulation index, coupled with a lock-in amplifier detection phase set at quadrature to the RAM variation, is the preferred technique. Unfortunately, the high modulation index signals continue to exhibit distortion (i.e. the harmonic signals at high m values are no longer associated with the desired derivatives, as discussed in chapter 2).
2. In terms of simultaneous gas concentration and pressure measurements in harsh industrial environments, this technique is not a viable option due to the

low SNR involved in using low m values, which is decreased further by detecting at a phase where the FM signal is reduced by $\sin(\psi)$.

3. The dependency of 1st derivative signal amplitudes on the systematic scaling factor $\delta\nu/\gamma^2$ remains a significant concern. This will be particularly troublesome in environments where the pressure and consequently the $\delta\nu/\gamma$ relationship is constantly varying and unknown.

Therefore, the technique still suffers from all the scaling factor and calibration issues that have made gas concentration and pressure measurements in field-deployable TDLS / WMS instruments difficult to achieve.

5.5 Novel Approach to Recovering the Absolute Absorption Line Transmission Function using TDLS with WMS Detection

5.5.1 Theoretical Principle

Recalling equation (5.6) it is clear that the 1st derivative signal associated with the 1st harmonic is distorted by a 1st harmonic RAM variation given by:

$$RAM_{\omega} = \Delta I(\nu_1) \cdot \cos(\omega t)[1 - \alpha(\nu_1)Cl] \tag{5.11}$$

The fact that the distortion is so significant suggests that this 1st harmonic RAM variation is comparable in magnitude to the FM induced 1st harmonic / derivative signal and therefore, is measurable through lock-in detection. Closer inspection of equation (5.11) reveals that the RAM variation follows the absolute absorption line transmission function. An alternative technique then is to null the FM contribution to the 1st harmonic signal (equation (5.6)) and recover only the DC RAM variation and the concentration dependant RAM variation by appropriate selection of the lock-

in amplifier detection phase. The experimental principle for detecting the RAM variation is described in figure 5.37. When the lock-in detection phase is set to an arbitrary value, the output 1st harmonic signal will be a combination of the 1st derivative FM signal and the DC and concentration dependent RAM signals (as given by equation (5.6)).

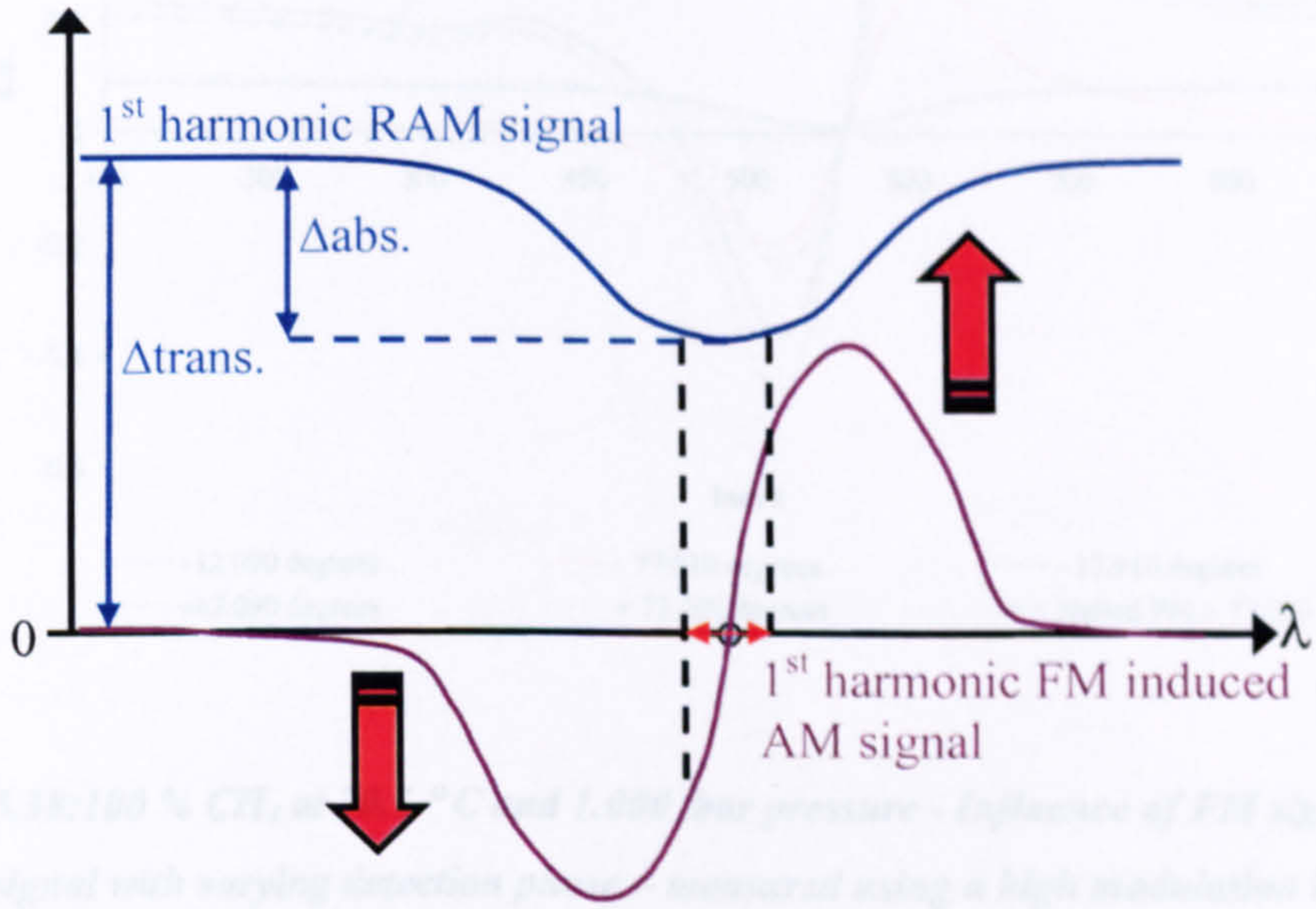

Figure 5.37: Influence of FM induced AM signal on RAM signal

It can be seen from figure 5.37 that the influence of the FM 1st harmonic signal on the RAM 1st harmonic signal (from mixing) is to shift the right-hand-side of the profile upwards, whilst shifting the left-hand-side downwards. The level of influence will be determined by the lock-in detection phase relative to the AM – FM separation phase. Intuitively, the influence of the FM signal upon the RAM signal will be at a minimum when the ratio of the absorption (Δabs.) to the transmission (Δtrans.) is at a minimum. Figure 5.38 shows the determination of the FM nulled RAM signal using this principle (again, an expanded version is shown over the page). The measurement was made using the usual high modulation index on a 100 % CH_4 composition with the view of making the desired features more noticeable. The changes to the lock-in amplifier set up are noted in table 5.4.

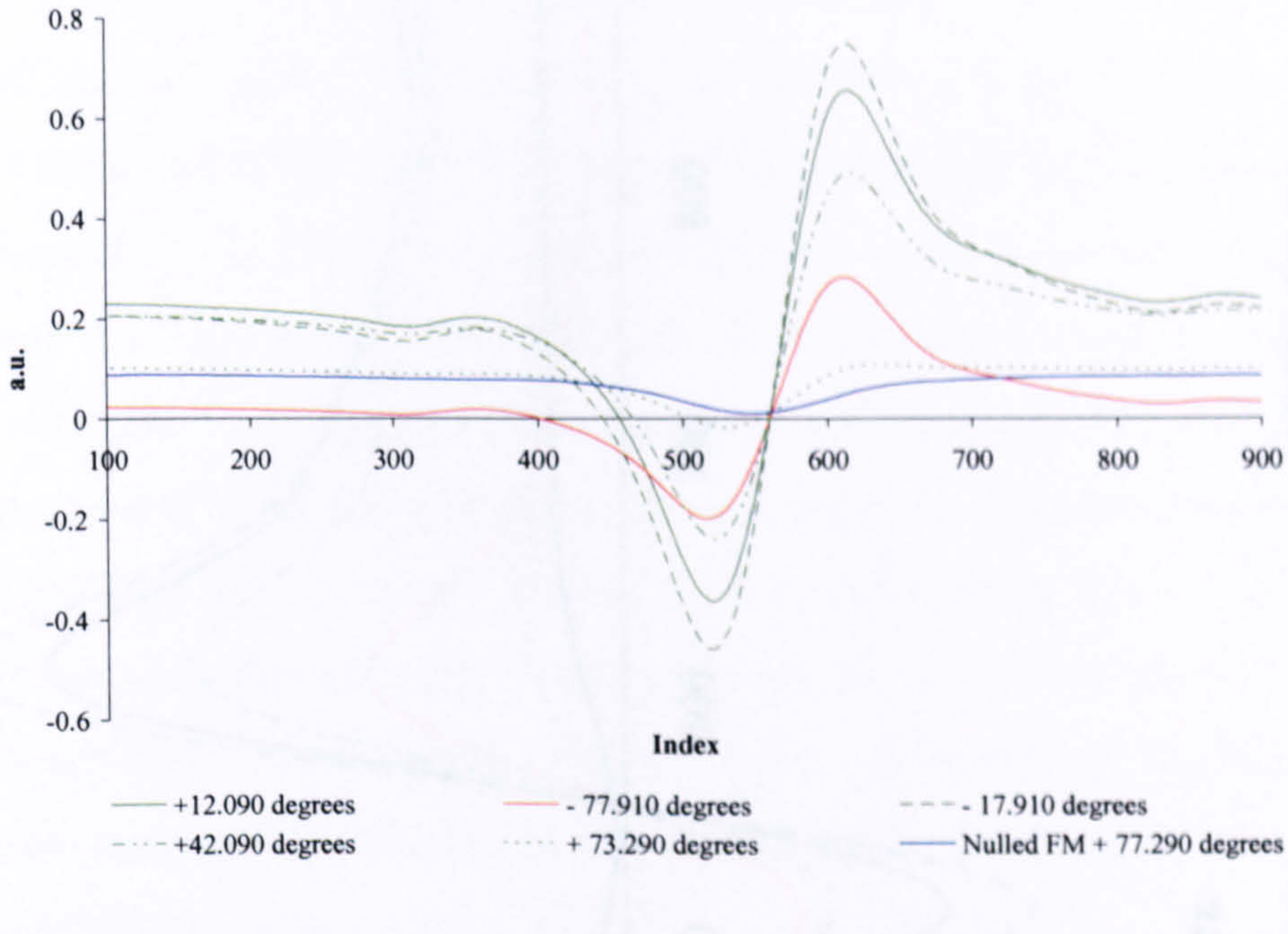

Figure 5.38:100 % CH_4 at 20.5 °C and 1.000 bar pressure - Influence of FM signal on RAM signal with varying detection phase – measured using a high modulation index

	High Modulation Index
AC Gain	14 dB, Dynamic Range:13
Sensitivity	50 mV
Time Constant	1 ms
Reference Harmonic	1^{st}

Table 5.4: New settings for Perkin Elmer DSP lock-in amplifier

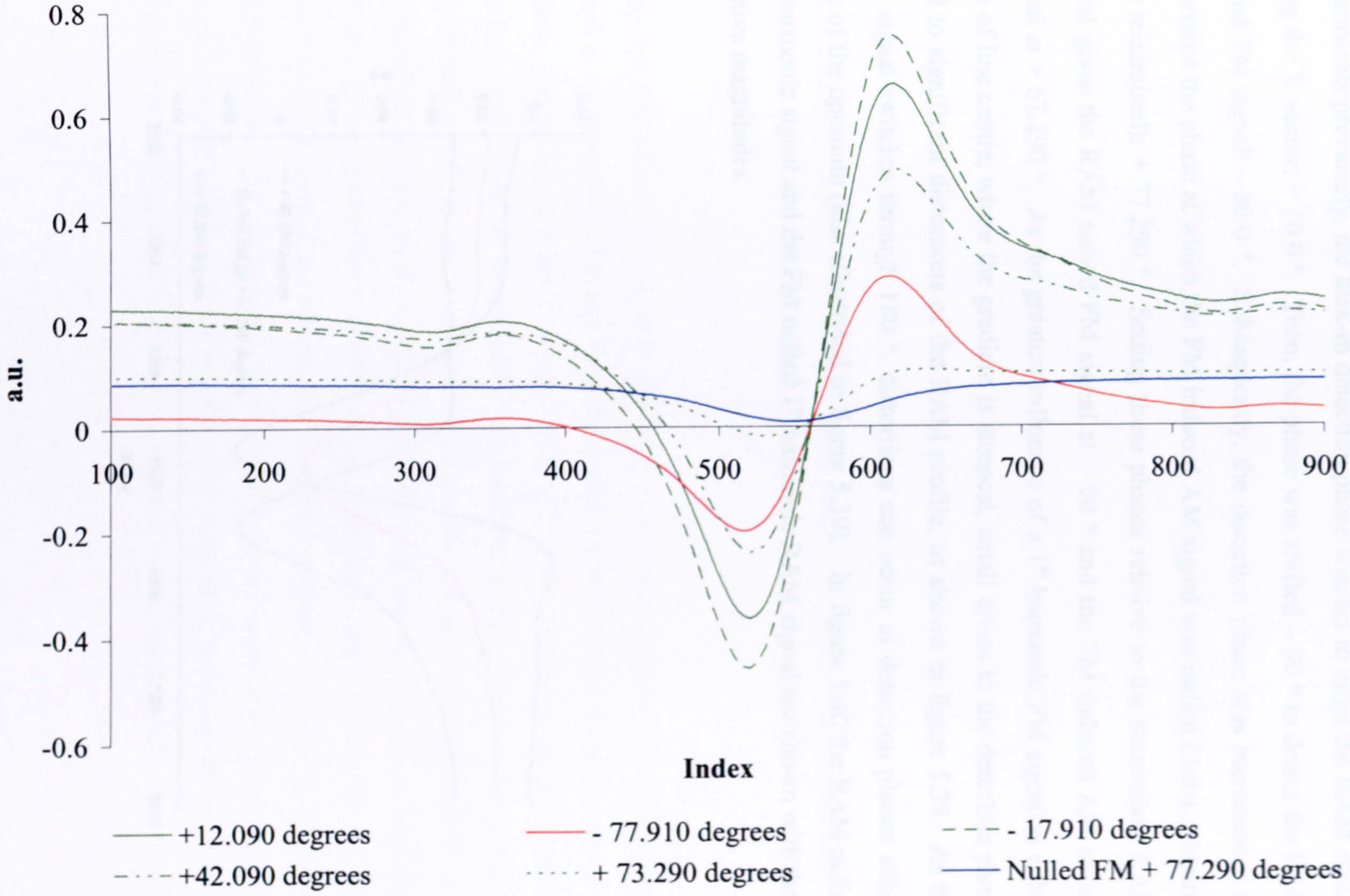
0.8
0.6
0.4
0.2
0
-0.2
-0.4
-0.6
a.u.
100
200
300
400
500
600
700
800
900
Index
+12.090 degrees
+42.090 degrees
- 77.910 degrees
+ 73.290 degrees
- 17.910 degrees
Nulled FM + 77.290 degrees

As can be seen from the figure, the influence of the FM 1st harmonic signal on the 1st harmonic RAM signal is significant and varying with detection phase. First, as in all experiments previously, the lock-in detection phase was set to align the RAM signal along the X vector: + 10.0 °. Then, the phase was shifted – 90 ° to detect the RAM nulled FM signal: - 80.0 °. Subsequently, the detection phase was incremented to determine the phase at which the FM induced AM signal was nulled (Δabs. / Δtrans. was minimised): + 77.290 °. Setting these phases relative to the maximised RAM signal gives the RAM nulled FM signal at – 90 ° and the FM induced AM nulled signal at + 67.290 °. As the greatest influence of a 1st harmonic FM signal is either side of line centre, where the gradient is steepest, small errors in the detection phase lead to significant distortions of the RAM profile, as shown in figure 5.39. As the FM signal switches through 180 °, distortions can occur at detection phases either side of the optimum (also illustrated in figure 5.39). In figure 5.40 the RAM nulled 1st harmonic signal and the FM nulled 1st harmonic RAM signal are shown with their relative magnitudes.

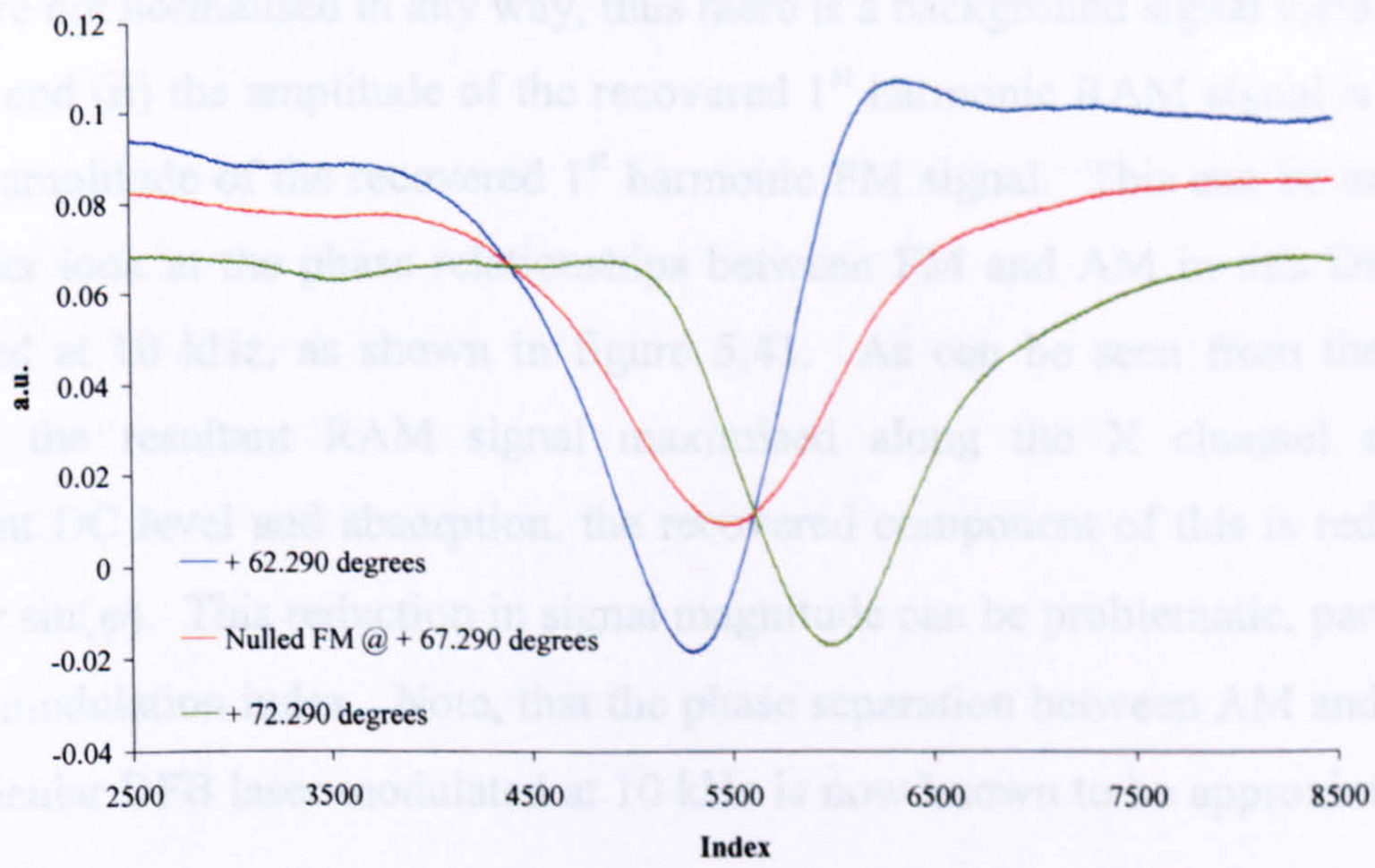

Figure 5.39: 100 % CH_4 at 20.5 °C and 1.000 bar pressure - Influence of FM signal on RAM signal with varying detection phase – measured using a high modulation index

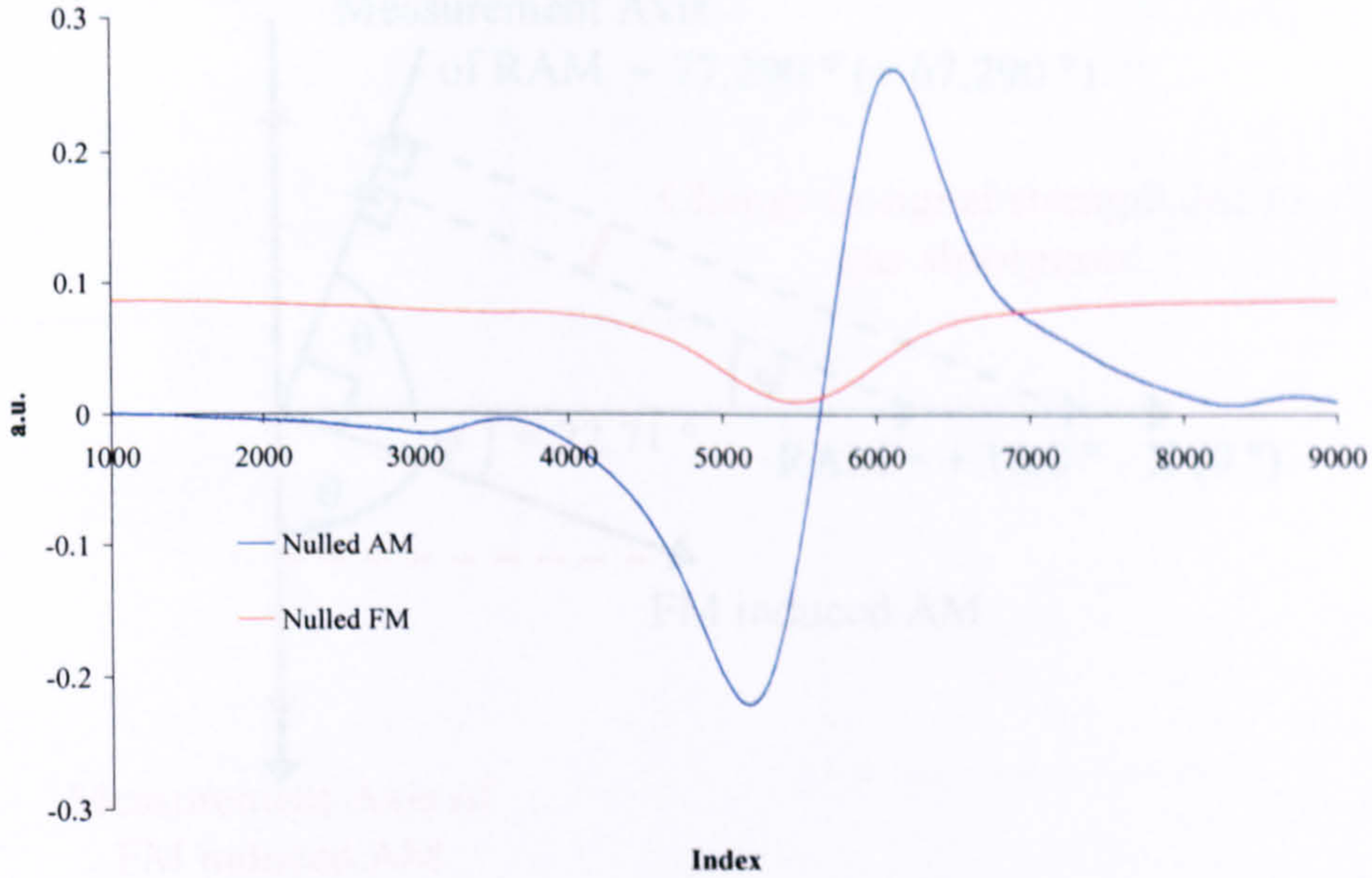

Figure 5.40: 100 % CH_4 at 20.5 °C and 1.000 bar pressure - Comparison of RAM nulled and FM nulled signals – measured using high modulation index

There are two points to note from the analysis of these signals: (i) the recovered signals are not normalised in any way, thus there is a background signal visible on all of them, and (ii) the amplitude of the recovered 1st harmonic RAM signal is smaller than the amplitude of the recovered 1st harmonic FM signal. This can be explained by another look at the phase relationships between FM and AM in this DFB laser modulated at 10 kHz, as shown in figure 5.41. As can be seen from the figure, although the resultant RAM signal maximised along the X channel shows a significant DC level and absorption, the recovered component of this is reduced by $\cos(\theta)$ or $\sin(\psi)$. This reduction in signal magnitude can be problematic, particularly at small modulation index. Note, that the phase separation between AM and FM for this particular DFB laser modulated at 10 kHz is now known to be approximately 23 °.

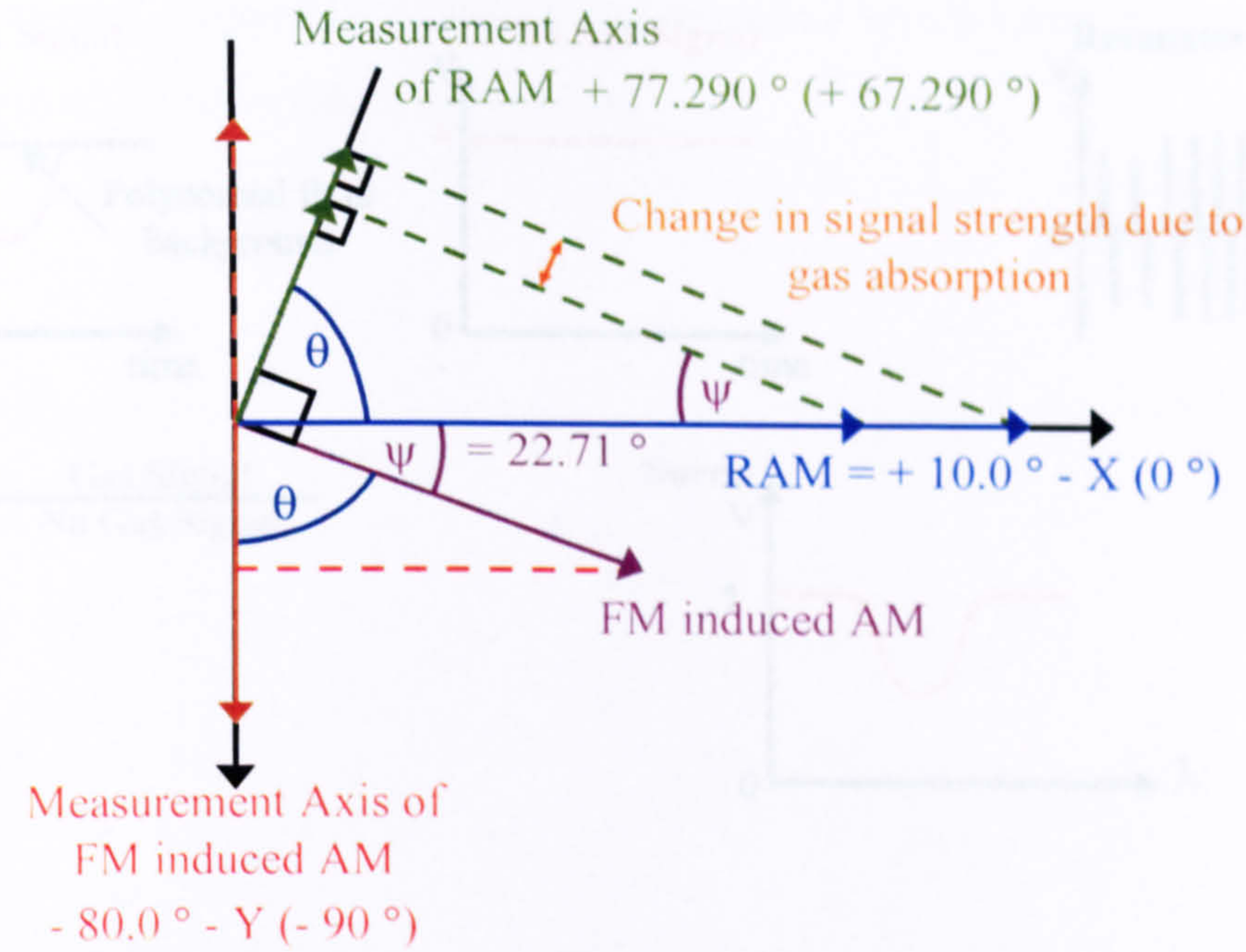

Figure 5.41: Phase relationships in DFB laser modulated at 10 kHz

5.5.2 Revised Experimental System and Procedure

There were only two changes made to the experimental system used to measure the RAM nulled FM signals: the lock-in amplifier detection phase was now set to null the FM contribution and, due to simpler system calibration (reported below), there was no need for a power reference signal. Figure 5.42 illustrates the calibration and signal processing procedures used in this new TDLS / WMS technique.

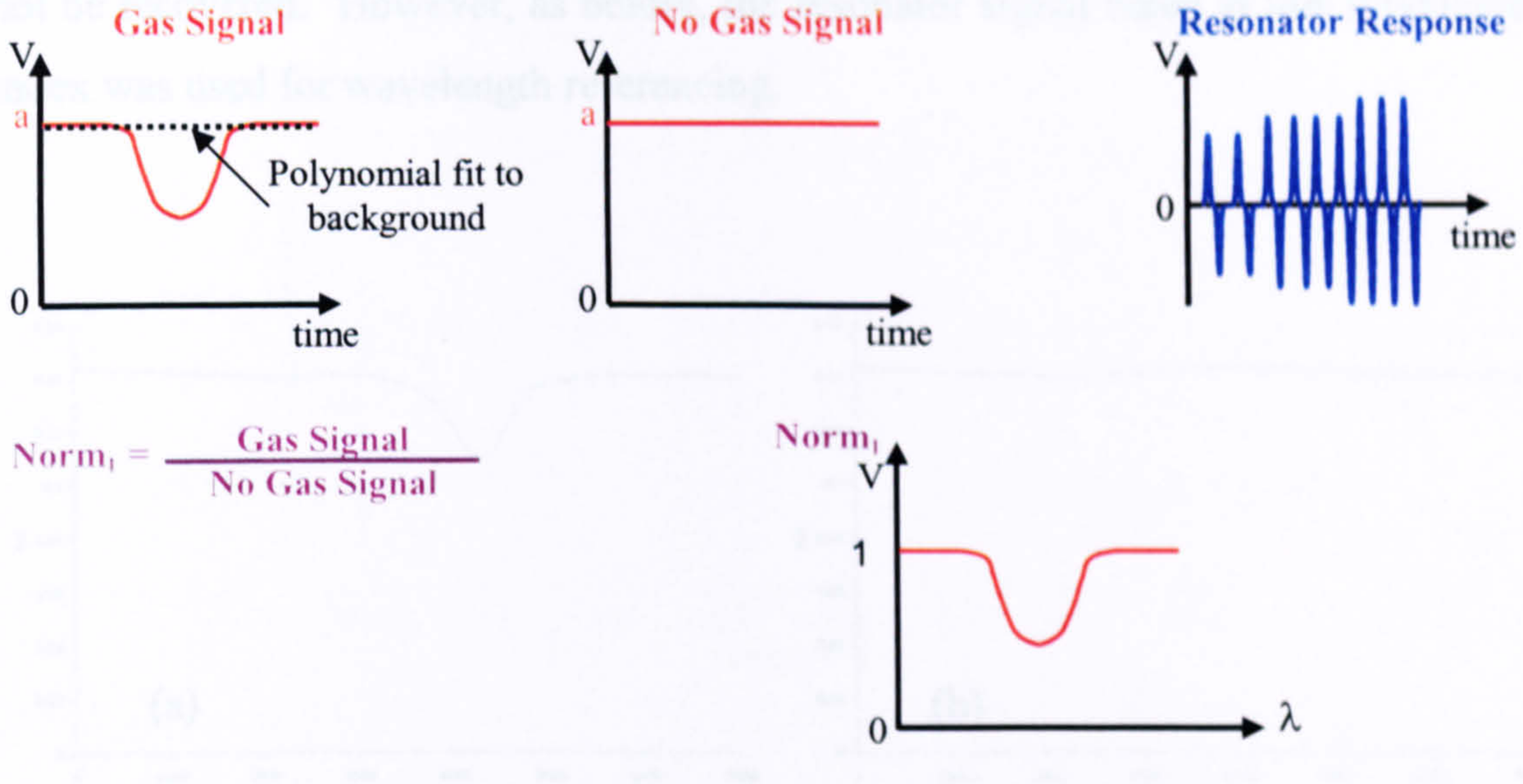

Figure 5.42: Calibration and normalisation procedures for FM nulling technique

The recovered 1st harmonic RAM signal is the concentration dependent RAM variation following the gas absorption line profile superimposed on the large RAM induced DC background. Dividing this signal by a "no gas signal" provided an absolute gas absorption line transmission function. It is important to note here that "no gas signals" were simple to achieve in this laboratory set up and proved the simplest way of measuring background signals. In field-deployable instruments we are not afforded this luxury; however, the background signal can be closely approximated by a polynomial fit through the off-line points either side of the absorption, as illustrated in figure 5.42 above. Again a 1st harmonic resonator signal was used to map this transmission profile onto a wavelength scale.

5.5.3 Results and Discussion

Example signals recovered using the new technique and the usual high modulation index (m ~ 2) are shown in figure 5.43 below. Unfortunately, the low SNR associated with low modulation index meant a reliable FM nulled RAM signal could

not be recovered. However, as before, the resonator signal taken at low modulation index was used for wavelength referencing.

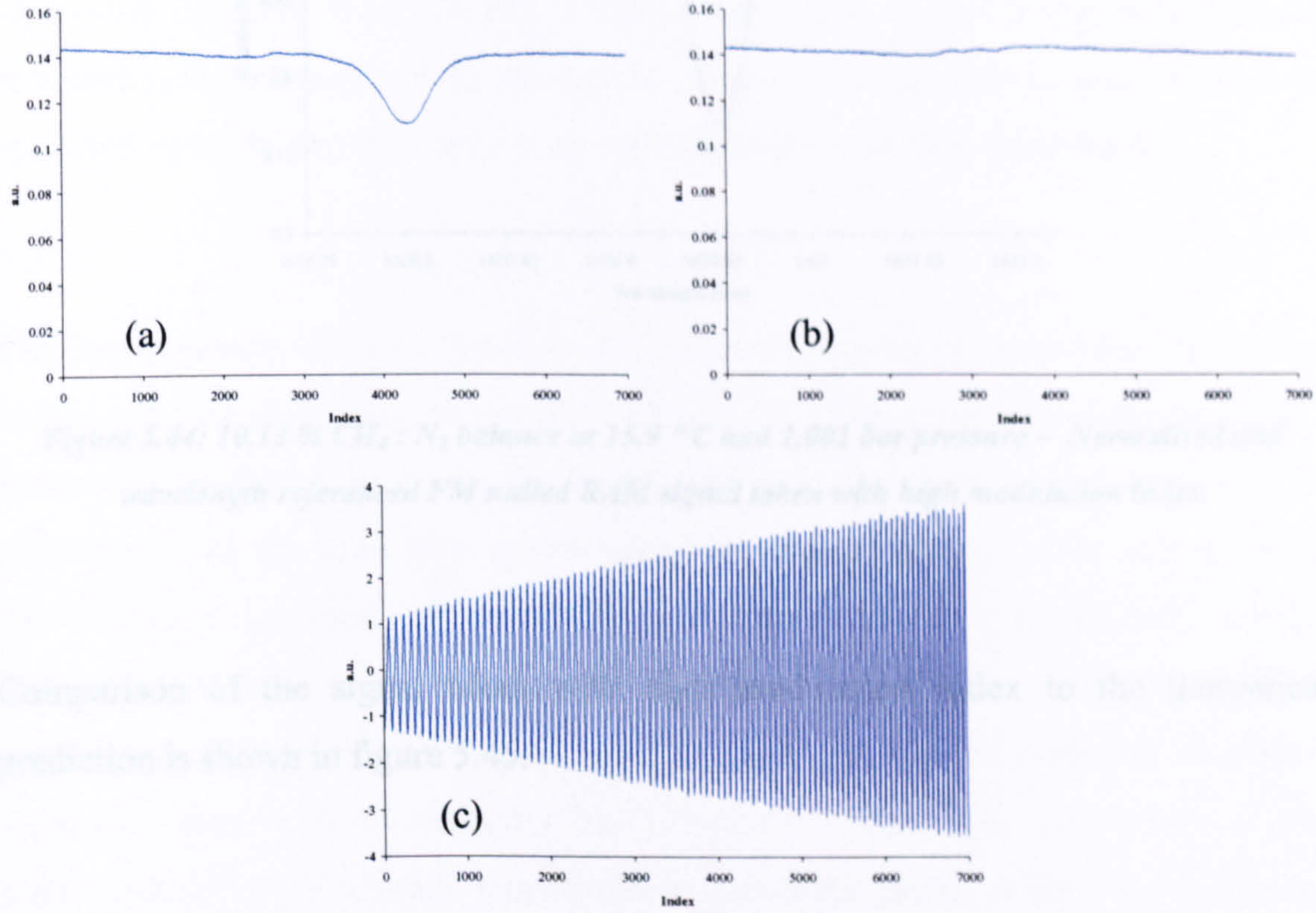

Figure 5.43: 10.13 % CH_4 : N_2 balance at 15.9 °C and 1.001 bar pressure – Experimentally measured signals using high modulation index: trimmed (a) gas signal, (b) no gas signal, (c) 1st harmonic resonator response (taken at low modulation index)

The normalised absolute transmission profile is then input, along with the 1st harmonic resonator response to a new MATLAB program, the code for which is detailed in Appendix C: 4. This MATLAB program follows the same principles as the previous two wavelength referencing programs, mapping a frequency scale, defined by the resonator 1st harmonic zero crossings, relative to the zero crossing closest to the peak absorption of the experimental transmission profile. The program then returns the wavelength referenced signal shown in figure 5.44 below.

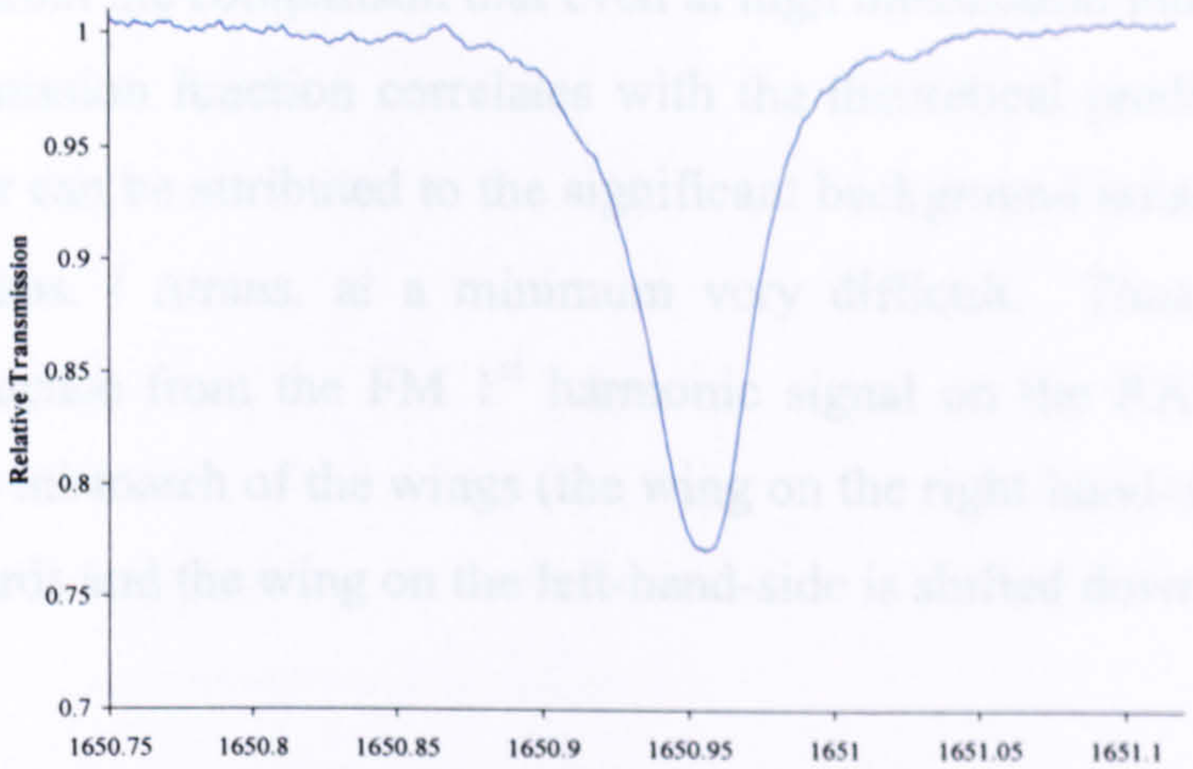

Figure 5.44: 10.13 % CH_4 : N_2 balance at 15.9 °C and 1.001 bar pressure – Normalised and wavelength referenced FM nulled RAM signal taken with high modulation index

Comparison of the signal taken with high modulation index to the theoretical prediction is shown in figure 5.45.

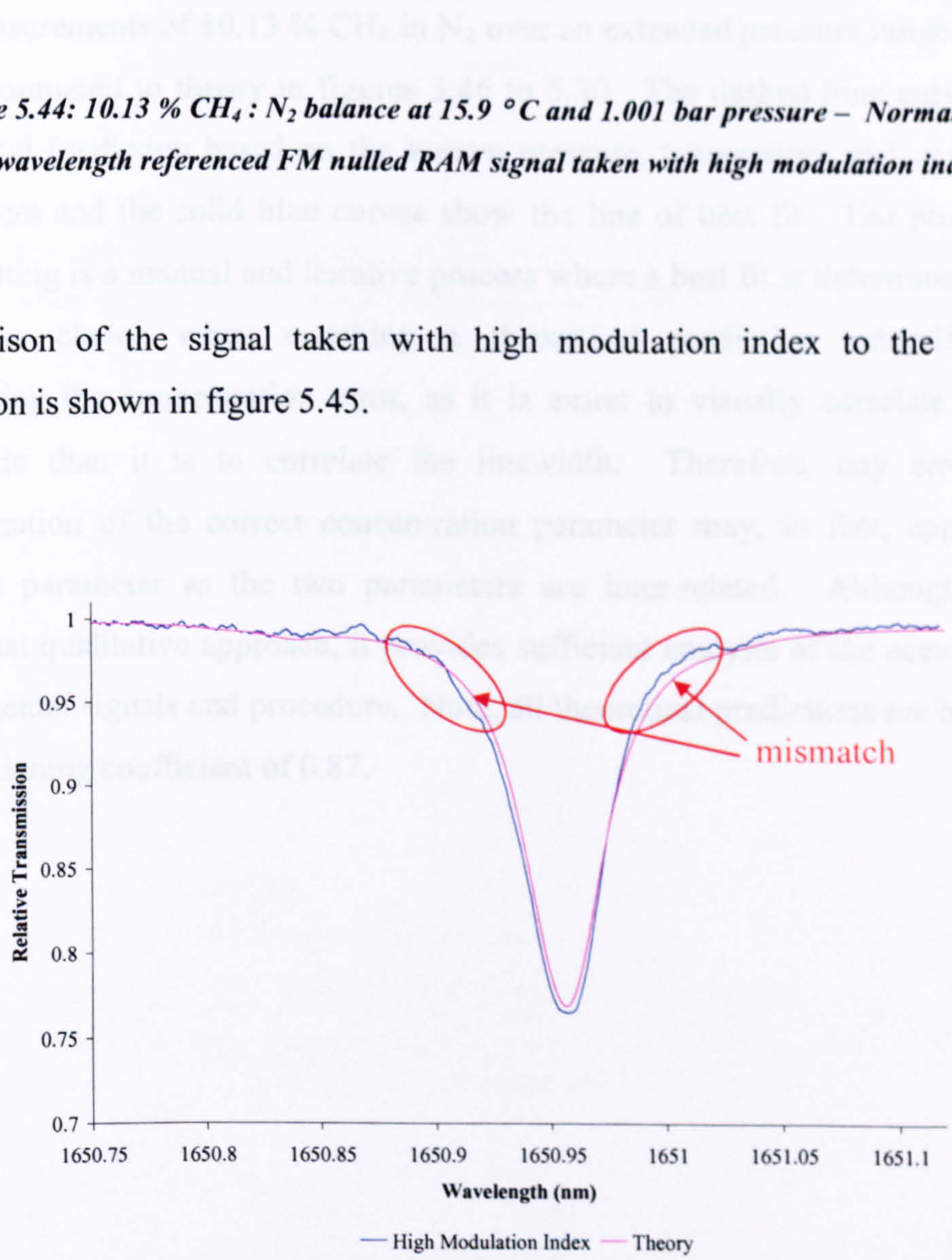

Figure 5.45: 10.13 % CH_4 : N_2 balance at 15.9 °C and 1.001 bar pressure – Comparison of 1st harmonic FM nulled RAM measurement, taken with a high modulation index, to theory

It can be seen from the comparison that even at high modulation index, the measured absolute transmission function correlates with the theoretical prediction reasonably well. The error can be attributed to the significant background noise level that made determining Δabs. / Δtrans. at a minimum very difficult. Thus, there is still a noticeable influence from the FM 1st harmonic signal on the RAM measurement, reflected in the mismatch of the wings (the wing on the right-hand-side of line centre is shifted upwards and the wing on the left-hand-side is shifted downwards).

The measurements of 10.13 % CH_4 in N_2 over an extended pressure range are shown below compared to theory in figures 5.46 to 5.50. The dashed blue curves show a theoretical prediction based on the known pressure, temperature and concentration parameters and the solid blue curves show the line of best fit. The procedure for curve fitting is a manual and iterative process where a best fit is determined visually. Parameter choice when matching a theoretical prediction naturally favours minimising the concentration error, as it is easier to visually correlate the signal amplitude than it is to correlate the linewidth. Therefore, any errors in the determination of the correct concentration parameter may, in fact, appear in the pressure parameter as the two parameters are inter-related. Although this is a somewhat qualitative approach, it provides sufficient analysis of the accuracy of the experimental signals and procedure. Note, all theoretical predictions are based on an N_2 broadening coefficient of 0.87.

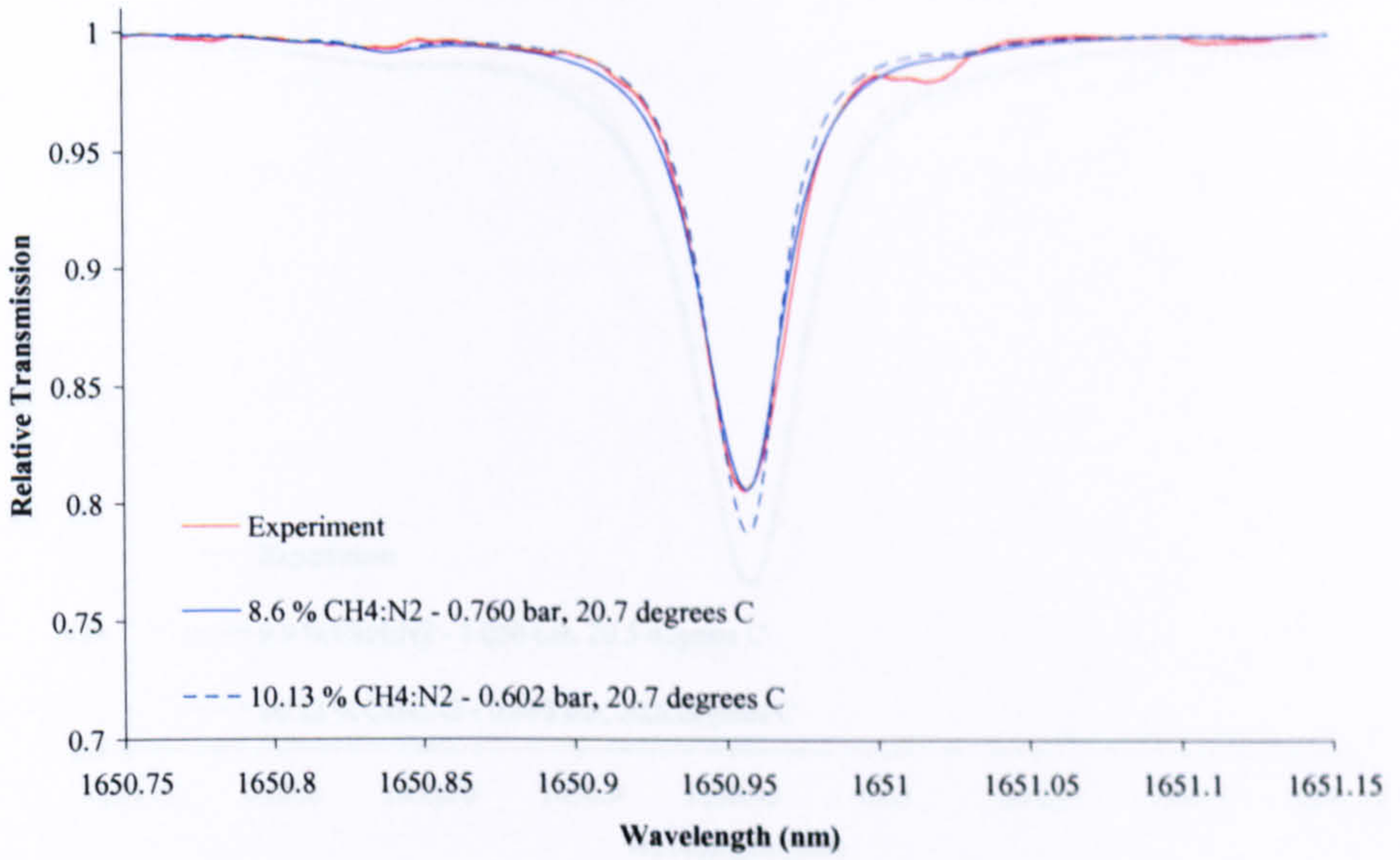

Figure 5.46: 10.13 % CH_4 : N_2 balance at 20.7 °C and 0.602 bar pressure – Comparison of 1st harmonic FM nulled RAM measurement, taken with high modulation index, to theory

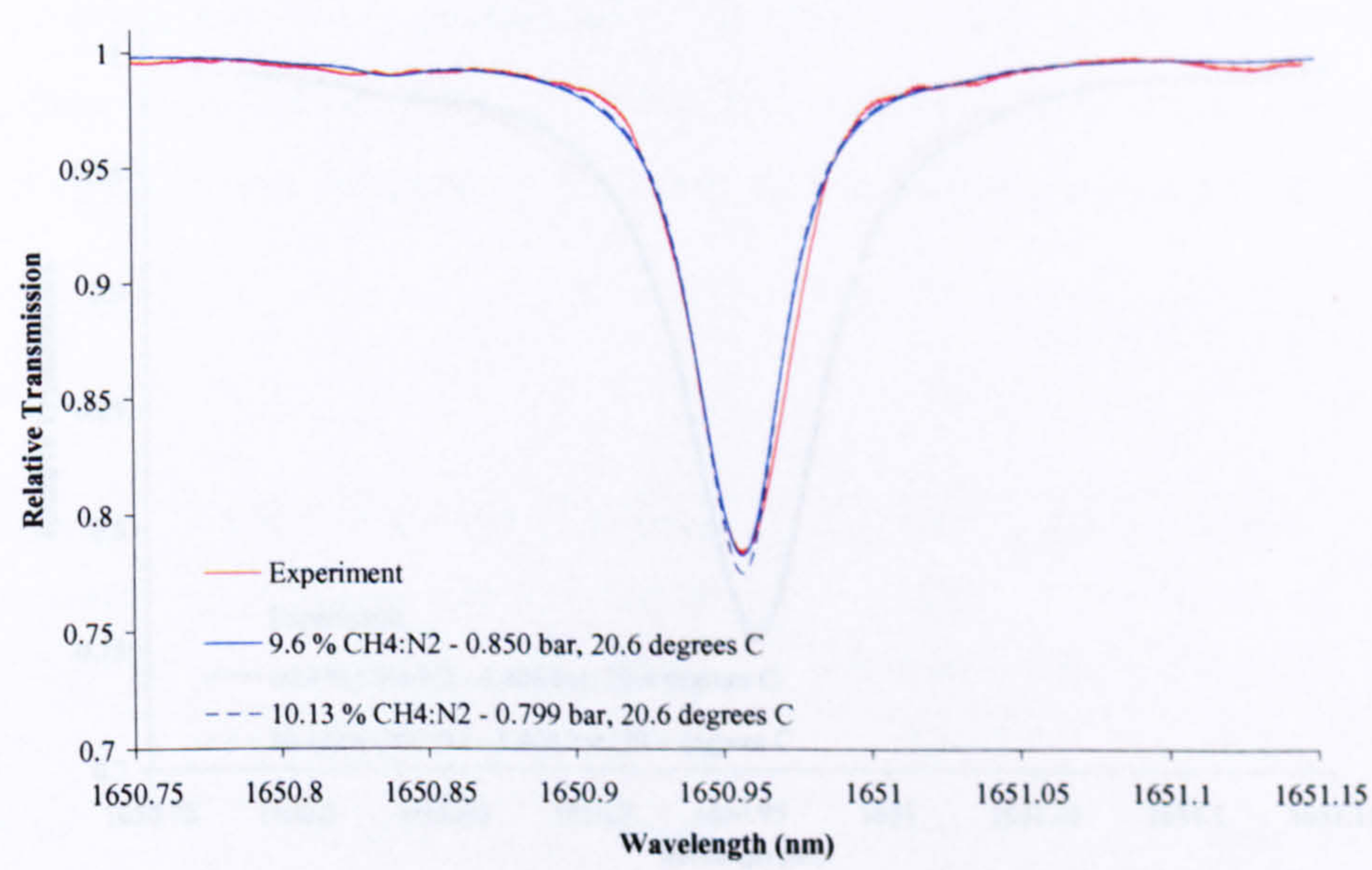

Figure 5.47: 10.13 % CH_4 : N_2 balance at 20.6 °C and 0.799 bar pressure – Comparison of 1st harmonic FM nulled RAM measurement, taken with high modulation index, to theory

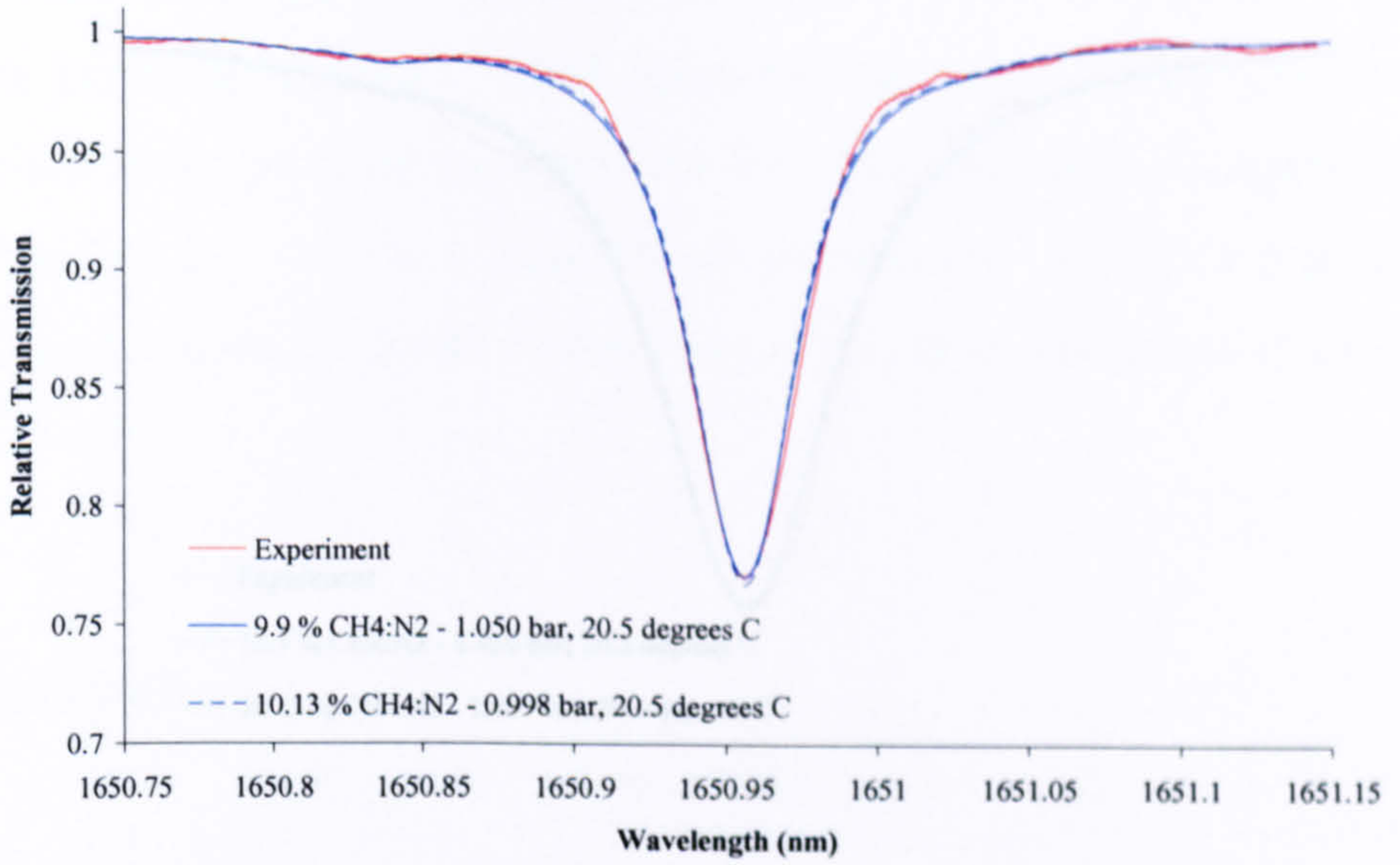

Figure 5.48: 10.13 % CH_4 : N_2 balance at 20.5 °C and 0.998 bar pressure – Comparison of 1st harmonic FM nulled RAM measurement, taken with high modulation index, to theory

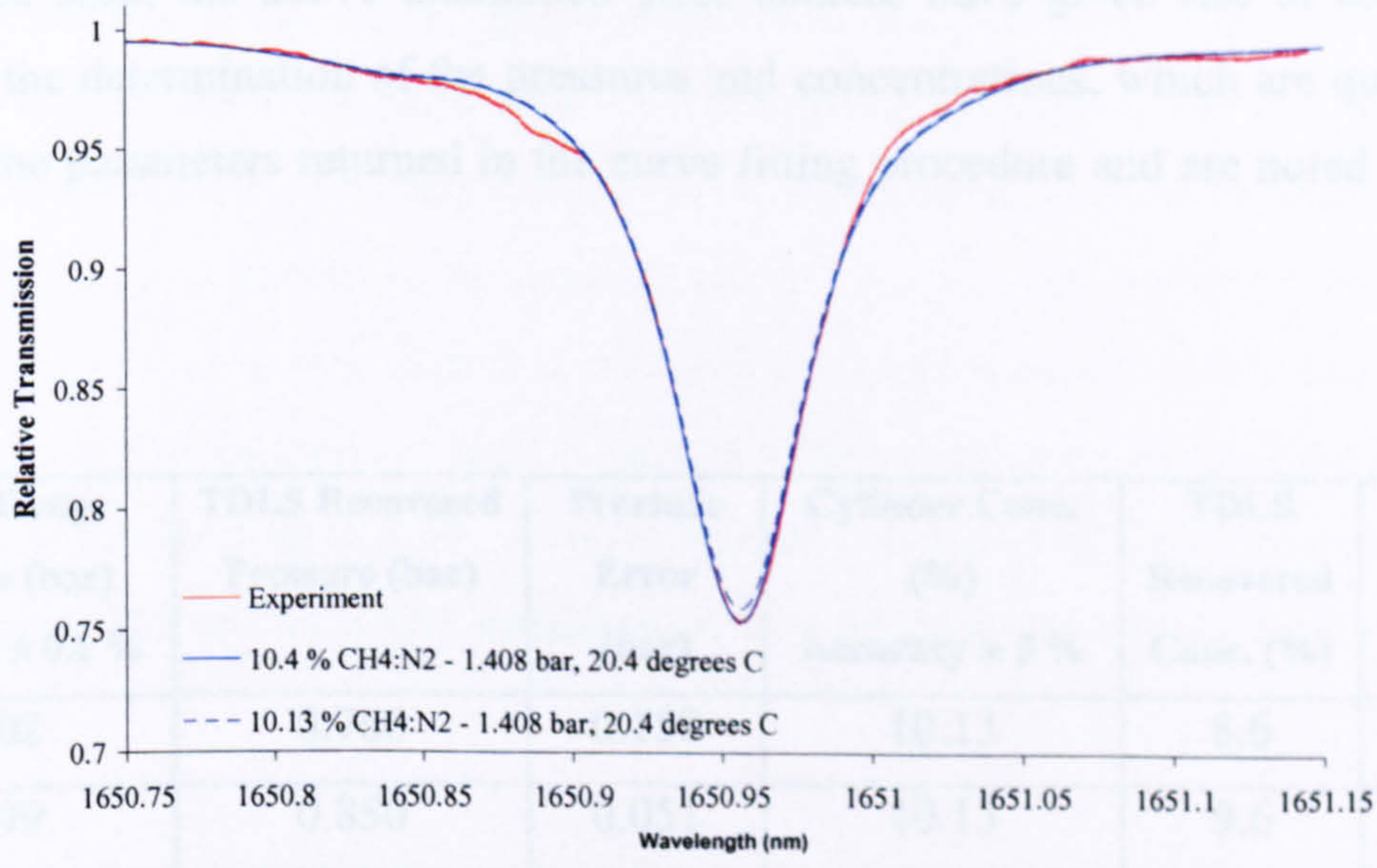

Figure 5.49: 10.13 % CH_4 : N_2 balance at 20.4 °C and 1.408 bar pressure – Comparison of 1st harmonic FM nulled RAM measurement, taken with high modulation index, to theory

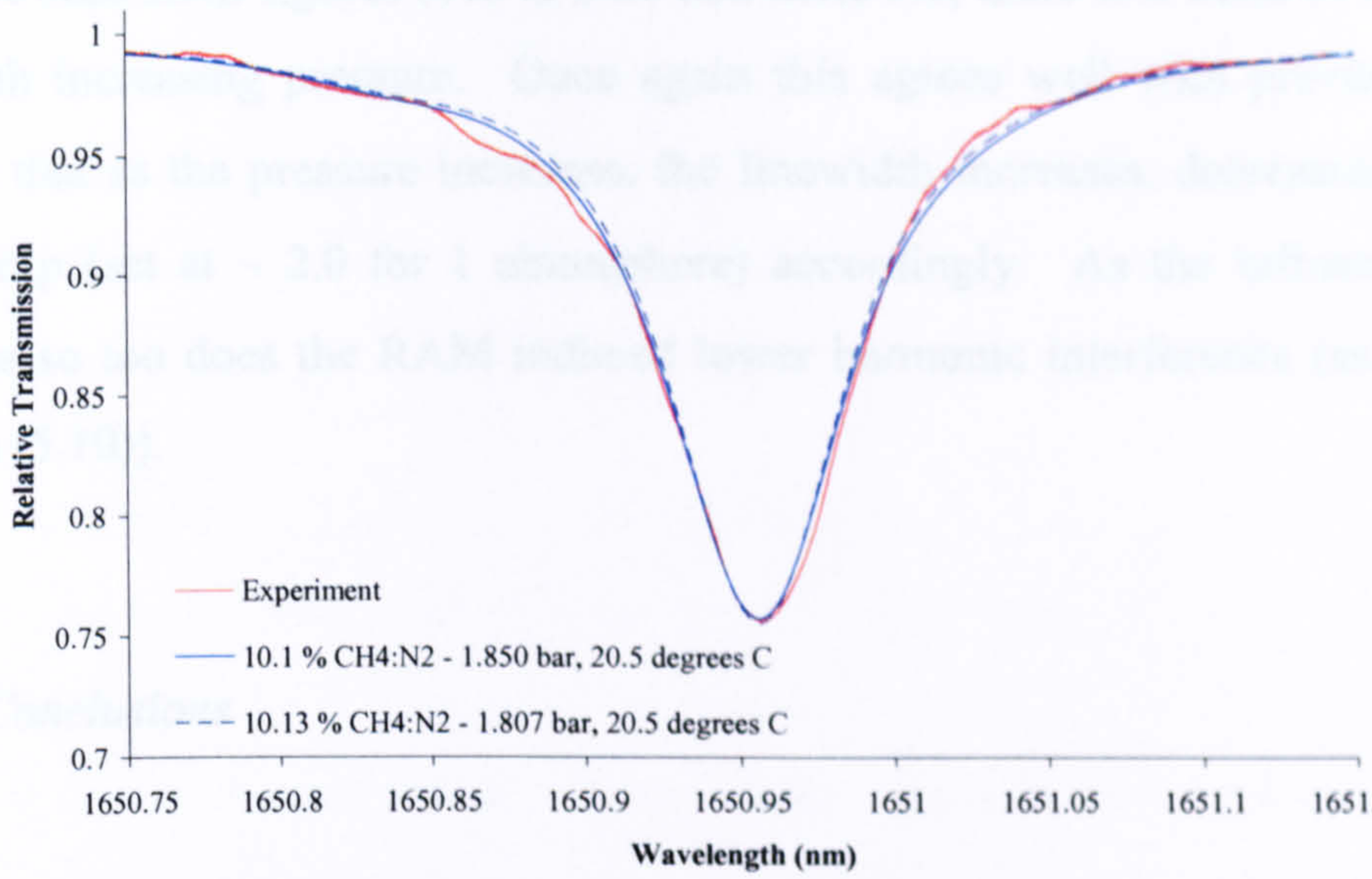

Figure 5.50: 10.13 % CH_4 : N_2 balance at 20.5 °C and 1.807 bar pressure – Comparison of 1st harmonic FM nulled RAM measurement, taken with high modulation index, to theory

As can be seen, the above mentioned error sources have given rise to combined errors in the determination of the pressures and concentrations, which are quantified through the parameters returned in the curve fitting procedure and are noted in table 5.5.

Digital Gauge Pressure (bar) Accuracy ± 0.1 %	TDLS Recovered Pressure (bar)	Pressure Error (bar)	Cylinder Conc. (%) Accuracy ± 5 %	TDLS Recovered Conc. (%)	Conc. Error (%)
0.602	0.760	0.158	10.13	8.6	15.1
0.799	0.850	0.051	10.13	9.6	5.23
0.998	1.050	0.052	10.13	9.9	2.27
1.408	1.408	0.000	10.13	10.4	2.6
1.807	1.850	0.043	10.13	10.1	0.3

Table 5.5: Error in pressure and concentration between theoretical predictions and experiment

As can be seen from figures 5.46 to 5.50 and table 5.5, there is a trend of decreasing error with increasing pressure. Once again this agrees well with previous results showing that as the pressure increases, the linewidth increases, decreasing the $\delta\nu/\gamma$ relationship (set at ~ 2.0 for 1 atmosphere) accordingly. As the influence of $\delta\nu$ decreases so too does the RAM induced lower harmonic interference (as shown in equation (5.10)).

5.5.4 Conclusions

Comparing a FM nulled 1st harmonic RAM signal (taken at high modulation index) to an integrated RAM nulled FM signal (taken at low modulation index) for the same gas composition, as shown below in figure 5.51, it can be seen that, even at high modulation index, the 1st harmonic RAM signal provides a better correlation to theory. Like TDLS with direct detection, this new TDLS / WMS technique permits the recovery of the absolute gas transmission signals that lead to accurate analysis and simultaneous extraction of gas concentration and pressure. The technique is absolute with no need for calibration. Of remaining concern is the low signal-to-noise ratio associated with recovering a RAM component reduced in amplitude by $\sin(\psi)$, where ψ is known to be approximately 23 ° for this particular DFB laser modulated at 10 kHz (i.e. signal is reduced by approximately 0.4). This means signals are only measurable at high m values, which may be a contributory factor to the errors in figures 5.46 to 5.50. A more detailed discussion of the errors incurred in 1st harmonic FM nulled RAM measurements at arbitrary m values is provided in chapter 6.

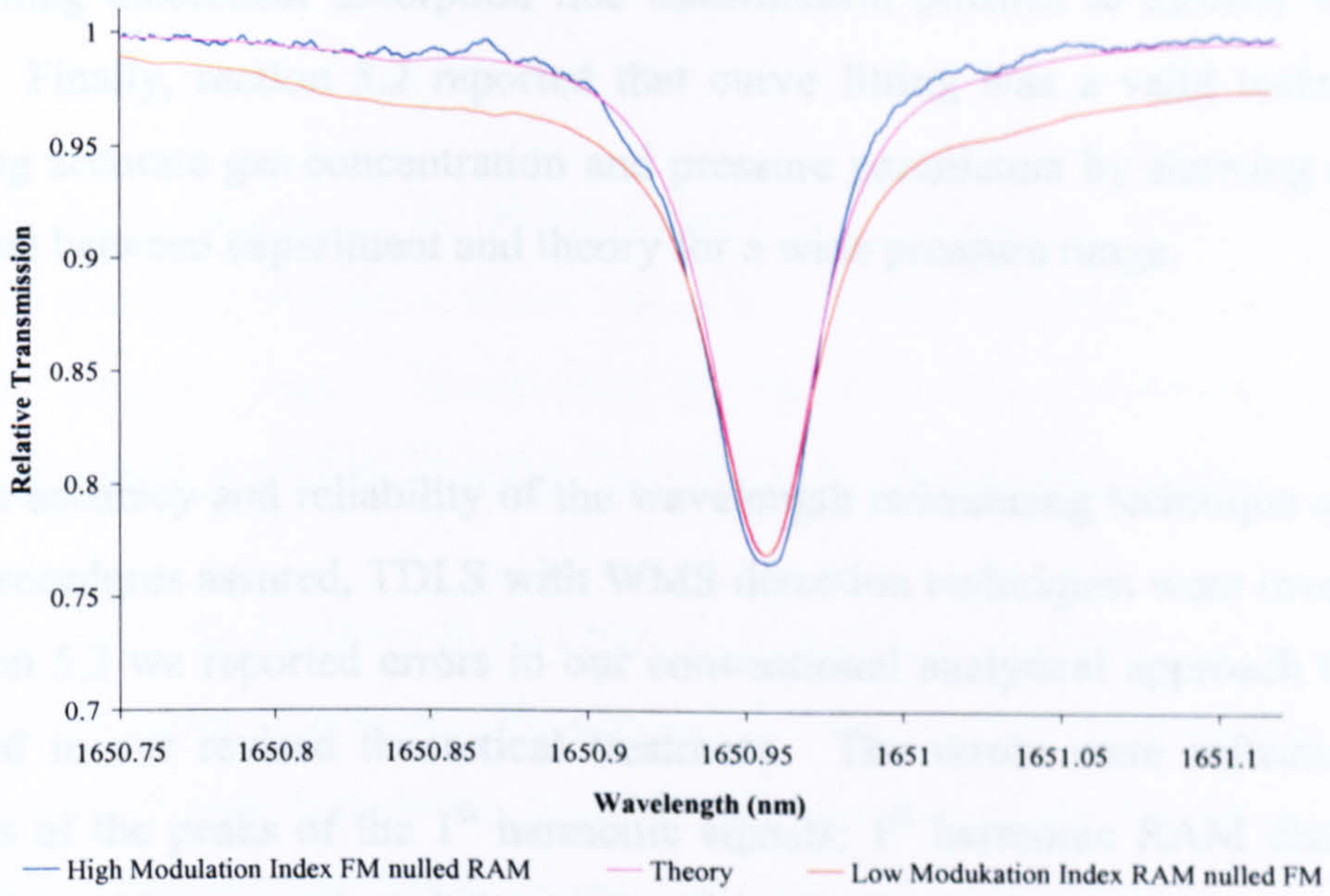

Figure 5.51: 10.13 % CH_4 : N_2 balance at 15.9 °C and 1.001 bar pressure – Comparison of FM nulled RAM signal (at high modulation index) to integrated RAM nulled FM signal (at low modulation index) and theory

5.6 Conclusion

This chapter principally demonstrated some of the issues that have limited accurate and simultaneous measurement of gas concentration and pressure in current industry-based gas detection technologies (direct TDLS and TDLS / WMS) and then, through careful signal and theoretical analysis, proposed techniques that could provide the basis of reliable solutions suitable for field-deployable instruments.

Section 5.2 reported on an accurate and reliable wavelength referencing technique that provided a solution to the problems of non-linearity and non-repeatability of the current vs. wavelength relationship in DFB lasers, whilst offering improved resolution and stability on previously reported bulk-optic approaches. In addition, this section reported on a technique for establishing host gas broadening coefficients

by matching theoretical absorption line transmission profiles to directly recovered signals. Finally, section 5.2 reported that curve fitting was a valid technique for extracting accurate gas concentration and pressure parameters by showing excellent agreement between experiment and theory for a wide pressure range.

With the accuracy and reliability of the wavelength referencing technique and curve fitting procedures assured, TDLS with WMS detection techniques were investigated. In section 5.3 we reported errors in our conventional analytical approach that were identified in our revised theoretical treatment. The errors were reflected in the locations of the peaks of the 1st harmonic signals; 1st harmonic RAM distortion at both high and low m values led to asymmetry in the peak amplitudes. From the theoretical analysis we proposed an approach to eliminating the RAM interference, which was successful but remained limited, in terms of accurate measurements of concentration and pressure, by scaling factor and calibration issues inherent to derivative analysis.

In section 5.5 we proposed a new approach, which, in principle, provides the absolute absorption line transmission function. In so doing, the technique can be absolute without the need for scaling factors or system calibration. This technique was experimentally investigated and we demonstrated that it could form the basis of an accurate technique for simultaneous measurements of concentration and pressure in field-deployable instruments, within certain limitations. The main limitation is in the recovered signal-to-noise ratio, where the recovered signal amplitude is scaled by $\sin(\psi)$. At this stage, achieving measurable signals requires a high modulation index (in this case m ~ 2), which introduces further errors due to distortion by higher order RAM interference. The following chapter looks at techniques to improve the signal-to-noise ratio of TDLS / WMS 1st harmonic RAM based detection.

5.7 References

[5.1] M. R. Hammond, T. D. Wilkerson and V. B. Wickwar, "High – Resolution Spectra of Atmospheric Water Vapor in the Near – IR using a Raman Shifted Alexandrite Laser," Proceedings of the Eleventh Atmospheric Radiation Measurement (ARM) Science Team Meeting, March 2001, Atlanta, Georgia.

[5.2] G. Durry, V. Zeninari, B. Parvitte, T. Le barbu, F. Lefevre, J. Ovarlez and R. R. Gamache, "Pressure - Broadening Coefficients and Linestrengths of H_2O near 1.39 μm: Application to the In Situ Sensing of the Middle Atmosphere with Balloonborne Diode Lasers," Journal of Quantitative Spectroscopy and Radiative Transfer, Vol. 94, pp. 387-403, 2005.

[5.3] M. Gharavi, S. G. Buckley, "Diode Laser Absorption Spectroscopy Measurement of Linestrengths and Pressure Broadening Coefficients of the Methane $2\nu_3$ Band at Elevated Temperatures," Journal of Molecular Spectroscopy, Vol. 229, pp. 78-88, 2005.

[5.4] A. S. Pine, "Self -, N_2, O_2, H_2, Ar, and He Broadening in the ν_3 Band Q Branch of CH_4," Journal of Chemical Physics, Vol. 97, No. 2, pp. 773-785, July 1992.

[5.5] L. C. Philippe and R. K. Hanson, "Laser Diode Wavelength – Modulation Spectroscopy for Simultaneous Measurement of Temperature, Pressure and Velocity in Shock – Heated Oxygen Flows," Applied Optics, Vol. 32, No. 30, pp 6090-6103, October 1993.

[5.6] P. Kluczynski and O. Axner, "Theoretical Description based on Fourier Analysis of Wavelength – Modulation Spectrometry in terms of Analytical and Background Signals," Applied Optics, Vol. 38, No. 27, pp 5803-5815, September 1999.

[5.7] S. Schilt, L. Thevenaz and P. Robert, "Wavelength Modulation Spectroscopy: Combined Frequency and Intensity Laser Modulation," Applied Optics, Vol. 42, No. 33, pp 6728-6738, November 2003.

[5.8] P. Werle, "A Review of Recent Advances in Semiconductor Laser based Gas Monitors," Spectrochimica Acta Part A: Molecular and Biomolecular Spectroscopy, Vol. 54, No. 2, pp 197-236, February 1998.

Chapter 6

Results and Analysis 2

6.1 Introduction

Throughout this thesis we have discussed the fact that conventional approaches to TDLS with WMS detection are not suitable for gas concentration and pressure measurements in stand-alone industrial sensors, due to issues regarding unknown system scaling and gas parameters. In chapter 5 we proposed a new approach and experimentally demonstrated that this technique can provide accurate, quantitative measurements of a gas composition, within certain limitations. The main limitation lies in the low SNR associated with recovering signal amplitudes scaled by $\sin(\psi)$, where ψ is the phase separation between the laser AM and FM. Intuitively, increasing this phase separation would lead to an increase in the recovered signal amplitude.

This chapter reports on the development of the new TDLS / WMS technique reported in Chapter 5 that leads to an increase in signal-to-noise ratio and, in so doing, provides greater accuracy in the simultaneous measurement of gas concentration and pressure.

6.2 Increasing the Modulation Frequency

6.2.1 Introduction

In [6.1] Jacobsen et al reported on the current / frequency modulation characteristics of frequency modulated lasers operating in the near infra-red region. Over modulation frequencies of 1 kHz to 500 MHz Jacobsen reported that the FM phase decreased monotonically from ~ - 20 ° at low frequency to - 180 ° at high frequency. This result was also confirmed by Schilt and Thevenaz [6.2] who illustrated experimentally that the FM phase delay changes from ~ -10 ° at 100 Hz to ~ -75 ° at 100 kHz in a 2μm DFB laser using a CO_2 gas absorption line. In both [6.1] and [6.2] the phase change with modulation frequency was attributed to two opposing effects in the semiconductor material that determine the FM: (i) a thermal effect, whereby a modulation of the injection current leads to a modulation of the temperature of the laser, thus altering the physical length of the laser cavity and (ii) a carrier density effect, whereby the carrier density is modulated by the modulation of the injection current, leading to a change in refractive index. The two effects combine to give the overall effect on the laser FM. The thermal effect is much larger in magnitude but is slower relative to the carrier density effect and, due to time averaging, diminishes in magnitude and influence with increasing modulation frequency; as a consequence the FM phase delay increases. It was stated in chapter 5 that the degree of coupling of the FM depends on, among other things, the individual structure and the operating point of the laser [6.3]. In addition, there are inherent phase shifts in the detection electronics and, therefore, the FM phase must be determined relative to the AM and

is unique to a particular laser. A detailed investigation of the modulation characteristics of diode lasers is beyond the scope of this thesis and interested readers are directed toward the following text: [6.4]. It was decided to increase the modulation frequency to 100 kHz initially as this provided a satisfactory level of improvement in the recovered signal (by increasing the measured sin(ψ) component), whilst falling within the modulation limits of conventional industrial TDLS techniques [6.3].

6.2.2 Revised Experimental System and Procedure

The laboratory system architecture remained unchanged from the one described in section 5.5.2 of chapter 5. When modulating at 100 kHz the signal amplitudes are different (discussed later in section 6.3) compared to signals at 10 kHz and, therefore, the lock-in amplifier sensitivity and gain settings must be altered along with the phase settings. Again, the settings are noted in tables at each measurement. The normalisation procedure of dividing the gas signal by the "no gas signal" and using the 1st harmonic response of the fibre resonator to reference the normalised signal to wavelength, remained unchanged also.

6.2.3 Results and Discussion

As with the previous investigations of TDLS / WMS at 10 kHz, the modulation amplitude was set to approximately 2*γ. As explained previously in chapter 4, 1 atmosphere of methane was added to the cell and the sinusoidal amplitude was increased until a maximum FM 1st harmonic signal was reached. The optimum amplitude was 1.2 V peak-to-peak (δV = 600 mV). Recalling that the 2*γ modulation amplitude for measurements at 10 kHz was 600 mV peak-to-peak (δV =

300 mV), this agrees well with Jacobsen et al [6.1] who reported that, between 10 kHz and 100 kHz the magnitude of the current / frequency transfer function (the magnitude of the frequency deviation relative to the amplitude of the injection current modulation), dropped by half. Shown below in figure 6.1 are the RAM nulled FM traces for a 10.13 % CH_4 in N_2 at 1.007 bar pressure and 19.4 °C gas composition at 10 kHz and 100 kHz, taken with the respective m ~ 2 modulation indexes. Table 6.1 lists the lock-in amplifier settings, including the required phase values that were used in the experiments.

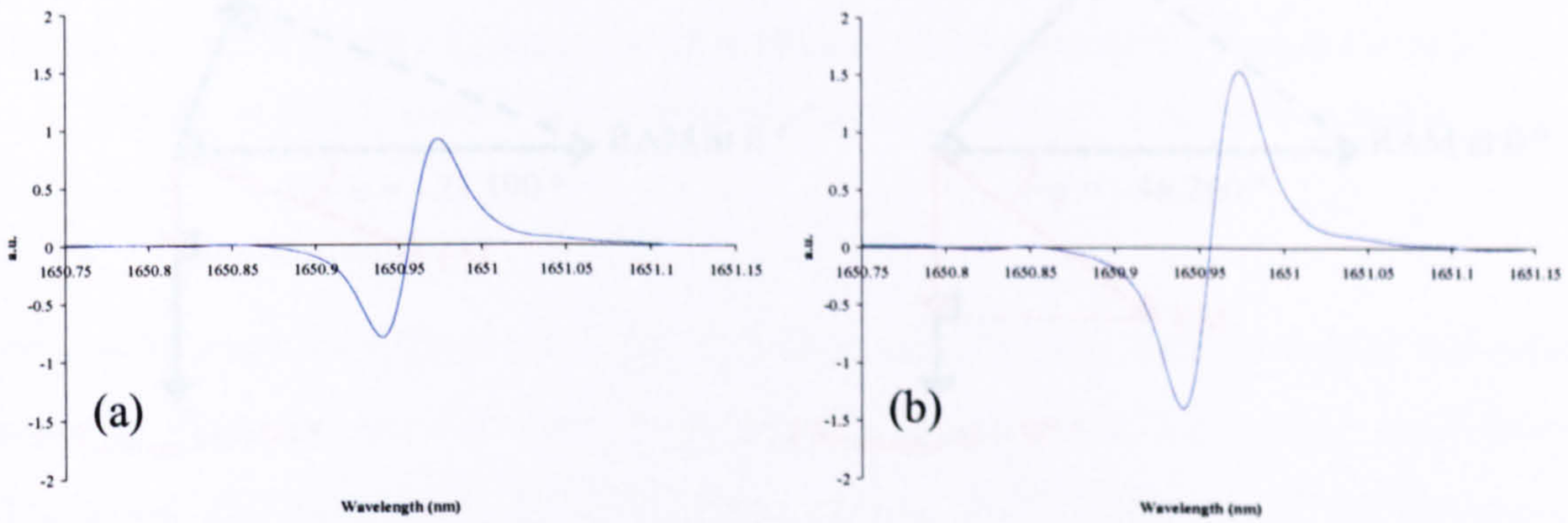

Figure 6.1: 10.13 % CH_4 : N_2 balance at 19.4 °C and 1.007 bar pressure – RAM nulled FM signals for (a) 10 kHz at m ~ 2 and (b) 100 kHz at m ~ 2

Modulation Frequency	10 kHz	100 kHz
AC Gain	26 dB, Dynamic Range:21	
Sensitivity	5 mV	
Time Constant	1 ms	
Reference Harmonic	1st	
Phase to Maximise RAM	+ 14.190 °	- 8.240 °
Phase to Null RAM	- 75.810 °	- 98.240 °
Phase to Null FM	+ 81.000 °	+ 35.5 °

Table 6.1: Settings for Perkin Elmer 7280 DSP lock-in amplifier

The relative magnitudes of the signals in figure 6.1 (a) and (b) appear, initially, not to agree with the diminishing FM hypothesis, but become more understandable when we consider the phase relationships and signal measurement process in more detail. In the phasor diagram shown in figure 6.2 below the phase relationships of the laser AM and FM at 10 kHz and 100 kHz are illustrated.

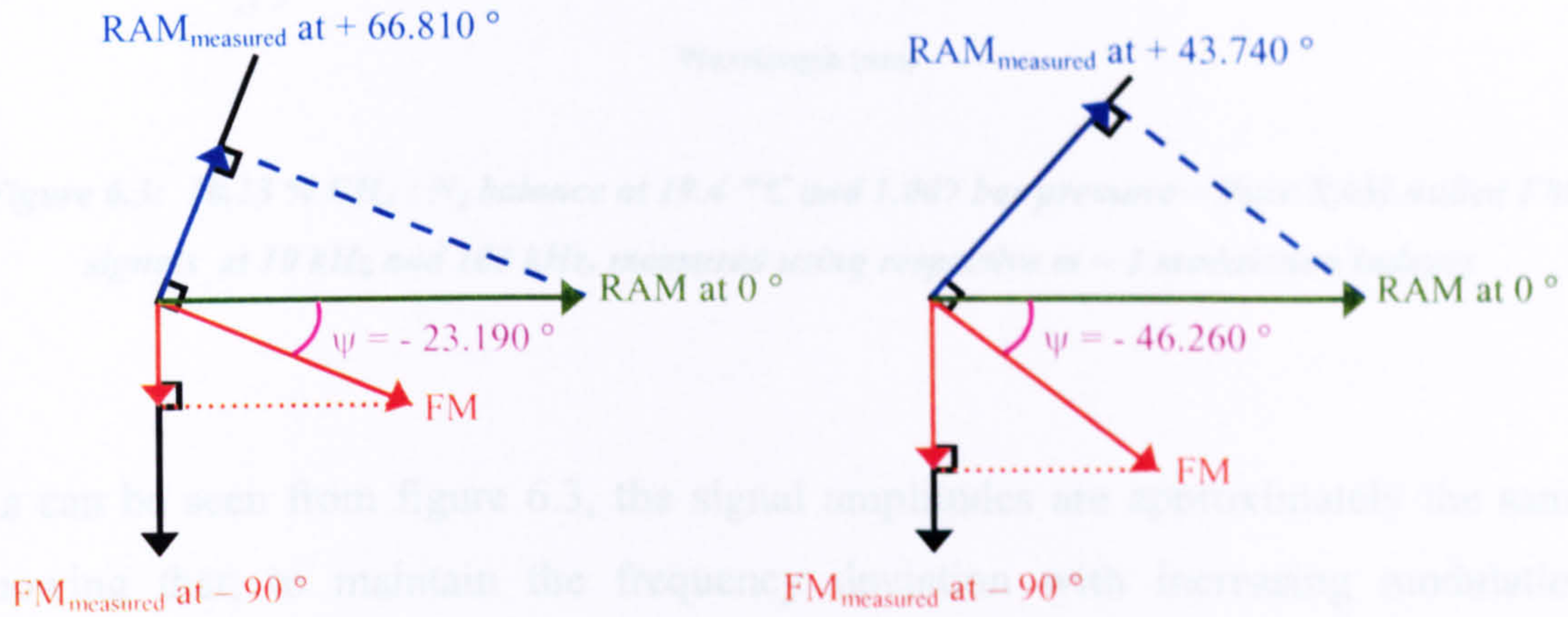

Figure 6.2: Phase relationships between AM and FM at (a) 10 kHz and (b) 100 kHz

It can be seen from figure 6.2 that when we modulate at a higher frequency the phase at which FM lags the AM increases as expected. In order to null the AM, detection of the FM signal always occurs at quadrature to the closely maximised RAM component on the X vector and as such, when the phase angle increases negatively, a greater proportion of the FM signal is projected onto the FM measurement axis. The FM component measured at 10 kHz is FM.sin(23.190 °) and at 100 kHz is FM.sin(46.260 °). Therefore, the amplitude of the pure FM component at 10 kHz is given by the amplitude of the signal in figure 6.1 (a) divided by sin(23.190 °) and the amplitude of the pure FM component at 100 kHz is given by the amplitude of the signal in figure 6.1 (b) divided by sin(46.260 °). The pure FM signals at 10 kHz and 100 kHz are shown in figure 6.3.

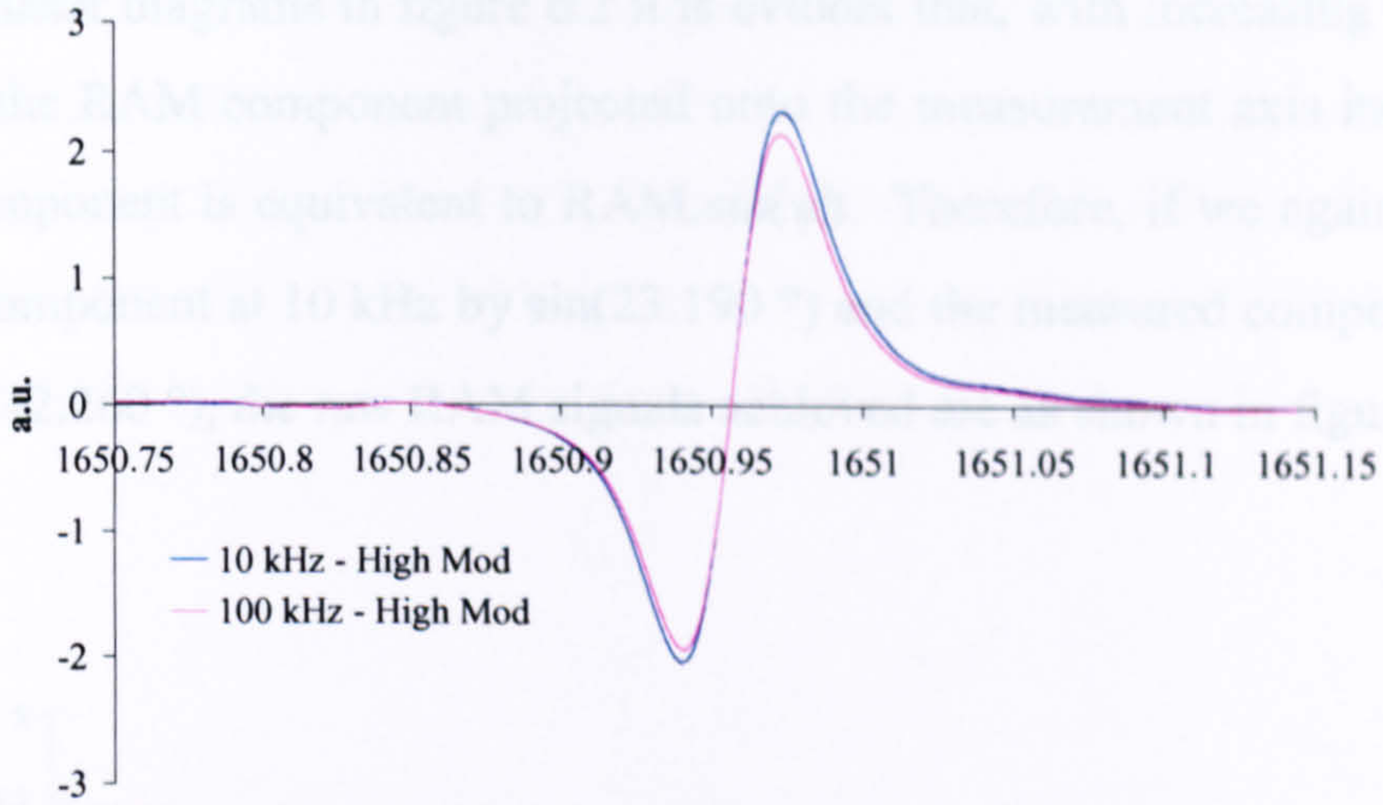

Figure 6.3: 10.13 % CH_4 : N_2 balance at 19.4 °C and 1.007 bar pressure – Pure RAM nulled FM signals at 10 kHz and 100 kHz, measured using respective m ~ 2 modulation indexes

As can be seen from figure 6.3, the signal amplitudes are approximately the same showing that, to maintain the frequency deviation with increasing modulation frequency, the amplitude of the injection current modulation has to be increased. The measured FM nulled RAM variation signals for 10 kHz and 100 kHz modulation frequency, at an optimised modulation index of m ~ 2 in each case, are shown in figure 6.4.

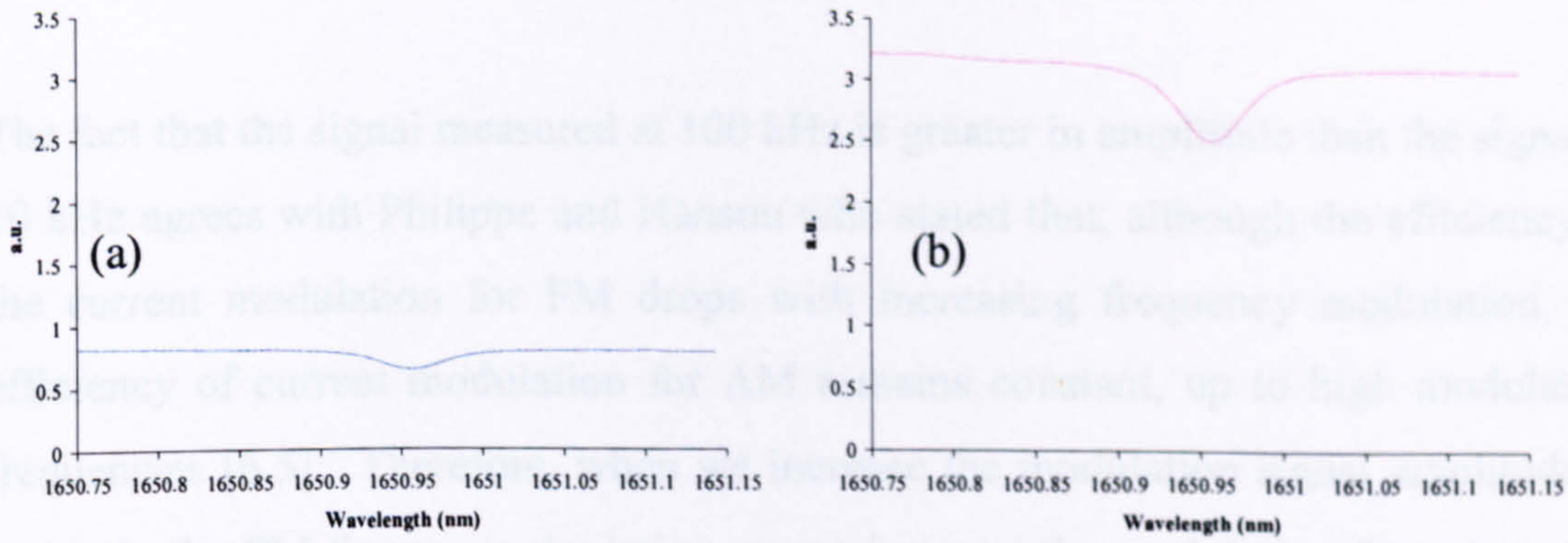

Figure 6.4: 10.13 % CH_4 : N_2 balance at 19.4 °C and 1.007 bar pressure – FM nulled RAM signals (a) 10 kHz and (b) 100 kHz, measured using m ~ 2 modulation index

From the phasor diagrams in figure 6.2 it is evident that, with increasing modulation frequency, the RAM component projected onto the measurement axis increases and that this component is equivalent to RAM.sin(ψ). Therefore, if we again divide the measured component at 10 kHz by sin(23.190 °) and the measured component at 100 kHz by sin(42.260 °), the raw RAM signals achieved are as shown in figure 6.5.

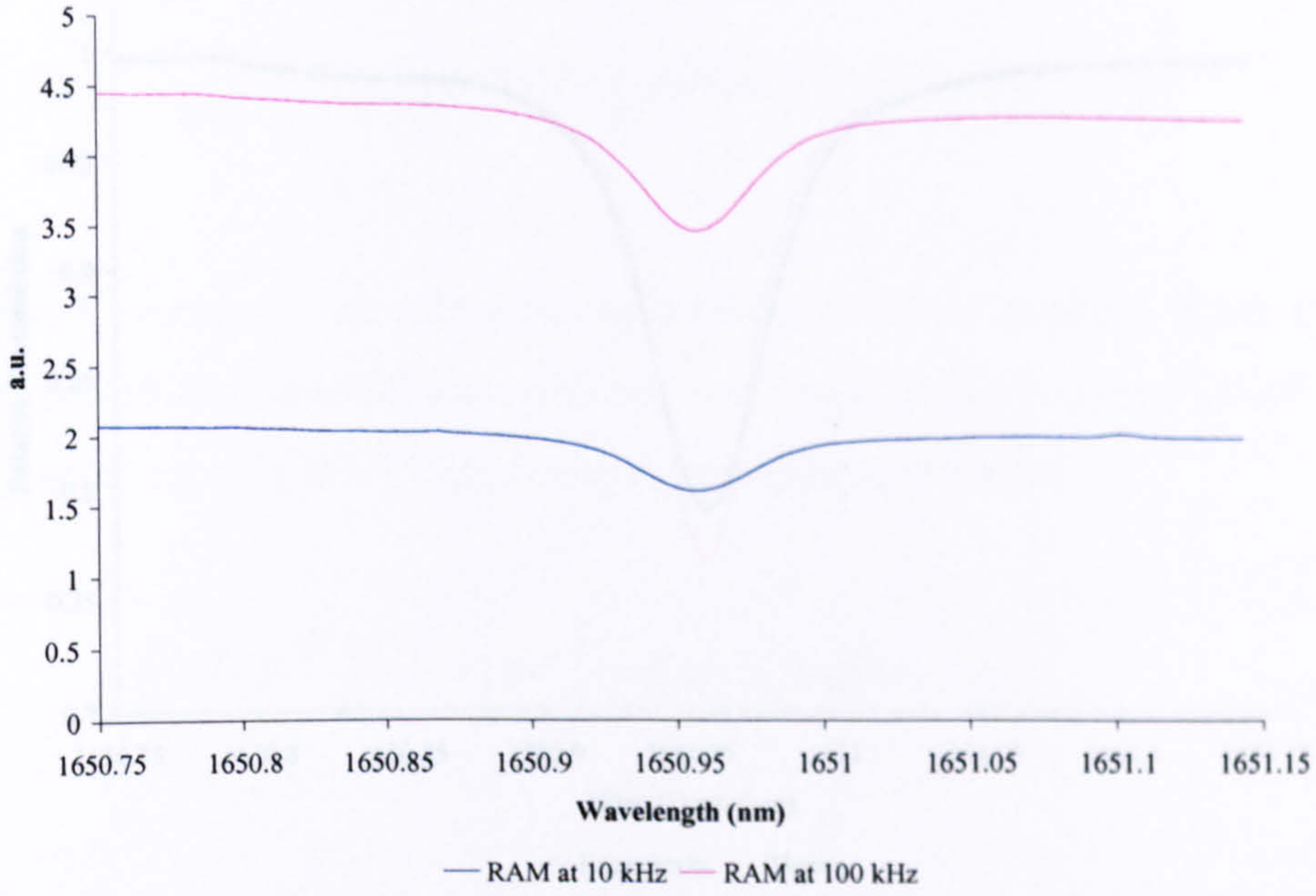

Figure 6.5: 10.13 % CH_4 : N_2 balance at 19.4 °C and 1.007 bar pressure – Pure FM nulled RAM signals at 10 kHz and 100 kHz, measured using m ~ 2 modulation index

The fact that the signal measured at 100 kHz is greater in amplitude than the signal at 10 kHz agrees with Philippe and Hanson who stated that, although the efficiency of the current modulation for FM drops with increasing frequency modulation, the efficiency of current modulation for AM remains constant, up to high modulation frequencies [6.5]. Therefore, when we increase the modulation signal amplitude to maintain the FM frequency deviation, as we increase the modulation frequency (δV = 300 mV at 10 kHz to 600 mV at 100 kHz), we increase the AM signal accordingly (RAM signal at 100 kHz is a factor of 2 greater than the RAM signal at 10 kHz). The SNR of this particular signal is further boosted by the fact that the AM-FM

phase separation, ψ, increases with increasing modulation frequency, increasing the magnitude of the RAM component projected onto the measurement axis. The FM nulled RAM signal measured using a high modulation index of m ~ 2 at 100 kHz, when addressing a 10.13 % CH_4:N_2 composition at a pressure of 1.007 bar and 19.4 °C, is compared to theory as shown in figure 6.6 below.

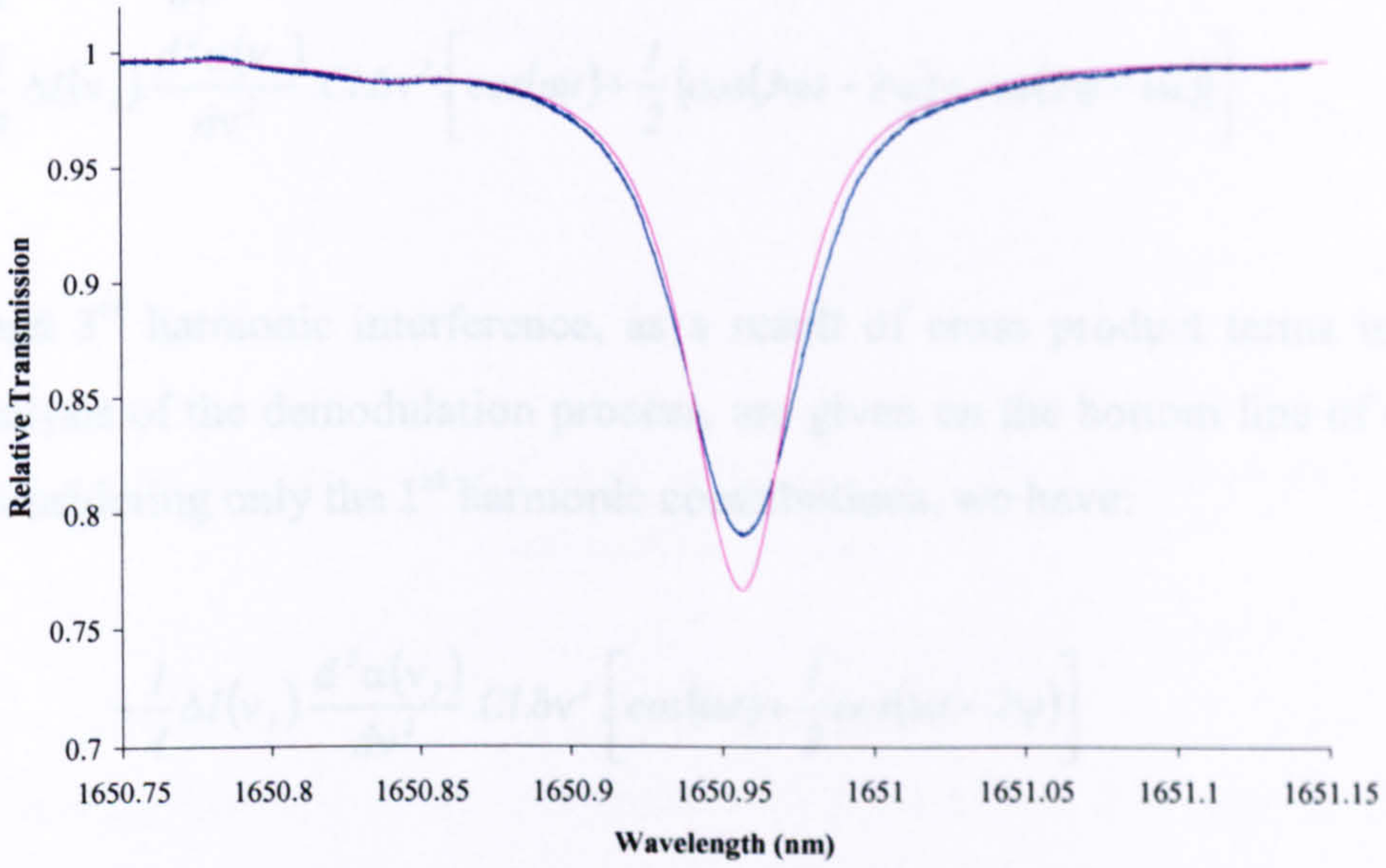

Figure 6.6: 10.13 % CH_4 : N_2 balance at 19.4 °C and 1.007 bar pressure – FM nulled RAM signal at 100 kHz, measured using m ~ 2 modulation index, compared to theory

As can be seen from figure 6.6, the significant error as a result of RAM induced harmonic interference associated with measurements at high m values, remains (previously discussed in section 5.3.3 of chapter 5). However, further analysis of these harmonic contributions can lead to the development of correction factors.

With increasing m, the FM amplitude increases; therefore, at any position on the absorption profile $\alpha(\nu_l)$, the laser frequency is being modulated and the recovered RAM variation is actually an averaged value of $\alpha(\nu_l)$ (averaged over the frequency

modulation amplitude, $\delta\nu$). Errors as a result of averaging will be negligible when addressing linear parts of the profile but most severe near the peak. Recalling equation (5.10) from chapter 5, repeated below for convenience (again, the full derivation of these terms is given in Appendix D):

$$-\frac{1}{2}\Delta I(\nu_1)\frac{d\alpha(\nu_1)}{d\nu}.Cl.\delta\nu.(cos(\psi)) \qquad (6.1)$$
$$-\frac{1}{4}I(\nu_1)\frac{d^2\alpha(\nu_1)}{d\nu^2}.Cl.\delta\nu^2$$
$$-\frac{1}{4}\Delta I(\nu_1)\frac{d^2\alpha(\nu_1)}{d\nu^2}.Cl.\delta\nu^2.\left[cos(\omega t)+\frac{1}{2}\{cos(3\omega t-2\psi)+cos(2\psi-\omega t)\}\right]$$

the 1st and 3rd harmonic interference, as a result of cross product terms in the 2nd order analysis of the demodulation process, are given on the bottom line of equation (6.1). Considering only the 1st harmonic contributions, we have:

$$-\frac{1}{4}\Delta I(\nu_1)\frac{d^2\alpha(\nu_1)}{d\nu^2}.Cl.\delta\nu^2.\left[cos(\omega t)+\frac{1}{2}cos(\omega t-2\psi)\right] \qquad (6.2)$$

Therefore, when considering a 2nd order approximation to the 1st harmonic RAM variation (for arbitrary values of $\delta\nu$) recovered by a lock-in amplifier, equation (5.11) in chapter 5 now becomes:

$$RAM_\omega = \Delta I(\nu_1)\cdot cos(\omega t)[1-\alpha(\nu_1)Cl] \qquad (6.3)$$
$$-\frac{1}{4}\Delta I(\nu_1)\frac{d^2\alpha(\nu_1)}{d\nu^2}.Cl.\delta\nu^2.\left[cos(\omega t)+\frac{1}{2}cos(\omega t-2\psi)\right]$$

Figure 6.7 shows these 1st harmonic contributions to the FM and AM measurements on a phasor diagram.

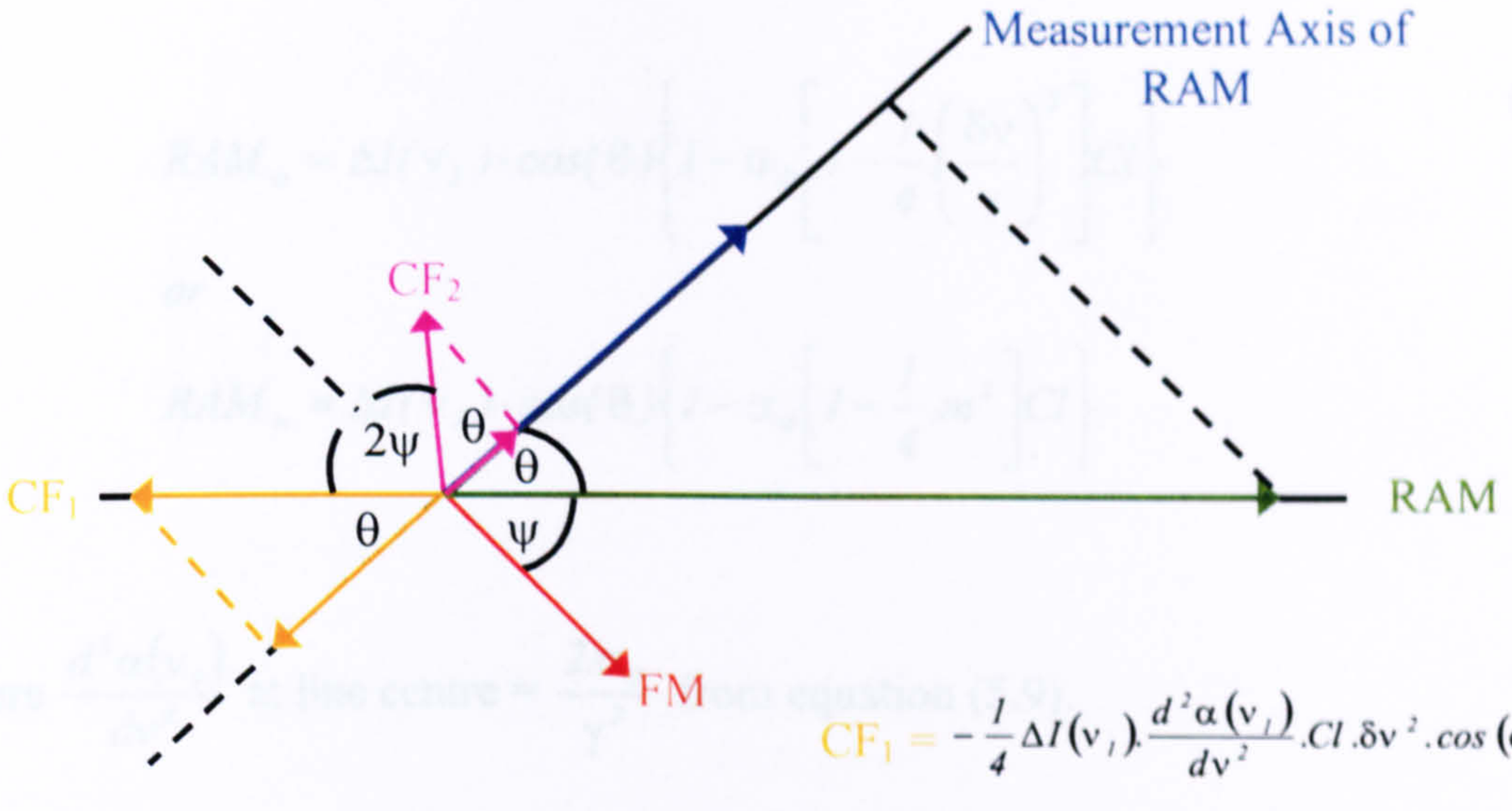

Figure 6.7: Phasor diagram showing 2nd order correction factors for 1st harmonic RAM detection with variable m values

If we consider detection of the FM nulled RAM signal at θ, it can be seen from figure 6.7 that the contributions are 180 ° out of phase and thus partially cancel each other out. The lock-in recovered 1st harmonic RAM signal at θ is thus given by:

$$RAM_{\omega} = \Delta I(\nu_1)\cdot\cos(\theta)[1-\alpha(\nu_1)Cl] \qquad (6.4)$$
$$-\frac{1}{4}\Delta I(\nu_1).\frac{d^2\alpha(\nu_1)}{d\nu^2}.Cl.\delta\nu^2.\cos(\theta)+\frac{1}{8}\Delta I(\nu_1).\frac{d^2\alpha(\nu_1)}{d\nu^2}.Cl.\delta\nu^2\cos(\theta)$$

This then simplifies to:

$$RAM_{\omega} = \Delta I(\nu_1)\cdot\cos(\theta)\left\{1-\left[\alpha(\nu_1)+\frac{1}{8}.\frac{d^2\alpha(\nu_1)}{d\nu^2}.\delta\nu^2\right]Cl\right\} \qquad (6.5)$$

As mentioned above, the errors are most severe at line centre and the 1st harmonic RAM signal at line centre is given by:

$$RAM_{\omega} = \Delta I(\nu_1) \cdot cos(\theta)\left\{1 - \alpha_0\left[1 - \frac{1}{4}.\left(\frac{\delta\nu}{\gamma}\right)^2\right]Cl\right\} \tag{6.6}$$

or

$$RAM_{\omega} = \Delta I(\nu_1) \cdot cos(\theta)\left\{1 - \alpha_0\left[1 - \frac{1}{4}.m^2\right]Cl\right\}$$

where $\frac{d^2\alpha(\nu_1)}{d\nu^2}$ at line centre = $\frac{2.\alpha_0}{\gamma^2}$ from equation (5.9).

Therefore, it can be concluded that, to a 2nd order approximation, the amplitude of the 1st harmonic FM nulled RAM signal can be reduced by as much as $\frac{1}{4}.m^2 \times 100$ %. This provides the possibility of detecting at high m values and applying the correction factor to the recovered signals; however, we would then be presented with the same issues that limited conventional TDLS approaches; whereby, the accuracy of the process would depend on how accurately the linewidth, γ, could be recovered from measured signals and how accurately $\delta\nu$ could be measured. The extent of the problem is reduced here as the errors on γ and $\delta\nu$ only apply to the correction factor and not to the entire signal. For very large values of m, higher order terms will also become more significant, leading to a greater magnitude of error.

Alternatively, as the signal-to-noise ratio has increased, it is possible to use lower m values. An FM nulled RAM signal measured using m ~ 0. 5 or ($\delta\nu \sim \gamma$ / 2) on a 10.13 % CH_4 in N_2 gas composition at 1.006 bar and 19.8 °C is shown compared to theory in figure 6.8 below. In principle, the worst case error is a decrease of signal amplitude by approximately 6 %.

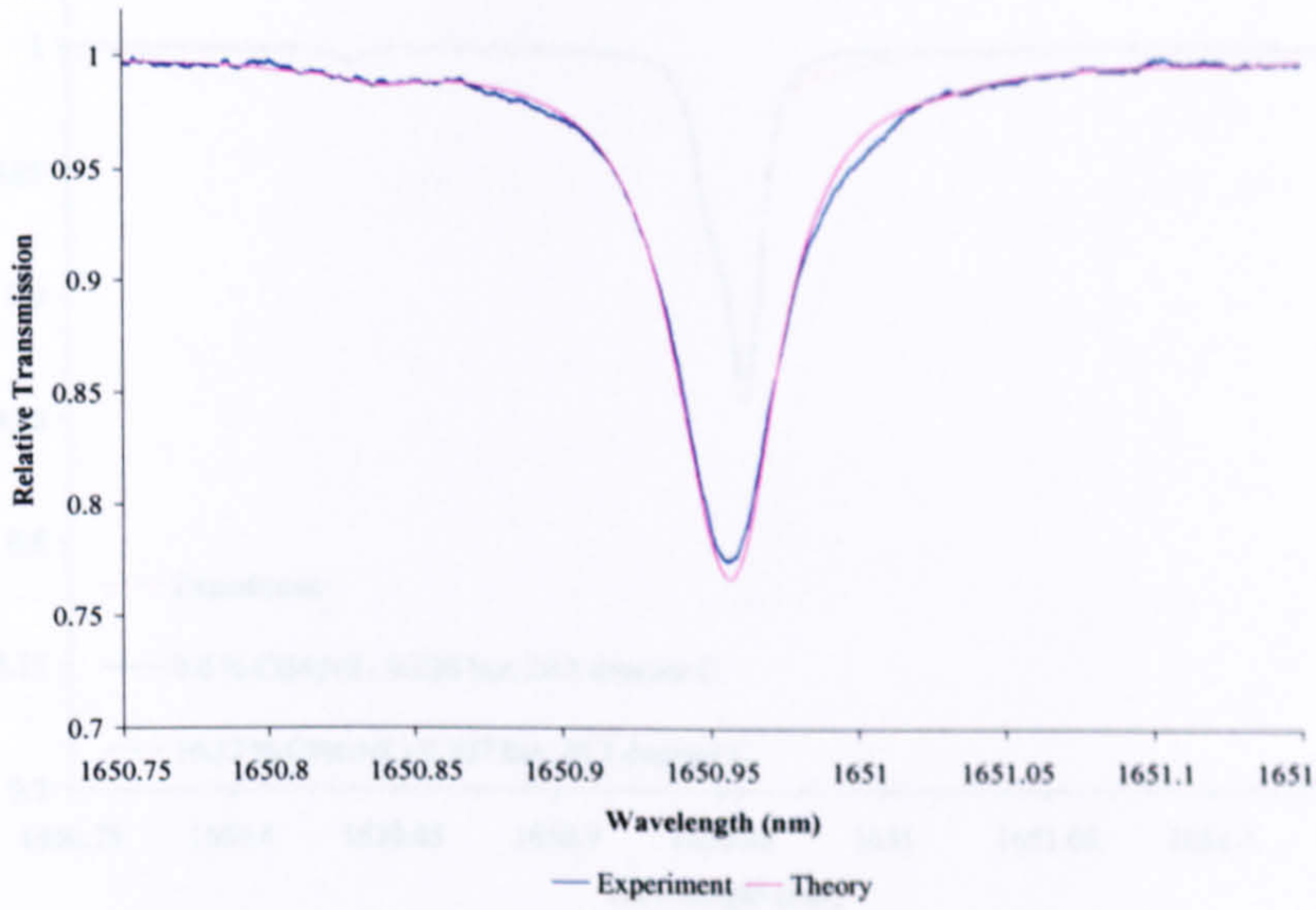

Figure 6.8: 10.13 % CH_4 : N_2 balance at 19.8 °C and 1.006 bar pressure – FM nulled RAM signal at 100 kHz, measured using m ~ 0.5 modulation index, compared to theory

Figures 6.9 to 6.13 show RAM measurements on 10.13 % CH_4 in N_2 at pressures ranging from 0.2 to 1.8 bar using a modulation index of m ~ 0.5. Table 6.2 shows the parameters used for the lock-in amplifier. The blue dashed curve is a theoretical prediction based on the calibrated gas mixture, digital gauge pressure and thermocouple temperature. The solid blue curve is a theoretical line of best fit; the parameters used in the curve fit are listed in the legends. Table 6.3 compares the parameters returned in the lines of best fit to the known parameters and lists the errors. Again, note that the curve fitting approach is a qualitative process, based on a visual match and, as such, the errors returned are approximate.

AC Gain	26 dB
Sensitivity	1 mV
Harmonic	1^{st}
Time Constant	1 ms

Table 6.2: Settings for Perkin Elmer 7280 DSP lock-in amplifier

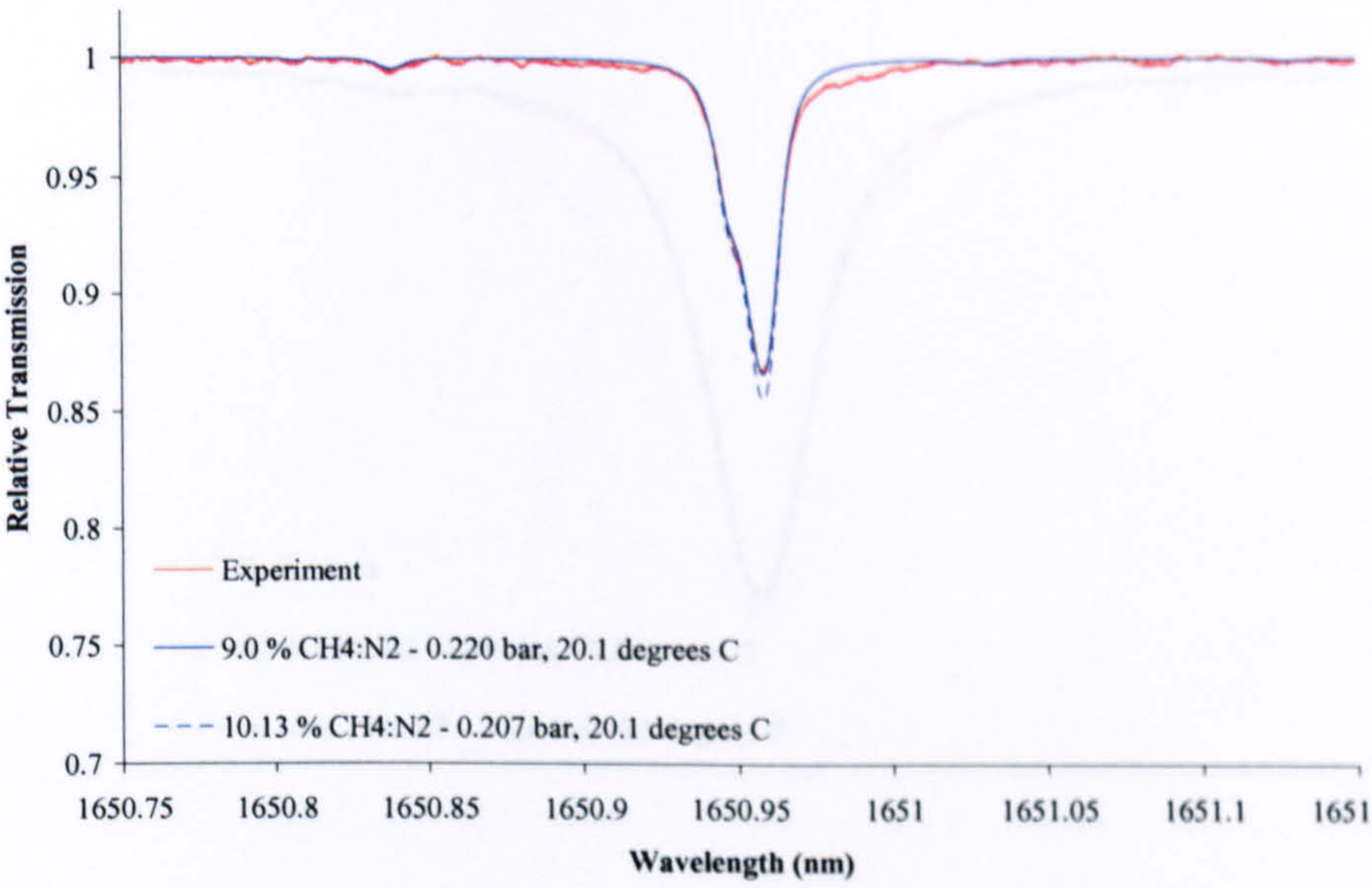

Figure 6.9: 10.13 % CH_4 : N_2 balance at 20.1 °C and 0.207 bar pressure – FM nulled RAM signal at 100 kHz, measured using m ~ 0.5 modulation index, compared to theory

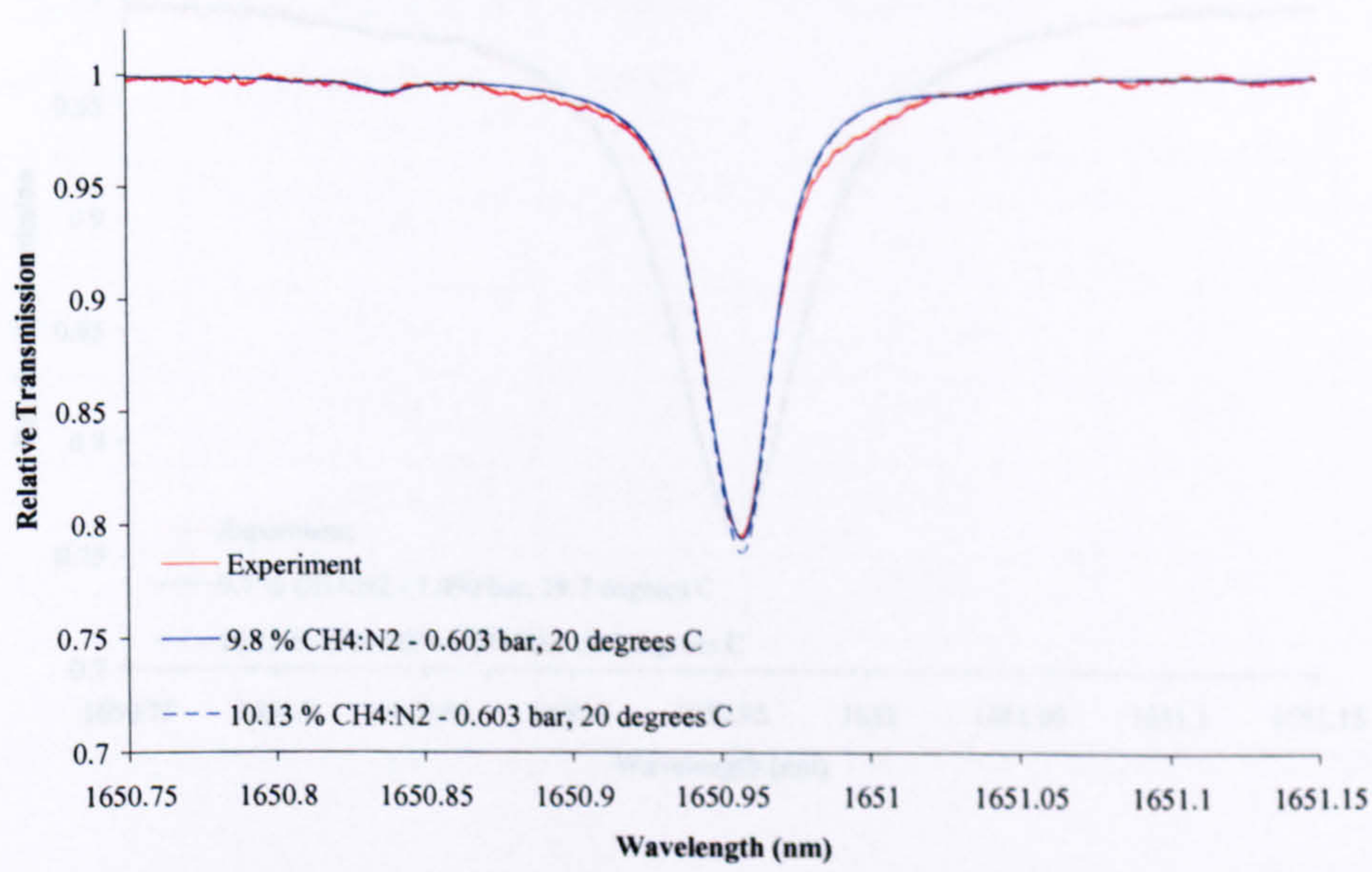

Figure 6.10: 10.13 % CH_4 : N_2 balance at 20.0 °C and 0.603 bar pressure – FM nulled RAM signal at 100 kHz, measured using m ~ 0.5 modulation index, compared to theory

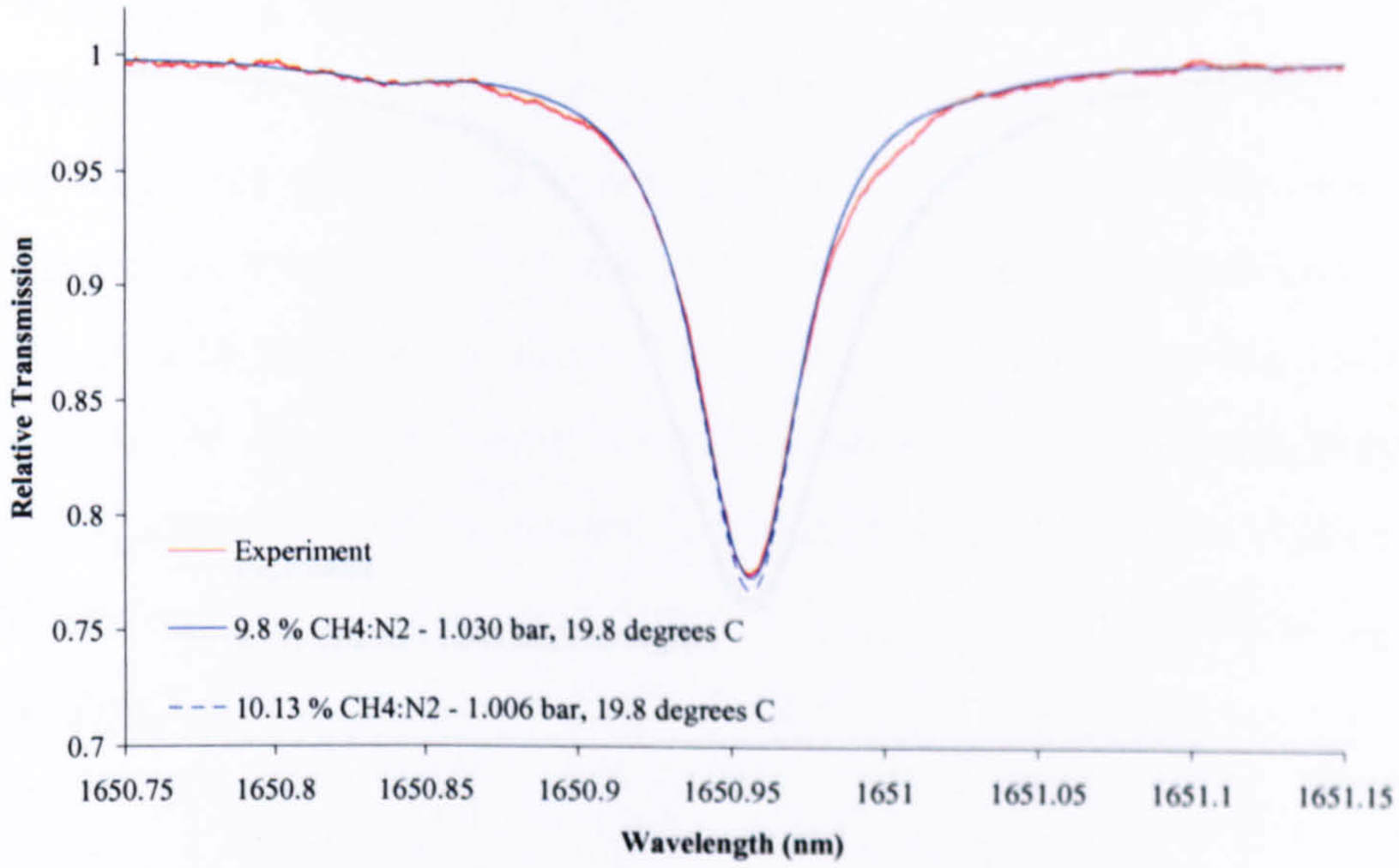

Figure 6.11: 10.13 % CH_4 : N_2 balance at 19.8 °C and 1.006 bar pressure – FM nulled RAM signal at 100 kHz, measured using m ~ 0.5 modulation index, compared to theory

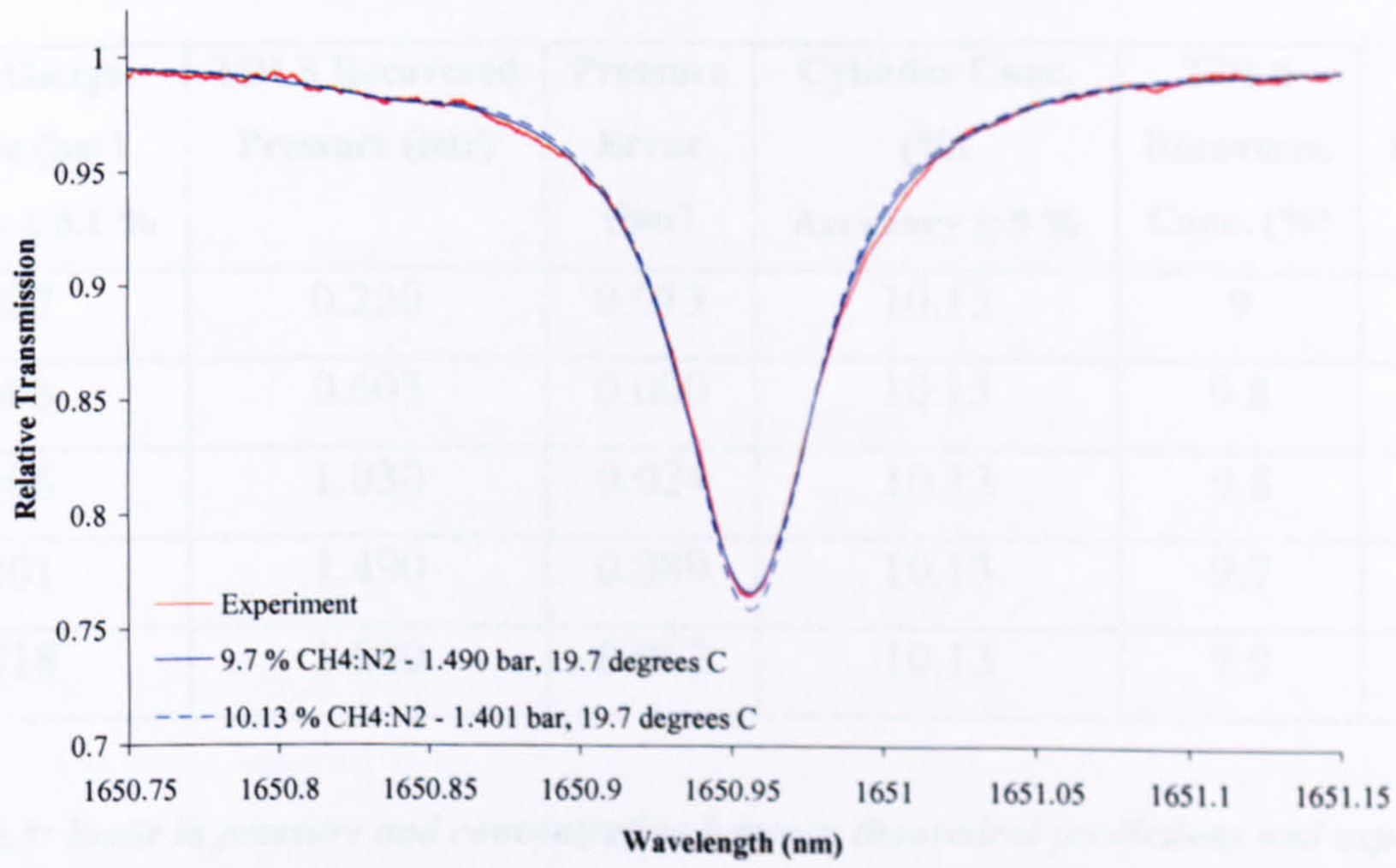

Figure 6.12: 10.13 % CH_4 : N_2 balance at 19.7 °C and 1.401 bar pressure – FM nulled RAM signal at 100 kHz, measured using m ~ 0.5 modulation index, compared to theory

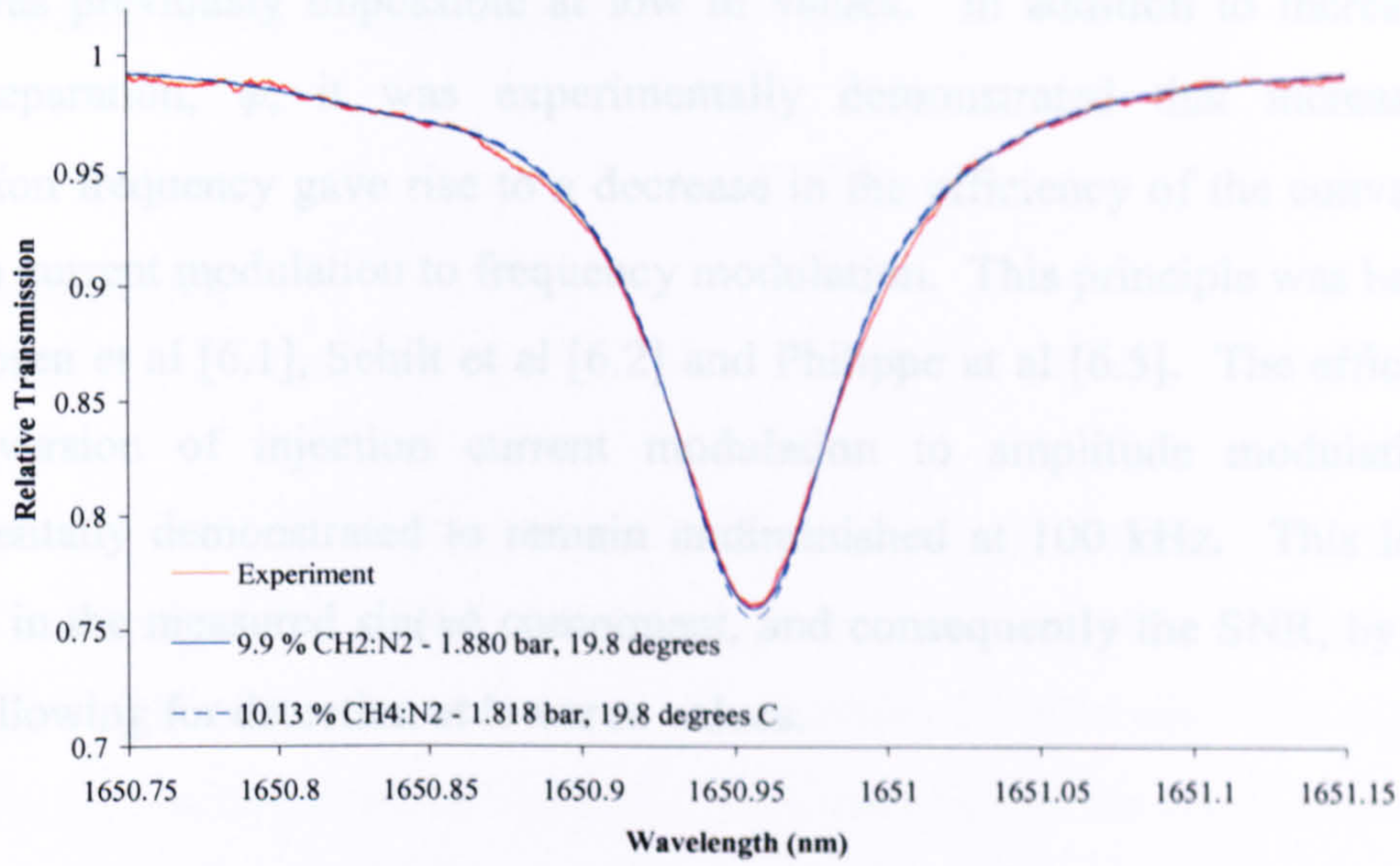

Figure 6.13: 10.13 % CH_4 : N_2 balance at 19.8 °C and 1.818 bar pressure – FM nulled RAM signal at 100 kHz, measured using m ~ 0.5 modulation index, compared to theory

Digital Gauge Pressure (bar) Accuracy ± 0.1 %	TDLS Recovered Pressure (bar)	Pressure Error (bar)	Cylinder Conc. (%) Accuracy ± 5 %	TDLS Recovered Conc. (%)	Conc. Error (%)
0.207	0.220	0.013	10.13	9	11.1
0.603	0.603	0.000	10.13	9.8	3.3
1.006	1.030	0.024	10.13	9.8	3.3
1.401	1.490	0.089	10.13	9.7	4.2
1.818	1.880	0.062	10.13	9.9	2.3

Table 6.3: Error in pressure and concentration between theoretical predictions and experiment

6.2.4 Conclusions

In this section we proposed increasing the modulation frequency from 10 kHz to 100 kHz in order to improve the signal-to-noise ratio, as detection of the FM nulled RAM

signal was previously impossible at low m values. In addition to increasing the phase separation, ψ, it was experimentally demonstrated that increasing the modulation frequency gave rise to a decrease in the efficiency of the conversion of injection current modulation to frequency modulation. This principle was backed up by Jacobsen et al [6.1], Schilt et al [6.2] and Philippe at al [6.5]. The efficiency of the conversion of injection current modulation to amplitude modulation was experimentally demonstrated to remain undiminished at 100 kHz. This led to an increase in the measured $\sin(\psi)$ component, and consequently the SNR, by a factor of ~ 2, allowing for detection at lower m values.

A review of the 2nd order contributions to 1st harmonic RAM variation measurements was provided, proposing that measurements could be made at any m value and the errors corrected; however, knowledge of the system parameters $\delta\nu$ and γ would be required, returning us to the issues that limited gas composition measurements in conventional industrial detectors.

With increased SNR it was possible to decrease the modulation index and, indeed, it was shown that, through curve fitting theoretical predictions to experimental data, measured using m ~ 0.5, simultaneous measurements could be made of the gas composition over an extended pressure range. A factor of ~ 2 improvement in the recovered RAM signals and a diminishing FM signal (meaning smaller errors due to inaccuracies in the selection of the FM nulling phase), by changing the modulation frequency from 10 kHz to 100 kHz, intuitively suggests that further increasing the modulation frequency would lead to further SNR improvement, meaning detection at smaller m values and greater accuracy in extracting the gas concentration and pressure. The following section describes an experimental technique for determining the optimum modulation parameters, with a view to achieving accurate and simultaneous gas concentration and pressure measurements over extended and ambient pressure ranges.

6.3 Finding the 90 ° Separation Point

6.3.1 Introduction

As mentioned above, increasing the modulation frequency further should lead to an increase in the AM-FM phase separation, ψ, and this, in turn, will increase the amplitude of the recovered RAM signal. A maximum 1st harmonic RAM signal will, obviously, be reached when ψ is 90 °. This section reports on an experimental procedure to determine the modulation frequency for the 90 ° separation phase using a fixed, known gas composition. Schilt et al [6.2] reported the characterisation of semiconductor lasers, measuring the AM-FM phase shift and the FM amplitude change with changing modulation frequency, using a CO_2 gas absorption line. In [6.2] Schilt only measured the relative FM signal phase and thus required two harmonic measurements in order to remove the effects of phase shifts in the detection electronics, as we measure components of both the AM and FM signals explicitly, we can measure the phase shift using only the 1st harmonic.

6.3.2 Revised Experimental System and Procedure

There were two notable issues with the previously reported experimental system architecture: (i) as the modulation frequency was extended in to the MHz range, the 1 MHz bandwidth offered by the LNP-2 photoreceiver was no longer adequate and (ii) the bandwidth of the SR830 DSP lock-in amplifier is restricted to only 100 kHz. For these reasons, the LNP-2s used to measure the signal from the gas cell and the signal from the fibre ring-resonator were replaced by PDA10CS InGaAs photodetectors (available bandwidth 17 MHz), and the SR830 DSP lock-in amplifier was replaced by a second Perkin Elmer 7280 DSP lock-in amplifier (available bandwidth 2 MHz).

The power reference signal monitors a change relative to the 5 Hz ramp sweep and so did not need replacing.

The procedure for finding the 90 ° separation was as follows: determination and measurement of the RAM nulled FM signal and the FM nulled RAM signal was carried out as previously described (chapter 5, sections 5.4 and 5.5) and the measurements of both were repeated at each increment of the modulation frequency. Again, as with previous experiments, measurements were made at a modulation amplitude of δV = 300 mV, giving a modulation index of m ~ 2 for the 10 kHz measurements. The fixed gas mixture for all measurements was 10.13 % CH_4 in N_2 at 1.030 bar and 23 °C. The lock-in amplifier settings used are noted in table 6.4 and the phase values for each measurement are noted in the figures below. Sensitivity settings had to be taken into account for each measurement as the signals were un-normalised and the lock-in amplifier automatically scaled the output relative to the sensitivity setting. i.e. the 10 kHz measurement was taken at 5 mV sensitivity and the higher frequency measurements were taken at 2 mV; the amplitudes of the 10 kHz signals then had to be scaled by 5/2 to normalise to the scaling of the lock-in amplifier.

	10 kHz	250 kHz and above
AC Gain	26 dB	26 dB
Sensitivity	5 mV	2 mV
Harmonic	1st	
Time Constant	1 ms	

Table 6.4: Settings for Perkin Elmer 7280 DSP lock-in amplifier

6.3.3 Results and Discussion

Figure 6.14 shows the FM phase lag increasing with increasing modulation frequency. It can be seen that at 1.25 MHz the phase lag is - 90 ° relative to the RAM. As the RAM is essentially aligned along the X, or in-phase, output of the dual phase lock-in amplifier, this then means that the FM is aligned along the Y or quadrature vector.

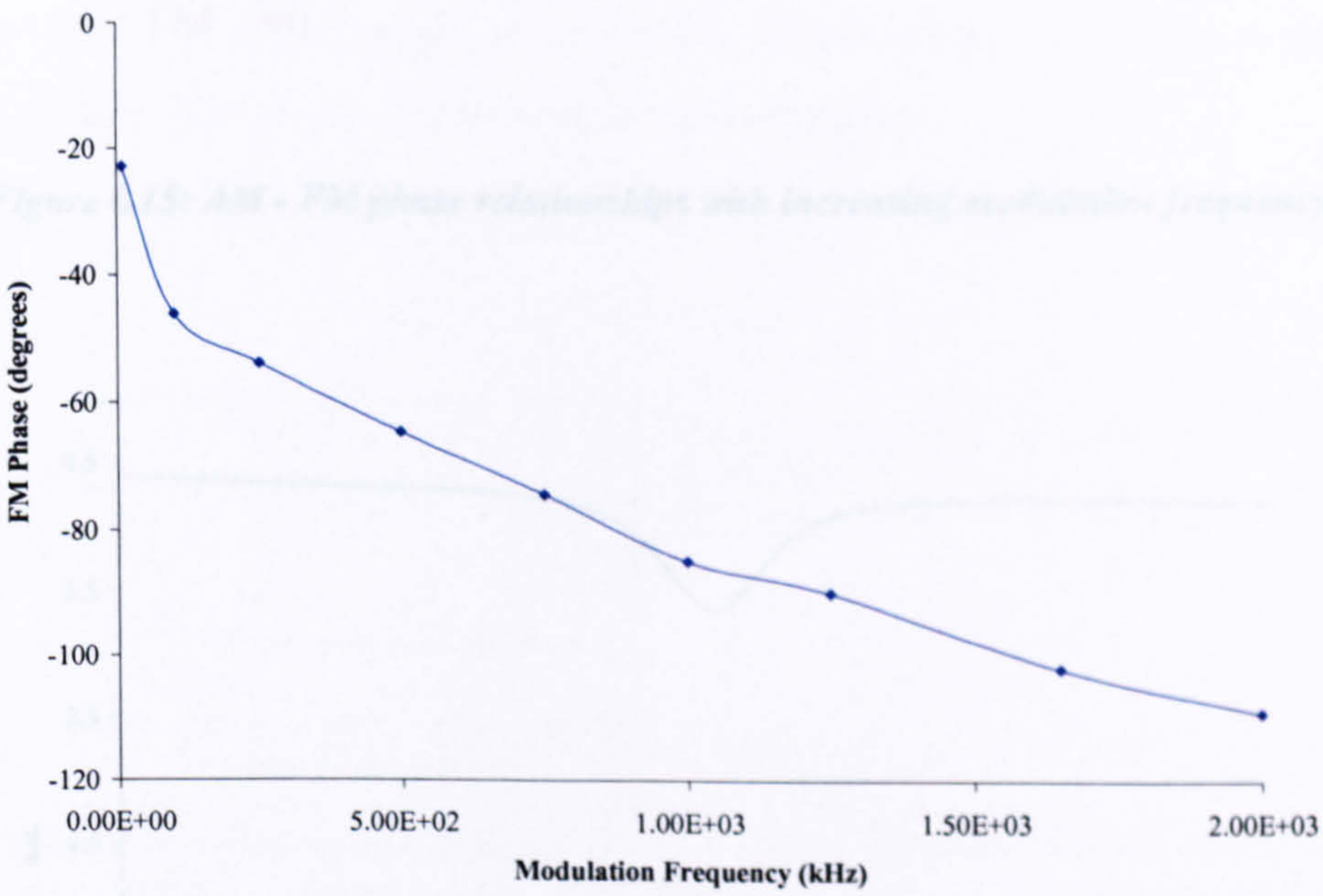

Figure 6.14: FM phase lag with increasing modulation frequency for 1650 nm DFB laser

The relative phases of the RAM and FM components at each increment of the modulation frequency are illustrated in figure 6.15 below. The lock-in outputs, X and Y, at the 90 ° separation point of 1.25 MHz are shown below in figure 6.16 and they prove that it is possible to make pure FM and pure AM measurements simultaneously.

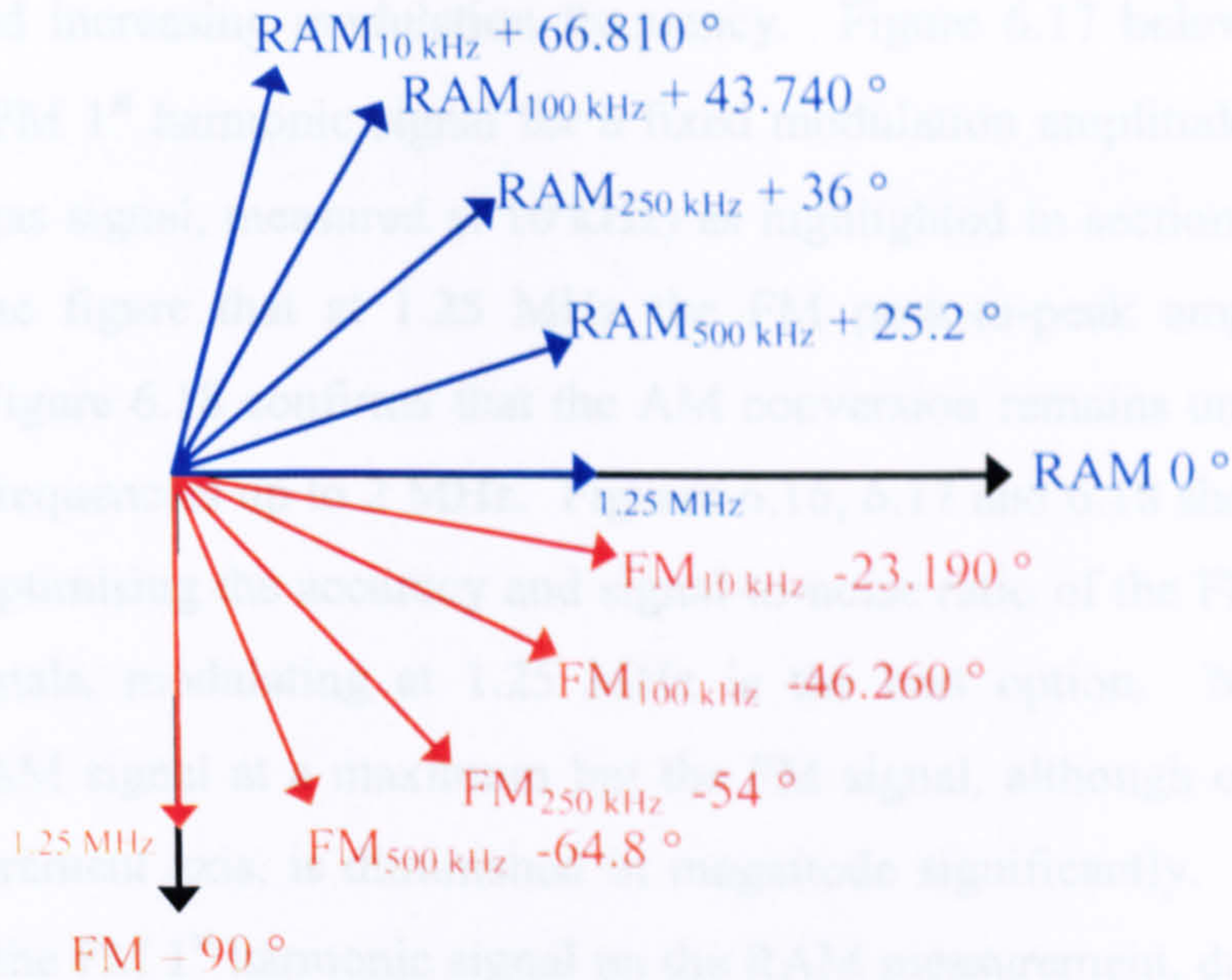

Figure 6.15: AM - FM phase relationships with increasing modulation frequency

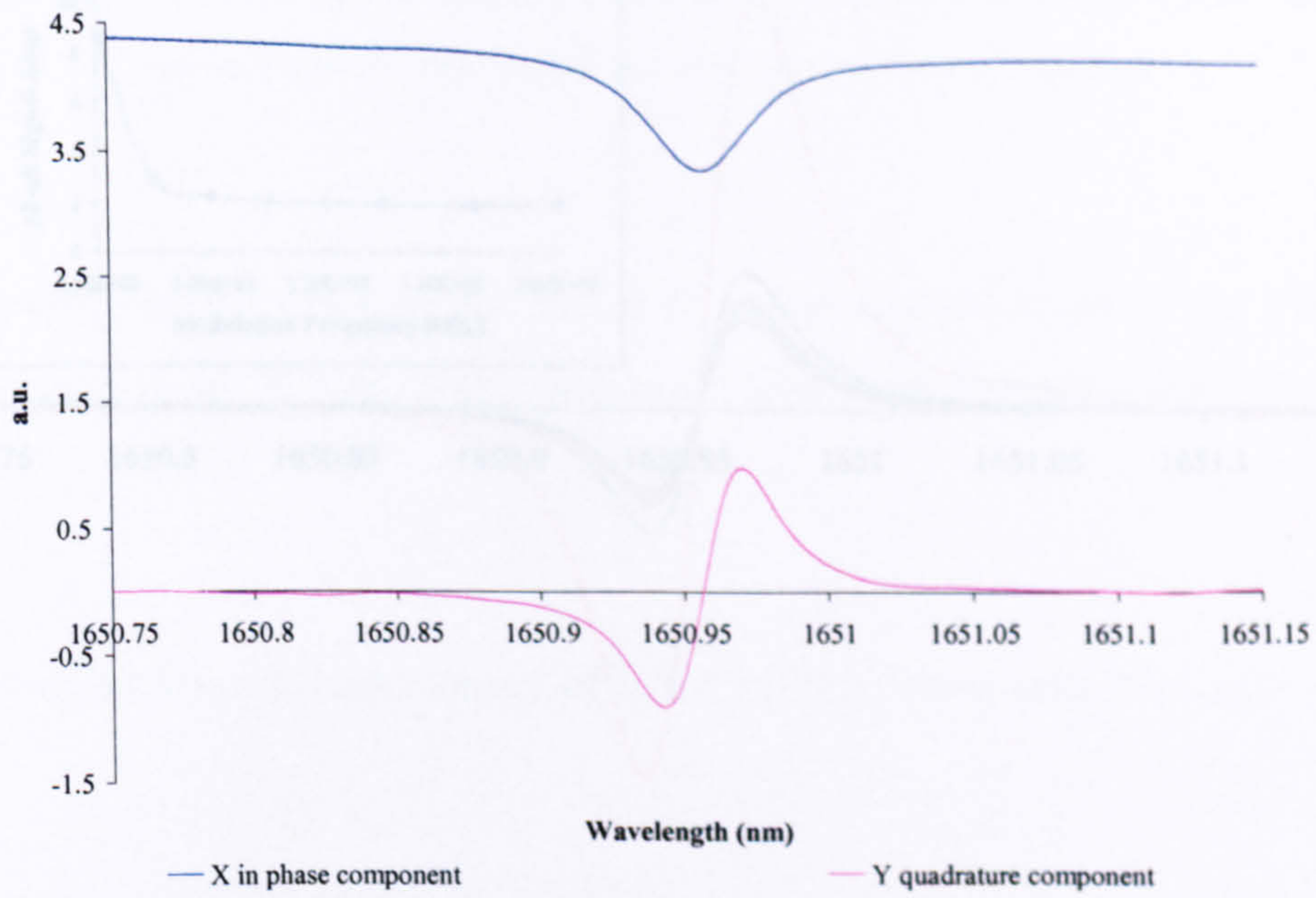

Figure 6.16: X – in phase and Y - quadrature components of the dual phase lock-in amplifier

From measurements on the gas absorption line we were also able to determine the efficiency of the AM and FM conversion for fixed injection current modulation

amplitude and increasing modulation frequency. Figure 6.17 below confirms the diminishing FM 1st harmonic signal for a fixed modulation amplitude (~ 2γ for ~ 1 atmosphere gas signal, measured at 10 kHz) as highlighted in section 6.2. It can be seen from the figure that at 1.25 MHz the FM peak-to-peak amplitude is at a minimum. Figure 6.18 confirms that the AM conversion remains undiminished for modulation frequencies up to 2 MHz. Figures 6.16, 6.17 and 6.18 show clearly that, in terms of optimising the accuracy and signal-to-noise ratio of the FM nulled RAM variation signals, modulating at 1.25 MHz is the best option. Not only is the measured RAM signal at a maximum but the FM signal, although optimised along the Y measurement axis, is diminished in magnitude significantly. Therefore, any influence of the FM 1st harmonic signal on the RAM measurement, due to inaccurate selection of detection phase and mixing, is at a minimum.

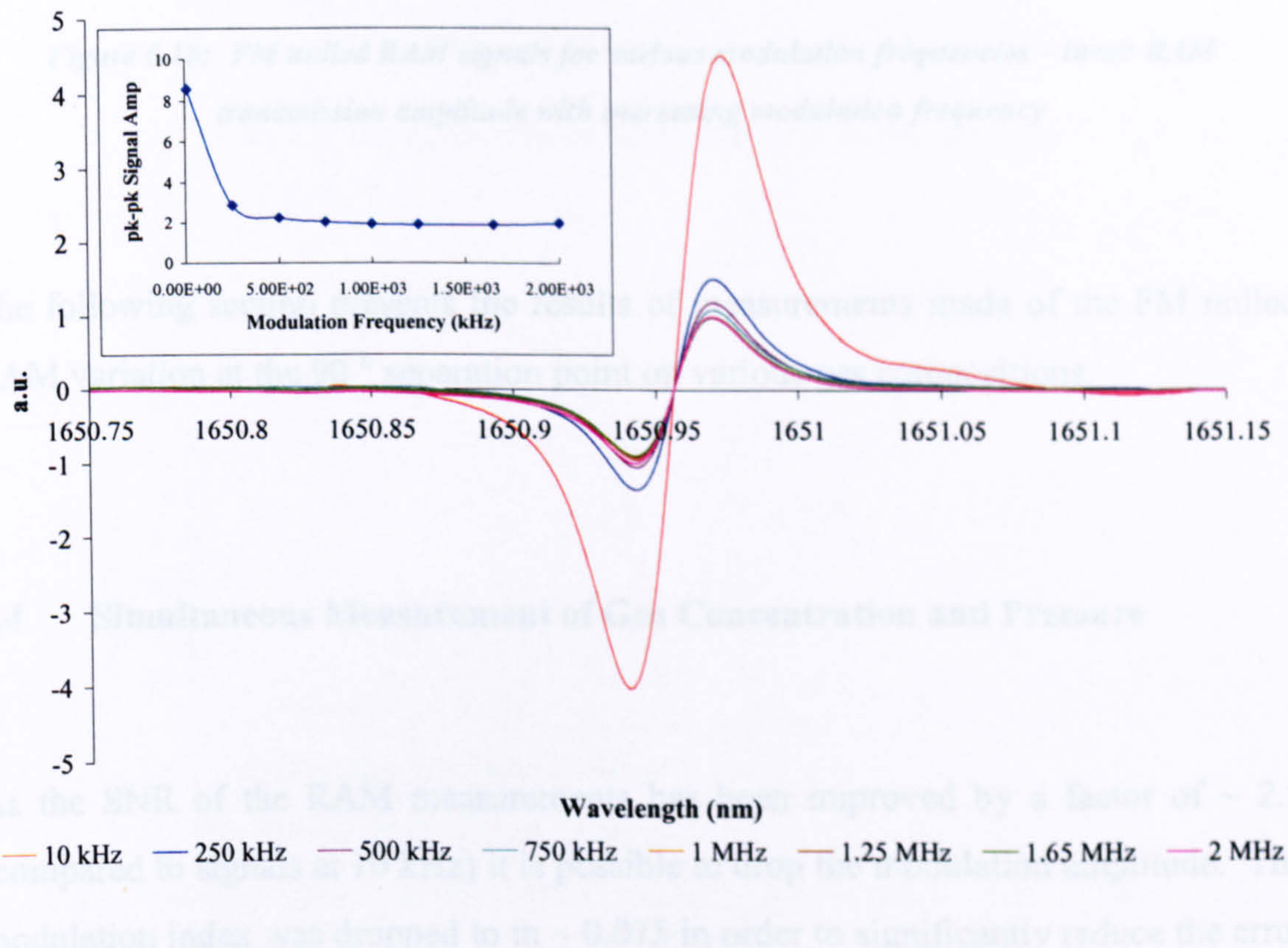

Figure 6.17: RAM nulled FM signals for various modulation frequencies – inset: FM peak-to-peak signal amplitude with increasing modulation frequency

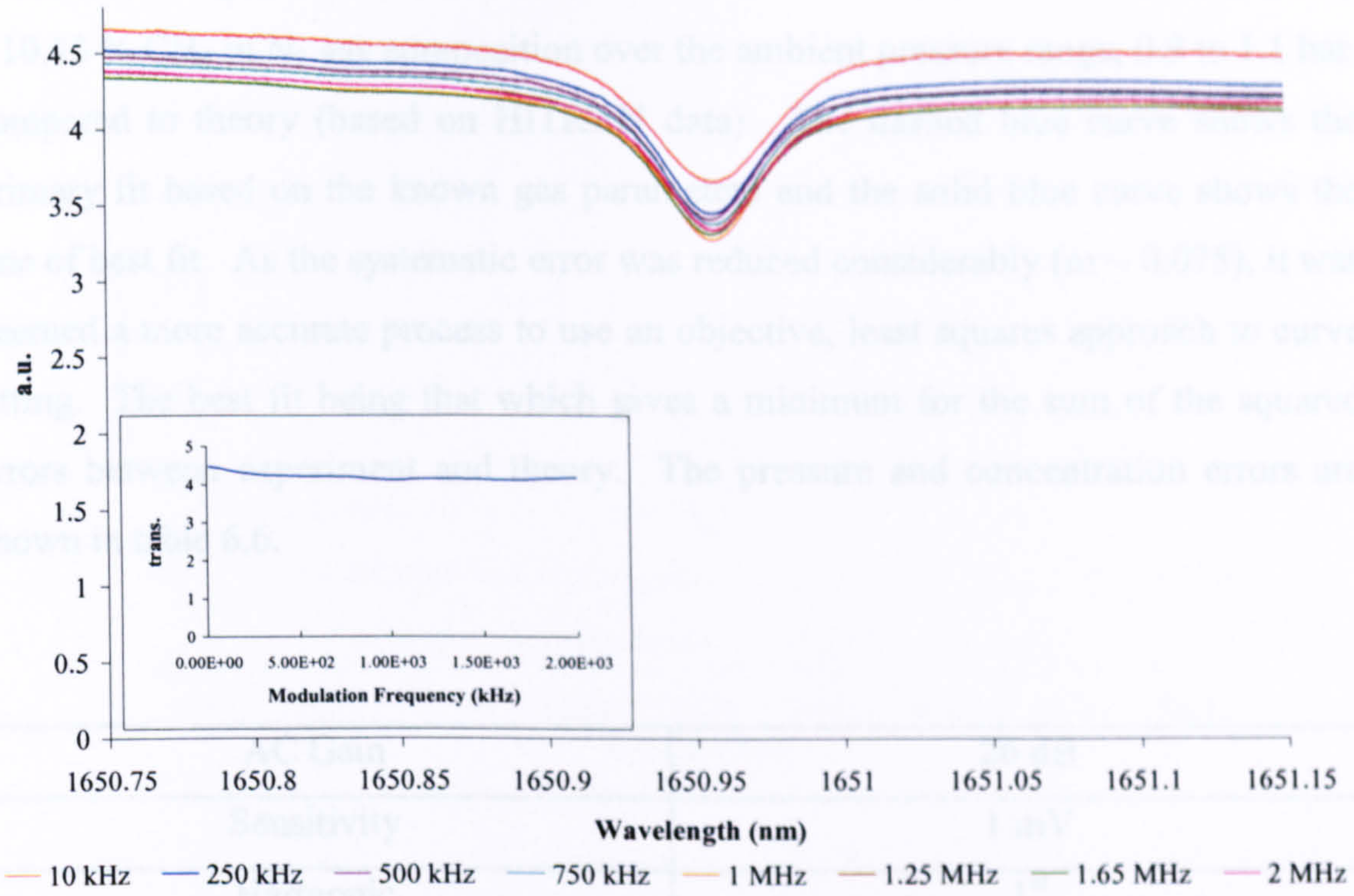

Figure 6.18: FM nulled RAM signals for various modulation frequencies – inset: RAM transmission amplitude with increasing modulation frequency

The following section presents the results of measurements made of the FM nulled RAM variation at the 90 ° separation point on various gas compositions.

6.4 Simultaneous Measurement of Gas Concentration and Pressure

As the SNR of the RAM measurements has been improved by a factor of ~ 2.5 (compared to signals at 10 kHz) it is possible to drop the modulation amplitude. The modulation index was dropped to m ~ 0.075 in order to significantly reduce the error from RAM induced harmonic interference (discussed in section 6.2.3). Due to the increased modulation frequency, the time constant for the 1st harmonic resonator measurement had to be changed to 20 μs. The lock-in amplifier settings are shown

in table 6.5. Figures 6.19 to 6.23 show measurements made of the RAM variation on a 10.13 % CH_4 in N_2 gas composition over the ambient pressure range, 0.9 to 1.1 bar, compared to theory (based on HITRAN data). The dashed blue curve shows the primary fit based on the known gas parameters and the solid blue curve shows the line of best fit. As the systematic error was reduced considerably (m ~ 0.075), it was deemed a more accurate process to use an objective, least squares approach to curve fitting. The best fit being that which gives a minimum for the sum of the squared errors between experiment and theory. The pressure and concentration errors are shown in table 6.6.

AC Gain	26 dB
Sensitivity	1 mV
Harmonic	1st
Time Constant	1 ms

Table 6.5: Settings for Perkin Elmer 7280 DSP lock-in amplifier

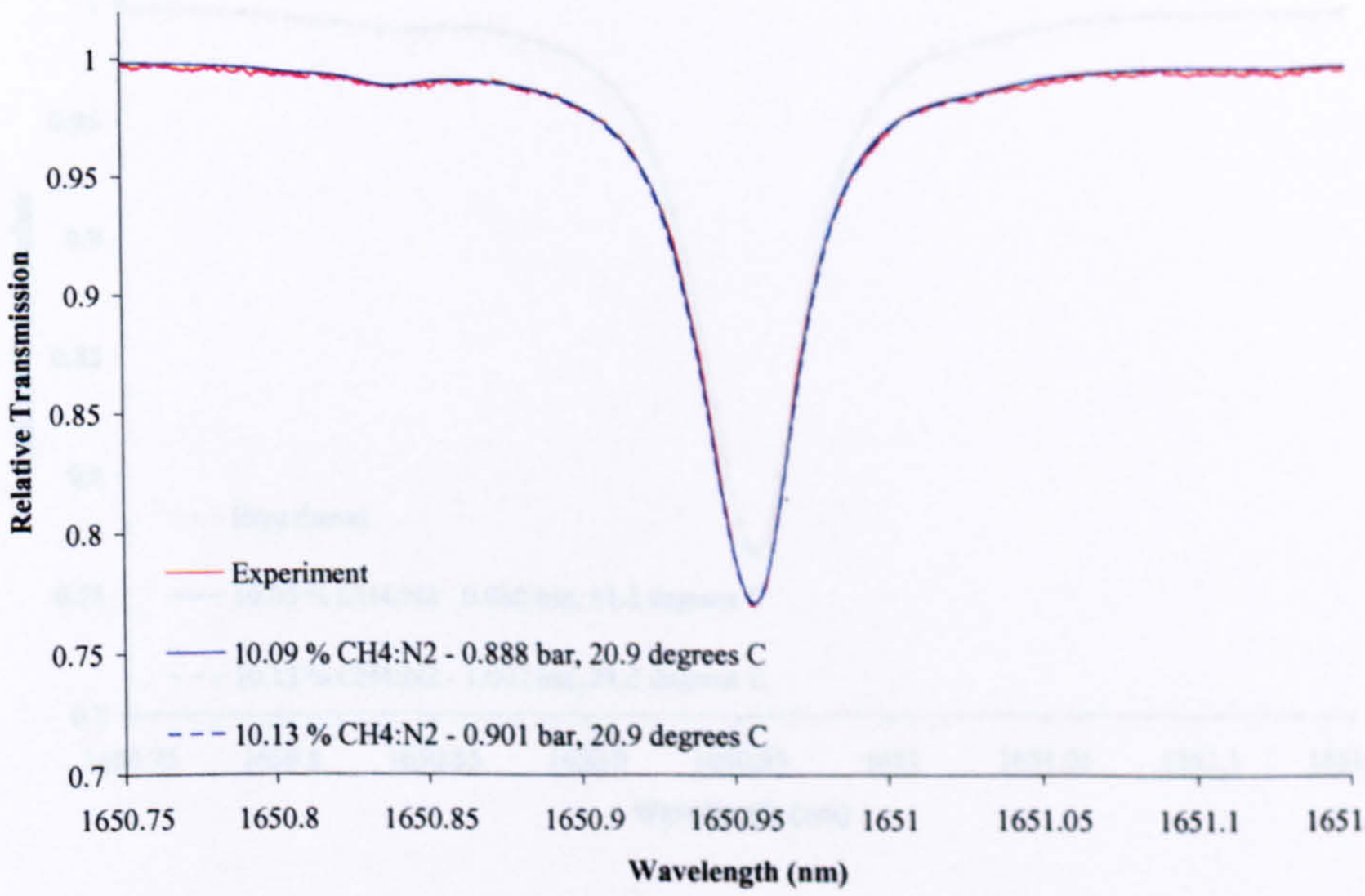

Figure 6.19: 10.13 % CH_4 : N_2 balance at 20.9 °C and 0.901 bar pressure – FM nulled RAM signal at 1.25 MHz, measured using m ~ 0.075, compared to theory

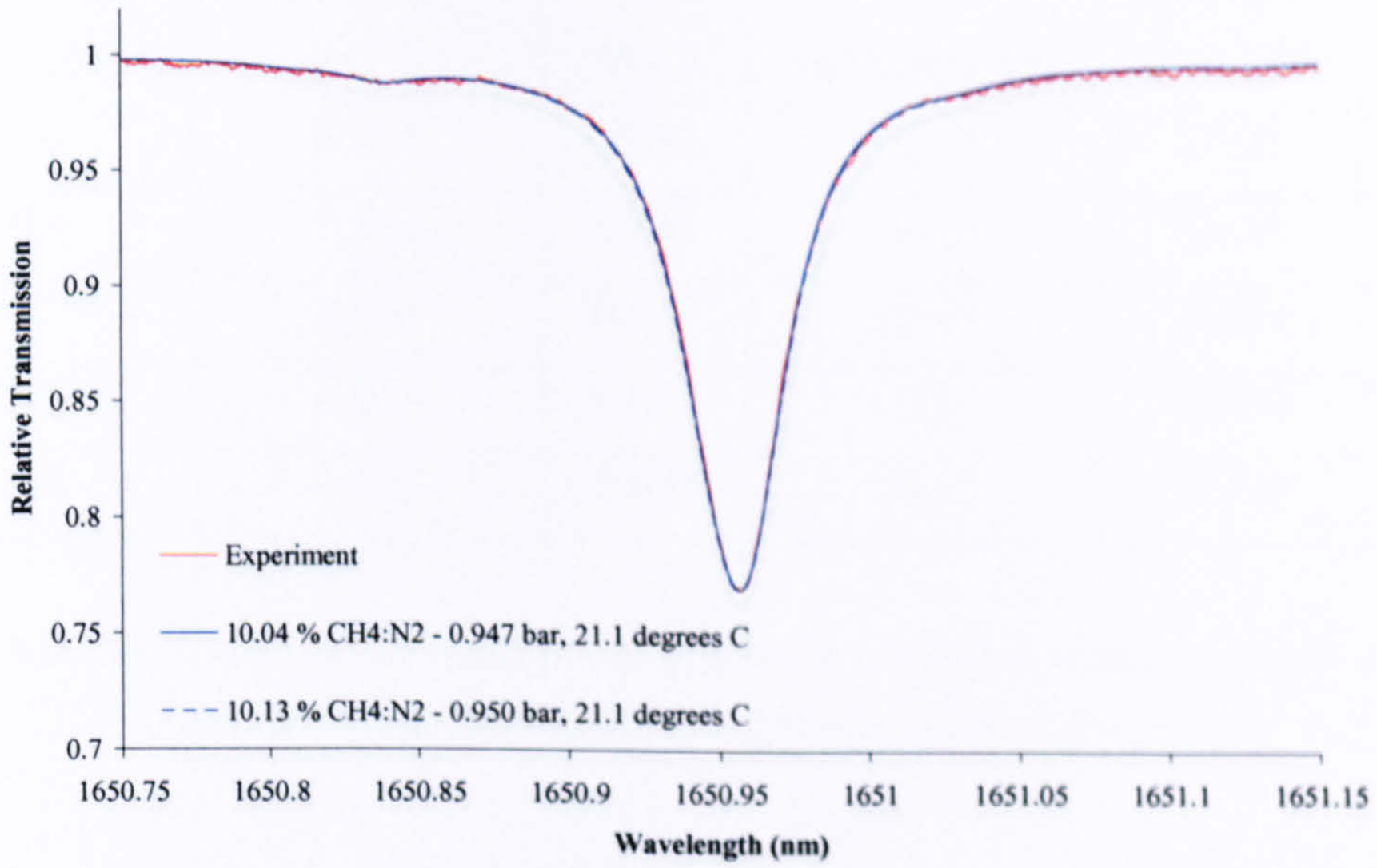

Figure 6.20: 10.13 % CH_4 : N_2 balance at 21.1 °C and 0.950 bar pressure – FM nulled RAM signal at 1.25 MHz, measured using m ~ 0.075, compared to theory

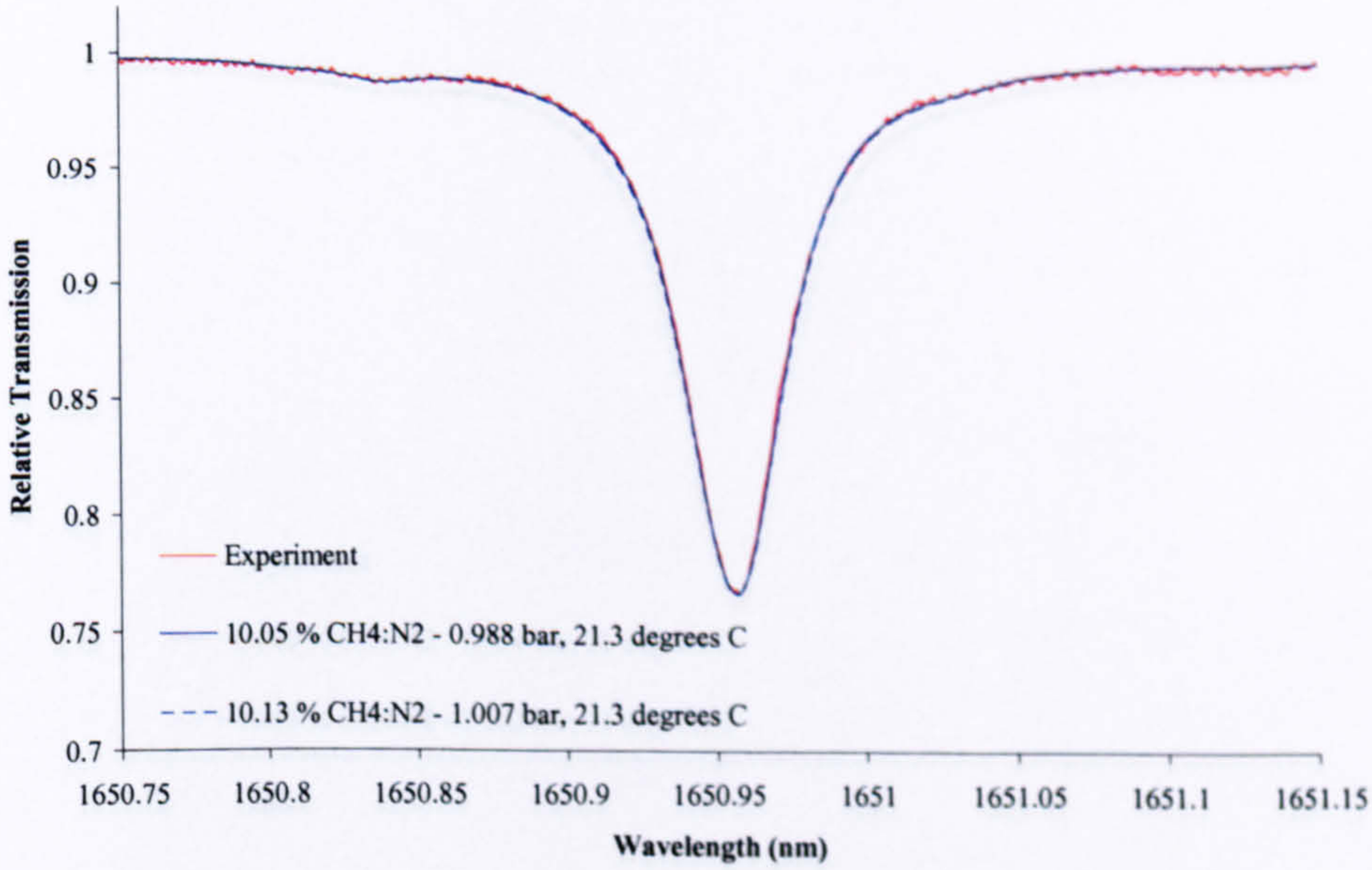

Figure 6.21: 10.13 % CH_4 : N_2 balance at 21.3 °C and 1.007 bar pressure – FM nulled RAM signal at 1.25 MHz, measured using m ~ 0.075, compared to theory

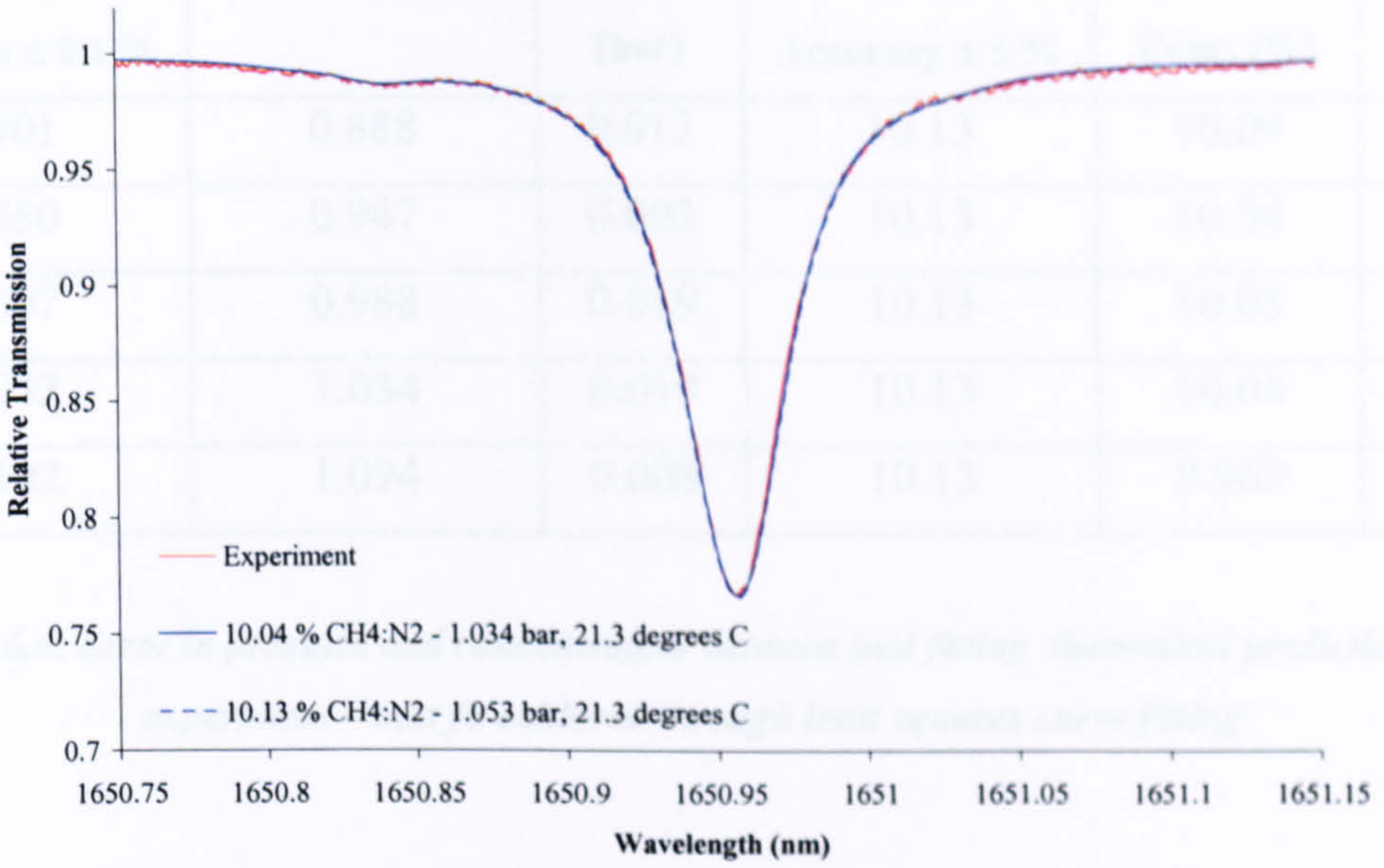

Figure 6.22: 10.13 % CH_4 : N_2 balance at 21 °C and 1.053 bar pressure – FM nulled RAM signal at 1.25 MHz, measured using m ~ 0.075, compared to theory

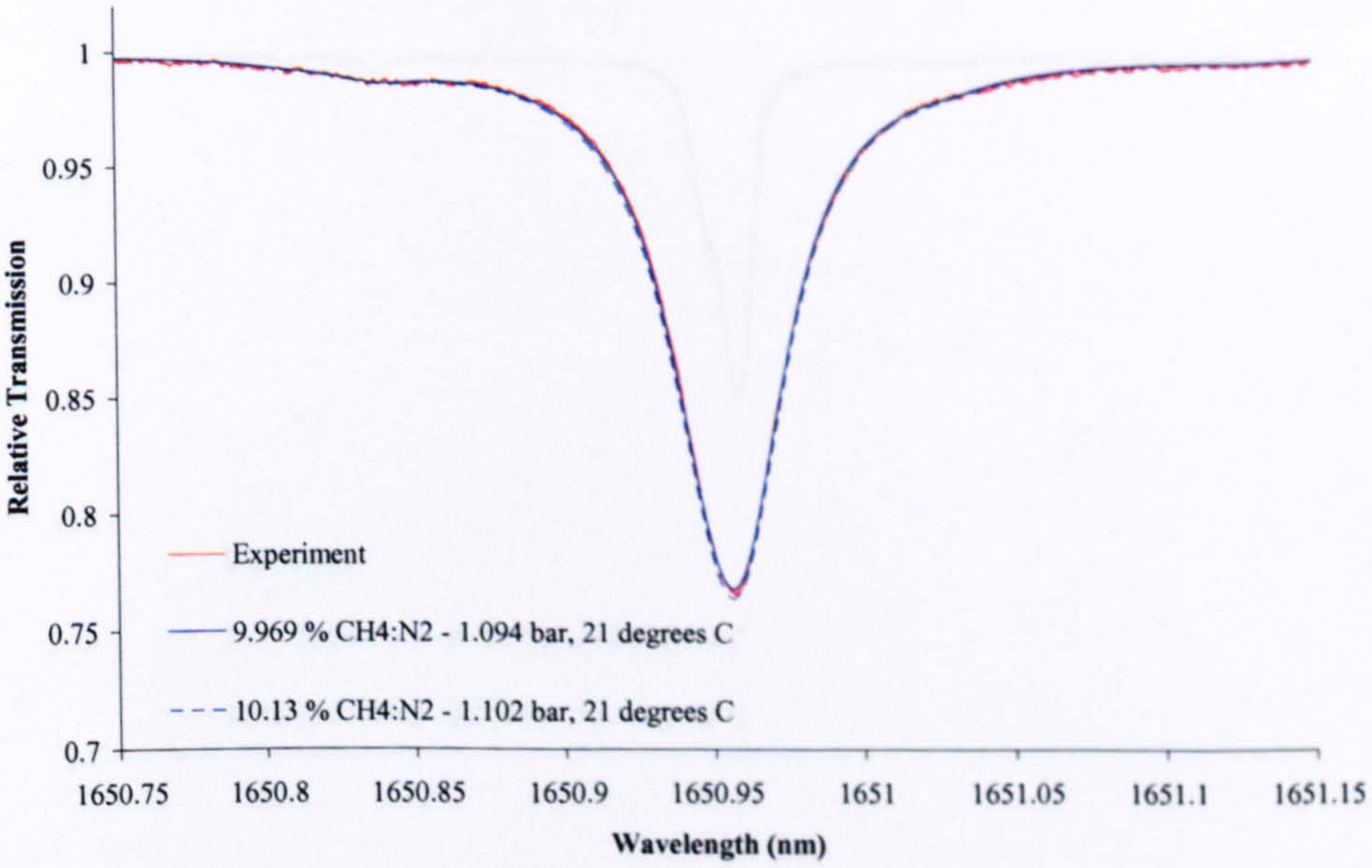

Figure 6.23: 10.13 % CH_4 : N_2 balance at 21 °C and 1.102 bar pressure – FM nulled RAM signal at 1.25 MHz, measured using m ~ 0.075, compared to theory

Digital Gauge Pressure (bar) Accuracy ± 0.1 %	TDLS Recovered Pressure (bar)	Pressure Error (bar)	Cylinder Conc. (%) Accuracy ± 5 %	TDLS Recovered Conc. (%)	Conc. Error (%)
0.901	0.888	0.013	10.13	10.09	0.39
0.950	0.947	0.003	10.13	10.04	0.89
1.007	0.988	0.019	10.13	10.05	0.49
1.053	1.034	0.019	10.13	10.04	0.89
1.102	1.094	0.008	10.13	9.969	1.59

Table 6.6: Error in pressure and concentration between best fitting theoretical prediction and experiment – best fit achieved through least squares curve fitting

Figures 6.24 to 6.28 show measurements of the RAM variation on a 10.13 % CH_4 in N_2 gas composition over the extended pressure range, 0.2 to 1.8 bar, compared to theory. The errors between theory and experiment are shown in table 6.7.

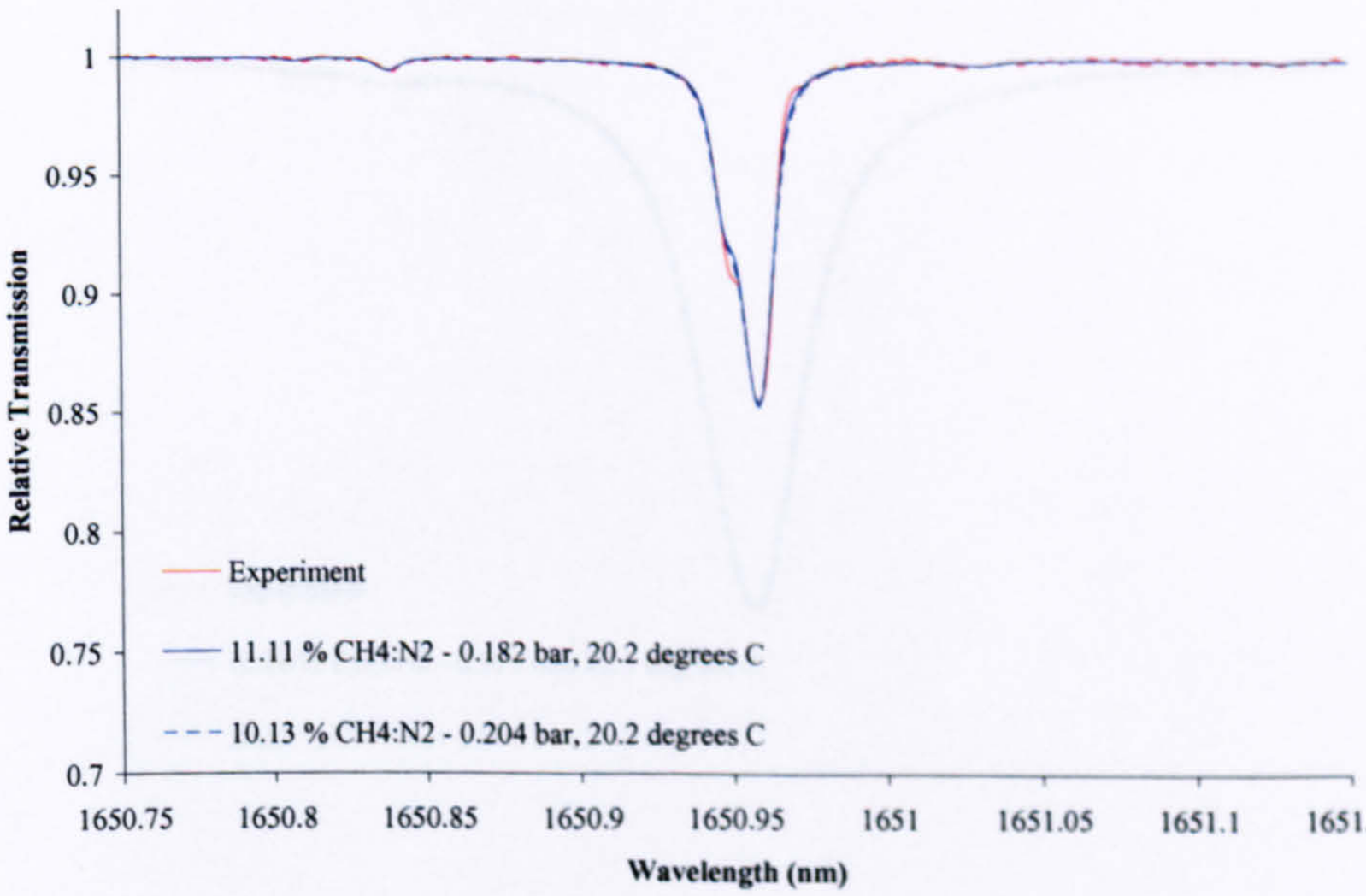

Figure 6.24: 10.13 % CH_4 : N_2 balance at 20.2 °C and 0.204 bar pressure – FM nulled RAM signal at 1.25 MHz, measured using m ~ 0.075, compared to theory

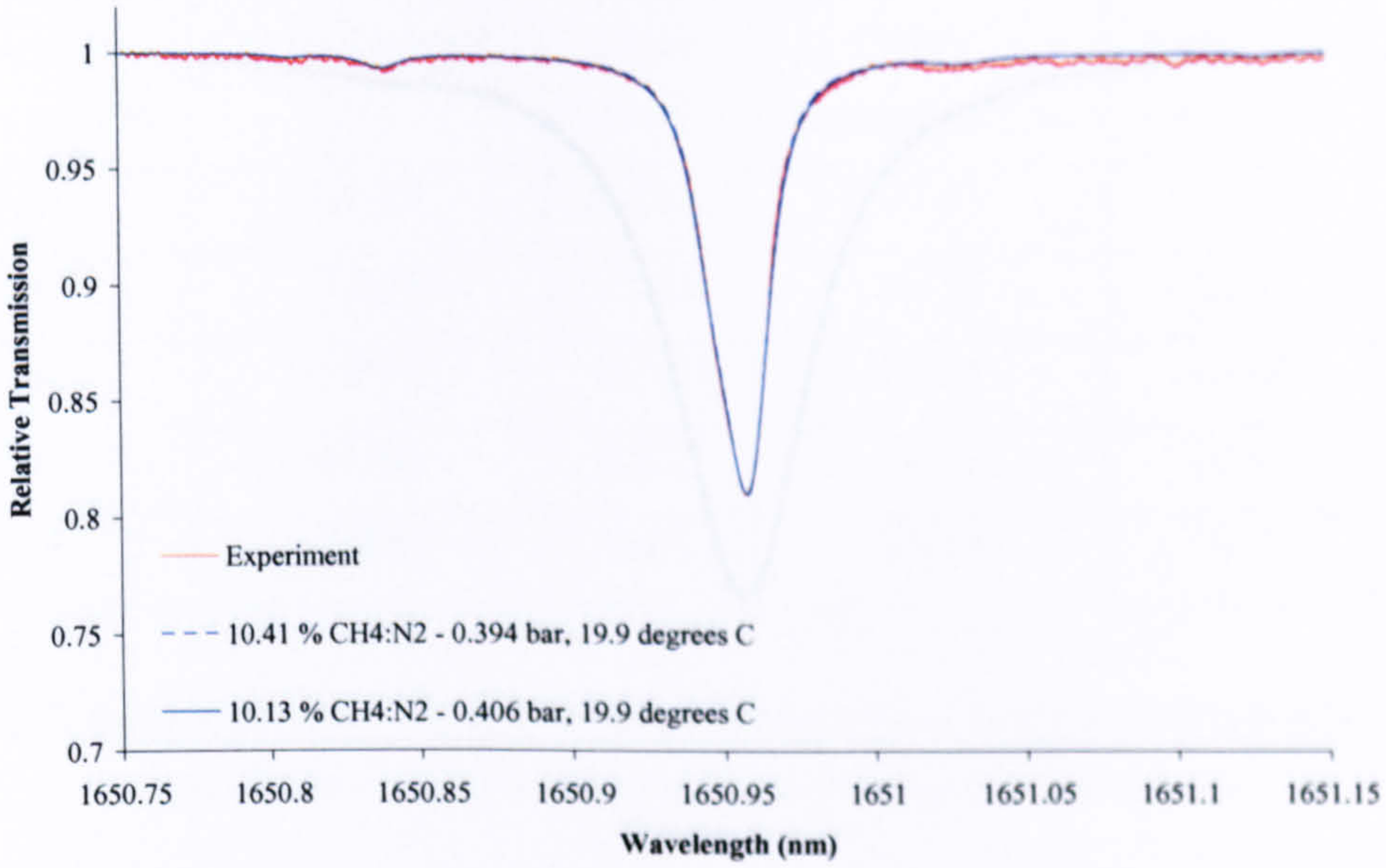

Figure 6.25: 10.13 % CH_4 : N_2 balance at 19.9 °C and 0.406 bar pressure – FM nulled RAM signal at 1.25 MHz, measured using m ~ 0.075, compared to theory

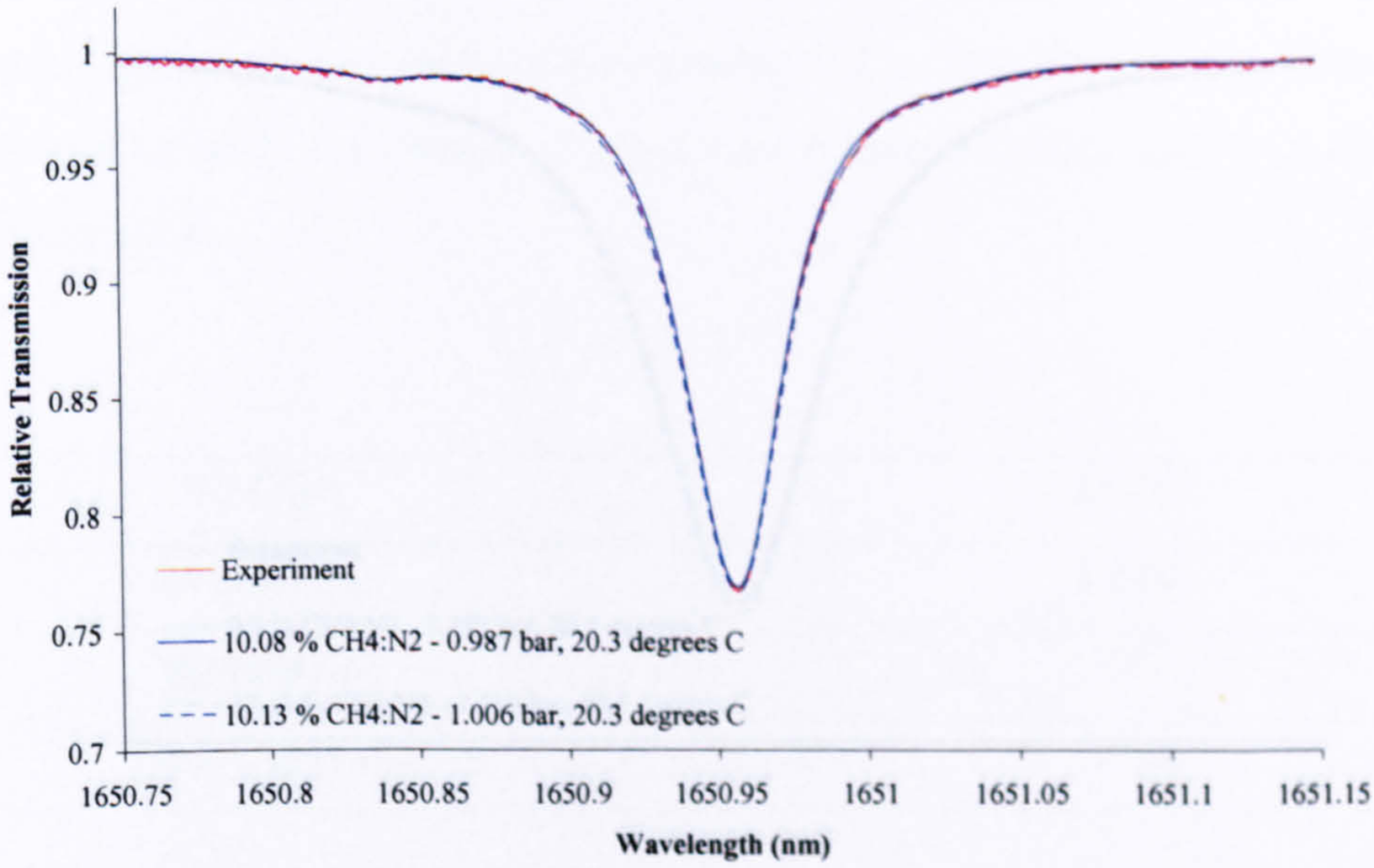

Figure 6.26: 10.13 % CH_4 : N_2 balance at 20.3 °C and 1.006 bar pressure – FM nulled RAM signal at 1.25 MHz, measured using m ~ 0.075, compared to theory

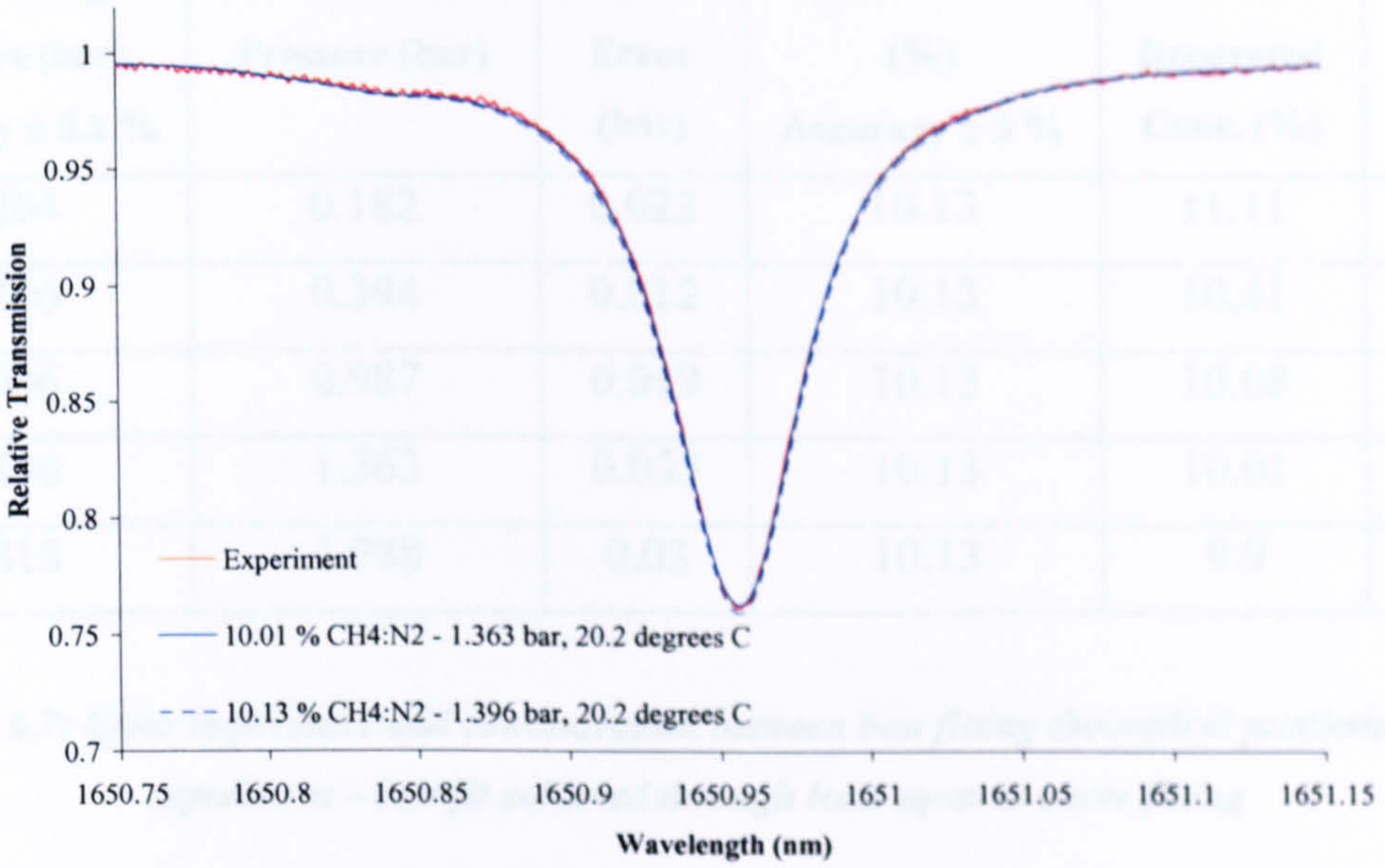

Figure 6.27: 10.13 % CH_4 : N_2 balance at 20.2 °C and 1.396 bar pressure – FM nulled RAM signal at 1.25 MHz, measured using m ~ 0.075, compared to theory

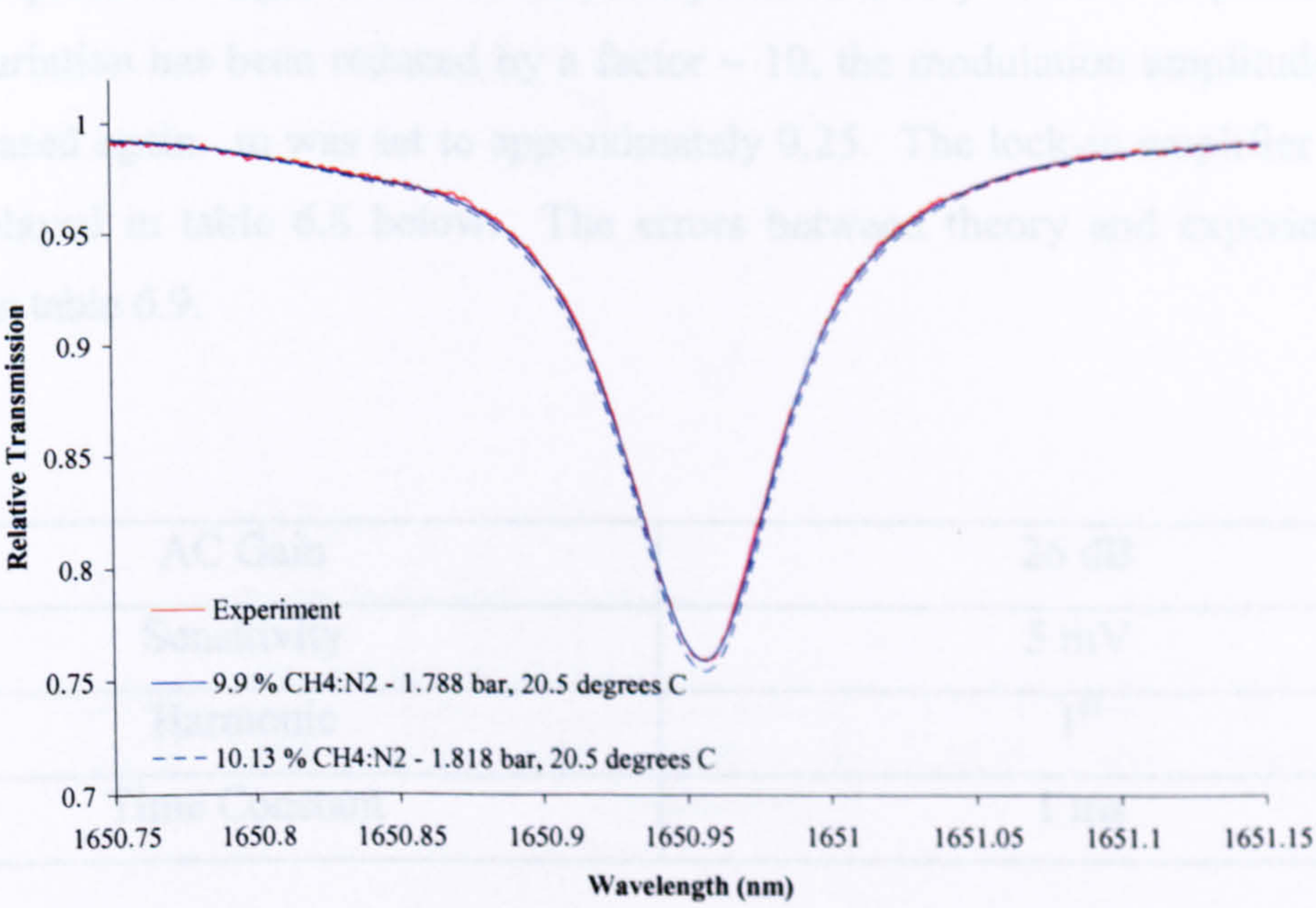

Figure 6.28: 10.13 % CH_4 : N_2 balance at 20.5 °C and 1.818 bar pressure – FM nulled RAM signal at 1.25 MHz, measured using m ~ 0.075, compared to theory

Digital Gauge Pressure (bar) Accuracy ± 0.1 %	TDLS Recovered Pressure (bar)	Pressure Error (bar)	Cylinder Conc. (%) Accuracy ± 5 %	TDLS Recovered Conc. (%)	Conc. Error (%)
0.204	0.182	0.022	10.13	11.11	9.67
0.406	0.394	0.012	10.13	10.41	2.76
1.006	0.987	0.019	10.13	10.08	0.49
1.396	1.363	0.033	10.13	10.01	1.18
1.818	1.788	0.03	10.13	9.9	2.27

Table 6.7: Error in pressure and concentration between best fitting theoretical prediction and experiment – best fit achieved through least squares curve fitting

With this much improved signal-to-noise ratio it is then possible to consider gas measurements at lower concentrations. Figures 6.29 to 6.33 show measurements made of the RAM variation on a 1.02 % CH_4 in N_2 gas composition over the extended pressure range, 0.4 to 1.8 bar, compared to theory. As the amplitude of the RAM variation has been reduced by a factor ~ 10, the modulation amplitude had to be increased again. m was set to approximately 0.25. The lock-in amplifier settings are displayed in table 6.8 below. The errors between theory and experiment are shown in table 6.9.

AC Gain	26 dB
Sensitivity	5 mV
Harmonic	1^{st}
Time Constant	1 ms

Table 6.8: Settings for Perkin Elmer 7280 DSP lock-in amplifier

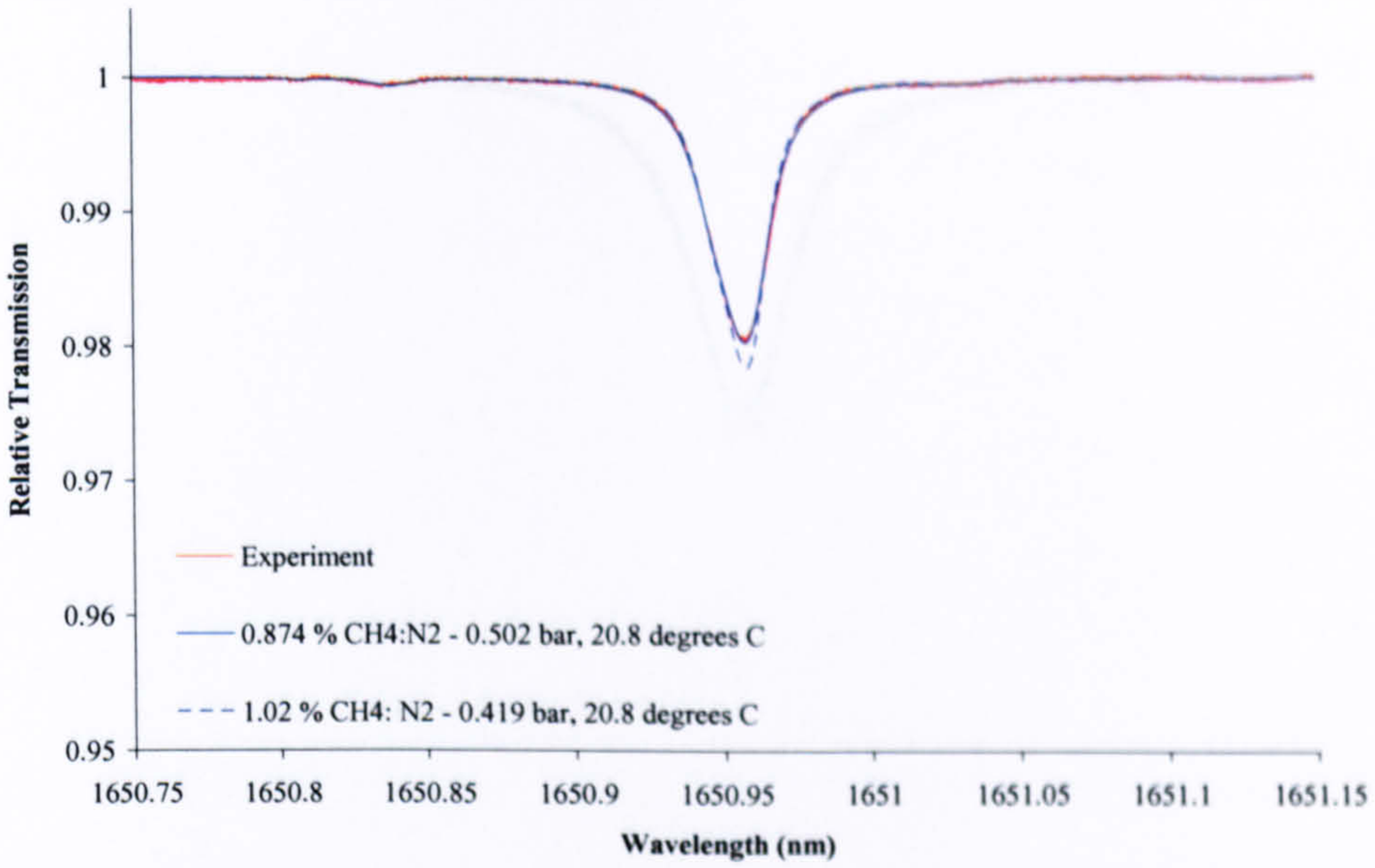

Figure 6.29: 1.02 % CH_4 : N_2 balance at 20.8 °C and 0.419 bar pressure – FM nulled RAM signal at 1.25 MHz, measured using m ~ 0.25, compared to theory

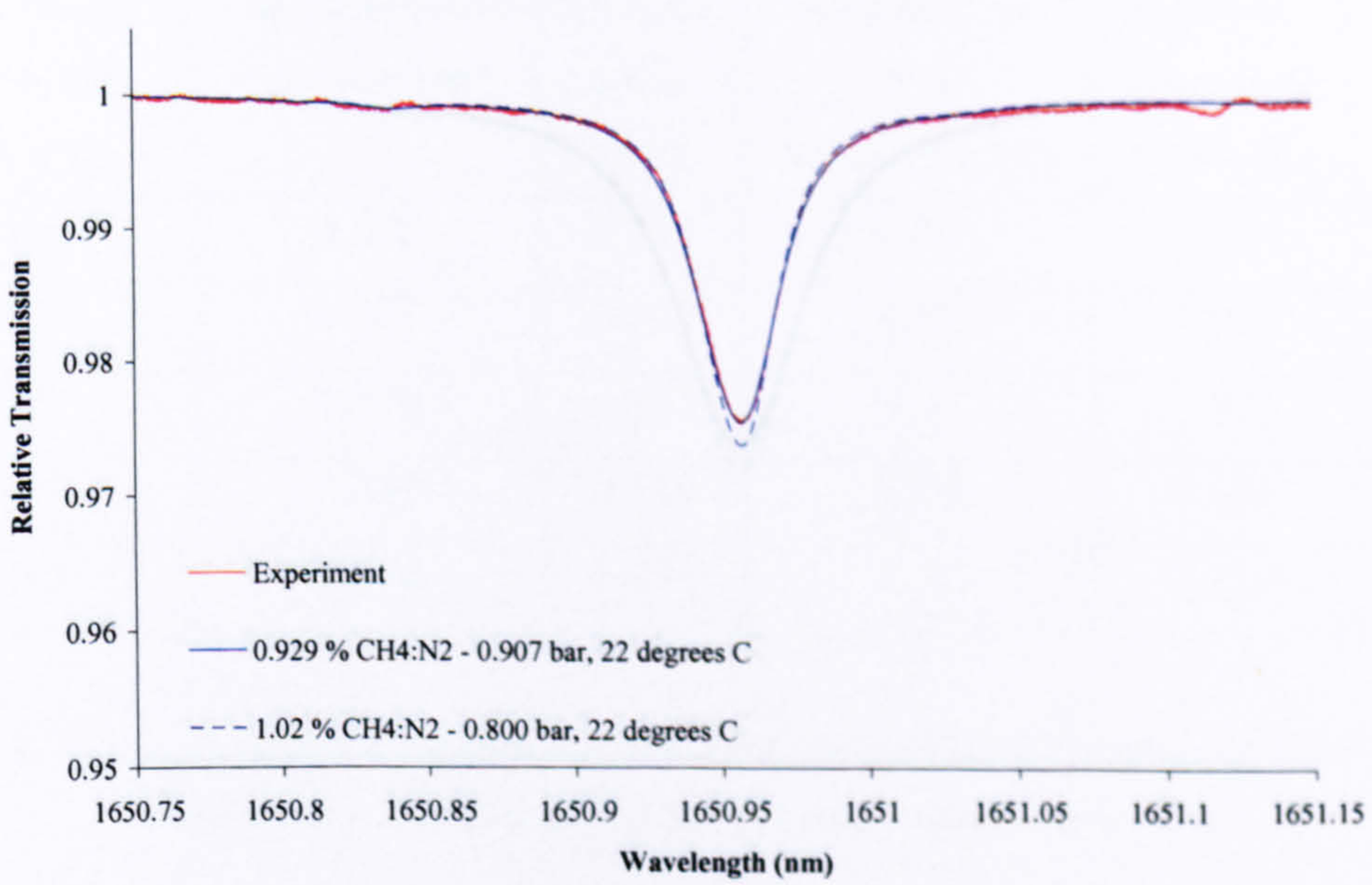

Figure 6.30: 1.02 % CH_4 : N_2 balance at 22 °C and 0.800 bar pressure – FM nulled RAM signal at 1.25 MHz, measured using m ~ 0.25, compared to theory

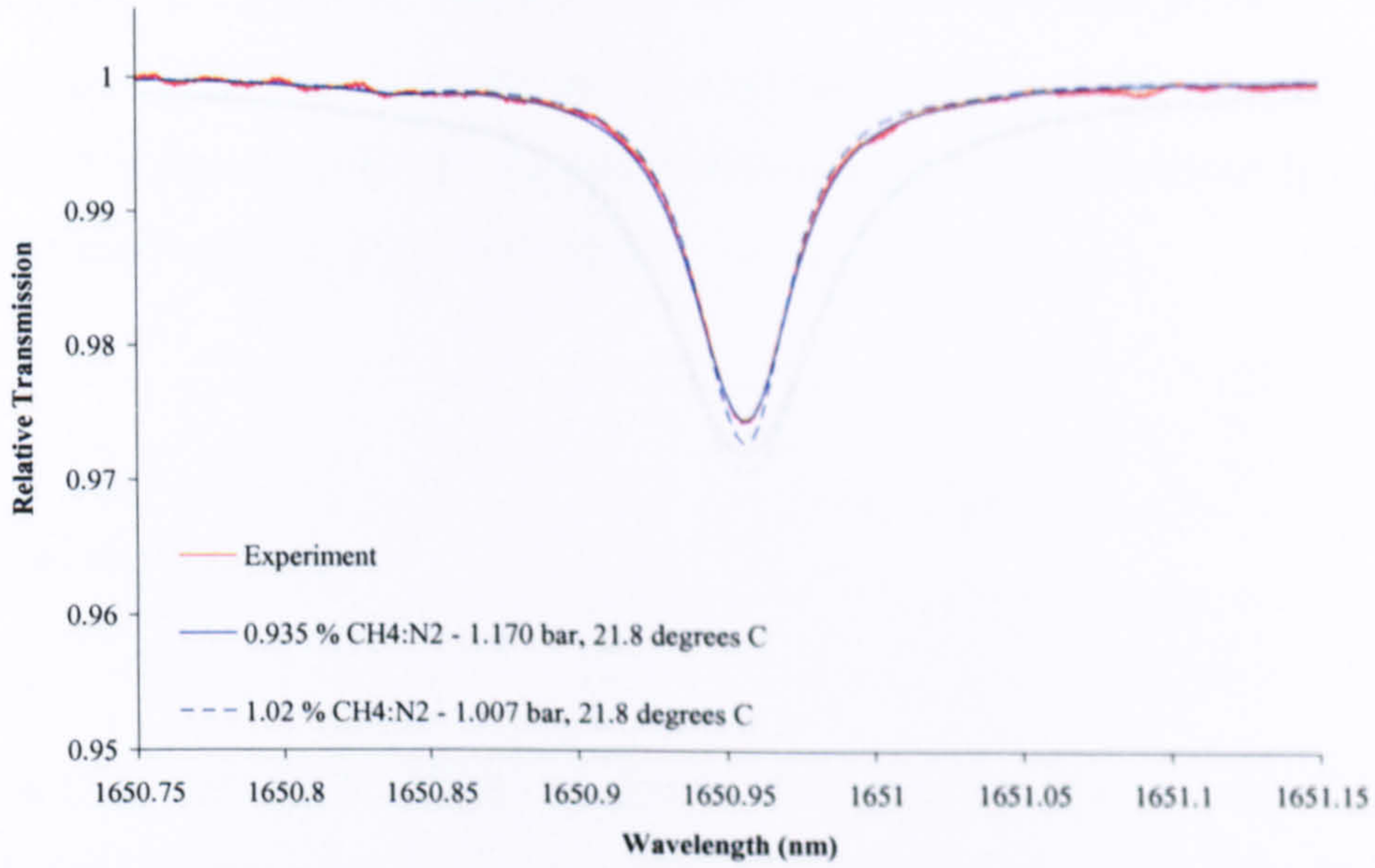

Figure 6.31: 1.02 % CH_4 : N_2 balance at 21.8 °C and 1.007 bar pressure – FM nulled RAM signal at 1.25 MHz, measured using m ~ 0.25, compared to theory

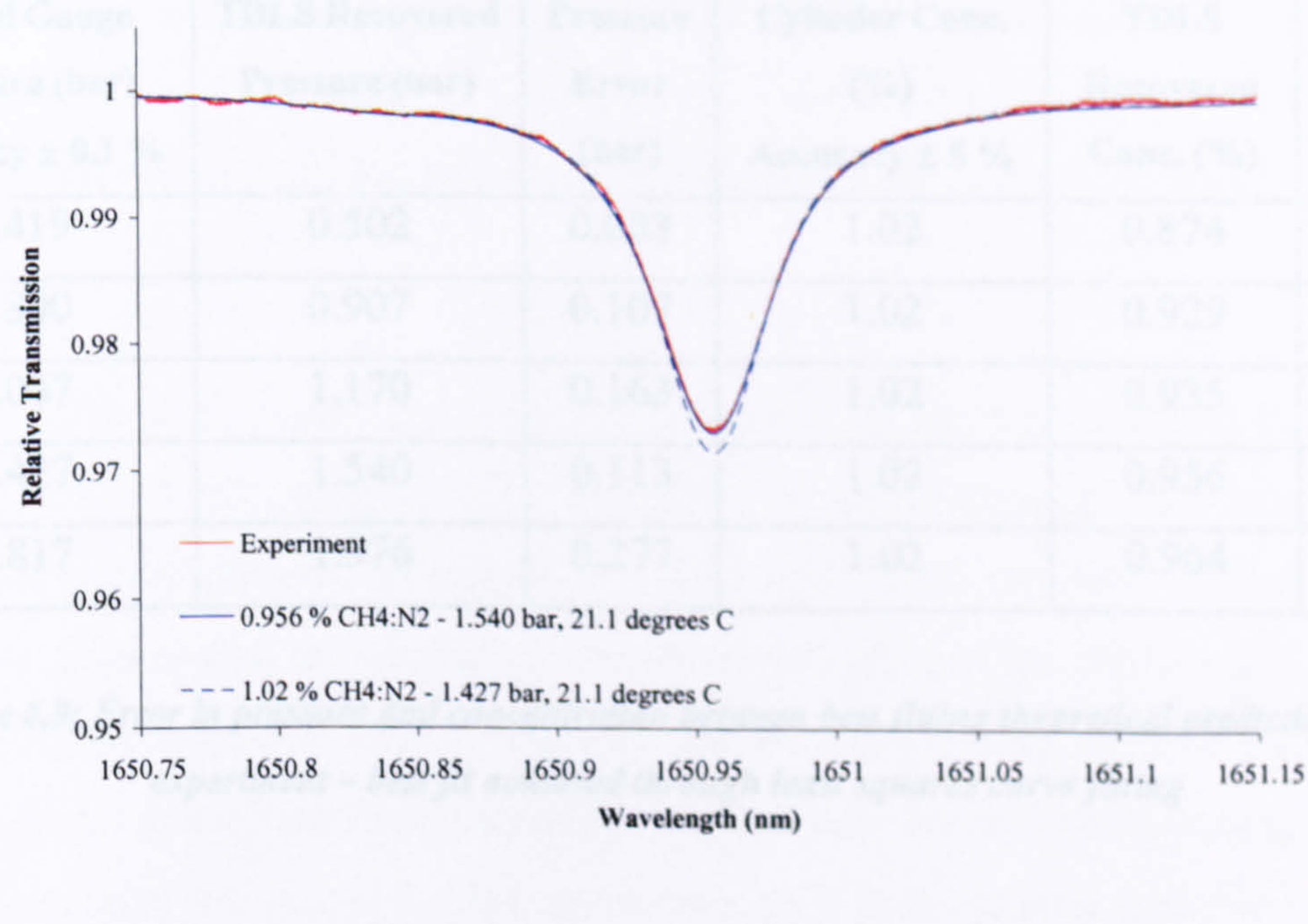

Figure 6.32: 1.02 % CH_4 : N_2 balance at 21.1 °C and 1.427 bar pressure – FM nulled RAM signal at 1.25 MHz, measured using m ~0.25, compared to theory

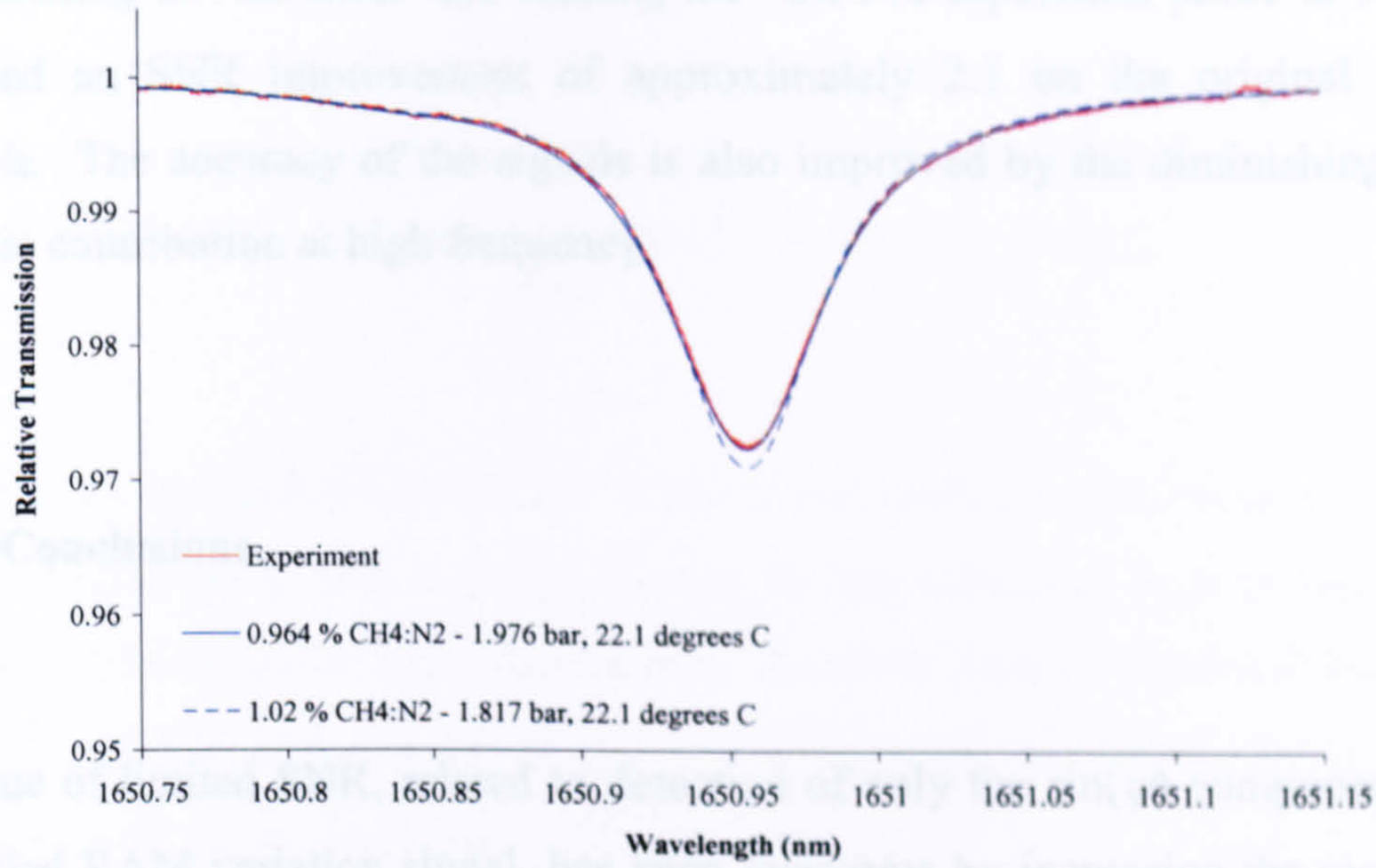

Figure 6.33: 1.02 % CH_4 : N_2 balance at 22.1 °C and 1.817 bar pressure – FM nulled RAM signal at 1.25 MHz, measured using m ~ 0.25, compared to theory

Digital Gauge Pressure (bar) Accuracy ± 0.1 %	TDLS Recovered Pressure (bar)	Pressure Error (bar)	Cylinder Conc. (%) Accuracy ± 5 %	TDLS Recovered Conc. (%)	Conc. Error (%)
0.419	0.502	0.083	1.02	0.874	14.3
0.800	0.907	0.107	1.02	0.929	8.9
1.007	1.170	0.163	1.02	0.935	8.3
1.427	1.540	0.113	1.02	0.956	6.27
1.817	1.976	0.277	1.02	0.964	5.5

Table 6.9: Error in pressure and concentration between best fitting theoretical prediction and experiment – best fit achieved through least squares curve fitting

It can be seen from analysis of these results that we have demonstrated simultaneous measurement of gas concentration and pressure for two gas concentrations over a wide range of pressures. The development of the TDLS / WMS detection process,

by modulating at 1.25 MHz and shifting the AM-FM separation phase to 90 °, has facilitated an SNR improvement of approximately 2.5 on the original 10 kHz approach. The accuracy of the signals is also improved by the diminishing FM 1st harmonic contribution at high frequency.

6.5 Conclusions

The issue of limited SNR, related to detection of only the sin(ψ) component of the FM nulled RAM variation signal, has been overcome by increasing the modulation frequency such that the measured signal is at a maximum. The hypothesis and viability of increasing the modulation frequency to give greater AM-FM phase separation was, initially, experimentally demonstrated at the modest modulation frequency of 100 kHz. Having gained a SNR improvement of just under 2 on the 10 kHz measurements, and having demonstrated that the FM 1st harmonic signal had lower potential for distorting the desired RAM variation signals due to its diminished amplitude, it was decided to expand the modulation frequency beyond the conventional frequencies and into the MHz region for further improvement.

At 1.25 MHz we demonstrated complete separation of the desired RAM signal from the FM, whilst maximising the recovered SNR, giving a factor of ~ 2.5 improvement on initial results reported in chapter 5. Although TDLS has now shifted to MHz detection frequencies, the technique still sits comfortably in the WMS regime, as it is commonly accepted that FMS techniques use modulation frequencies comparable to the target gas absorption half-linewidth. Typical half-linewidths of atmospheric gas absorption lines are around 3 GHz, more than 2000 times greater than the 1.25 MHz modulation frequency. As well as determining the 90 ° separation between the AM and FM, we characterised the AM and FM conversion efficiency of the injection current modulation for this particular 1650 nm DFB laser, over the frequency range of 10 kHz to 2 MHz. We experimentally demonstrated, using a CH_4 gas absorption

line, that the efficiency of FM conversion diminishes and the efficiency of AM conversion remains constant with increasing modulation frequency. These results, including the increasing FM phase lag with increasing modulation frequency, agree well with the findings of Jacobsen et al [6.1] and Schilt et al [6.2].

An analytical approach (based on a 2nd order Taylor series expansion of a Lorentzian broadened absorption line) to compensating for the effects of high m values in 1st harmonic RAM detection was also reported. However, like conventional approaches to TDLS / WMS, knowledge of the gas absorption half-linewidth, γ, and the frequency modulation amplitude, $\delta\nu$, is required.

With increased signal-to-noise ratio in the 1st harmonic RAM variation measurements and decreased influence from the FM, accurate and simultaneous measurements of gas concentration and pressure were made on two different gas compositions, namely: 10 % and 1 % CH_4 in N_2 over a wide range of pressures. With a suitable choice of modulation index, the measurements on the 10 % CH_4 composition exhibited an error of less than 3 % and the 1 % CH_4 composition measurements gave errors of approximately 8 % at atmospheric pressure. These results fit well within the British Standards for industrial methane detection. Therefore, we have demonstrated the basis of a reliable and accurate TDLS / WMS technique for gas composition measurements that has the potential to be applied to a field-deployable instrument.

6.6 References

[6.1] G. Jacobsen, H. Olesen, F, Birkedahl and B. Tromborg, "Current / Frequency – Modulation Characteristics for Directly Optical Frequency – Modulated Injection Lasers at 830 nm and 1.3 μm," Electronics Letters, Vol. 18, No. 20, pp 874 – 876, September 1982.

[6.2] S. Schilt and L. Thevenaz, "Experimental Method based on Wavelength - Modulation Spectroscopy for the Characterization of Semiconductor Lasers under Direct Modulation," Applied Optics, Vol. 43, No. 22, pp 4446-4453, August 2004.

[6.3] P. Werle, "A Review of Recent Advances in Semiconductor Laser based Gas Monitors," Spectrochimica Acta Part A: Molecular and Biomolecular Spectroscopy, Vol. 54, No. 2, pp 197-236, February 1998.

[6.4] K. Petermann, "Laser Diode Modulation and Noise," Advances in Optoelectronics (ADOP), Kluwer Academic Publishers, 1988.

[6.5] L. C. Philippe and R. K. Hanson, "Laser Diode Wavelength – Modulation Spectroscopy for Simultaneous Measurement of Temperature, Pressure and Velocity in Shock – Heated Oxygen Flows," Applied Optics, Vol. 32, No. 30, pp 6090-6103, October 1993.

Chapter 7

Conclusions and Further Work

7.1 Conclusions

The fundamental aim of this project was to determine a robust method for measuring gas concentration and pressure (or to compensate for pressure variations in the analysis) that could be used in a TDLS instrument, deployable in harsh industrial environments. It was evident from the review of current approaches to industrial gas monitoring that TDLS-based methods provided the greatest potential compared to pellistor-based or NDIR-based gas detection schemes. Near infra-red TDLS exploits the use of inexpensive and widely available near infra-red semiconductor diode lasers, conventionally used for communications, to provide high power and stable frequency scanning of individual rotation-vibration gas absorption lines. This gives SNRs comparable with mid infra-red detection schemes, without suffering interference from other atmospheric gases. The compatibility of these near infra-red

diode lasers with optical fibre also facilitates multi-point, remote detection, making TDLS systems intrinsically safe. Thermal and current feedback control of the laser frequency and the use of zero-point referencing mean TDLS gas analysers are calibration stable.

In TDLS with direct detection the absolute transmission function of a single vibration-rotation gas absorption line is recovered, permitting direct extraction of the linewidth and line strength for pressure and concentration measurements. TDLS with wavelength modulation spectroscopy offers greater sensitivity by providing AC detection at high frequencies where laser and 1/f noise is minimised. The use of a lock-in amplifier provides reduction in detection bandwidth and consequently noise to provide SNR improvements of around two orders of magnitude. The WMS approach offers solutions in applications where optical access or low received powers can be a problem. In addition, the high infra-red background signals that hinder direct detection schemes in high temperature situations are eliminated. With these advantages in mind, it would seem that TDLS with WMS detection is the most suitable approach for modern industrial gas sensing applications; however, the increased complexity of signal analysis and scope for error, compared to direct detection, has been the stumbling block for current state-of-the-art detection schemes. The critical issue is the dependence of harmonic / derivative signal amplitudes on the systematic scaling factor $\delta\nu/\gamma$ ($\delta\nu/\gamma^2$ for the 1st derivative and $\delta\nu^2/\gamma^3$ for the 2nd derivative) and errors in determining these parameters accumulate to determine the overall error on the extracted concentration and / or pressure. It is particularly problematic in environments where the pressure is varying and unknown as γ has to be determined from the recovered signals and with RAM distortion effects and a lack of reliable *in-situ* wavelength referencing, large errors are possible!

Specific objectives were consequently devised in order to realise the overall aim of the project:

1. The first objective was to develop a robust wavelength referencing scheme, using a fibre ring-resonator and signal processing, to make absolute, *in-situ* measurements of the laser's centre wavelength as it is scanned across the target gas absorption line.
2. The second objective was to develop signal processing techniques to completely remove the effects of RAM from FM signals.
3. The third objective was to calibrate and scale recovered TDLS / WMS signals such that they could be compared to theoretical predictions for the extraction of the gas concentration and pressure data. Two options were proposed: (i) curve fit the derivatives of the theoretical predictions of the absolute absorption line transmission profiles to recovered, pure derivative signals associated with the measured harmonic and (ii) directly fit theoretical predictions of the absorption line transmission function to numerically integrated measured derivatives.

In chapter 2 we reviewed the approach to *in-situ* wavelength referencing (using a low finesse etalon) by Philippe and Hanson [7.1] and decided that an in-fibre solution would be a better approach. Fibre ring-resonators provide greater resolution than conventional bulk-optics approaches and allow the whole system to remain in-fibre. In chapter 4 we described the construction and characterisation of the fibre ring-resonator as well as the signal processing techniques for mapping the relative frequency information onto an absolute wavelength scale for the experimental time-based data. In chapter 5 the accuracy and reliability of our wavelength referencing approach was fully validated by reporting good agreement between experiment and theory for directly recovered gas absorption line transmission functions at 10 % concentration, over a range of pressures and temperatures. The wavelength referencing technique provided a satisfactory solution to the problems of non-linearity and non-repeatability of the current vs. wavelength relationship in DFB lasers.

In chapter 5 we reported significant errors in conventional TDLS / WMS signals and through a revised theoretical treatment (based on a simple Taylor series expansion) identified the specific sources of error. Interference from RAM variations (proportional to derivatives of the absorption line transmission function) led to errors in the FM 1st harmonic peak locations, including a significant asymmetry in the peak amplitudes. From further analysis of the theory we proposed an approach to eliminating the RAM distortion by appropriate selection of the lock-in amplifier detection phase, which was very successful (reflected in the now symmetrical FM 1st harmonic peak amplitudes). However, the technique remained limited due to the same scaling factor and calibration issues (inherent to derivative analysis) that hindered conventional WMS approaches. Therefore, despite extensive efforts, including the numerical integration of the FM 1st harmonic signals with a view to recovering the absolute absorption line transmission function, extracting concentration and pressure measurements through comparisons to theory failed.

Also in chapter 5 we proposed a novel approach to recovering the absolute absorption line transmission function from TDLS / WMS signals. By appropriate selection of the lock-in amplifier detection phase we are able to measure a 1st harmonic RAM signal (undistorted by FM interference) that varies in proportion to the gas absorption line. Normalisation to an off-line measurement then provides an absolute signal. As the technique is absolute, there is no need for scaling factors or extensive calibration and the approach provides simultaneous and accurate measurements of gas concentration and pressure within certain limitations. The main limitation is due to the low SNR associated with the $\sin(\psi)$ component measured at 10 kHz; however, in chapter 6 we reported that increasing the modulation frequency into the MHz region provides a suitable increase in ψ and, consequently, the sensitivity. Chapter 6 reported on the extraction of pressure and concentration for two gas concentrations, namely: 10 % and 1 %, for a range of pressures and temperatures. The promising results show that we have significantly advanced TDLS technology towards realising an instrument for determining accurate gas

composition measurements in harsh industrial environments, although there is potential for improvement (discussed further in section 7.2).

As well as addressing the above mentioned objectives and achieving the overall aim of the project, there were several other significant contributions to the research field:

1. In chapter 5 we reported on a technique for determining host gas broadening coefficients by curve fitting theoretical predictions (based on HITRAN data) to directly measured gas absorption line transmission functions.
2. Also in chapter 5, we determined that the process of curve fitting theoretical predictions to experimental signals was a valid method for the accurate extraction of gas concentration and pressure parameters. However, as previously mentioned, the curve fitting was based on a visual comparison that is qualitative and not purely objective. This issue was resolved in chapter 6 by using a least squares minimisation approach to curve fitting where a best fit is determined by a minimum value for the sum of the squared errors between measured signals and theory (based on HITRAN data).
3. Finally, in chapter 6 we proposed 2nd order correction factors to counter the signal averaging of TDLS / WMS 1st harmonic RAM variation signals at high modulation index values. This gives the potential of improving signal-to-noise ratio, whilst maintaining accuracy in the recovered linewidth and line strength, from which to extract pressure and concentration respectively.

7.2 Further Work

Although the aim of the project has been met and a significant contribution to the field has been made, there remains potential to take the technique forward.

As mentioned previously, TDLS with WMS detection is a popular approach in industrial gas sensing due to its significant advantages over TDLS with direct detection, namely: significant (1 to 2 orders of magnitude) improvement in SNR and the elimination of infra-red background signals in high temperature applications. However, although this proposed new approach to TDLS / WMS of detecting the 1st harmonic RAM variation offers many of the same advantages, the SNR remains limited by the fact we detect small signals relative to a large background. We propose a simple addition to the laboratory system architecture, shown below in figure 7.1, that would provide a significant level of SNR improvement, making this new detection technique competitive (in terms of minimum detectable sensitivity) with conventional TDLS / WMS approaches.

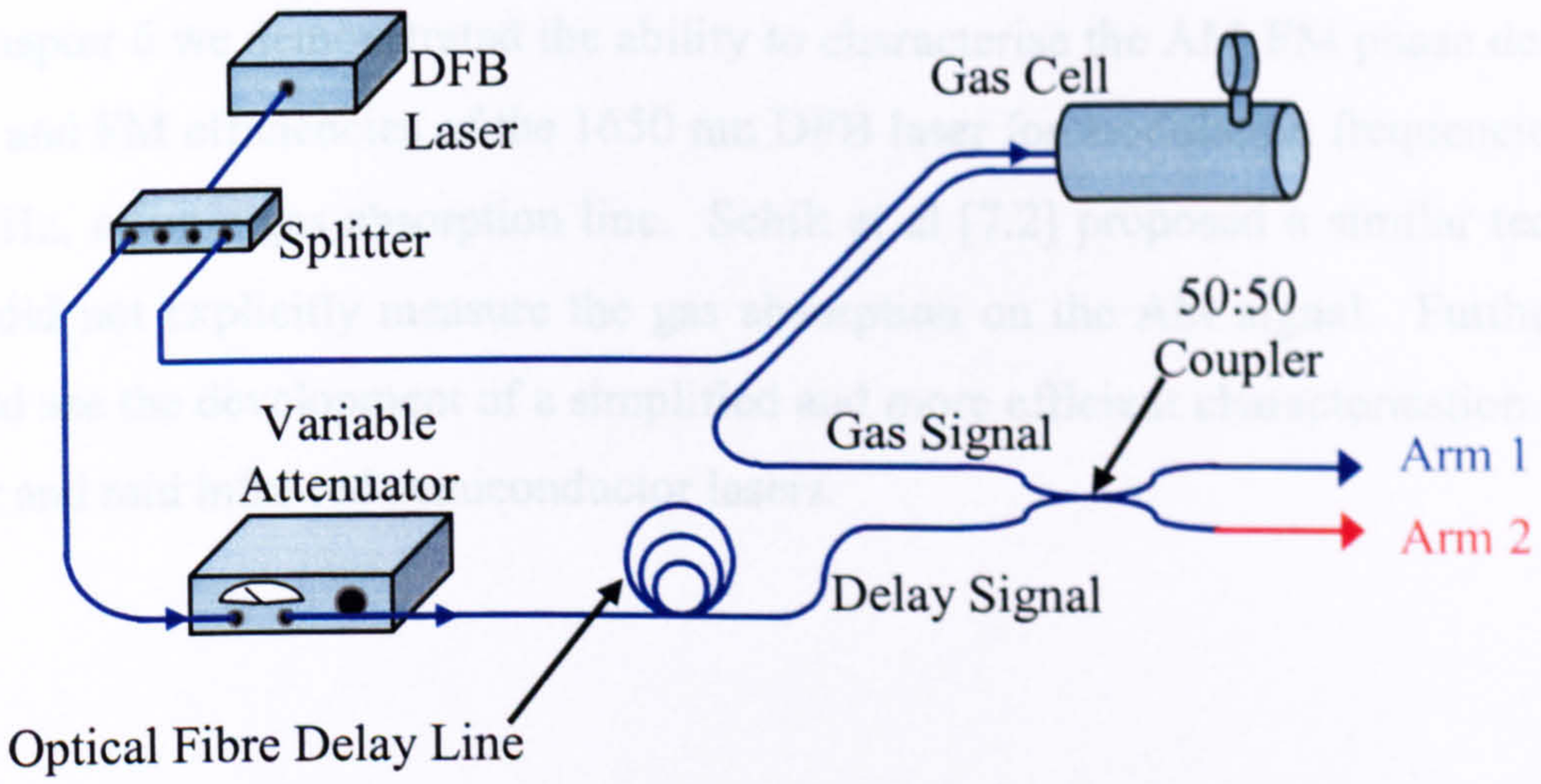

Figure7.1: Diagram of system for nulling RAM

Note that the rest of the laboratory system has been removed from figure 7.1 for clarity. The principle behind the technique is to use a suitable length of fibre in the delay line to create a 180 ° phase shift between the gas signal and the delay signal (both modulated at the same 1.25 MHz frequency) such that, when added together, the signals cancel each other out through destructive interference. A standard 50:50 coupler will inherently have a minor discrepancy in the split ratio and will most likely be around 49:51. With adjustment of the attenuation in the delay signal to

match the amplitude of the gas signal at arm 1, the RAM should be nulled when no gas is present in the cell. At arm 2 a residual RAM signal should be present due to the uneven split ratio. When gas is present in the cell an imbalance in arm 1 will give a signal proportional to the gas absorption line transmission function at the front end of the lock-in amplifier. The imbalance will be relative to a zero background and thus the operation of the lock-in amplifier can be optimised to recover signals at an optimum SNR. The residual signal in arm 2 can be scaled linearly by the split ratio of the coupler to yield the desired background level for normalisation of the RAM variation in arm 1, to give an absolute transmission signal as before. This way we should have sensitivities comparable to conventional TDLS / WMS approaches, whilst measuring an absolute transmission signal.

In chapter 6 we demonstrated the ability to characterise the AM-FM phase delay and AM and FM efficiencies of the 1650 nm DFB laser for modulation frequencies up to 2 MHz, using a gas absorption line. Schilt et al [7.2] proposed a similar technique but did not explicitly measure the gas absorption on the AM signal. Further work could see the development of a simplified and more efficient characterisation tool for near and mid infra-red semiconductor lasers.

7.3 References

[7.1] L. C. Philippe and R. K. Hanson, "Laser Diode Wavelength – Modulation Spectroscopy for Simultaneous Measurement of Temperature, Pressure and Velocity in Shock – Heated Oxygen Flows," Applied Optics, Vol. 32, No. 30, pp 6090-6103, October 1993.

[7.2] S. Schilt and L. Thevenaz, "Experimental Method based on Wavelength - Modulation Spectroscopy for the Characterization of Semiconductor Lasers under Direct Modulation," Applied Optics, Vol. 43, No. 22, pp 4446-4453, August 2004.

Appendix A – Research Publications

A.1 Conferences:

K. Duffin, W. Johnstone, G. Stewart and D. Moodie, "Investigation into Tunable Diode Laser Spectroscopy for use in Harsh Industrial Environments," 5th International Conference on Tunable Diode Laser Spectroscopy, July 2005, Florence, Italy.

W. Johnstone, K. Duffin, A. McGettrick, G. Stewart, A. Cheung and D. Moodie, "Tunable Diode Laser Spectroscopy Over Optical Fibres for Gas Measurements in Harsh Industrial Environments," SPIE Congress on Optics and Optoelectronics, September 2005, Warsaw, Poland.

A. Cheung, B. Culshaw, K. Duffin, W. Johnstone, A. McGettrick and D. Moodie, "Gas Spectroscopy in the Near Infrared Optical Fibre Network," Australasian Conference on Optics, Lasers and Spectroscopy, December 2005, Rotura, New Zealand.

W. Johnstone, K. Duffin, A. McGettrick and G. Stewart, "Recent Advances in Optical Gas Sensing for Industrial Process Monitoring," Invited Paper at the International Conference Photonics 2006, December 2006, Hyderabad, India.

W. Johnstone, K. Duffin and A. McGettrick, "Recent Advances in Tunable Diode Laser Spectroscopy," Invited Paper at the British Council International Workshop on Optical Fibre Systems, December 2006, New Delhi, India.

A.2 Journals:

K. Duffin, A. J. McGettrick, W. Johnstone, G. Stewart and D. Moodie, "Tunable Diode Laser Spectroscopy with Wavelength Modulation: a Calibration-Free Approach to the Recovery of Absolute Gas Absorption Line-Shapes," Submitted to Journal of Lightwave Technology, February 2007.

Appendix B – Fibre Ring-Resonator MATLAB Program

```
%-------------------------------------------------------------------------
%Kevin Duffin
%
%19th August 2006
%
%Program models fibre ring-resonator response based on equations by
%P.Urquhart, see:
%
%(1)"Compound Optical-Fiber-based Resonators,"
%Journal of Optical Society of America, Vol. 5, No. 6, June 1988
%
%(2)"Transversely Coupled Fiber Fabry-Perot Resonator: Theory,"
%Journal of Applied Optics, Vol. 26, No. 3, February 1987.
%
%Change ring lengths l1 and l2 for varying frequency response.
%Change coupling ratios K1 and K2 for varying contrast ratio and
%finesse.
%
%-------------------------------------------------------------------------

format long;

%     Declare variables....

%     Ring lengths of couplers 1 and 2 in metres
l1=0.2;
l2=0.2;

%     Fibre field loss, typically 0.22 dB/m = 10^(2.2e-4/10)
alpha=0.000050658;

%     Wavelength range in  metres
lambda = 1650.9e-9:0.000005e-9:1650.95e-9;

%     Coupling coefficients of couplers 1 and 2
K1=0.8;
K2=0.8;

%     Excess losses of couplers 1 and 2
gamma1 = 0.0;
gamma2 = 0.0;

%     Declare equations....
epsilon1=((1-K1)^0.5)*((1-gamma1)^0.5)*exp(-2*alpha*l1);
epsilon2=((1-K2)^0.5)*((1-gamma2)^0.5)*exp(-2*alpha*l2);
epsilon1_dash=((K1)^0.5)*((1-gamma1)^0.5)*exp(-2*alpha*l1);
epsilon2_dash=((K2)^0.5)*((1-gamma2)^0.5)*exp(-2*alpha*l2);
res_top=(((epsilon1_dash*epsilon2_dash)^2)/exp(-
2*alpha*(l1+(2*l2))));

%     Calculate for each value of wavelength
n = 1:length(lambda);
for n = 1 : length(lambda)
      res_resp(n) = res_top/((1-
      (epsilon1*epsilon2))^2+(4*epsilon1*epsilon2*(sin(((2.88*pi)/la
      mbda(n))*(l1+l2)))^2));

%     Precision issues (max of 10 decimal places) so multiply to
bring to nanometres
      lambda2(n) = lambda(n)*1e9;
```

```
end

plot(lambda2, res_resp)
%     Create matrix of resonator values against wavelength
new_plot = [lambda2' res_resp'];

%     Save matrix
dlmwrite('resonator_resp.txt', new_plot, 'delimiter', '\t',
'precision', '%.10f');
```

Appendix C: 1 – Direct Wavelength Referencing MATLAB Program

```
%-------------------------------------------------------------------------
% Andrew McGettrick and Kevin Duffin
%
% 4th August 2005
%
% Updates:
% Wavelength references the correct way round - i.e. increasing
%wavelength with increasing current! In previous versions, this is
%not the case and can therefore cause a problem!!
% ALSO to use the theoretical spacing to do the wavelength
%referencing properly - problems in every version before this one.
%-------------------------------------------------------------------------
%This script file, when called, asks the user for three files:
%
%1. A Resonator data file.
%2. A theory plot of the specific gas at specific concentration,
%pressure and temperature.
%3. An experimental plot of the aforementioned gas at the
%aforementioned concentration, pressure and temperature.
%
%The data is used to convert the index scale in the experimental
%plot to wavelength.  The amplitude vs. wavelength experimental data
%is then plotted.
%
%-------------------------------------------------------------------------

format long;
%     1.0 Ask user for resonator data file
res_file = input('\n Input resonator data file: ','s');

%     1.1 Load in resonator data file
X = csvread(res_file);
%-------------------------------------------------------------------------

%     2.0 Ask user for theory data file
theory_file = input('\n Input theory data file: ','s');

%     2.1 Load in theory gas line data file
Y = csvread(theory_file);

%     2.2 Theory gas is 2 col matrix - need to extract seperate
%wavelength and index vectors
amps = Y(:,2)'; % Amplitudes in 2nd column of matrix, transpose into
%row
waves = Y(:,1)'; % Wavelengths in 1st column of matrix, transpose
into row
%-------------------------------------------------------------------------

%     3.0 Ask user for experimental data file
exp_file = input(' \n Input experimental data file: ', 's');

%     3.1 Load in experimental gas line data file
Z = csvread(exp_file);

%     3.2  Amplitudes in 1st column of matrix, transpose into row
amps_exp = Z(:,1)';
%-------------------------------------------------------------------------
```

```
%     4.0 Find the resonator peaks

%     4.1 Identify all peak and trough locations in resonator plot
[I JJ]=findpeak(X);

% Declaration of variables
d=2;
dd=1;
ddd=1;
peak=JJ;

%     4.2 Discount any spurious peaks
while ddd<length(JJ)
% If there's a spurious peak overwrite it with the next peak, thus
%shifting all values on the r.h.s of the spurious value left one
%place
   if (JJ(d)-JJ(d-1)) <20
      dd=d;
   while dd<(length(JJ))
      peak(dd)=peak(dd+1);
      dd=dd+1;
   end;
   peak(end)=0;
   peak=peak(1:(end-1));
end;
d=d+1;
ddd=ddd+1;

end;

%     4.3 Declare new vector of correctly identified peaks
JJ=peak;
%-------------------------------------------------------------------

%     5.0 Find the line centre wavelength / frequency of theory
%trace
K = min(amps); % Find the minimum amplitude in the theory plot
K_Index = find(amps == K); % Returns index of the minimum value
Line_Cent_Wave = waves(K_Index); % Wavelength at index K is the
%centre wavelength
Line_Cent_Wave=(3e8/Line_Cent_Wave); % Convert to frequency
%-------------------------------------------------------------------

%     6.0 Find the line centre index from the experimental plot
Q = min(amps_exp); % Find the minimum amplitude in the experimental
%plot
Q_Index = find(amps_exp == Q); % Returns index of the minimum value
Line_Cent_Index = Q_Index(1); % Index at Q is the centre index
%-------------------------------------------------------------------

%     7.0 Find the location of the resonator peak closest to line
%centre
[error1, closest_peak]=min(abs(JJ-Line_Cent_Index));

closest_peak_index=JJ(closest_peak);
%-------------------------------------------------------------------

% Frequency spacing
delta_f= 0.427476249;

%     8.0 Convert resonator peak indices to frequencies
%     8.1 Declare vector for storing frquencies
Res_Peak_Wave = [];

Res_Peak_Wave(closest_peak)=150000;
```

```
FF=length(JJ)+1;
nn=1;
pp=closest_peak;
while nn < FF
   if nn<pp
      Res_Peak_Wave(nn)=[150000+((pp-nn)*delta_f)];
      % Constant added to maintain relevant frequency scale
   end;

   if nn>pp
      Res_Peak_Wave(nn)=[150000-((nn-pp)*delta_f)];
   end;
nn=nn+1;
end;
%-------------------------------------------------------------------------
%     9.0 Make a second order polynomial fit to interpolate between
%the resonator frequencies
P=polyfit(JJ,Res_Peak_Wave,2);
xx=length(amps_exp);
x=[1:1:xx];
YYY=polyval(P, x);
%-------------------------------------------------------------------------

%     10.0 Shift this polynomial to match the experimental file at
%line centre and outwards
YYY_rel=YYY;
shift=Line_Cent_Wave-YYY(Line_Cent_Index);
YYY=YYY+shift;
%-------------------------------------------------------------------------

% Plot experimental values against frequency
plot(YYY, amps_exp);
xlabel('Frequency (GHz)');
ylabel('Relative Transmission');
title('Comparison of theory and experiment');
hold on;

% Save plot
new_plot = [YYY amps_exp];
save_plot = input('\n Save frequency referenced plot as? ','s');
csvwrite(save_plot, new_plot);
%-------------------------------------------------------------------------

figure; %new figure for the wavelength scale

% Plot experimental values against wavelength
YYY_wavelength=3e8./YYY;
plot(YYY_wavelength, amps_exp);
xlabel('Wavelength (nm)');
ylabel('Relative Transmission');

% Save plot
new_plot2 = [YYY_wavelength' amps_exp'];
save_plot2 = input('\n Save wavelength referenced plot as? ','s');
csvwrite(save_plot2, new_plot2);
%-------------------------------------------------------------------------
```

Appendix C: 2 – FINDPEAK MATLAB Program

```
%FINDPEAK  Find the peaks (and valleys) of an arbitrary function.
%
%   FINDPEAK(X) finds the peaks in the data vector X.
%
%   FINDPEAK(X,S) ignores S "peaks" from either end of X.
%   This is necessary when the first and last points of X are not
%   peaks themselves, since ordinarily FINDPEAK(...) considers the
%   endpoints of X to be peaks.
%   The default value for S=1, which for noiseless oscillations X is
%   sufficient to discard the endpoints as being peaks.  Use S=0 to
%   retain the endpoints as being peaks themselves, or some value
%   S>1 to remove false peaks from oscillations with noisy
%endpoints.
%
%   FINDPEAK(...) by itself plots X and marks the peaks and valleys
%   with small crosshairs.
%
%   I=FINDPEAK(...) returns the indices I closest to the valleys and
%   peaks.  The first column contains the valley indices, the second
%   column the peak indices.  LENGTH(I) will thus give the total
%   number of peaks and valleys.
%
%   [I,J]=FINDPEAK(...) returns the indices I closest to each peak
%   minimum, and the indices J closest to each peak maximum.
%   LENGTH(I)+LENGTH(J) will thus equal the total number of peaks
%   and valleys.
%
%   If no peaks are detected then I=J=0 is returned.
%
%   See also SETTLING, STEADY, ZCROSS, PHDIFF.
%
function [minima, maxima] = findpeak(x, strip)
%=======================================================================
%  Copyright © 1998-2000 Julian Andrew de Marchi, Ph.D.
(julian@matlinks.net)
%  Use & distribution covered by GNU General Public License
(www.gnu.org)
%=======================================================================


%If strip = 0, ignore start and end points

%If nargin == 0, no data
%If nargin == 1, data


%------------------
% parse the inputs
%------------------
if (nargin == 0),  error('No data vector X supplied.');
elseif (nargin == 1),  strip = 1;
end;


%-----------------------------
% find the peak_inx and maxima
%-----------------------------
```

```
% Improvement Borja
maxima=[];
minima=[];
%------------------

peak_inx = 1;  inx = 2;  n = 1;

% Check if the first endpoint in 'x' is a maximum or a minimum peak:
if x(2) > x(1)
    minima=[minima 1];
    while (n < length(x)),
        % find the next negative inflection (maxima)
        while (n < length(x) & x(n) <= x(n+1)),
            n = n + 1;
        end;
        if n ~= length(x)
            maxima=[maxima n];
            peak_inx(inx) = n;  n = n + 1;  inx = inx + 1;
        end;
        % find the next postive inflection (minima)
        while (n < length(x) & x(n) >= x(n+1))
            n = n + 1;
        end;
        if n ~= length(x)
            minima=[minima n];
            peak_inx(inx) = n;  n = n + 1;  inx = inx + 1;
        end;
    end;
else
    maxima=[maxima 1];
    while (n < length(x)),
        % find the next postive inflection (minima)
        while (n < length(x) & x(n) >= x(n+1))
            n = n + 1;
        end;
        if n ~= length(x)
            minima=[minima n];
            peak_inx(inx) = n;  n = n + 1;  inx = inx + 1;
        end;

        % find the next negative inflection (maxima)
        while (n < length(x) & x(n) <= x(n+1)),
            n = n + 1;
        end;
        if n ~= length(x)
            maxima=[maxima n];
            peak_inx(inx) = n;  n = n + 1;  inx = inx + 1;
        end;
    end;
end;

if (length(peak_inx) == 1),
  warning('No peaks detected.');
  return;
end;

%-----------------------
% strip boundary peaks
%-----------------------
if (strip),
  strip = min([strip fix(length(peak_inx)/2)]);
  peak_inx = peak_inx(1+strip : length(peak_inx)-strip);
  for i=1:strip
      [aux min_aux]=min([minima(1) maxima(1)]);
```

```
        if min_aux==1
            minima=minima(2:end);
        else
            maxima=maxima(2:end);
        end;
        [aux max_aux]=max([minima(end) maxima(end)]);
        if max_aux==1
            minima=minima(1:end-1);
        else
            maxima=maxima(1:end-1);
        end;
    end;
    clear min_aux max_aux aux;
end;

if (nargout == 0),                          % plot the peaks %
    hold off, plot(x), hold on, plot(1:length(x), x, 'c.');
    plot(minima, x(minima), 'm+', minima, x(minima), 'y.');
    plot(maxima, x(maxima), 'g+', maxima, x(maxima), 'y.');
    title('Peaks'),
    xlabel('i'), ylabel('x(i)'), hold off, zoom on;

end;

if (nargout <= 1),                          % set combination return value %
    minima = peak_inx;
end;
%=========================================================================
% End-of-File
%=========================================================================
```

Appendix C: 3 – Derivative Wavelength Referencing MATLAB Program

```
%-------------------------------------------------------------------------
% Andrew McGettrick & Kevin Duffin
% 4th August 2005
% Wavelength referencing program for 1st derivative signals using
%polynomial fits
%-------------------------------------------------------------------------
%This script file, when called, asks the user for three files;
%
%1. A resonator data file.
%2. A theory plot of the specific gas at specific concentration,
%pressure and temperature.
%3. An experimental plot of the aforementioned gas at the
%aforementioned concentration, pressure
%and temperature.
%
%The data is used to convert the index scale in the experimental
%plot to wavelength.  The
%1st harmonic amplitude vs. wavelength / frequency experimental data
%is then plotted.
%The 1st harmonic signal is also reconstructed to form the absolute
%gas
%absorption line transmission function.
%
%-------------------------------------------------------------------------

format long;

%     1.0 Ask user for resonator data file
res_file = input('\n Input resonator data file: ','s');

%     1.1 Load in resonator data file
X = csvread(res_file);
%-------------------------------------------------------------------------

%     2.0 Ask user for theory data file
theory_file = input('\n Input theory data file: ','s');

%     2.1 Load in theory data file
Y = csvread(theory_file);

%     2.2 Theory data file is 2 column matrix - need to extract
%separate wavelength and index vectors

%     Amplitudes in 2nd column of matrix, transpose into row
amps = Y(:,2)';

%     Wavelengths in 1st column of matrix, transpose into row
waves = Y(:,1)';
%-------------------------------------------------------------------------

%     3.0 Ask user for experimental data file
exp_file = input(' \n Input experimental data file: ', 's');

%     3.1 Load in experimental data file
Z = csvread(exp_file);

%     3.2 Amplitudes in 1st column of matrix, transpose into row
amps_exp = Z(:,1)';
%-------------------------------------------------------------------------
```

```
%     4.0 Identify correct locations of peaks and troughs in
%resonator plot

%     4.1 Identify all peak and trough locations in resonator plot
[I JJ]=findpeak(X);

%     Declaration of variables
d=2;
dd=1;
ddd=1;
peak=JJ;

%     4.2 Discount any spurious peaks
while ddd<length(peak)

%     If there's a spurious peak overwrite it with the next peak,
%thus shifting all values on the r.h.s of the spurious value left
%one place
   if (peak(d)-peak(d-1)) <20
      dd=d;
   while dd<(length(peak))
      peak(dd)=peak(dd+1);
      dd=dd+1;
   end;
   peak(end)=0;
   peak=peak(1:(end-1));
end;
d=d+1;
ddd=ddd+1;

end;

%     4.3 Declare new vector of correctly identified peaks
JJ=peak;

%     Declaration of variables
d=2;
dd=1;
ddd=1;
troughs=I;

%     4.4 Discount any spurious troughs
while ddd<length(troughs)

%     If there's a spurious trough overwrite it with the next
%trough, thus shifting all values on the r.h.s of the spurious value
%left one place
   if (troughs(d)-troughs(d-1)) <20
      dd=d;
   while dd<(length(troughs))
      troughs(dd)=troughs(dd+1);
      dd=dd+1;
   end;
   troughs(end)=0;
   troughs=troughs(1:(end-1));
end;
d=d+1;
ddd=ddd+1;

end;

%     4.5 Declare new vector of correctly identified troughs
I=troughs;
%-------------------------------------------------------------------

%     5.0 Identify correct locations for zero crossings
```

```
%     5.1 Create matrix for storing zero crossing locations
zero_crossings=[];

%     Zero crossings are located half-way between peaks and troughs
zz=1;
while zz <= length(JJ) & zz <= length(I)
   zero_crossings(zz)=(JJ(zz)+I(zz))/2;
   zz=zz+1;
end;

zz=1;

%     5.2 Declare new vector of correctly identified zero-crossings
JJ=zero_crossings;
%-------------------------------------------------------------------

%     6.0 Find the line centre wavelength of the theory plot
K = min(amps);
K_Index = find(amps == K);
Line_Cent_Wave = waves(K_Index);

%     Create an arb. constant to set up relative wavelength /
%frequency scale

Line_Cent_Wave= 150000;
%-------------------------------------------------------------------


%     7.0 Find the line centre index from the experimental plot
Q = min(amps_exp);
Q_Index = find(amps_exp == Q);
QQ = max(amps_exp);
QQ_Index = find(amps_exp == QQ);

positive_peak= QQ_Index(1);
negative_peak= Q_Index(1);

%     Declare variables
nnn=1;
zero_amps = [];

%     7.1 Declare a vector containing the experimental values
%between the positive and negative peaks
while nnn<positive_peak

if nnn>negative_peak
   zero_amps(nnn-negative_peak)=amps_exp(nnn);
end;

nnn=nnn+1;

end;

%     7.2 Find the value closest to zero in the new vector
%"zero_amps"
[error111, closest_zero_amps]=min(abs(zero_amps-0));
closest_zero_amps=closest_zero_amps + negative_peak;

Line_Cent_Index = closest_zero_amps(1);
%-------------------------------------------------------------------

%     8.0 Find location of closest zero-crossing to the line centre
%of the experimental plot
[error1, closest_peak]=min(abs(JJ-Line_Cent_Index));
%-------------------------------------------------------------------

%     Frequency spacing
```

```
delta_f= 0.427476249;

%     9.0 Convert zero-crossing indices to frequencies
%     9.1 Declare vector for storing frequencies
Res_Peak_Wave = [];

Res_Peak_Wave(closest_peak)=150000;

FF=length(JJ)+1;
nn=1;
pp=closest_peak;
while nn < FF
   if nn<pp
      Res_Peak_Wave(nn)=[Line_Cent_Wave+((pp-nn)*delta_f)];
   end;
   if nn>pp
      Res_Peak_Wave(nn)=[Line_Cent_Wave-((nn-pp)*delta_f)];
   end;
nn=nn+1;
end;
%-------------------------------------------------------------------

%     10.0 Make a second order polynomial fit to interpolate between
%the resonator frequencies
P=polyfit(JJ,Res_Peak_Wave,2);
xx=length(amps_exp);
x=[1:1:xx];

% Extract values of polynomial fit at each increment x
YYY=polyval(P, x);
%-------------------------------------------------------------------

%     11.0 Shift this polynomial to match the experimental file at
%ine centre and outwards
Line_Cent_freq = 3e8./waves(K_Index);
shift=Line_Cent_freq-YYY(Line_Cent_Index);
YYY=YYY+shift;
%-------------------------------------------------------------------

%     12.0 Plot Experimental values against frequency
plot(YYY, amps_exp);
xlabel('Frequency (GHz)');
ylabel('a.u.');
title('Frequency Referenced Plot');
hold on;

%     Save plot
new_plot = [YYY' amps_exp'];
dlmwrite('frequency.txt', new_plot, 'delimiter', '\t', 'precision',
'%.6f');

figure;

%     13.0 Plot Experimental values against wavelength
YYY_wavelength=3e8./YYY;
plot(YYY_wavelength, amps_exp);
xlabel('Wavelength(nm)');
ylabel('a.u.');
title('Wavelength Referenced Plot');
%-------------------------------------------------------------------

%     14.0 Integrate 1st derivative to return to fundamental
%transmission profile
reconstructed_line=cumtrapz(YYY_wavelength, amps_exp);
figure;
%-------------------------------------------------------------------
```

```
%     15.0 Plot integrated Experimental values against wavelength
plot(YYY_wavelength,cumtrapz(YYY_wavelength, amps_exp));
xlabel('Wavelength (nm)');
ylabel('Relative Transmission');
title('Wavelength Referenced Reconstructed PLot');

grid on;

%      Save plots
waves_exp = YYY_wavelength';
new_amps_exp = amps_exp';
new_plot2 = [waves_exp new_amps_exp];
new_plot3=[waves_exp reconstructed_line'];
dlmwrite('wavelength.txt', new_plot2, 'delimiter', '\t',
'precision', '%.6f');
dlmwrite('reconstructed.txt', new_plot3, 'delimiter', '\t',
'precision', '%.6f');
%-------------------------------------------------------------------------
```

Appendix C: 4 – RAM Wavelength Referencing MATLAB Program

```
%-------------------------------------------------------------------------
% Kevin Duffin and Andrew McGettrick
% 4th August 2005
% Wavelength referencing program for Separated R.A.M signals using
%polynomial fits
%-------------------------------------------------------------------------

%This script file, when called, asks the user for three files;
%
%1. A resonator data file.
%2. A theory plot of the specific gas at specific concentration,
%pressure and temperature.
%3. An experimental plot of the aforementioned gas at the
%aforementioned concentration, pressure
%and temperature.
%
%The data is used to convert the index scale in the experimental
%plot to wavelength.  The
%amplitude vs. wavelength experimental data is then plotted.
%
%-------------------------------------------------------------------------

format long

%     1.0 Ask user for resonator data file
res_file = input('\n Input resonator data file: ','s');

%     1.1 Load in resonator data file
X = csvread(res_file);
%-------------------------------------------------------------------------

%     2.0 Ask user for theory data file
theory_file = input('\n Input theory data file: ','s');

%     2.1 Load in theory data file
Y = csvread(theory_file);

%     2.2 Theory data file is 2 column matrix - need to extract
%separate wavelength and index vectors

%     Amplitudes in 2nd column of matrix, transpose into row

%     Wavelengths in 1st column of matrix, transpose into row
amps = Y(:,2)'; waves = Y(:,1)';
%-------------------------------------------------------------------------

%     3.0 Ask user for experimental data file
exp_file = input(' \n Input experimental data file: ', 's');

%     3.1 Load in experimental data file
Z = csvread(exp_file);

%     3.2 Amplitudes in 1st column of matrix, transpose into row
amps_exp = Z(:,1)';
%-------------------------------------------------------------------------

%     4.0 Identify correct locations of peaks and troughs in
%resonator plot

%     4.1 Identify all peak and trough locations in resonator plot
```

```
[I JJ]=findpeak(X);

%     Declaration of variables
d=2;
dd=1;
ddd=1;
peak=JJ;

%     4.2 Discount any spurious peaks
while ddd<length(peak)
%     If there's a spurious peak overwrite it with the next peak,
%thus shifting all values on the r.h.s of the spurious value left
%one place
   if (peak(d)-peak(d-1)) <20
      dd=d;
   while dd<(length(peak))
      peak(dd)=peak(dd+1);
      dd=dd+1;
   end;
   peak(end)=0;
   peak=peak(1:(end-1));
end;
d=d+1;
ddd=ddd+1;

end;

%     4.3 Declare new vector of correctly identified peaks
JJ=peak;

%     Declaration of variables
d=2;
dd=1;
ddd=1;
troughs=I;

%     4.4 Discount any spurious troughs
while ddd<length(troughs)
%     If there's a spurious trough overwrite it with the next
%trough, thus shifting all values on the r.h.s of the spurious value
%left one place
   if (troughs(d)-troughs(d-1)) <20
      dd=d;
   while dd<(length(troughs))
      troughs(dd)=troughs(dd+1);
      dd=dd+1;
   end;
   troughs(end)=0;
   troughs=troughs(1:(end-1));
end;
d=d+1;
ddd=ddd+1;

end;

%     4.5 Declare new vector of correctly identified troughs
I=troughs;
%-----------------------------------------------------------------

%     5.0 Identify correct locations for zero crossings
%     5.1 Create matrix for storing zero crossing locations
zero_crossings=[];

%      Zero crossings are located half-way between peaks and troughs
zz=1;
while zz <= length(JJ) & zz <= length(I)
   zero_crossings(zz)=(JJ(zz)+I(zz))/2;
```

```
   zz=zz+1;
end;

zz=1;
%    5.2 Declare new vector of correctly identified zero-crossings
JJ=zero_crossings;
%-----------------------------------------------------------------

%     6.0 Find the line centre wavelength / frequency of theory
%trace

% Find the minimum amplitude in the theory plot
K = min(amps);
K_Index = find(amps == K); % Returns index of the minimum value

Line_Cent_Wave = waves(K_Index); % Wavelength at index K is the
%centre wavelength
Line_Cent_Wave=(3e8/Line_Cent_Wave); % Convert to frequency
%-----------------------------------------------------------------


%     7.0 Find the line centre index from the experimental plot
Q = min(amps_exp); % Find the minimum amplitude in the experimental
%plot
Q_Index = find(amps_exp == Q); % Returns index of the minimum value
Line_Cent_Index = Q_Index(1); % Index at Q is the centre index
%-----------------------------------------------------------------


%     8.0 Find resonator peak location of closest resonator peak to
%the line centre of the experimental plot
[error1, closest_peak]=min(abs(JJ-Line_Cent_Index));
%-----------------------------------------------------------------

% Frequency spacing
delta_f= 0.427476249;

%     9.0 Convert resonator peak indices to frequencies
%     9.1 Declare vector for storing frquencies
Res_Peak_Wave = [];

Res_Peak_Wave(closest_peak)=150000;

FF=length(JJ)+1;
nn=1;
pp=closest_peak;
while nn < FF
   if nn<pp
      Res_Peak_Wave(nn)=[150000+((pp-nn)*delta_f)];
      % Constant added to set up relevant frequency scale
   end;

   if nn>pp
      Res_Peak_Wave(nn)=[150000-((nn-pp)*delta_f)];
   end;
nn=nn+1;
end;
%-----------------------------------------------------------------

%     10.0 Make a second order polynomial fit to interpolate between
%the resonator frequencies
P=polyfit(JJ,Res_Peak_Wave,2);
xx=length(amps_exp);
x=[1:1:xx];
YYY=polyval(P, x);
%-----------------------------------------------------------------
```

```
%     11.0 Shift this polynomial to match the experimental plot at
%line centre and outwards
YYY_rel=YYY;
shift=Line_Cent_Wave-YYY(Line_Cent_Index);
YYY=YYY+shift;
%-------------------------------------------------------------------

%     Plot experimental values against frequency
plot(YYY, amps_exp);
xlabel('Frequency (GHz)');
ylabel('Relative Transmission');
title('Comparison of theory and experiment');
hold on;

%     Save plot
new_plot = [YYY amps_exp];
dlmwrite('frequency.txt', new_plot, 'delimiter', '\t', 'precision',
'%.6f');
%-------------------------------------------------------------------

figure; %new figure for the wavelength scale

%     Plot experimental values against wavelength
YYY_wavelength=3e8./YYY;
plot(YYY_wavelength, amps_exp);
xlabel('Wavelength (nm)');
ylabel('Relative Transmission');

%     Save plot
new_plot2 = [YYY_wavelength' amps_exp'];
dlmwrite('lambda.txt', new_plot2, 'delimiter', '\t', 'precision',
'%.6f');
%-------------------------------------------------------------------
```

Appendix D – 2nd Order Taylor Series Expansion of Lorentzian Broadened Absorption Line

The intensity (I) of the laser source at a particular frequency (ν_1) is given by:

$$I = I(\nu_1) + \Delta I(\nu_1)\cos(\omega t) \tag{A1}$$

The output intensity from an absorbing medium is thus given by:

$$I_{out} \approx [I(\nu_1) + \Delta I(\nu_1)\cos(\omega t)](1 - \alpha(\nu)Cl) \tag{A2}$$

A Taylor series expansion of the lineshape $\alpha(\nu_1)$ around ν_1 is:

$$\alpha(\nu) = \alpha(\nu_1) + \frac{d\alpha(\nu_1)}{d\nu}.[\nu - \nu_1] + \frac{1}{2}.\frac{d^2\alpha(\nu_1)}{d\nu^2}.[\nu - \nu_1]^2 + \ldots \tag{A3}$$

Therefore:

$$I_{out} \approx [I(\nu_1) + \Delta I(\nu_1)\cos(\omega t)]\times \tag{A4}$$
$$\left(1 - \alpha(\nu_1).Cl - \alpha'(\nu_1).Cl.\delta\nu.\cos(\omega t - \psi) - \frac{1}{2}.\alpha''(\nu_1).Cl.\delta\nu^2.\cos^2(\omega t - \psi)\right)$$

Multiplying out bracketed terms in equation (A4) gives

$$\begin{aligned} I_{out} = {} & I(\nu_1) + \Delta I(\nu_1).\cos(\omega t) \\ & - I(\nu_1).\alpha(\nu_1).Cl - \Delta I(\nu_1).\alpha(\nu_1).cl.\cos(\omega t) \\ & - I(\nu_1).\alpha'(\nu_1).Cl.\delta\nu.\cos(\omega t - \psi) - \Delta I(\nu_1).\alpha'(\nu_1).cl.\delta\nu.\cos(\omega t)\cos(\omega t - \psi) \\ & - \frac{1}{2}I(\nu_1).\alpha''(\nu_1).Cl.\delta\nu^2.\cos^2(\omega t - \psi) - \frac{1}{2}\Delta I(\nu_1).\alpha''(\nu_1).cl.\delta\nu^2.\cos(\omega t)\cos^2(\omega t - \psi) \end{aligned} \tag{A5}$$

Using the trigonometric identities:

$$cos(\omega t)cos(\omega t-\psi)=\frac{1}{2}(cos(2\omega t-\psi)+cos(\psi))$$

and

$$cos^2(\omega t-\psi)=\frac{1}{2}(1+cos\,2(\omega t-\psi))$$

equation (A5) now becomes:

$$\begin{aligned}I_{out}&=I(\nu_1)+\Delta I(\nu_1).cos(\omega t)\\&-I(\nu_1).\alpha(\nu_1).Cl-\Delta I(\nu_1).\alpha(\nu_1).cl.cos(\omega t)\\&-I(\nu_1).\alpha'(\nu_1).Cl.\delta\nu.cos(\omega t-\psi)-\frac{1}{2}\Delta I(\nu_1).\alpha'(\nu_1).cl.\delta\nu.(cos(2\omega t-\psi)+cos(\psi))\\&-\frac{1}{4}I(\nu_1).\alpha''(\nu_1).Cl.\delta\nu^2.(1+cos\,2(\omega t-\psi))\\&-\frac{1}{4}\Delta I(\nu_1).\alpha''(\nu_1).cl.\delta\nu^2.\left[cos(\omega t)+\frac{1}{2}\{cos(3\omega t-2\psi)+cos(2\psi-\omega t)\}\right]\end{aligned}\tag{A6}$$

The DC term then becomes:

$$I_{DC}=I(\nu_1)\cdot\{1-\alpha(\nu_1)Cl\}\tag{A7}$$

With the lock-in set to the 1st harmonic the output becomes:

$$\begin{aligned}I_{\omega}&=\Delta I(\nu_1)\cdot cos(\omega t)-\Delta I(\nu_1)\cdot\alpha(\nu_1)\cdot Cl\cdot cos(\omega t)\\&-I(\nu_1)\cdot\alpha'(\nu_1)\cdot Cl\cdot\delta\nu\cdot cos(\omega t-\psi)\end{aligned}\tag{A8}$$

With the lock-in set to the 2nd harmonic the output becomes:

$$\begin{aligned}I_{2\omega}&=-\frac{1}{2}\cdot\Delta I(\nu_1)\cdot\alpha'(\nu_1)\cdot Cl\cdot\delta\nu\cdot cos(2\omega t-\psi)\\&-\frac{1}{4}\cdot I(\nu_1)\cdot\alpha''(\nu_1)\cdot Cl\cdot\delta\nu^2\cdot cos\,2(\omega t-\psi)\end{aligned}\tag{A9}$$

The terms left over and considered negligible for small $\delta\nu$ are:

$$I_{negligible} = -\frac{1}{2}\Delta I(\nu_1).\alpha'(\nu_1).Cl.\delta\nu.(cos(\psi)) \qquad \text{(A10)}$$

$$-\frac{1}{4}I(\nu_1).\alpha''(\nu_1).Cl.\delta\nu^2$$

$$-\frac{1}{4}\Delta I(\nu_1).\alpha''(\nu_1).Cl.\delta\nu^2.\left[cos(\omega t)+\frac{1}{2}\{cos(3\omega t-2\psi)+cos(2\psi-\omega t)\}\right]$$